



**Universitat**  
de les Illes Balears

DOCTORAL THESIS

---

**Gravitational wave data analysis for  
the advanced detector era**

---

*Author:*  
Miquel OLIVER ALMIÑANA

2019





**Universitat**  
de les Illes Balears

DOCTORAL THESIS  
2019

Doctoral Programme of Physics

---

# Gravitational wave data analysis for the advanced detector era

---

*Author:*

Miquel OLIVER ALMIÑANA

*Supervisors:*

Dr. Alicia M. SINTES OLIVES

Dr. Sascha HUSA

*Tutor:*

Dr. Carles BONA GARCIA

*Doctor by the Universitat de les Illes Balears*





**Universitat**  
de les Illes Balears

WE, THE UNDERSIGNED DECLARE:

That the thesis titles

*Gravitational wave data analysis for the  
advanced detector era,*

presented by Sr. Miquel Oliver Almiñana to obtain a doctoral degree, has been completed under my supervision Dra. Alicia Magdalena Sintes Olives and Dr. Sascha Husa.

For all intents and purposes, I hereby sign this document.

Palma de Mallorca,

---

Sr. Miquel Oliver Almiñana

---

Dra. Alicia Magdalena Sintes Olives

---

Dr. Sascha Husa



## *List of Publications*

- Oliver, Miquel, David Keitel, and Alicia M. Sintes (2019). “The Adaptive Transient Hough method for long-duration gravitational wave transients”. In: *Phys. Rev.* arXiv: 1901.01820 [gr-qc].
- Driggers, J. C. et al. (2019). “Improving astrophysical parameter estimation via offline noise subtraction for Advanced LIGO”. In: *Phys. Rev. D* 99.4, p. 042001. doi: 10.1103/PhysRevD.99.042001. arXiv: 1806.00532 [astro-ph.IM].
- Oliver, Miquel et al. (2018). “Matched-filter study and energy budget suggest no detectable gravitational-wave ‘extended emission’ from GW170817”. In: *Monthly Notices of the Royal Astronomical Society*, Volume 485, Issue 1, May 2019, Pages 843–850. doi: 10.1093/mnras/stz439. arXiv: 1812.06724 [astro-ph.HE].
- Abbott, B. P. et al. (2018c). “Search for gravitational waves from a long-lived remnant of the binary neutron star merger GW170817”. In: *The Astrophysical Journal Letters*, Volume 851, Number 1. doi: 10.3847/2041-8213/aa9a35. arXiv: 1810.02581 [gr-qc]
- Covas, P. B. et al. (2018). “Identification and mitigation of narrow spectral artifacts that degrade searches for persistent gravitational waves in the first two observing runs of Advanced LIGO”. In: *Phys. Rev.* 97.8, p. 082002. doi: 10.1103/PhysRevD.97.082002. arXiv: 1801.07204 [astro-ph.IM].
- Abbott, Benjamin P. et al. (2018e). “Full Band All-sky Search for Periodic Gravitational Waves in the O1 LIGO Data”. In: *Phys. Rev. D* 97.10, p. 102003. doi: 10.1103/PhysRevD.97.102003. arXiv: 1802.05241 [gr-qc].
- Walker, M. et al. (2017). “Effects of transients in LIGO suspensions on searches for gravitational waves”. In: *Rev. Sci. Instrum.* 88.12, p. 124501. doi: 10.1063/1.5000264. arXiv: 1702.04701 [astro-ph.IM].
- Abbott, Benjamin P. et al. (2017f). “All-sky Search for Periodic Gravitational Waves in the O1 LIGO Data”. In: *Phys. Rev. D* 96.6, p. 062002. doi: 10.1103/PhysRevD.96.062002. arXiv: 1707.02667 [gr-qc].
- Walsh, Sinead et al. (2016). “Comparison of methods for the detection of gravitational waves from unknown neutron stars”. In: *Phys. Rev. D* 94.12, p. 124010. doi: 10.1103/PhysRevD.94.124010. arXiv: 1606.00660 [gr-qc].





UNIVERSITAT DE LES ILLES BALEARS

*Abstract*

Universitat de les Illes Balears  
Doctoral Programme of Physics

Doctor of Physics

**Gravitational wave data analysis for the advanced detector era**

by Miquel OLIVER ALMIÑANA

## ENGLISH

Gravitational wave astronomy became a reality on September 2015 with the LIGO-Virgo discovery of a distant and massive binary black hole coalescence. The more recent discovery of a binary neutron star merger in August 2017, followed by a gamma ray burst and a kilonova, reinforces the expectation of observing the first almost monochromatic continuous gravitational wave; these type signals are supposed to be emitted by spinning non-axisymmetric compact objects e.g neutron stars. This thesis is devoted to the search of gravitational wave emissions from isolated compact objects in our own galaxy. However, even after considering their relative proximity compared to the compact binary mergers we have observed to date, these gravitational-wave are very elusive as their strain amplitudes are orders of magnitude weaker i.e.  $O(10^{-25})$  compared to the typical  $O(10^{-21})$  observed from compact binary mergers. Due to this the detection of such weak signals would be the result of long time spans integration of data, this problem translates in a threshold sensitivity and parameter space volume due to limited computational resources.

The main work has focused on the development and optimization of semi-coherent methods, based on the Hough transform, to search for continuous sinusoidal gravitational wave signals from unknown continuous sources e.g neutron stars that do not beam a radio signal in the earth's direction and for signals of intermediate durations (of the order of hours to days) as applied in the GW170817 post-merger remnant search for a newborn neutron star.

The work I present here has been crucial for a number of continuous wave searches in data from the advanced LIGO detectors, which are collected in this thesis. My contributions have been included in three LIGO-Virgo full collaboration papers in which I had a leading role, as well as in several short author papers. I have also been involved in multiple updates of the LSC Data Analysis Software (*LIGO Algorithm Library - LALSuite*), including a new full search for transient gravitational waves of intermediate duration.

## CATALAN

L'astronomia de les ones gravitacionals es va iniciar al setembre de 2015 amb el descobriment d'una coalescència binària distant i massiva de forats negres, portada a terme per la col·laboració LIGO-Virgo. El més recent descobriment d'una fusió d'estrelles de neutrons binaris, seguit d'un esclat de raigs gamma i una kilonova, reforcen l'interès d'aquesta nova etapa, en la que aviat podrem veure altres fonts d'ones gravitacionals, incloent les contínues, senyals gairebé monocromàtiques emeses per objectes compactes que giren, especialment les estrelles de neutrons no axisimètriques, en la nostra pròpia galàxia. Malgrat la seva relativa proximitat (diversos kpc davant de desenes a centenars de Mpc), s'espera que aquestes fonts produeixin amplituds d'ones gravitacionals en ordres de magnitud més feble que els vistos a coalescències de sistemes binaris compactes, és a dir,  $O(10^{-25})$  o més petit en comparació amb  $o(10^{-21})$ .

La nostra única possibilitat de detectar senyals tan febles prové de la integració de dades sobre períodes de llarga durada, però aquestes integracions incorren, en la majoria de les recerques, en enormes costos computacionals per a cobrir de manera sistemàtica una porció rellevant de l'espai de paràmetres. Aquesta tesi està dedicada a la recerca d'emissions d'ones gravitacionals per objectes compactes aïllats: estrelles de neutrons. El treball principal s'ha centrat en el desenvolupament i optimització

de mètodes semi coherents, basats en la transformada de Hough, per buscar senyals d'ones gravitacionals sinusoidals contínues de fonts contínues desconegudes: estrelles de neutrons que no emeten una ràdio senyal en direcció a la Terra, i per a senyals de durades intermèdies (de l'ordre d'hores a dies) -com aplicat en la recerca de romanents post-fusió GW170817 per un estel de neutrons acabat de néixer.

El treball que present ha estat crucial per a les publicacions sobre les ones contínues utilitzant les dades dels detectors LIGO avançats que es recopilen en aquesta tesi. Les seves contribucions han estat incloses en tres publicacions de la col·laboració completa de LIGO-Verge, en què el meva feina va tenir un paper protagonista, així com en diverses publicacions amb llistes breus d'autors. Ha estat involucrat en múltiples actualitzacions de les dades de LSC.Software d'anàlisi (*LIGO Algorithm Library - LALSuite*), inclosa una nova recerca completa d'ones gravitacionals transitòries de durada intermèdia.

## SPANISH

La astronomía de las ondas gravitacionales se inició en septiembre de 2015 con el descubrimiento de una coalescencia binaria distante y masiva de agujeros negros, llevada a cabo por la colaboración LIGO-Virgo. El más reciente descubrimiento de una fusión de estrellas de neutrones binarios, seguido de un estallido de rayos gamma y una kilonova, refuerzan el interés de esta nueva etapa, en la que pronto podremos ver otras fuentes de ondas gravitacionales, incluyendo las continuas, señales casi monocromáticas emitidas por objetos compactos que giran, especialmente las estrellas de neutrones no axisimétricas, en nuestra propia galaxia. A pesar de su relativa cercanía (varios kpc frente a decenas a cientos de Mpc), se espera que tales fuentes produzcan amplitudes de ondas gravitacionales en órdenes de magnitud más débil que los vistos en coalescencias de sistemas binarios compactos, es decir,  $O(10^{-25})$  o más pequeño en comparación con  $O(10^{-21})$ .

Nuestra única posibilidad de detectar señales tan débiles proviene de la integración de datos sobre periodos de larga duración, pero estas integraciones incurren, en la mayoría de las búsquedas, en enormes costes computacionales para cubrir de manera sistemática una porción relevante del espacio de parámetros. Esta tesis está dedicada a la búsqueda de emisiones de ondas gravitacionales por objetos compactos aislados: estrellas de neutrones. El trabajo principal se ha centrado en el desarrollo y optimización de métodos semi coherentes, basados en la transformada de Hough, para buscar señales de ondas gravitacionales sinusoidales continuas de fuentes continuas desconocidas: estrellas de neutrones que no emiten una radio señal en dirección a la Tierra, y para señales de duraciones intermedias (del orden de horas a días) aplicado en la búsqueda de remanentes post-fusión GW170817 para una estrella de neutrones recién nacida.

El trabajo que presento ha sido crucial para una de publicaciones sobre las ondas continuas utilizando los datos de los detectores LIGO avanzados que se recopilan en esta tesis. Sus contribuciones han sido incluidas en tres publicaciones de la colaboración completa de LIGO-Virgo, en los que mi papel tuvo un caracter protagonista, así como en varias publicaciones con listas breves de autores. Ha estado involucrado en múltiples actualizaciones de los datos de LSC.Software de análisis (*LIGO Algorithm Library - LALSuite*), incluida una nueva búsqueda completa de ondas gravitacionales transitorias de duración intermedia.



## *Acknowledgements*

First and foremost I would like to express my gratitude to those who have advised me and who gave me a clear path:

Alicia M. Sintes Olives for extreme patience and comprehension; for allowing me to learn my own way, but pushing me always in a good direction; most of all for giving me the opportunity to contribute and collaborate in the most exiting adventure of my life. Sascha Husa for his proximity and willingness to talk and explain details of this exciting but complex field. Irene Di Palma for all the conversations an encouragement given to me during this time, to David Keitel for helping develop some of my projects, many great discussions and advice, to the members of the Gravitational Physics group of the Universitat de les Illes Balears and specially to Rafel, Juan, Xisco, Hector, Rodrigo and all the other students. The Hanford group members whom I will never forget, especially Michael Landry for giving me the opportunity to live first hand the GW140915 event, also to Jeff Kissel for the patience and mostly for the good times, as well as to all the fellows that where with me during that special moment, supported by the LIGO LSC Fellows Program.

The research related to this thesis has been done as a member of the Continuous Wave data analysis working group of the LIGO Scientific Collaboration and supported by the Spanish Agencia Estatal de Investigación and Ministerio de Ciencia, Innovación y Universidades project FPA2013-41042-P via the FPI grant BES-2014-068162 and grants FPA2016-76821-P, FPA2017-90687-REDC, FPA2017-90566-REDC, FIS2016-81770-REDT, FPA2015-69815-REDT, FPA2015-68783-REDT, and FPA2015-69037-REDC.

I also acknowledge the support of the the Vicepresidencia i Conselleria d'Innovació, Recerca i Turisme del Govern de les Illes Balears, the European Union FEDER funds, and the EU COST Actions CA16104, CA16214, CA17137 and CA18108.

I also had the privilege to spend three months at the AEI Hannover, funded by BES-2014-068162.



# Contents

<b>List of Publications</b>	<b>iii</b>
<b>Abstract</b>	<b>vi</b>
<b>Acknowledgements</b>	<b>ix</b>
<b>1 Introduction</b>	<b>3</b>
1.1 Gravitational wave characterization . . . . .	4
1.2 Mass-quadrupole moment of an isolated object . . . . .	4
1.3 Astrophysical Priors . . . . .	6
1.4 Detector’s response . . . . .	8
1.5 Detector’s sensitivity . . . . .	9
1.6 Signal recovery strategies . . . . .	10
1.6.1 Semi-coherent analysis . . . . .	11
1.7 Search sensitivity estimate . . . . .	12
1.8 CW Searches with Astrophysical Priors . . . . .	13
<b>2 The Hough transform search for continuous GWs</b>	<b>19</b>
2.1 The <i>SkyHough</i> pipeline implementation . . . . .	19
2.1.1 The Short-time Fourier Transform of the signal . . . . .	20
2.1.2 The Hough maps . . . . .	21
2.1.3 Resolution in the space of sky-positions and spin-down parameters: . . . . .	23
2.2 The Hough post-processing . . . . .	23
2.2.1 Critical Ratio - $\Psi$ . . . . .	24
2.2.2 Derivation of the $\chi^2$ statistics . . . . .	24
2.2.3 Construction of coincidences . . . . .	26
2.2.4 Clustering method . . . . .	27
<b>3 A comparison of methods for the detection of gravitational waves from unknown neutron stars</b>	<b>29</b>
S. WALSH, M. PITKIN, M. OLIVER, S. D’ANTONIO, V. DERGACHEV, A. KRÓLAK, P. ASTONE, M. BEJGER, M. DI GIOVANNI, O. DOROSH, S. FRASCA, P. LEACI, S. MASTROGIOVANNI, A. MILLER, C. PALOMBA, M. A. PAPA, O. J. PICCINNI, K. RILES, O. SAUTER, A. M. SINTES	
3.1 Introduction . . . . .	29
3.2 The signal . . . . .	30
3.3 Current methods . . . . .	30
3.3.1 Powerflux . . . . .	31
3.3.2 Sky Hough . . . . .	32
3.3.3 Time domain $\mathcal{F}$ -Statistic . . . . .	32
3.3.4 Einstein@Home . . . . .	32
3.3.5 Frequency Hough . . . . .	33
3.4 The mock data challenge . . . . .	33
3.4.1 The data . . . . .	34

3.4.2	The MDC search . . . . .	34
3.4.3	Defining detections . . . . .	35
3.5	Comparison of methods . . . . .	36
3.5.1	Detection efficiency . . . . .	36
3.5.2	Parameter estimation . . . . .	36
3.5.3	Computational cost . . . . .	36
3.6	Implementation . . . . .	37
3.6.1	Powerflux . . . . .	37
3.6.2	Sky Hough . . . . .	38
3.6.3	Time domain $\mathcal{F}$ -statistic . . . . .	39
3.6.4	Einstein@Home . . . . .	39
3.6.5	Frequency Hough . . . . .	40
3.7	Results . . . . .	41
3.7.1	Detection efficiency . . . . .	41
3.7.1.1	Robustness in the presence of detector artifacts . . . . .	41
3.7.1.2	Dependence on signal frequency or spindown . . . . .	42
3.7.1.3	Dependence on signal second order spindown . . . . .	46
3.7.2	Signal parameter recovery . . . . .	46
3.8	Conclusion . . . . .	50
3.A	Comparing results with known and blind injections . . . . .	53
<b>4</b>	<b>All-sky Search for periodic gravitational waves in the O1 LIGO data.</b>	<b>55</b>
4.1	Introduction . . . . .	55
4.2	Advanced LIGO interferometers and the O1 observing run . . . . .	56
4.3	Data selection and preparation . . . . .	57
4.4	The search set-up . . . . .	59
4.5	The post-processing step . . . . .	60
4.5.1	The $\chi^2$ veto . . . . .	61
4.5.2	The multi-detector consistency veto . . . . .	63
4.6	Upper limit computation . . . . .	66
4.7	The <i>SkyHough</i> search results . . . . .	70
4.8	Conclusions . . . . .	73
<b>5</b>	<b>The Adaptive Transient Hough method for long-duration gravitational wave transients</b>	<b>77</b>
	M. OLIVER, D. KEITEL, A. M. SINTES	
5.1	INTRODUCTION . . . . .	77
5.2	THE TRANSIENT SIGNAL MODEL . . . . .	78
5.3	The Adaptive Transient Hough Method . . . . .	80
5.3.1	Length of Short-duration Fourier Transforms . . . . .	80
5.3.2	The peak-gram . . . . .	81
5.3.3	Resolution in $\tau$ and $n$ space . . . . .	81
5.4	STATISTICAL PROPERTIES . . . . .	84
5.4.1	The coherent statistic . . . . .	84
5.4.2	The incoherent number-count statistic . . . . .	86
5.4.3	Setting up the threshold . . . . .	87
5.4.4	Calibration of the weights . . . . .	88
5.4.5	Critical Ratio $\Psi$ . . . . .	89
5.5	Vetoed on Critical ratio and Time Consistency . . . . .	91
5.5.1	The Critical ratio $\Psi$ -veto . . . . .	91
5.5.2	The time-inconsistency veto . . . . .	92



5.6	Search sensitivity . . . . .	92
5.7	CONCLUSIONS . . . . .	94
5.A	Testing the Gaussian approximation for the weighted number count $\nu$ . . . . .	96
<b>6</b>	<b>Matched-filter study and energy budget suggest no detectable gravitational-wave 'extended emission' from GW170817</b> . . . . .	<b>99</b>
	M. OLIVER, D. KEITEL, A. MILLER, H. ESTELLES, A. M. SINTES	
6.1	Introduction . . . . .	99
6.2	Signal model and energy budget . . . . .	100
6.3	Optimal matched-filter (non-)detectability . . . . .	102
6.4	Practical checks on real and simulated data . . . . .	105
6.5	Conclusions . . . . .	107
6.A	GW energy integral . . . . .	109
6.B	Time-Domain Matched Filtering . . . . .	110
6.C	Modified signal models . . . . .	110
	6.C.1 Setting $f_0 = 0$ . . . . .	112
	6.C.2 r-mode GW emission . . . . .	112
	6.C.3 Constant $h_0$ . . . . .	112
	6.C.4 Ad-hoc $h(t)$ model for constant SNR contribution over time . . . . .	113
<b>7</b>	<b>Conclusions</b> . . . . .	<b>115</b>
	<b>Bibliography</b> . . . . .	<b>117</b>
<b>A</b>	<b>Permissions for Chapter 3</b> . . . . .	<b>127</b>
<b>B</b>	<b>Permissions for Chapter 5</b> . . . . .	<b>147</b>
<b>C</b>	<b>Permissions for Chapter 6</b> . . . . .	<b>151</b>



# List of Abbreviations

<b>aLIGO</b>	advanced <b>LIGO</b>
<b>ATNF</b>	<b>A</b> ustralia <b>T</b> elescope <b>N</b> ational <b>F</b> acility
<b>BNS</b>	<b>B</b> inary <b>N</b> eutron <b>S</b> tar
<b>CR</b>	<b>C</b> ritical <b>R</b> atio
<b>CW</b>	<b>C</b> ontinuous <b>W</b> aves
<b>DFT</b>	<b>D</b> iscrete <b>F</b> ourier <b>T</b> ransform
<b>EM</b>	<b>E</b> lectro <b>M</b> agnetic
<b>EOS</b>	<b>E</b> quation <b>O</b> f <b>S</b> tate
<b>GR</b>	<b>G</b> eneral <b>R</b> elativity
<b>GRB</b>	<b>G</b> amma <b>R</b> ay <b>B</b> urst
<b>GW</b>	<b>G</b> ravitational <b>W</b> ave
<b>H1</b>	<b>L</b> IGO <b>H</b> anford
<b>L1</b>	<b>L</b> IGO <b>L</b> ivingston
<b>LIGO</b>	<b>L</b> aser <b>I</b> nterferometer <b>G</b> ravitational <b>W</b> ave <b>O</b> bservatory
<b>LSC</b>	<b>L</b> IGO <b>S</b> cientific <b>C</b> ollaboration
<b>LVC</b>	<b>L</b> IGO and <b>V</b> irgo <b>C</b> ollaboration
<b>MDC</b>	<b>M</b> ock <b>D</b> ata <b>C</b> hallenge
<b>NS</b>	<b>N</b> eutron <b>S</b> tar
<b>PHM</b>	<b>P</b> artial <b>H</b> ough <b>M</b> ap
<b>SFT</b>	<b>S</b> hort <b>F</b> ourier <b>T</b> ransform
<b>SN</b>	<b>S</b> uper <b>N</b> ova
<b>SNR</b>	<b>S</b> ignal-to- <b>N</b> oise <b>R</b> atio
<b>SSB</b>	<b>S</b> olar <b>S</b> ystem <b>B</b> arycenter
<b>TT</b>	<b>T</b> ransverse <b>T</b> raceless
<b>THM</b>	<b>T</b> otal <b>H</b> ough <b>M</b> ap



*Ho dedic, com no, aos meus pares, també aos avis i abuelos per  
mostrar-me un camí de bondat, a la meva germana per sempre  
ser el seny, al meu tio Pere Oliver per guiar-me per aquest camí, i  
a tots els qui m'han sabut dir 'cap de fava' per ajudar-me a ser  
on i com som*



---

The thesis is structured as follows:

Chapter 1 contains an introduction to continuous gravitational waves searches. It summarises the physics behind the phenomena we study, the techniques to detect them, and the astrophysical priors that can be used at the present time.

Chapter 2 describes how the Hough transform can be used as a semi-coherent method to search for continuous gravitational waves. The chapter also gives a detailed account of how post-processing techniques can be applied to reduce the false alarm probability, while optimizing the detection probability.

Chapter 3 corresponds to the publication (Walsh, S. and Pitkin, M. and Oliver, M. and D’Antonio, S. and Dergachev, V. and Królak, A. and Astone, P. and Beijger, M. and Di Giovanni, M. and Dorosh, O. and Frasca, S. and Leaci, P. and Mastrogiovanni, S. and Miller, A. and Palomba, C. and Papa, M. A. and Piccinni, O. J. and Riles, K. and Sauter, O. and Sintès, A. M., 2016), which compares the performance of five different search methods: PowerFlux, Sky-Hough, frequency Hough, Einstein@Home, and time domain F-statistic; to the detected unknown isolated neutron stars. I have contributed to this article as one of the principal authors leading the Sky-Hough pipeline results.

Chapter 4 includes the results of (Abbott, 2017f; Abbott, 2018e), where again I was one of the principal authors leading the Sky-Hough pipeline. Both articles refer to the two all-sky searches for periodic gravitational waves during Advanced LIGO’s first observational run, covering the frequency band between 50 – 2000 Hz and a frequency time derivative range of  $[-1.0, +0.1] \times 10^{-8}$  Hz/s. The targeted signals were galactic spinning and non-axisymmetric isolated neutron stars. No gravitational-wave signals were observed, and upper limits are presented on their strengths i.e strain amplitude.

Chapter 5 corresponds to the publication (Oliver, Keitel, and Sintès, 2019), and describes a new semi-coherent method to search for transient gravitational waves of intermediate duration (hours to days). In this chapter, we model the frequency evolution of the signal as a power law in order to search for newborn isolated neutron stars. We present the technical details for sensitivity estimate. A first example application of this method was in the search for GW170817 post-merger signals. Contained in the publication (Abbott, 2018c) for which Mr. Miquel Oliver was one of the principal authors leading the results of this pipeline.

Chapter 6 corresponds to the publication (Oliver et al., 2018), which responds to the report of a possible detection of gravitational-wave ‘extended emission’ from a neutron star remnant of GW170817 from (Putten and Della Valle, 2018). We conclude that even in the most optimistic case an increase in energy and extreme parameters would be required for a confident detection with LIGO sensitivity as of 2018-08-17.





## Chapter 1

# Introduction

Gravitational waves (GWs) are ripples in the fabric of spacetime first predicted by Einstein and detected a century later by advanced interferometric observatories; an astrophysical revolution that is beginning to reveal the hidden feature of black holes and neutron stars.

The advanced Laser Interferometer Gravitational-Wave Observatory (aLIGO) in Washington and Louisiana and the Virgo Gravitational-Wave Observatory in Italy detected 11 gravitational-wave events during the first two observation runs of the advanced detectors era. From which 10 consist of binary black holes mergers (the first, GW150914 (Abbott, 2016b), detected on September 14, 2015) and one matches the gravitational wave and electromagnetic signals expected from the merger of two neutron stars, GW170817. In all cases, the waveform matched the prediction from Einstein's theory of general relativity.

The passing waves were in the frequency band in the order of seconds for the binary black hole events and around 100 seconds for the merging neutron stars. Such rapid pulses, however, are not the only gravitational wave we aim to detect. Isolated neutron stars could emit a quasi-monochromatic continuous signal as they spin, containing important details of the stars equation of state.

A neutron star is the remnant from the collapse of a giant star that had a mass of 10 to 29 solar masses (Glendenning, 1997). These type of stars are the smallest and densest; not counting the hypothetical quark stars or strange stars. Their radius is of the order of 10 kilometers and the mass is below 2.16 solar masses (Rezzolla, Most, and Weih, 2018).

The theoretical calculations and the observational evidence suggest that neutron stars are the most ideally spherical macroscale objects existing. However, even these small imperfections can have major consequences, giving rapidly rotating neutron stars the possibility to emit quasi-monochromatic GWs as they spin, as mentioned above; only if they are rotating on a non axi-symmetric axes. Such signals are commonly referred to as 'continuous gravitational waves' (CW). These sources of gravitational waves are less efficient emitter than the merger of compact objects.

Nevertheless we are optimistic that in the near future we will observe the first continuous gravitational waves from rotating neutron stars, using the sophisticated search techniques that we have developed. This will provide important information and could contain real surprises that might lead to extraordinary discoveries, as exciting or more than the observation of GW170817, with its association with a short gamma ray burst (GRB) and a kilonova (Abbott, 2017b). This last detection motivated also the search for a long duration gravitational wave transient signal after the merger, product of a possible new born neutron star, that is also covered in this thesis.

## 1.1 Gravitational wave characterization

Gravitational waves in general relativity are characterized by two polarizations, known as  $+$  and  $\times$ , that differ by a  $\pi/4$  rotation around their propagation axis. Both of them travel at the speed of light, creating a purely transverse perturbation. The GW emission is generally well-described by the quadrupole formula

$$h_{jk}^{TT}(t) = \frac{2G}{c^4 r} \left( \ddot{J}_{jk}(t - r/c) \right)^{TT}, \quad (1.1)$$

where  $J_{jk}$  is the mass-quadrupole moment of the source (Thorne, 1980),  $h_{jk}^{TT}$  corresponds to the small metric perturbation in the linearized version of general relativity, in the transverse-traceless gauge denoted by  $TT$ ,  $G$  is Newton's gravitational constant,  $c$  is the speed of light and  $r$  is the distance to the source. The quotient  $r/c$  accounts for the time delay, and dots represent time derivatives. For sources with weak internal gravity, i.e. for weak gravitational fields and small stresses,  $J_{jk}$  can be expressed in terms of the mass density distribution  $\rho(\mathbf{x})$  using the reduced traceless quadrupole moment

$$J_{jk} = \int \rho(\mathbf{x}) \left( x_j x_k - \frac{1}{3} r^2 \delta_{jk} \right) d^3 x. \quad (1.2)$$

The emitted gravitational wave energy has to be proportional to the square of the time-derivative of the wave amplitude, i.e. it will be a function of the sum of the squares of the components  $d^3 J_{jk}/dt^3$ . Although the energy flux scales with  $1/r^2$ , the computation of the total energy emission involves a surface integral over a sphere of radius  $r$ , yielding a finite value. The total energy emission or luminosity  $L_{\text{GW}}$  includes a factor  $G/c^5$  on dimensional grounds and a  $1/5$  that comes from a careful general relativity calculation (Landau and Lifschits, 1975). It can be expressed in terms of a time average  $\langle \cdot \rangle$  and the mass-quadrupole moment as

$$L_{\text{GW}} = \frac{dE}{dt} = \frac{G}{5c^5} \langle \ddot{J}_{jk} \ddot{J}^{jk} \rangle. \quad (1.3)$$

This result shows that a time-varying mass distribution emits GWs.

## 1.2 Mass-quadrupole moment of an isolated object

We will proceed to the characterization of the GW emission of a non-axisymmetric rotating isolated neutron star, the main focus of this thesis. Such objects are expected to produce continuous gravitational waves, and they may be considered the most likely source of gravitational waves to be detected in addition to binary systems of compact objects.

To understand this emission, let us consider an ellipsoidal neutron star with semi-axes  $a$ ,  $b$ ,  $c$ , and approximate it as a rigid object with uniform density  $\rho$ . Then, its moment of inertia is given by

$$I_{ij} = \int_V \rho \left( x_i x_j \delta_{ij} - x_i x_j \right) dx^3, \quad (1.4)$$

$$I_{ij} = \frac{M}{5} \begin{bmatrix} (b^2 + c^2) & 0 & 0 \\ 0 & (c^2 + a^2) & 0 \\ 0 & 0 & (a^2 + b^2) \end{bmatrix} = \begin{bmatrix} I_1 & 0 & 0 \\ 0 & I_2 & 0 \\ 0 & 0 & I_3 \end{bmatrix}, \quad (1.5)$$

where  $I_1, I_2$  and  $I_3$  are the principal moments of inertia.

Now, let us consider a rotation with frequency  $\Omega$  and evaluate the new coordinates

$$\mathbf{x}' = \mathbf{R}\mathbf{x}. \quad (1.6)$$

Here,  $\mathbf{x}' = (x', y', z')$  are cartesian coordinates in the object frame, and  $\mathbf{x} = (x, y, z)$  are cartesian coordinates in an inertial frame, with both sets of coordinates sharing the origin at the center of mass of the system; and  $\mathbf{R}$  is the rotation matrix defined by the Euler angles

$$\mathbf{R} = \begin{bmatrix} \cos \phi \cos \Psi - \cos \theta \sin \phi \sin \Psi & \cos \Psi \sin \phi + \cos \theta \cos \phi \sin \Psi & \sin \theta \sin \Psi \\ -\cos \theta \cos \Psi \sin \phi - \cos \phi \sin \Psi & \cos \theta \cos \phi \cos \Psi - \sin \phi \sin \Psi & \cos \Psi \sin \theta \\ \sin \theta \sin \phi & -\cos \phi \sin \theta & \cos \theta \end{bmatrix}. \quad (1.7)$$

We can transform  $I_{ij}$  to the inertial frame  $x_i$  as

$$I_{ij} = (\mathbf{R}^T \mathbf{I}' \mathbf{R})_{ij}. \quad (1.8)$$

We will consider two main cases according to the relation among moments of inertia: The non-precessing case, in which  $I_1 - I_2 = \Delta I_d$  and  $\theta = \pi/2$ ; and the freely-precessing case, in which  $I_1 - I_3 = \Delta I_d, I_1 = I_2$  and  $\theta \in (0, \pi/2)$ .

The evaluation of both cases will be done by fixing the angular momentum vector  $\mathbf{J}$  parallel to the  $\hat{e}_z$  axis. Then, following (Landau and Lifshitz, 1976), the angular velocity and the symmetry axis  $\hat{e}_3$  rotate around  $\hat{e}_z$  at  $\dot{\phi} = J/I_1 = \Omega$  with  $\dot{\theta} = 0$  and  $\dot{\Psi} = \dot{\phi} \Delta I_d \cos \theta / I_3$ . Solving the system, the moment of inertia in the inertial frame reads:

$$I_{xx} = \frac{1}{2} \Delta I_d \sin^2 \theta \cos(2\Omega t) + \text{const}, \quad (1.9)$$

$$I_{yy} = -\frac{1}{2} \Delta I_d \sin^2 \theta \cos(2\Omega t) + \text{const}, \quad (1.10)$$

$$I_{zz} = \text{const}, \quad (1.11)$$

$$I_{xy} = I_{yx} = \Delta I_d \sin^2 \theta \sin(2\Omega t) + \text{const}, \quad (1.12)$$

$$I_{xz} = I_{zx} = -\Delta I_d \sin \theta \cos \theta (\sin(\Omega t) + \text{const}), \quad (1.13)$$

$$I_{yz} = I_{zy} = \Delta I_d \sin \theta \cos \theta (\cos(\Omega t) + \text{const}). \quad (1.14)$$

It can be shown that the trace of the moment of inertia verifies  $\text{Tr} I = I_{xx} + I_{yy} + I_{zz} = \text{Tr} I' = \text{constant}$ . With this result, the mass-quadrupole moment from equation(1.1) is given by

$$J_{jk} = -\left(I_{ij} - \frac{1}{3} \delta_{jk} \text{Tr} I\right) = -I_{ij} + \text{const}. \quad (1.15)$$

To facilitate the description of the emitted wave, we introduce two orthogonal unit vectors  $\hat{v}$  and  $\hat{w}$  with its cross product directed towards the observer. We will also assume that the observer is situated in the  $(\hat{e}_y, \hat{e}_x)$  plane, where the line of sight and  $\hat{e}_z$  are characterized by the angle  $\iota$ :

$$\hat{v} = \hat{e}_y \cos \iota - \hat{e}_z \sin \iota, \quad (1.16)$$

$$\hat{w} = -\hat{e}_x. \quad (1.17)$$

Hereby, we can construct a base for the two polarizations  $\times$  and  $+$ , and describe the  $h_{jk}^{TT}$  perturbation as

$$\hat{e}_+ = \hat{v} \otimes \hat{v} - \hat{w} \otimes \hat{w}, \quad (1.18)$$

$$\hat{e}_\times = \hat{v} \otimes \hat{w} + \hat{w} \otimes \hat{v}, \quad (1.19)$$

$$h_+ = \frac{1}{2} h_{jk}^{TT} \hat{e}_+^{jk}, \quad (1.20)$$

$$h_\times = \frac{1}{2} h_{jk}^{TT} \hat{e}_\times^{jk}. \quad (1.21)$$

Using equations (1.1) and (1.15), we recover the results found by (Zimmermann and Szedenits, 1979):

$$h_+(\Omega) = \frac{2\Omega^2 G}{c^4} \Delta I_d \sin i \cos i \sin \theta \cos \theta \cos(\Omega t), \quad (1.22)$$

$$h_\times(\Omega) = \frac{2\Omega^2 G}{c^4 r} \Delta I_d \sin i \sin \theta \cos \theta \sin(\Omega t), \quad (1.23)$$

$$h_+(2\Omega) = \frac{2\Omega^2 G}{c^4 r} 2\Delta I_d (1 + \cos^2 i) \sin^2 \theta \cos(2\Omega t), \quad (1.24)$$

$$h_\times(2\Omega) = \frac{2\Omega^2 G}{c^4 r} 2\Delta I_d \cos i \sin^2 \theta \sin(2\Omega t). \quad (1.25)$$

It is easy to see that a non-precessing object can radiate gravitational waves at double of the spin frequency  $2\pi f_{\text{GW}} = 2\Omega$ . On the other hand, freely-precessing objects radiate gravitational waves at two frequencies, namely  $2\pi f_{\text{GW}} = 2\Omega$  and  $\Omega$ . For the sake of completeness, we evaluate the energy loss due to gravitational wave radiation with equation (1.3):

$$L_{\text{GW}} = \frac{dE}{dt} = -\frac{1}{5} \frac{G}{c^5} \Delta I_d^2 \Omega^6 \sin^2 \theta (16 \sin^2 \theta + \cos^2 \theta). \quad (1.26)$$

The luminosity is 0 for any axisymmetric object rigidly rotating around its symmetry axis, i.e.,  $\Delta I_d = 0$ . A more general case of free precession where  $I_1 < I_2 < I_3$  is included in (Zimmermann and Szedenits, 1979). Another crucial factor to characterize and later evaluate the probability of detection is the strain amplitude  $h_0$ :

$$h_0 = \frac{4\pi^2 G}{c^4} \frac{\epsilon I_{zz} \sin \theta f_{\text{GW}}^2}{r}. \quad (1.27)$$

Here,  $\epsilon = \Delta I_d I_{zz}$  is the neutron star ellipticity and  $I_{zz}$  its principal moment of inertia.

### 1.3 Astrophysical Priors

The only available priors for  $f$  and  $\dot{f}$  correspond to a particular type of neutron stars known as pulsars. Figure 1.1 shows the Gaussian density distribution  $gd_A(f, \dot{f})$  for the pulsars contained in the ATNF Pulsar Catalogue (Hobbs et al., 2004). Using the observed spin down, we can define a limit on the ellipticity of a neutron star  $\epsilon$  based on the expected maximum GW luminosity. If we consider that all the loss in kinetic energy  $E_{\text{rot}} = 2\pi^2 f^2 I_{zz}$  is due to GW radiation, then:

$$L_{\text{GW}} \leq -\dot{E}_{\text{rot}} = -2\pi^2 \left( 2I_{zz} f \dot{f} + f^2 \dot{I}_{zz} \right). \quad (1.28)$$

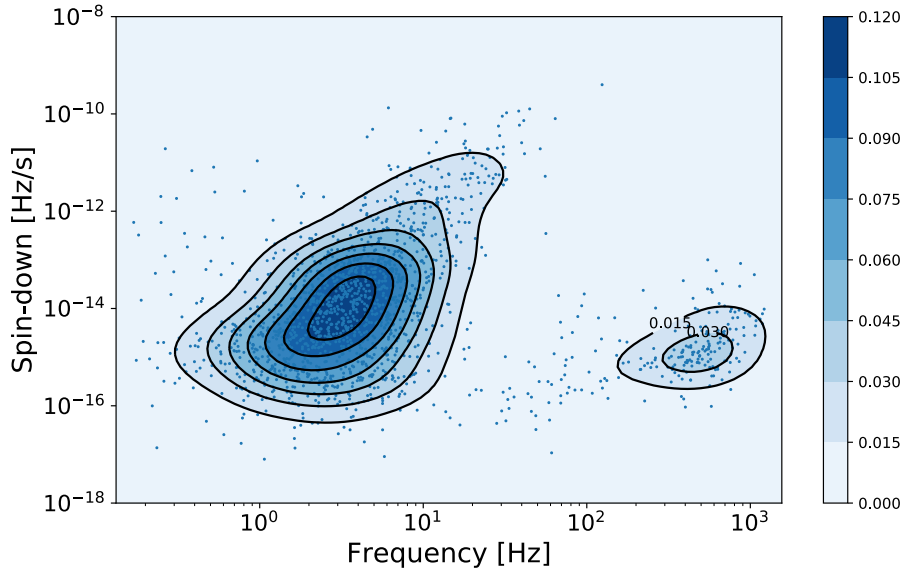


FIGURE 1.1: The Gaussian density distribution for the known pulsars contained in the ATNF Pulsar Catalogue (Hobbs et al., 2004).

After assuming that the moment of inertia is constant in time, we obtain the spin-down limit

$$\epsilon_{\text{sd}} \leq \sqrt{\frac{5c^5}{32\pi^4 G I_{\text{zz}}} \frac{|\dot{f}|}{f^5}}, \quad (1.29)$$

$$h_{\text{sd}} \leq \frac{1}{r} \sqrt{\frac{5G I_{\text{zz}}}{2c^3} \frac{|\dot{f}|}{f}}. \quad (1.30)$$

We can also impose the age of the pulsar defined by the ATNF Pulsar Catalogue, which shows the Gaussian density distribution  $gd_{\gamma}(f, \dot{f})$  for pulsars younger than 4 Myrs contained in the ATNF Pulsar Catalogue. This quantity is very useful since it allows us to compare the ATNF Pulsar Catalogue with different population synthesis studies, e.g., (Popov et al., 2000), which states that there should be around 100 and 140 neutron stars with  $\tau_{\text{g}} < 4$  Myrs within 600 pc, even though only 15 exist in the ATNF Pulsar Catalogue.

Another important prior we can include is a spatial distribution as shown in (Schmidt, Hohle, and Neuhauser, 2014). This work indicates that the Supernova (SN) rate in the Solar vicinity should be roughly constant for the last few Myr. Using this assumption, it is stated that all the early SN progenitors within 600pc have to be distributed within an 8% of the sky area.

The last piece of information comes from gravitational wave searches of known pulsars. This type of searches allows us to derive an upper limit to the factor  $F_{\text{spin}}$  between the energy loss and the luminosity, i.e the spindown limit factor. (Abbott, 2019b) is the latest search of this type, using data from the first and second observing runs of the aLIGO detectors (O1 & O2) to cover 222 known pulsars. This search constrained the spindown limit factor for 20 young pulsars, with PSR J0534+2200 (Crab) and PSR J0534+2200 (Crab) being the ones with the smallest limit,  $F_{\text{spin}} =$

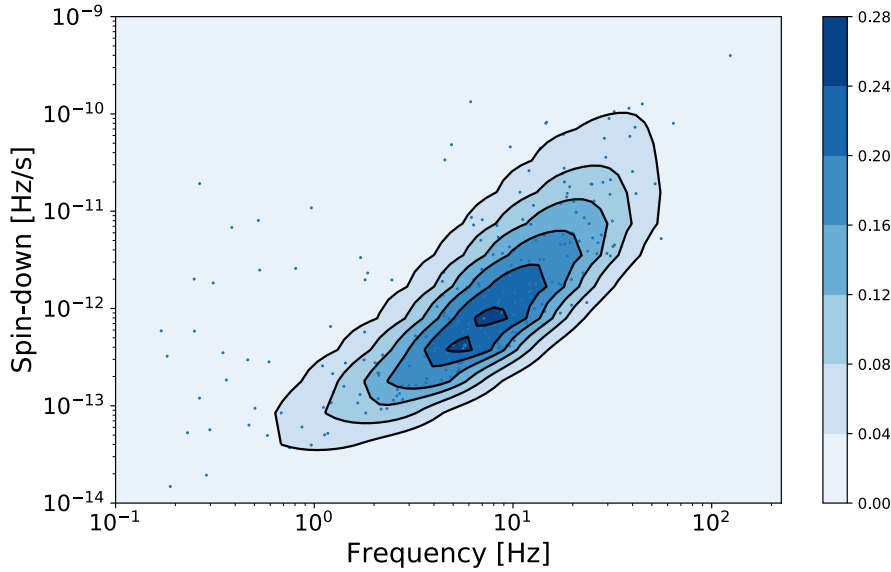


FIGURE 1.2: The gaussian density distribution for the known pulsars contained in the ATNF Pulsar Catalogue (Hobbs et al., 2004), younger than 4 Myrs.

0.017%.

## 1.4 Detector's response

The effect of a GW on two freely falling test-masses separated by a distance  $l$  is given by a time-dependent perturbation  $\delta l$ . Ground-based gravitational wave interferometers sensitive in the audio band have proven to be an excellent tool to measure such a perturbation. The measured strain of this type of detectors is defined as  $h(t) \equiv \delta l_1/l_1 - \delta l_2/l_2$ , where the two interferometer arms have lengths  $l_{1,2}$  and form a right angle. If the arm length of the detector is much smaller than the wavelength of the GW, i.e.  $\lambda/2\pi \gg l_{1,2}$ , the long wave approximation can be used (Schutz and Tinto, 1987) to relate the detector strain to the metric perturbation due to gravitational waves:

$$h(t) = \frac{1}{2}(e_1^j e_1^k - e_2^j e_2^k) h_{jk}^{TT}(t) \quad (1.31)$$

$$= F_+(t)h_+(t) + F_\times(t)h_\times(t), \quad (1.32)$$

where  $\hat{e}_{1,2}$  are unit vectors along the two interferometers arms. The detector's sensitivity to each of the polarizations  $+$  and  $\times$  is described by the antenna-pattern functions  $F_{+,\times}(t; \psi, \mathbf{n}) \in [-1, 1]$ , where  $\mathbf{n}$  corresponds to the unit vector pointing towards the GW source from the detector and  $\psi$  is the polarization angle:

$$F_+(t) = \sin \zeta [a(t) \cos 2\psi + b(t) \sin 2\psi], \quad (1.33)$$

$$F_\times(t) = \sin \zeta [b(t) \cos 2\psi - a(t) \sin 2\psi]. \quad (1.34)$$

The two functions  $a(t)$  and  $b(t)$  are related to the movement of the detector's frame with respect to the solar system barycenter SSB. Their derivation can be found in

(Jaranowski, Krolak, and Schutz, 1998).

Another important characteristic of the detector's response is the relation between the detector's time of arrival  $t$  and the time of emission at the source  $t_{\text{NS}}$ . For the sake of simplicity, we will neglect relativistic corrections such as the Shapiro and Einstein delays (Jaranowski, Krolak, and Schutz, 1998), yielding

$$t_{\text{NS}}(t, \mathbf{n}) = t + \frac{\mathbf{r}(t) \cdot \mathbf{n}}{c}, \quad (1.35)$$

where  $\mathbf{r}(t)$  points from the SSB to the detector and the term  $\mathbf{r}(t) \cdot \mathbf{n}/c$  is the Roemer-delay. By assuming a quasi-monochromatic emission, the phase of the signal  $\Phi(t_{\text{NS}})$  can be modeled as a Taylor series expansion

$$\Phi(t_{\text{NS}}) = \Phi_0 + 2\pi \sum_{k=0}^s \frac{f^{(k)}(t_0)}{(k+1)!} \Delta t_{\text{NS}}^{k+1}, \quad (1.36)$$

where  $(k)$  represents the  $k^{\text{th}}$  time derivative and  $\Delta t_{\text{NS}} = t_{\text{NS}} - t_0$ . The frequency evolution of the signal at the detector frame is then given by:

$$f(t) = \sum_{k=0}^s \frac{f^{(k)}(t_0)}{(k)!} \left( t - t_0 - \frac{(\mathbf{r}(t) - \mathbf{r}(t_0)) \cdot \mathbf{n}}{c} \right)^k \left( 1 + \frac{\mathbf{v}(t) \cdot \mathbf{n}}{c} \right), \quad (1.37)$$

$$f(t) = \hat{f}(t) \left( 1 + \frac{\mathbf{v}(t) \cdot \mathbf{n}}{c} \right), \quad (1.38)$$

where the Doppler contribution appears in its familiar, non-relativistic formulation.

## 1.5 Detector's sensitivity

The time-domain output of the aLIGO and aVirgo detectors  $x(t)$  does not only contain the desired signal. Rather, it can be seen as a linear combination between a gravitational wave signal  $h(t)$  and some background noise  $n(t)$ :

$$x(t) = h(t) + n(t). \quad (1.39)$$

To study the presence of a signal within the noise, the first step is to understand the expected noise spectral energy distribution or power spectral density (PSD):

$$S_n(f) = 2 \int_{-\infty}^{\infty} d\tau \langle n(t)n(t+\tau) \rangle e^{-2\pi i f \tau}. \quad (1.40)$$

One can define the amplitude spectral density (ASD) as the square root of the PSD.

If the noise is assumed to be a real and stationary, Gaussian, and with zero mean, the averaged Fourier transform of its autocorrelation function is independent of  $t$ :

$$\langle \tilde{n}^*(f') \tilde{n}(f) \rangle = \left\langle \int_{-\infty}^{\infty} dt' \int_{-\infty}^{\infty} dt n(t)n(t') e^{2\pi i f' t'} e^{-2\pi i f(t')} \right\rangle, \quad (1.41)$$

$$= \left\langle \int_{-\infty}^{\infty} dt' \int_{-\infty}^{\infty} d\tau n(t')n(t'+\tau) e^{2\pi i f' t'} e^{-2\pi i f(t'+\tau)} \right\rangle, \quad (1.42)$$

$$= \int_{-\infty}^{\infty} dt' e^{-2\pi i(f-f')t'} \int_{-\infty}^{\infty} d\tau e^{-2\pi i f \tau} \langle n(t')n(t'+\tau) \rangle, \quad (1.43)$$

where  $\tilde{n}$  stands for the Fourier transform of  $n$ . With this in mind, equation (1.5) can be rewritten as

$$S_n(f) = \frac{2\langle \tilde{n}^*(f')\tilde{n}(f) \rangle}{\delta(f-f')}. \quad (1.44)$$

To analyze a finite time series of length  $T$ , the Dirac delta function needs to be substituted by the appropriate Fourier response

$$\delta(f-f') \approx \frac{\sin(\pi(f-f')T)}{\pi(f-f')}. \quad (1.45)$$

Taking the limit  $(f-f') \rightarrow 0$ , equation (1.44) becomes

$$S_n(f_k) \approx \frac{2\langle \tilde{n}^*(f')\tilde{n}(f) \rangle}{T}. \quad (1.46)$$

The value of the sensitivity during the second science run of the aLIGO (O2) detectors is shown in figure 1.3.

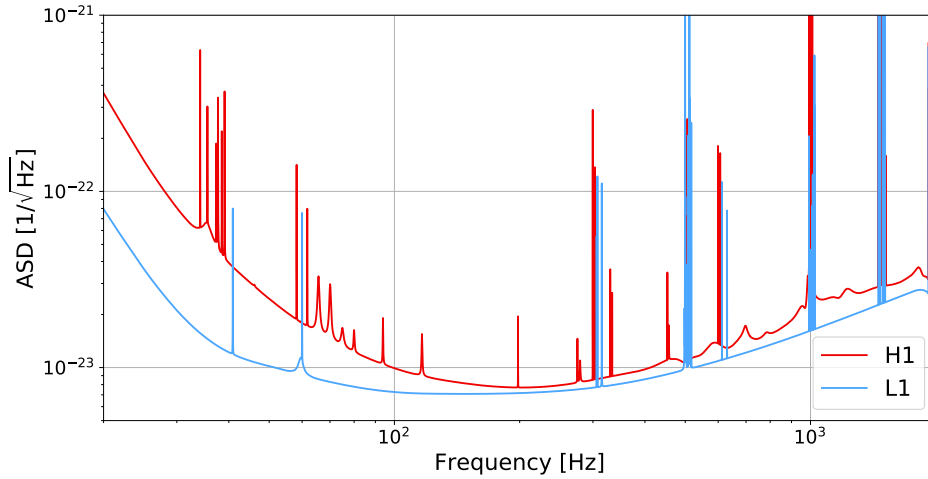


FIGURE 1.3: Noise strain amplitude spectral density (ASD) curves of LIGO Hanford (H1) and Livingston (L1) for O2 averaged over 1800s stretches during the GW170817 event.

## 1.6 Signal recovery strategies

The standard method in GW data analysis when well modeled signals are considered is matched filtering. This corresponds to the optimal linear filter which maximizes the signal-to-noise ratio SNR in the presence of additive Gaussian noise

$$SNR^2 = (h|x) \quad (1.47)$$

$$= 4\text{Re} \int_0^\infty df \frac{\tilde{x}(f)\tilde{h}^*(f)}{S_n(f)}, \quad (1.48)$$

where  $h$  is the template, i.e. the gravitational wave signal that we want to match with the detector data  $x$ , and  $S_n(f)$  is the previously defined single-sided noise power



spectral density (PSD) of a detector. In this work we will use the PSD from the L1 detector during the O2 run, which was computed from the GW170817 open data event and is shown on figure 1.3.

It is clear that the optimal SNR, commonly defined as  $\rho \equiv \sqrt{\langle h|h \rangle}$  in the GW literature, is an important quantity to take into account when a search is designed. The optimal SNR for a monochromatic stationary gravitational wave signal without precession is given by

$$\rho^2 = h_0^2 \left( \frac{(1 + \cos^2 \iota)}{2} \langle F_+^2 \rangle + \cos \iota \langle F_\times^2 \rangle \right) \frac{T_{\text{obs}}}{S_n(f)}, \quad (1.49)$$

where  $T_{\text{obs}}$  is the observation time, i.e the time of integration of the signal,  $F_{+,\times}(t; \psi, \mathbf{n}) \in [-1, 1]$  is the antenna-pattern (Jaranowski, Krolak, and Schutz, 1998),  $\mathbf{n}$  corresponds to the unit vector pointing towards the GW source,  $\psi$  is the polarization angle and  $\iota$  is the angle between the propagation direction and line of sight. Ignoring SNR leakage and averaging over the  $\cos \iota$ , the polarization angle  $\psi$  and the sky location, we obtain a 4/25 prefactor:

$$\rho^2 = \frac{4}{25} \frac{h_0^2 T_{\text{obs}}}{S_n(f)}. \quad (1.50)$$

The sensitivity of wide-parameter searches is limited by the number of templates, i.e., the number of signals we want to search for in the data. In order to fully cover a region in the parameter space, one needs to ensure that the SNR loss between templates is small. This sensitivity loss is due to the mismatch metric  $g_{ij}$  as defined in (Prix, 2007), where it is also shown that the required number of templates  $dN$  per small parameter space region  $d^4\lambda = d\Theta \cdot df \cdot d\hat{f}$  (with sky solid-angle  $d\Theta$ ) is, at least,

$$dN \propto |\det g_{ij}| d^4\lambda \propto T_{\text{obs}}^5 f^2 d^4\lambda. \quad (1.51)$$

The computational cost per template is proportional to  $T_{\text{obs}}$ , therefore the total computational cost of a search  $C_{\text{search}}$  is proportional to

$$C_{\text{search}} \propto T_{\text{obs}}^6 f^2 d^4\lambda. \quad (1.52)$$

From equation (1.6) we see that an increase of  $T_{\text{obs}}$  results in an improve in the SNR with a consequent increase in computational cost by a factor of  $T_{\text{obs}}^6$ , making the cost of a wide parameter space search computationally prohibitive.

### 1.6.1 Semi-coherent analysis

In order to reduce the computational cost, several semi-coherent methods have been developed. The main idea is to split the total observation time  $T_{\text{obs}}$  into segments of length  $T_{\text{coh}}$ . For this method, the SNR of the search exploits a summation of the power contained on each segment

$$S\hat{N}R^2 = \sum_{i=0}^{N_{\text{coh}}} (h_i | x_i), \quad (1.53)$$

where  $x_i$  and  $h_i$  are the corresponding data and template for the  $i - th$  segment and  $N_{\text{coh}}$  is the number of segments. It can be shown that the optimal SNR of a semi-coherent method, assuming no mismatch and a constant noise power spectral density, is the same as the one found for the fully-coherent case. There are three main variants of this type of analysis, namely ‘‘StackSlide’’ (also known as the ‘‘Radon transform’’)

(Brady and Creighton, 2000), “PowerFlux” (Dergachev, 2005; Dergachev and Riles, 2005) and the “Hough transform” Krishnan et al., 2004. The equivalent estimation on the number of templates and computational costs for this method yields

$$dN \propto \frac{d\Omega df d\dot{f}}{\delta_{\theta}^2 \delta_f \delta_{\dot{f}}}, \quad (1.54)$$

$$\propto T_{\text{obs}} T_{\text{coh}}^4 f^2 d^4 \lambda, \quad (1.55)$$

$$C_{\text{search}} \propto T_{\text{obs}}^2 T_{\text{coh}}^4 f^2 d^4 \lambda. \quad (1.56)$$

Therefore, the computing cost is substantially reduced when compared against the fully coherent case.

## 1.7 Search sensitivity estimate

To characterize the difference between the fully-coherent and semi-coherent approaches, one needs to evaluate their sensitivity. This quantity will impose, given a false alarm and a false dismissal probability, a required signal strength amplitude  $h_0$  in order to claim a detection. Assuming stationary, zero mean Gaussian noise on eq.(1.6), we obtain a sum of the squares of 2 independent, standard normal random variables; therefore,  $S\hat{N}R^2$  follows a non-central  $\chi^2$  distribution with  $2 \cdot N_{\text{coh}}$  degrees of freedom and non-centrality parameter  $\rho^2$ ; some pipelines differentiate between signal polarizations, increasing the number of degrees of freedom by a factor 2. With this in mind, we see that the mean and the variance when no signal is present increases linearly with  $N_{\text{coh}}$  between the fully-coherent and the semi-coherent approach. Now, we can write the false-alarm and the detection probability for a single template as

$$p_{\text{FA}}(S\hat{N}R_{\text{th}}) = \int_{S\hat{N}R_{\text{th}}}^{\infty} \chi_{4N_{\text{coh}}}^2(S\hat{N}R^2, 0) dS\hat{N}R, \quad (1.57)$$

$$p_{\text{det}}(S\hat{N}R_{\text{th}}, \rho^2) = \int_{S\hat{N}R_{\text{th}}}^{\infty} P(\mu) \chi_{4N_{\text{coh}}}^2(S\hat{N}R^2, \rho^2) dS\hat{N}R, \quad (1.58)$$

where  $P(\mu)$  is the mismatch distribution. In this work we will consider  $P(\mu) = 1$  a more detail integration could be done as in practice this can induce a  $\sim 5\%$  discrepancy for searches like Stack-Slide as shown in (Dreissigacker, Prix, and Wette, 2018). The false dismissal is  $p_{\text{FD}} = 1 - p_{\text{det}}$ . At this point, the most common approach is to derive a threshold using a given false alarm probability to evaluate the required  $\rho^2$  to obtain the desired  $p_{\text{det}}$ . Typically,  $p_{\text{FA}}$  and  $p_{\text{FD}}$  are chosen to be 1% and 10%. From eqs. (1.27,1.6) we can express the expected  $p_{\text{FD}}$  upper limits at fixed  $p_{\text{FA}}$  assuming stationary zero mean Gaussian noise as

$$h_0^{1-p_{\text{FD}}} = \rho_{th}(p_{\text{FA}}, p_{\text{FD}}, N_{\text{coh}}) \frac{25 S_n(f)}{4 T_{\text{obs}}}, \quad (1.59)$$

where  $\rho_{th}$  is a function of  $p_{\text{FA}} = 1\%$ ,  $p_{\text{FD}} = 90\%$ ,  $T_{\text{coh}}$ ,  $T_{\text{obs}}$ . A common approximation states that, for  $N_{\text{coh}} > 1000$ , we can use  $\rho_{th}(p_{\text{FA}} = 1\%, p_{\text{FD}} = 90\%) \propto N_{\text{coh}}^{1/4}$  (Wette, 2012). Fig.1.4 shows  $h_0^{90\%}$  estimate at  $p_{\text{FA}} = 1\%$  for different values of  $T_{\text{coh}}$  and  $f$  with a fixed  $T_{\text{obs}} = 3\text{months}$ .

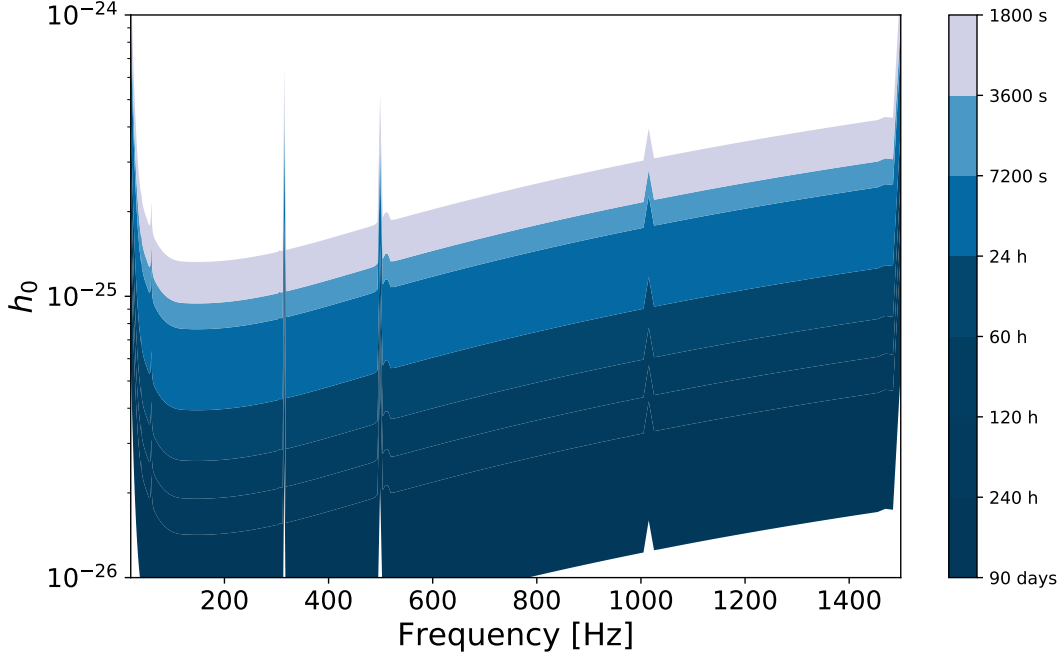


FIGURE 1.4: This figure shows  $h_0^{90\%}$  from eq.(1.59) for different values of  $T_{coh}$  and  $f$  with a fixed  $T_{obs} = 3\text{months}$ . We have set  $p_{FA} = 1\%$ ,  $p_{FD} = 90\%$  and used the  $S_n(f)$  of L1 during O2, shown on fig.1.3.

## 1.8 CW Searches with Astrophysical Priors

In this section we will define a set of guidelines to perform an all-sky search based on the astrophysical priors from sec.1.3. From eqs.1.30,1.59 we can derive the observable distance  $d$  as a function of  $(p_{FA}, p_{FD}, T_{coh}, T_{obs}, f, \dot{f}, F_{spin})$ , i.e the maximum distance at which we can observe a source at a given  $p_{FA} = 1\%$ ,  $p_{FD} = 90\%$ . Fig.1.5 shows the effect of  $T_{coh}$  over this observable distance for  $\dot{f} = 10^{-10}\text{Hz/s}$  applying an optimistic spindown limit factor of  $F_{spin} = 0.1\%$  and  $T_{obs} = 3\text{ months}$  at  $p_{FA} = 1\%$ , and  $p_{FD} = 90\%$ . It is clearly seen that the maximum distance for a given  $T_{coh}$  is located at the sweet spot of the detector, i.e. the frequency with the minimum value of  $S_n$ . A simple way to optimize a search would be to maximize a search volume coverage based on the required  $T_{coh}$  and the computational budget.

To visualize the influence of the priors, we can evaluate the required  $T_{coh}$  as a function of  $f$  and  $\dot{f}$  in order to reach 600 pc. This result is shown in fig. (1.6), overlapped with the information from the two Gaussian density prior distributions for  $f$  and  $\dot{f}$ , shown on figs. (1.1,1.2). If the assumptions are valid, fig.1.6 can help us to identify the most-likely region in which a CW detection could happen e.g. below 200Hz and above a spin-down value of  $10^{-12}\text{Hz/s}$ . As expected, the distribution for young NS should be the main target, since they have the highest expected spindown, allowing for a larger deformation that, in general, implies a larger amplitude  $h_0$ .

In order to generalize and have a qualitative result for different set-ups, we need to evaluate the detection probability  $P$ . This is done by integrating the product of the pulsar density distribution  $g(f, \dot{f})$  with a normalized spatial density pulsar population  $\hat{\rho}(r, sky)$  and a range probability function  $p(r, sky, f, \dot{f})$ .

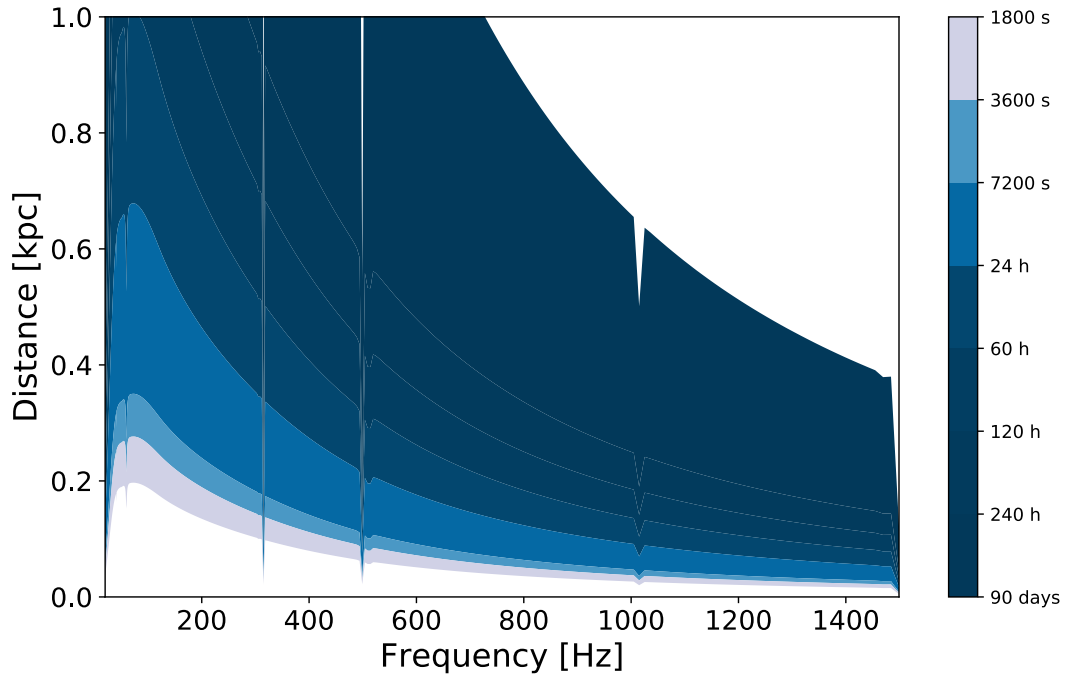


FIGURE 1.5: Observable distance using eqs.(1.30,1.59) for different values of  $T_{\text{coh}}$  and  $f$  with a fixed  $T_{\text{obs}} = 3$  months, fixed  $\dot{f} = 10^{-10}\text{Hz/s}$  and an optimistic spindown limit factor of  $F_{\text{spin}} = 0.1\%$ . The false alarm and false dismissal probabilities are set to  $p_{\text{FA}} = 1\%$ ,  $p_{\text{FD}} = 90\%$ , and the  $S_n(f)$  is that of the L1 detector during the O2 science run, shown on fig.1.3.

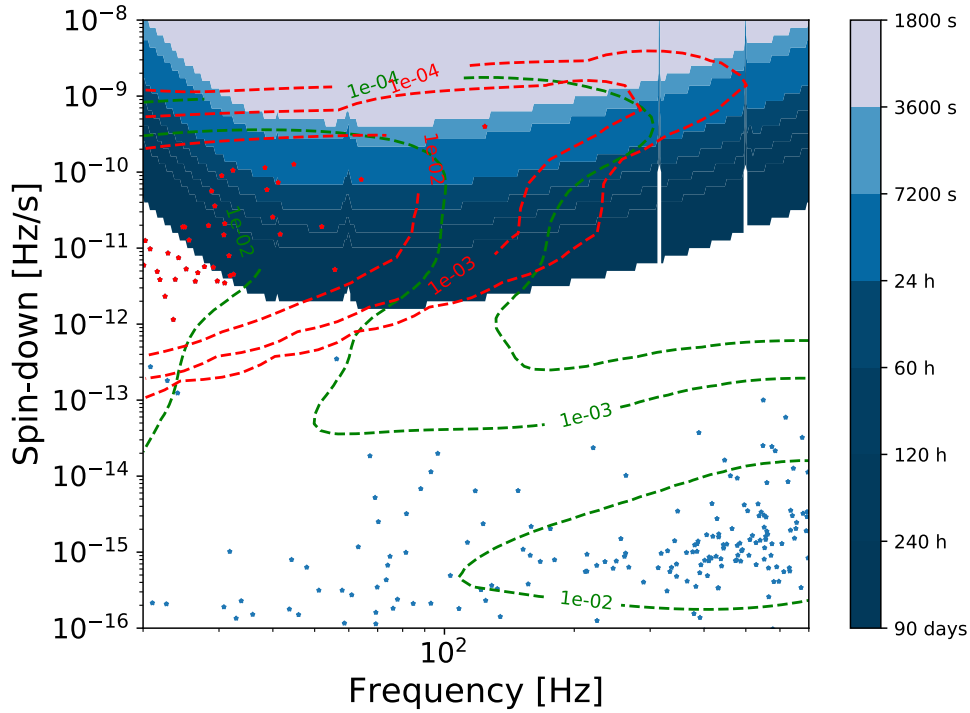


FIGURE 1.6: (Colormap) Required  $T_{coh}$  to satisfy a given observable distance of 600pc for different values of  $f$  and  $\dot{f}$  with a fixed  $T_{obs} = 3$  months and a spindown limit factor of 0.1%. (Dashed Lines) Gaussian density product distribution of all the known isolated pulsar from the ATNF Pulsar Catalogue. (Dots) Known pulsars from the ATNF Pulsar Catalogue. The false alarm and false dismissal probabilities are set to  $p_{FA} = 1\%$ ,  $p_{FD} = 90\%$ , and the  $S_n(f)$  is that of the L1 detector during the O2 science run, shown on fig.1.3.

$$P = \int \hat{\rho}(r, sky) g(f, \dot{f}) p(r, sky, f, \dot{f}) d^4 \lambda dr. \quad (1.60)$$

In this work we assume a homogeneous sky distribution where all the pulsars are located at a distance  $d_{\text{obs}}$ , at the same time we have used a Dirac delta function normalized at 1 parametrized with the astrophysical range to define the range probability function:

$$P = \int g(f, \dot{f}) \delta(d_{\text{obs}} - d(\dots)) df d\dot{f}, \quad (1.61)$$

where  $d(\dots)$  corresponds to the astrophysical range. In general, a more complete model could be used to define the distance using multiple layers.

While the detection probability is an important quantity to compare between different set-ups, a new measure, called efficiency, can be defined by combining eqs.1.8 and the computational cost of the set-up  $C_s$  as follows:

$$E = \frac{P(T_{\text{coh}})}{C_s}. \quad (1.62)$$

Without information on the cost, we could use  $C_s = C_0 T_{\text{obs}}^2 T_{\text{coh}}^4 \Delta f^3 \Delta \dot{f} S_{\text{sky}}$  as a first guess, where  $C_0$  is a computational proportionality to compare different pipelines, we will use  $C_0 = 1$  in this work, where  $S_{\text{sky}}$  is the percentage covered of the sky surface and  $\Delta f$  and  $\dot{f}$  are the frequency and spindown search ranges.

On figs.(1.7,1.8) we show the results for the probability from eq.(1.8) and the efficiency from eq.(1.8). For the sake of simplicity, we have used the same frequency derivative range of  $[-1.0, +0.1] \times 10^{-8}$  Hz/s for all the cases with  $p_{\text{FA}} = 1\%$ ,  $p_{\text{FD}} = 90\%$ ,  $F_{\text{spin}} = 0.1\%$  and  $T_{\text{obs}} = 3$  months. Using this table, it becomes clear that a pure all-sky search like (Abbott, 2017f; Abbott, 2018e) on O1, which covered the entire sky along a frequency band between 20 Hz and 2000 Hz and the mentioned frequency derivatives range, yields  $P = 2.54e - 03\%$  for young NSs inside the 600 pc radius and  $P \sim 4.04e - 04\%$  for the entire population.

Using the prior from the temporally and spatially resolved Supernova rates introduced by (Schmidt, Hohle, and Neuhauser, 2014), we can reduce the sky parameter space to search only across an 8% without losing detection probability for young NSs inside a 600 pc radius, i.e.  $1 = \int_0^{8\%} \rho_{600\text{pc}}(sky) dsky$ . For  $T_{\text{coh}} = 24\text{h}$   $P \sim 2.7e - 02\%$  and the efficiency would improve a factor 12.5, on the other hand, considering a homogeneous  $\rho(sky)$ , this search would yield  $P \sim 4e - 04\%$  for the entire population. In this specific case, the efficiency of this search compared to the one performed in O1 is a factor of almost  $\sim 1e + 5$  times larger for young NSs. At the same time from fig.1.8 we see that the most efficient searches are in the  $f \in (20, 200)\text{Hz}$  range and for young pulsars 0.5h seems to be extremely efficient after 100Hz, nevertheless we could reevaluate this efficiency values by splitting the frequency band into subsets but this is not the intention of this work.

A future work could define a hierarchical set-up method, similar to the one presented in (Ming et al., 2016), in order to optimize a search by splitting the initially desired coverage volume into smaller cells and, then, assigning individual set-ups to each cell in order to maximize the overall detection probability while maintaining a fixed computational cost.

Here we have shown a simple way to evaluate the efficiency of different searches, as well as given an intuition on how to properly set them up to cover the most significant regions of the parameter space. Although it is important to devote part of

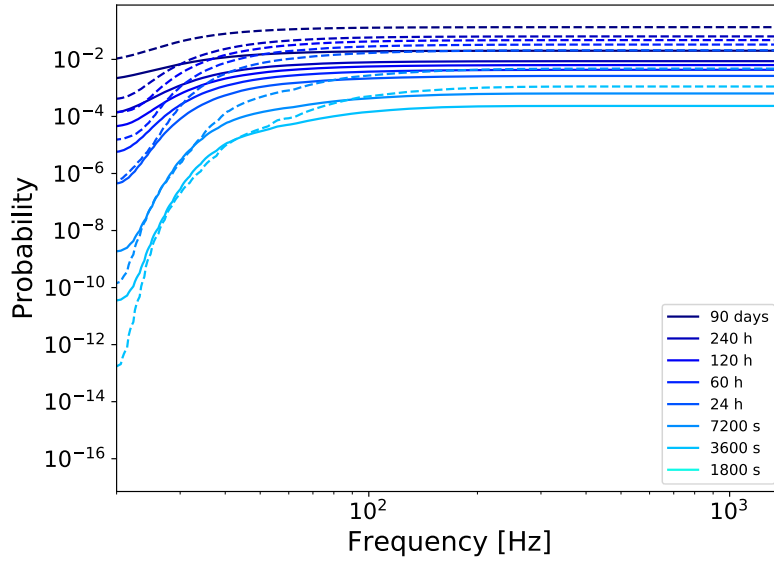


FIGURE 1.7: This figure shows the probability from eq.(1.8) where the dashed lines correspond to the *Young* set of pulsars with an age  $\tau_g < 4$  Myrs from 1.2 and the continuous lines to the full set from figs.1.1. For this figure we have set  $T_{\text{obs}} = 3$  months and integrated cumulatively in frequency,  $\dot{f} \in [-1.0, +0.1] \times 10^{-8}$  Hz/s and we have considered an all sky search.

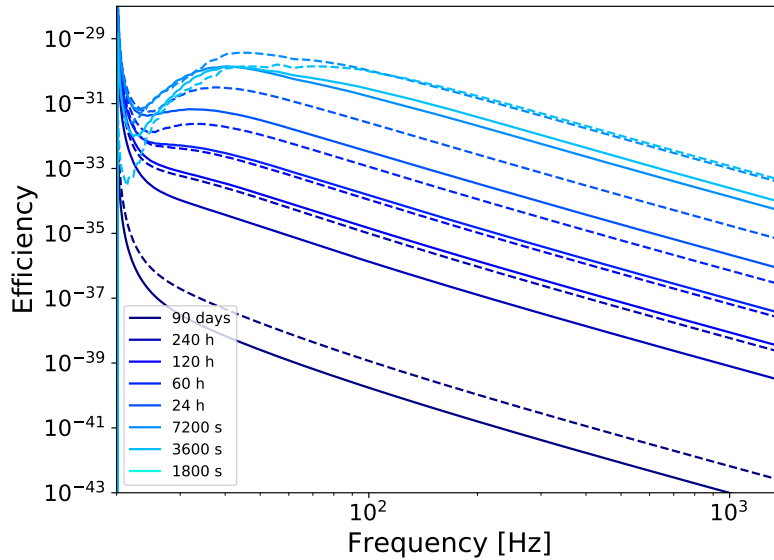


FIGURE 1.8: This figure shows the efficiency from eq.(1.8) where the dashed lines correspond to the *Young* set of pulsars with an age  $\tau_g < 4$  Myrs from 1.2 and the continuous to the full set from figs.1.1. For this figure we have set  $T_{\text{obs}} = 3$  months and integrated cumulatively in frequency,  $\dot{f} \in [-1.0, +0.1] \times 10^{-8}$  Hz/s and we have considered an all sky search.

the computational resources to cover the entire LIGO frequency range in order to cover the unexpected (Riles, 2017) e.g to take into account the large population of expected gravitars (neutron stars with gravitationally dominated frequency evolutions), we have shown that an astrophysical prior-based search should improve the detection probability as well as state stronger constrains over its own assumptions, therefore they should be an extension to the already defined list of searches for CW. This is just a preliminary analysis, and a more detailed study should be done in order to fully optimize CW searches. From figs.(1.7,1.8) we see that, as mentioned before, a frequency band splitting and a multi-distance approach should be implemented in order to optimize the low and the high frequency.

This section points out a way to increase the efficiency of a search at an acceptable cost, legitimating the introduction of a hierarchical set-up as the optimal way to proceed for future searches.



## Chapter 2

# The Hough transform search for continuous GWs

This chapter will be devoted to the *SkyHough* semi-coherent method for Continuous Gravitational Wave Searches. We will expose the different steps of this pipeline, as well as its implementation and integration within the continuous wave searches of the LIGO Scientific Collaboration.

The first step of the method conforms the core step into the search: The Hough Transform. Conceived as a pattern recognition algorithm, it constructs a map between power tracks on the data spectrogram and continuous wave parameters that generate such tracks. After an initial implementation (Krishnan et al., 2004), several strategies were proposed in order to include further information from the detector, namely the amplitude modulation of the signal due to the antenna pattern functions and the varying noise floor. After an initial idea (Sintes and Krishnan, 2006), based on a variable threshold on the data, a different weighted-statistics approach was proposed (Sintes and Krishnan, 2007), significantly increasing the search sensitivity for all-sky searches (Abbott, 2008; Aasi, 2014a) and effectively constructing the modern form of SkyHough.

The second step is a new post-processing method. The objective is to reduce the false alarm i.e a manageable amount of outliers to be follow-up, and keeping a competitive efficiency. It exploits the required signal consistency between detectors to eliminate univocal noise sources and the creation of clusters to further reduce the amount of outliers that have a common origin.

These steps were introduced as a whole during the Mock Data Challenge (MDC) of the S6 LIGO science run (Walsh, S. and Pitkin, M. and Oliver, M. and D’Antonio, S. and Dergachev, V. and Królak, A. and Astone, P. and Bejger, M. and Di Giovanni, M. and Dorosh, O. and Frasca, S. and Leaci, P. and Mastrogiovanni, S. and Miller, A. and Palomba, C. and Papa, M. A. and Piccinni, O. J. and Riles, K. and Sauter, O. and Sintes, A. M., 2016), proving to conform the most robust search against noise disturbances up to that point. As a result, these same strategies were applied to the first science run of the Advanced LIGO detectors (O1) (Abbott, 2017f; Abbott, 2018e), and have served as a substrate for further improvements during the second science run of such detectors (O2).

The software related to this method is publicly available at the standard LIGO Algorithm Library (*LIGO Algorithm Library - LALSuite*).

### 2.1 The *SkyHough* pipeline implementation

We start by introducing the implementation of the Hough Transform. Further details can be found in (Krishnan et al., 2004; Sintes and Krishnan, 2007). Since the main behavior of the continuous signal is reflected into modulations of the frequency, the

Short-time Fourier Transform (SFT) is used as the main analysis tool, providing a fine control on the frequency resolution to contain the desired modulation within the desired scale by computing Fourier transforms of data segments.

The first step is to divide the full observation time  $T_{\text{obs}}$  in  $N$  segments of length  $T_{\text{coh}}$ , each of which will result in a SFT; the length of such segments  $T_{\text{coh}}$  will be discussed during the next section. Then, we compute the Discrete Fourier Transform (DFT) of each segment as

$$\tilde{x}[f_k] = \frac{1}{f_s} \sum_{l=0}^{M-1} x[T_l] e^{-2\pi i f_k T_l}, \quad (2.1)$$

where  $[\cdot]$  represents a discrete function,  $x[T_l]$  corresponds to the data point at time  $T_l$  and  $M$  corresponds to the number of points within a data segment. Being  $f_s$  the sampling frequency of the detector, around  $16\text{kHz}$  for the current Advanced LIGO detectors,  $M = T_{\text{coh}} f_s$ . This DFT can be further modified according to the standards of the LIGO Scientific Collaboration in order to construct a proper SFT ([SFT Data Format Version 2 Specification](#))

The final step computes a normalized power spectrum for each frequency bin  $f_k$  as

$$\rho_k \approx \frac{2|\tilde{x}[f_k]|^2}{T_{\text{coh}} S_n[f_k]}, \quad (2.2)$$

which expresses the power of each frequency bin in units of the noise power of the detector, as discussed in 1.

### 2.1.1 The Short-time Fourier Transform of the signal

The use of Short-time Fourier Transforms introduces a degree of freedom into gravitational wave searches, since one has to decide on how long the data segments are going to be.

Considering each data segment of length  $T_{\text{coh}}$  is *coherently* analyzed, being  $T_{\text{coh}}$  the coherent length of a SFT. A general criteria, introduced on (Jaranowski, Krolak, and Schutz, 1998) asserts that any physical effect that contributes less than  $\frac{1}{4}$  of the signal phase cycle during a coherent time does not have to be taken into account; in terms of continuous wave signal parameters, the criterion is expressed as  $|\dot{f}| \leq T_{\text{coh}}^{-2}$ . This may yield a segment-wise 10% loss in SNR (Jaranowski and Krolak, 1999, appendix A).

Moreover, there are two frequency modulations involved in the signal of an isolated neutron star: The spin-down of the source and the Doppler modulation, consequence of the Earth motion.

Let us first acknowledge the constrain imposed by the spin-down of the signal model eq.(1.37). The largest value of spindown is assumed to be  $\sim 10^{-8}$  Hz/s, yielding  $T_{\text{coh}} < 7 \times 10^4$  as a constraint on  $T_{\text{coh}}$ .

As for the Doppler modulation, we reproduced the argument given by (Krishnan et al., 2004), i. e. differentiate  $v(t)$  on eq.(1.37) considering a fixed source frequency  $\hat{f}$ :

$$\dot{f} \approx \frac{\hat{f}}{c} \frac{d\vec{v}}{dt} \cdot \vec{n} \leq \frac{\hat{f}}{c} \frac{dv}{dt}. \quad (2.3)$$

Then, a simple comparison allows one to further simplify this constrain by considering the daily rotation of the Earth as the most important contribution to the acceleration

$$|\dot{f}|_{\max} = \frac{\hat{f} v_e^2}{c R_e} = \frac{\hat{f} 4\pi^2 R_e}{c T_e^2}, \quad (2.4)$$

where  $v_e$  is the linear velocity of the Earth surface due to its rotation movement,  $T_e$  is the period of a full rotation and  $R_e$  is the radius of the Earth. Therefore, the Doppler shift imposes the following boundary on  $T_{\text{coh}}$

$$T_{\text{coh}} < 4 \times 10^3 \text{s} \times \sqrt{\frac{500\text{Hz}}{f_0}}, \quad (2.5)$$

which results in a stronger constraint than the spin-down modulation.

The vast majority of CW, including the S6 MDC and the O1 analysis, use  $T_{\text{coh}} = 1800\text{s}$ , which satisfies eq.(2.5) up to  $\sim 2450$  Hz. Moreover, the  $\frac{1}{4}$  criteria allows the antenna pattern functions  $F_{\times,+}$  to be considered constant inside of each SFT when such  $T_{\text{coh}}$  is used. This is one of the key factors that differentiates the standard Hough transform (Krishnan et al., 2004), which effectively averaged those functions along the whole observation time  $T_{\text{obs}}$ , and the improved *SkyHough* implementation (Sintes and Krishnan, 2007), which averaged the antenna pattern function on each SFT.

Finally, a last approximation with respect to the exact signal model is required: The constant amplitude approximation  $|\dot{h}_0(T_I)|T_{\text{coh}}/h_0(T_I) \leq 10\%$ , being  $h_0(T_I)$  the strain amplitude of a signal at time  $T_I$ . It assumes that the signal strength is constant inside of an SFT, and it is valid due to the typical  $\sim 10\%$  amplitude calibration error.

### 2.1.2 The Hough maps

The Hough transform works over a digitalized spectrum i.e the method differentiates between two flavors of bins. In order to construct such a spectrum, the *SkyHough* approach thresholds the normalized power  $\rho_k$  defined in equation 5.14; that is, if the value of the  $k$  – th frequency bin satisfies  $\rho_k \geq \rho_{\text{th}}$ , then it gets assigned a 1; otherwise, it gets assigned a 0. In the end, this process yields a distribution of ones and zeros over the time-frequency plane of the data, known as the peak-gram.

If we assume the signal to be well resolved within a frequency bin, then the optimal threshold is given by  $\rho_{\text{th}} = 1.6$ , and yields a peak selection false alarm  $\alpha = 0.2$ . We refer to (Krishnan et al., 2004; Sintes and Krishnan, 2007) for a derivation of this threshold.

Looking at eq.(1.37), let us define a template as  $\vec{\xi} = (\{f_s\}, \vec{n})$ , i.e the required parameters of the signal. Given a set of templates that differ only on the sky position  $\vec{n}$ , we can rewrite eq.(1.37) as:

$$\cos\phi = \frac{\vec{v} \cdot \vec{n}}{v(t)} = \frac{c}{v(t)} \frac{f(t) - \hat{f}(t)}{f(t)}. \quad (2.6)$$

Therefore, each frequency observed by the detector  $f$  at each time  $t$  is consistent with a certain set of sky locations. Due to the segmentation of the data, in segments of length  $T_{\text{coh}}$ , the observed frequency is quantize in terms of  $\delta f = \pm 1/(2T_{\text{coh}})$  and such sets of sky locations are shaped like annulus with certain thick given by

$$\delta\phi \approx \frac{c}{v} \frac{\delta f}{\hat{f} \sin\phi}, \quad (2.7)$$

Reusing eq.(2.6) on the discrete, observable frequencies  $f_k = \hat{f} + n\delta f$  with  $n$  as an integer at time  $T_I$ , we obtain:

$$\cos\phi_n = \frac{nc\delta f}{v\hat{f}(T_I)}. \quad (2.8)$$

Each annulus gets assigned to 1 or to 0, depending on the peak-gram value for that certain  $f_k$  at  $T_I$ . Such a collection of ones and zeros along the sky is called Partial Hough Map (PHM).

The *DriveHoughMulti.c* code does not compute the complete collection of PHMs for each template on each segment or SFT. The reason behind this is that Partial Hough Maps are practically insensitive to small deviation on the frequency for a given time; i.e they are reusable inside a certain data segment and a certain range of  $\hat{f}$ . To evaluate the validity of the PHM, let us consider the variation of a given annulus  $n$  on eq.(2.8) due to small changes in  $\hat{f}$ :

$$\frac{d\hat{f}}{\hat{f}^2} = \frac{v}{nc\delta f} \sin\phi_n d\phi_n. \quad (2.9)$$

By setting  $d\phi_n = r(\delta\phi)_{\min}$  and  $d\hat{f} = \kappa\delta f$ , where  $r$  is a tolerance factor and  $\kappa$  is the allowed frequency shift in frequency bins, the previous equation can be written as:

$$\kappa = \frac{rc}{v} \tan\phi_n = \frac{rc}{v} \sqrt{\frac{n_0^2}{n^2} - 1}, \quad (2.10)$$

where  $n_0 = v\hat{f}/(c\delta f)$ . As argued in (Krishnan et al., 2004),  $(\delta\phi)_{\min} = \frac{c}{v} \frac{\delta f}{\hat{f}}$  and the previous equation can be approximated as:

$$\kappa \approx \frac{rc}{v} (\delta\phi)_{\min} = 40r \sqrt{\frac{500\text{Hz}}{\hat{f}}}. \quad (2.11)$$

As an example for  $n_0 = 90$ ,  $T_{\text{coh}} = 1800\text{s}$ ,  $\hat{f} = 500\text{Hz}$ ,  $v/c = 10^{-4}$  and a tolerance value of  $r = 0.1$ , the annulus for  $n = 89$  is valid over 150 bins. If applied correctly, this strategy can greatly reduce the computational cost, since PHMs can be stored inside Look Up Tables to reduce the number of operations to be performed.

The sum of all the PHMs is known as the Total Hough Map THM, and its a matrix for a given set of spind-down values  $\{f_s\}$  containing the number count of each sky position. In general, the search will consider any  $f_{s>1}$  as zero, i.e it will only search over one spin-down parameter.

To do the summation the code ignores the term  $\Delta r$  in eq.(1.37). This approximation holds if the spin-down age of the neutron star  $\tau = \hat{f}/f_{(1)}$  is much larger than the light travel time  $\Delta r/c$ . With this approximation. it is easy to find the group of PHMs that need to be added together according to the right trajectory in the time-frequency plane, as shown on fig.2.1.2 from (Krishnan et al., 2004).

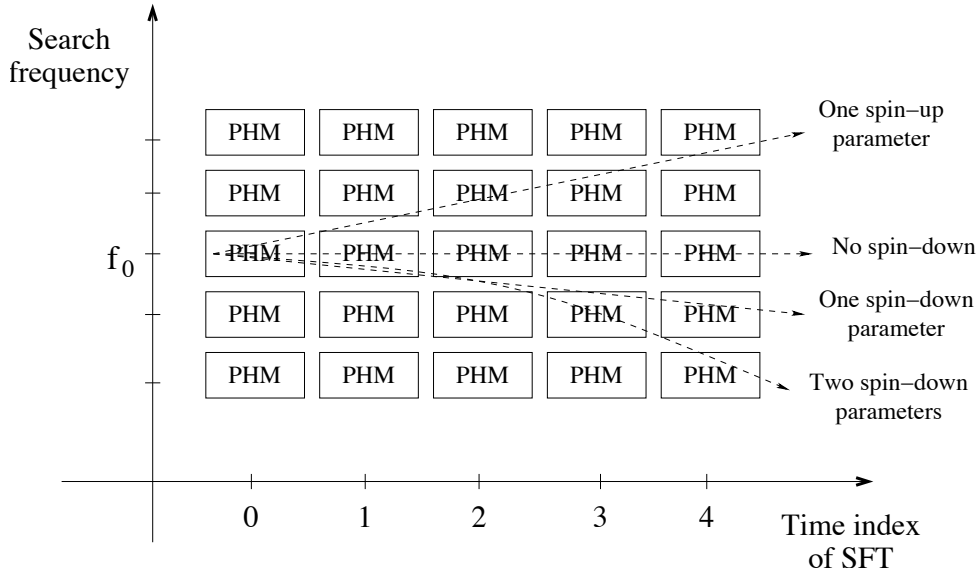


FIGURE 2.1: A Partial Hough Map  $i(\text{PHM})$  is a histogram in the sky-position plane  $\vec{n} = (\alpha, \delta)$  constructed from all the frequencies selected at a *given* time and for a *given* value of the source frequency  $\hat{f}$ . A total Hough map is obtained by summing over the appropriate Partial Hough Maps. The PHMs to be summed over are determined by the choice of spin-down parameters, which give a trajectory in the time-frequency plane. For example, a single spin down parameter will give a straight line as shown in the figure, while two spin-down parameters will lead to a parabola. This figure and caption come from (Krishnan et al., 2004)

### 2.1.3 Resolution in the space of sky-positions and spin-down parameters:

Given the previous calculation of the annuli width, sky discretization  $\delta\theta$ , known as *pixel size*, is taken to be a fraction of the thinnest annulus  $\delta\phi_{\min}$ .

$$\delta\theta = \frac{\delta\phi_{\min}}{P_{\text{sky}}}, \quad (2.12)$$

where  $P_{\text{sky}}$  corresponds to a refinement parameter known as the pixel factor; this factor will have a direct impact over the efficiency and the computational cost of the search.

For the resolution on spin-down  $\delta f_s$  the obvious choice is given by

$$\delta f_n = n! \frac{\delta f}{T_{\text{obs}}^n}. \quad (2.13)$$

## 2.2 The Hough post-processing

In this section we will focus on the treatment and classification of the results of the Hough Transform.

To conduct this post-processing step, we start by splitting the total amount of SFTs into two independent subsets, each of which will contain a similar amount of SFTs with similar sensitivities, otherwise our results would be thresholded by the worst subset. The first step is to study the statistical significance of each template using

the Total Hough Map results and comparing them against a stationary zero-mean Gaussian noise. A detail analysis for the statistical interpretation of this process can be seen in (Krishnan et al., 2004; Sintes and Krishnan, 2007), and an equivalent derivation is also included in chapter 5.

Due to the large number of templates in a search  $\sim 10^{19}$ , only a portion of them will be saved, i.e the search will generate lists containing the most significant  $N_t$  templates, i.e. toplists; each template in such toplists is known as a candidate. Each toplists will enclose candidates from a certain frequency band, typically between 0.1Hz and 0.15Hz

### 2.2.1 Critical Ratio - $\Psi$

The critical ratio  $\Psi$  is a new random variable defined to evaluate the significance of a given template. Based on the results for the weighted number-count  $n$ , the peak selection false alarm  $\alpha$  and the assumption over the detector noise following a stationary zero-mean Gaussian distribution, we define the critical ratio as

$$\Psi = \frac{n - \langle n \rangle}{\sigma} \quad (2.14)$$

$$= \frac{\sum_{l=1}^{N_{\text{coh}}} w_l (n_l - \alpha)}{\sqrt{\sum_{l=1}^{N_{\text{coh}}} (w_l)^2 \alpha (1 - \alpha)}}, \quad (2.15)$$

where  $n_i$  corresponds to the  $i$ -th digitalized bin in a given template's power track and  $w_i \propto (a_i^2 + b_i^2)/S_{n,i}$ , where  $a_i$  and  $b_i$  are amplitude functions of the antenna patten as described in (Jaranowski, Krolak, and Schutz, 1998) at the  $i$ -th time step.  $S_{n,i}$  is the power spectral density at that given bin. As mentioned in (Sintes and Krishnan, 2007), any normalization of the weights will leave  $\Psi$  unchanged, as well as the sensitivity.

The threshold for a search is determined by considering  $\Psi$  to follow a Gaussian distribution with zero-mean and  $\sigma = 1$ . If the critical ratio of candidate lays below a pre-specified threshold, then it is disregarded. To compute this threshold, one needs to have into account the overall false-alarm probability of the search  $\alpha_S = \frac{2\alpha_I}{N_t}$

$$\Psi_{\text{th}} = \sqrt{2} \text{erfc}^{-1} \left( \frac{2\alpha_I}{N_t} \right). \quad (2.16)$$

See 5.4.5 for more details about this result.

### 2.2.2 Derivation of the $\chi^2$ statistics

The  $\chi^2$ -test was first implemented in the *SkyHough* analysis of the initial LIGO era, during the S5 science run Aasi, 2014a. It was introduced as a way to study the power deviations of a template during the total observation time, allowing us to effectively establish a veto on templates with ill-behaved power with respect to this new  $\chi^2$ -like statistic.

In order to generate a veto, a  $\chi^2$  discriminator needs to be established. The basic idea is that a continuous wave signal has to be detected in a continuous manner through the observation time. Therefore, if we divide the total amount of segments into  $p$  subsets with roughly the same amount of segments  $N_j$ , the results for the critical ratio on each of the subsets should be similar. Let us define the incoherent

statistic as:

$$M := \sum_{j=1}^p N_j, \quad n^j := \sum_{i \in S_j} n_i, \quad A^j := \sum_{i \in S_j} w_i, \quad (2.17)$$

where  $M$  corresponds to the total number of SFTs and  $S_j$  is the set of SFT for each of the  $p$  subsets. As described in (Krishnan et al., 2004; Sintès and Krishnan, 2007), again under the assumption of stationary zero-mean Gaussian detector noise, the number count statistics are given by

$$\langle n \rangle = \sum_{j=1}^p \sum_{i \in S_j} w_i \alpha = \sum_{j=1}^p \langle n^j \rangle, \quad (2.18)$$

$$\sigma_j = \sum_{i \in S_j} \eta_i (1 - \eta_i) w_i \approx \eta (1 - \eta) \sum_{i \in S_j} w_i, \quad (2.19)$$

where  $\eta_i \approx \eta$  and  $\eta = \langle n \rangle / N_{\text{coh}}$  is the probability of obtaining a 1 on the  $i$ -th SFT in the presence of a signal.

With this information we can construct a  $\chi^2$  discriminator following a  $\chi^2$ -distribution with  $p - 1$  degrees of freedom:

$$\chi^2 = \sum_{j=1}^p \frac{(n^j - \langle n \rangle) (\sum_{i \in S_j} w_i / \sum_{i=0}^{N_{\text{coh}}} w_i)^2}{\sigma_j}. \quad (2.20)$$

See Jordana and Sintès, 2008 for a more detailed derivation.

In order to use this statistic as a veto, a characterization of the response under different conditions is required, being the easiest way to evaluate the results of a large set of injections that populate the  $\Psi_{\text{th}} - \chi^2$  plane to discriminate possible signals from noise. The *MCInjectHoughMultiChi2Test.c* code, part of the (*LIGO Algorithm Library - LALSuite*), was developed to perform this characterization by following a Monte Carlo (MC) approach.

The first step is to select a set of clean,  $\sim 0.1\text{Hz}$  frequency bands, that is, free of spectral disturbances. Then a MC is used to simulate a set of signals and include (i. e. *inject* them) into the clean bands. After that, the nearest templates around the injection are evaluated, and the results are grouped into batches of  $N_b$  templates, sorted by their CR. For each batch, we compute the mean  $\Psi$  and the standard deviation of  $\chi^2$ . Finally, we use a curve to model the results. The most common choice follows a power law

$$\chi^2 = p - 1 + A_1 \Psi^{A_2} + \sigma \left( \sqrt{2(p - 1)} + B_1 \Psi^{B_2} \right), \quad (2.21)$$

where  $A_1$  and  $A_2$  are the fitting parameters corresponding to the mean and  $B_1$  and  $B_2$  are the ones related to the standard deviation.  $\sigma$  is a multiplying factor of the standard deviation term that will define how strict the veto is; it is directly related to the false dismissal of the veto. In the case of stationary zero-mean Gaussian noise and no mismatch between the signal and template parameters,  $p - 1$  represents the expected value of the mean, and  $\sqrt{2(p - 1)}$  represents the expected value of the  $\chi^2$  standard deviation. Once the fitting parameters are computed, a convenient threshold  $\sigma_{\text{th}}$  can be assigned as veto to any template that does not satisfy the following expression:

$$\sigma_{\text{th}} > \frac{\chi^2 - p + 1 - A_1 \Psi^{A_2}}{(\sqrt{2(p - 1)} + B_1 \Psi^{B_2})} \quad (2.22)$$

### 2.2.3 Construction of coincidences

This step is intended to reduce most of the spurious candidates from univocal sources of noise included in the toplists. In general, the reference time of each candidate is defined by the first SFT of a set, fact that may lead to inconsistencies among different subsets. The translation from each subset to a common one takes into account the spin-down value of the candidate  $\dot{f}$  and the time difference between the original reference time and the new one  $\Delta t$ :

$$f_{\text{common}} = f_{\text{old}} - \dot{f}\Delta t. \quad (2.23)$$

From this point on, we will differentiate two toplists as  $X$  and  $Y$ .

After establishing a common reference time on both toplists, we compute the number of bins of distance in the parameter space between candidates by using the following metric

$$D_{\dot{f}}^{ij} = \frac{2|X_{\dot{f}}^i - Y_{\dot{f}}^j|}{\delta X_{\dot{f}}^i + \delta Y_{\dot{f}}^j}, \quad (2.24)$$

$$D_{\theta}^{ij} = \frac{2|X_{\theta}^i - Y_{\theta}^j|}{\delta X_{\theta}^i + \delta Y_{\theta}^j}, \quad (2.25)$$

$$D_{\text{sky}}^{ij} = \frac{4 \arccos(\cos X_{\theta}^i \cos Y_{\theta}^j \cos(X_{\alpha}^i - Y_{\alpha}^j) + \sin X_{\theta}^i \sin Y_{\theta}^j)}{\delta X_{\theta}^i + \delta Y_{\theta}^j}, \quad (2.26)$$

where the subindex corresponds to the parameter under scope and the superindex identifies the candidate.  $\delta f = 1/T_{\text{coh}}$ ,  $\delta \dot{f} = 1/T_{\text{coh}}/T_{\text{obs}}$ ,  $\delta \theta = c\delta f/(\dot{f}vP_{\text{sky}})$ , and the denominators define an average resolution for each parameter. Therefore the total geodesic distance, or radius, between the pair  $(X^i, Y^j)$  is given by

$$D^{ij} = \sqrt{(D_{\dot{f}}^{ij})^2 + (D_{\theta}^{ij})^2 + (D_{\text{sky}}^{ij})^2}. \quad (2.27)$$

We define a coincidental pair will be as a pair of candidates  $(X^i, Y^j)$  that lay closer than a distance  $D_{\text{coincidence}}$  from each other, i.e  $D^{ij} \leq D_{\text{coincidence}}$ . In general, the correct choice for the coincidence distance  $D_{\text{coincidence}}$  is often ambiguous as the noise is far from Gaussian; it is required an extensive analysis with software-injected signals in order to overcome this issue.

To condense the information from coincidental candidates, a unique list of centers is created. For each coincidental pair  $(X^i, Y^j)$ , a center point  $XY^v$  is generated as follows:

$$XY_{\dot{f}}^v = \frac{X_{\dot{f}}^i + Y_{\dot{f}}^j}{2}, \quad (2.28)$$

$$XY_{\dot{f}}^v = \frac{\dot{f}_X^i + \dot{f}_Y^j}{2}, \quad (2.29)$$

$$XY_{\Psi}^v = \frac{X_{\Psi}^i + Y_{\Psi}^j}{2}. \quad (2.30)$$



$$\hat{g}^\nu = (X_\Psi^i X_{\hat{n}}^i + Y_\Psi^j Y_{\hat{n}}^j) / (X_\Psi^i + X_\Psi^j); \quad (2.31)$$

$$XY_\alpha^\nu = \mathbb{R}(\text{atan}_2(g_2^\nu, g_1^\nu)), \quad (2.32)$$

$$XY_\theta^\nu = \mathbb{R}(\text{asin}(g_3^\nu / |\hat{g}^\nu|)). \quad (2.33)$$

$$(2.34)$$

Where the subindex  $\hat{n}$  indicate the use of Cartesian coordinates to define the sky location. To avoid excessively large lists of centers, a toplist of  $N_g$  centers is created using the frequency bands from the initial toplist and the shared critical ratio  $XY_\Psi^\nu$  as a ranking statistic.

### 2.2.4 Clustering method

The last step is intended to identify centers which share a common origin, clustering them according to its distance in the parameter space. A cluster is defined by a closed set of centers laying within certain radius  $R_{\text{cluster}}$  from one another or with a common neighbor between them; i.e, the center  $i$  is part of the same cluster as center  $j$ , even if  $D^{ij} < R_{\text{cluster}}$  or there is a center  $k$  which verifies  $D^{ik} \leq R_{\text{cluster}}$  and  $D^{jk} \leq R_{\text{cluster}}$ . In other words, a cluster is the full graph of centers that satisfy the following expression:

$$D^{ij} \leq R_{\text{cluster}}. \quad (2.35)$$

It is important to realize that a center by itself defines a cluster of population one, which is the minimum size of a cluster. The maximum is defined by the total number of centers. In general, the selected radius is  $R_{\text{cluster}} = D_{\text{coincidence}}$ , to respect the false alarm set on the coincidence step.

A cluster is characterized by its population  $C_P$ , that is, the number of centers that conform the cluster; the correspondent contributions from each subset  $C_X, C_Y$ ; the maximum critical ratios  $XY_\Psi, Y_\Psi, X_\Psi$  and the cluster critical ratio

$$C_\Psi^j = \frac{\sum_{i \in v_j} XY_\Psi^i}{C_P^j}, \quad (2.36)$$

where  $v_j$  contains all the centers for the cluster  $j$ . With this information, a population veto will consider any cluster that does not satisfy the following expression as noise:

$$C_P^j \leq C_P^{\text{th}} \quad C_X^j \leq C_X^{\text{th}} \quad C_Y^j \leq C_Y^{\text{th}}. \quad (2.37)$$

The surviving clusters from each band are ranked according to their  $C_P^j$ , selecting a maximum of  $N_{\text{cb}}$ . An important addition to the ranking is that a cluster overlapping with a known line (Covas, 2018) will be down ranked below the last non-disturbed cluster for that band. The selected clusters will define the follow-up centers as follows:

$$C_f^j = \sum_{i \in v_j} \frac{XY_\Psi^i XY_f^i}{C_\Psi^j C_P^j}, \quad (2.38)$$

$$C_f^j = \sum_{i \in v_j} \frac{XY_\Psi^i XY_f^i}{C_\Psi^j C_P^j}, \quad (2.39)$$

$$(2.40)$$

$$\hat{g}^j = \sum_{i \in v_j} C_{\Psi}^i C_{\hat{n}}^i; \quad (2.41)$$

$$C_{\alpha}^j = \mathbb{R}(\text{atan}_2(g_2^j/g_1^j)), \quad (2.42)$$

$$C_{\theta}^j = \mathbb{R}(\text{asin}(g_3^j/|\hat{g}^j|)). \quad (2.43)$$

$$(2.44)$$

Therefore any follow-up procedure will cover the area enclosed by the entire cluster and some wings based on their sky-location and the available computing power.

## Chapter 3

# A comparison of methods for the detection of gravitational waves from unknown neutron stars

S. WALSH, M. PITKIN, M. OLIVER, S. D'ANTONIO, V. DERGACHEV, A. KRÓLAK, P. ASTONE, M. BEJGER, M. DI GIOVANNI, O. DOROSH, S. FRASCA, P. LEACI, S. MASTROGIOVANNI, A. MILLER, C. PALOMBA, M. A. PAPA, O. J. PICCINNI, K. RILES, O. SAUTER, A. M. SINTES

Certificate on Appendix [A](#)

### 3.1 Introduction

Continuous gravitational waves (CWs) from isolated neutron stars (NSs) are a potential source of detectable gravitational waves. CW radiation is emitted by rotating NSs with non-axisymmetric deformations. The signal is expected to be relatively stable over many years. While the amplitude of CW signals is expected to be small, the continuous nature of the signal allows us to integrate the signal over large time spans of data to distinguish it from noise.

Broad-band all-sky searches cover the whole sky over a broad range of frequency and frequency derivative in order to detect CW radiation from unknown NSs. All-sky searches in the initial Laser Interferometer Gravitational-Wave Observatory (LIGO) Abbott, 2009b; Aasi, 2015b and Virgo Acernese, 2008 data have so far not resulted in detection. Instead upper limits have been placed on the amplitude of CWs from isolated NSs Abbott, 2016c; Abadie, 2012; Isi et al., 2018; Aasi, 2014b; Aasi, 2014a. The advanced detectors, which began operation in 2015, will eventually have a sensitivity to these weak signals over an order of magnitude more than that of the previous generation, with the largest gains at frequencies below 100 Hz.

The purpose of the study presented in this article is to examine and compare the efficiency of the methods that will be used to perform all-sky searches in data from the advanced LIGO and Virgo detectors. This comparison is made using a mock data challenge *MDC*, for the standard CW signal model described in Sections 3.2 and 3.4. In a blind all-sky search, detectable CW signals may deviate from this model, for example if the NS glitches. For an accurate comparison of the all-sky search methods, further studies will be needed which include deviations from the standard CW model. The study presented here serves as a first benchmark for the search methods, assuming the signal consistently follows the model.

A brief overview of the search methods is presented in Section 3.3; the search parameters for the various searches are presented in 3.6. Section 3.5 describes how

the methods are compared. The results of the comparison are presented in Section 3.7.

## 3.2 The signal

Gravitational waves (GWs) emitted from non-axisymmetric NSs are typically described by a signal model which remains relatively stable over years of observation Jaranowski, Krolak, and Schutz, 1998. The strain amplitude of the GW is proportional to the ellipticity,  $\varepsilon$ , defined as

$$\varepsilon = \frac{|I_{xx} - I_{yy}|}{I_{zz}}, \quad (3.1)$$

where  $I_{zz}$  is the principal moment of inertia of the star, and  $I_{xx}$  and  $I_{yy}$  are the moments of inertia about the axes. The strain amplitude of the GW at the detector, assuming a rigidly rotating triaxial body, is then given by

$$h_0 = \frac{4\pi^2 G}{c^4} \frac{I_{zz} f^2 \varepsilon}{d}, \quad (3.2)$$

where  $f$  is the frequency of the GW,  $G$  is Newton's constant,  $c$  is the speed of light, and  $d$  is the distance to the NS. For a star steadily rotating around a principal axis of inertia, the frequency of the GW is at twice the rotational frequency of the NS. The frequency evolves over time as energy is lost due to various dissipation mechanisms, including GW emission. The first time derivative of the frequency,  $\dot{f}$ , is referred to as spindown.

The signal arriving at the detectors is modulated by the motion of the Earth around the Sun and by the rotation of the Earth. Therefore, the signal in the detector reference frame depends on the sky position  $(\alpha, \delta)$  of the source.

The signal model is described by eight parameters, four phase evolution parameters  $(f_0, \dot{f}, \alpha, \delta)$  and four amplitude parameters  $(h_0, \iota, \psi, \phi_0)$ , where  $\iota$  is the inclination angle between the line of sight to the NS and its rotation axis,  $\psi$  is the polarisation angle and  $\phi_0$  is the initial phase of the signal at a reference time.

In a blind all-sky search there is also the potential for the detection of signals produced by different source models (e.g.  $r$ -modes Owen, 2010). The ability of the all-sky search methods to recover such signals is not examined in this study. Here we assume the signal follows the model described above.

## 3.3 Current methods

The most sensitive search for CW signals is performed with a fully coherent integration over a large timespan of data. The computational power required for the integration increases rapidly with the observation time of the data. When searching for CW signals over a broad frequency and spindown range, and over the whole sky, a fully coherent search quickly becomes computationally unfeasible. Frasca, Astone, and Palomba, 2005; Krishnan et al., 2004

This is the motivation for semi-coherent search methods. The data is split into shorter segments which are searched separately with a coherent method using a coarse grid in parameter space. The results of the coherent search in each segment are then combined incoherently on a finer search grid. For limited available computing power,

these semi-coherent search methods achieve a higher sensitivity than could be achieved with a fully coherent search with a tractable coherence time Krishnan et al., 2004.

Some searches use segments which are short enough, on the order of 1800s, so that the signal remains within a single Fourier frequency bin in each segment. In this case, the power of the GW signal is extracted with a single Fourier transform in each segment. Other searches use longer segment times, hours to days, to increase the SNR of the signal in each segment. In this case, the coherent integration uses the more computationally demanding  $\mathcal{F}$ -statistic Jaranowski, Krolak, and Schutz, 1998 to take into account signal modulations. Each search method uses a different variable to quantify SNR, so the numeric values of the SNR thresholds used by each search can not be directly compared.

The sensitivity of the semi-coherent searches is improved by taking a hierarchical approach. After the semi-coherent all-sky search, candidates are selected with a threshold which is lower than needed to claim a detection. A refined, more sensitive search is then performed in the parameter space surrounding each candidate. In principle, the significance of recovered candidates increases in the presence of signal, but not if an original candidate is due to a random noise outlier.

The refinement stages are designed such that any signal passing the first stage has a high probability of being recovered at each following stage. Therefore, the threshold at the first stage ultimately determines the sensitivity of the search.

The deepest searches are performed by the Einstein@Home pipeline, which benefits from the large computing power provided by the Einstein@Home project (Section 3.3.4). Einstein@Home searches take many months before the presence of signal can be confirmed or excluded. There are also quick-look search pipelines which have a much shorter turnaround time. Each all-sky search makes different tradeoffs in the sensitivity vs. robustness against deviations from the assumed phase models. In the following we provide a brief overview of the search procedure employed by each pipeline, and the distinguishing characteristics of each method.

### 3.3.1 Powerflux

The Powerflux method is described in Abadie, 2012; Abadie, 2012; Abbott, 2016a. This search uses 1800-s Hann-windowed short Fourier Transforms (SFTs), with an effective coherence length on the order of 900 s. The power from each SFT is recorded along the track corresponding to each point in parameter space in the time-frequency plane, accounting for Doppler shift and spindown. The power is then weighted, according to noise and detector antenna pattern, to reduce outliers from noise artifacts and maximise the signal-to-noise ratio.

The dataset is partitioned into  $\sim 1$  month stretches, and the sum of the weighted power along the track is produced independently for any contiguous combination of these stretches. High-SNR candidates are identified based on their persistence across contiguous stretches of data.

The candidates are then confirmed as signal or rejected as noise with four additional search stages around each candidate. The parameter space refinement increases with each stage, and the last three stages use the Loosely Coherent detection pipeline Dergachev, 2010. In addition to searching over the four-dimensional parameter space  $(f, \dot{f}, \alpha, \delta)$ , Powerflux also searches over polarisation angle  $\psi$ .

### 3.3.2 Sky Hough

The Sky Hough method is described in Abadie, 2012; Aasi, 2014a. For this search, 1800-s SFTs are digitised by setting a threshold of 1.6 on their normalised power. Thereby, each SFT is replaced by a collection of zeros and ones called a peak-gram. The Hough number count is the weighted sum of the peak-grams along the track corresponding to each point in parameter space in the time-frequency plane, accounting for Doppler shift and spindown. This sum is weighted based on the detector antenna pattern and the noise level, to suppress outliers from detector artifacts. Candidates are selected based on the deviation of the weighted number count from its value in Gaussian noise.

The data is split into two sets containing an equal number of SFTs. The search parameter space is split into sub regions in frequency and sky location. For every region the search returns a toplist of the most significant candidates for both datasets. These candidates are required to pass a significance threshold, and a  $\chi^2$  test is applied to eliminate candidates coming from detector artifacts. Candidates which are not within a coincidence window of each other in both datasets are discarded.

A clustering algorithm is then applied to coincident candidates. The most significant cluster candidate per 0.1 Hz is chosen based on its distance to all other candidates in the toplist, weighted by some significance. Passing candidates are confirmed or rejected with a refinement stage, which covers a reduced parameter space around each candidate with higher resolution in spindown and sky.

### 3.3.3 Time domain $\mathcal{F}$ -Statistic

The Time domain  $\mathcal{F}$ -statistic search method uses the algorithms and pipeline described in Aasi, 2014b; Astone et al., 2010. This analysis uses fast Fourier Transformed data segments of two sidereal days each, split into bands of 0.25 Hz. A coherent search is performed in each segment, and candidates with an  $\mathcal{F}$ -statistic above threshold are recovered. Recovered candidates around known detector artifacts are vetoed, as are those with similar profiles to stationary noise lines and those close to the polar caps in equatorial coordinates.

The method then searches for coincidences among candidates in each two-day segment. Candidate frequencies are converted to a common reference time, using the candidate spindown. Coincident candidates are counted, within a coincidence window large enough to account for Doppler modulation. The coincidence with the highest multiplicity is considered the most significant candidate, which is then selected or rejected based on a threshold on its false alarm probability.

### 3.3.4 Einstein@Home

Einstein@Home is a volunteer-driven distributed computing project where members of the public donate their idle computing power to the search for GWs *Einstein@Home*. The donated computing power allows for broader and more sensitive searches for CWs. The Einstein@Home search is described in Abbott, 2016c. The search begins with 1800-s SFTs. SFT bins which overlap with known detector artifacts are cleaned by replacing them with Gaussian noise. For the coherent analysis, the SFTs are combined into segments of a few days. The  $\mathcal{F}$ -statistic is computed for each segment and for each parameter space point on a coarse grid. An average  $2\mathcal{F}$ -statistic is then calculated by summing the  $2\mathcal{F}$  values at each segment at the appropriate coarse

grid point to approximate the  $2\mathcal{F}$  at a given fine grid point Pletsch and Allen, 2009. The logKeitel:2013wga statistic, described in Keitel et al., 2014, is calculated for each point. This is derived from the  $2\mathcal{F}$ -statistic, and suppresses detector artifacts appearing in one detector.

The search parameter space is split into regions in frequency and sky. The search is performed for each region, and a toplist of the candidates ranked by logKeitel:2013wga is returned. Candidates from the toplist are selected for further study based on their  $2\mathcal{F}$  value. The threshold applied depends on the total number of candidates above this threshold. There must be few enough that they can all be studied further with a refined search. These candidates are expected to be predominantly from Gaussian noise.

The search proceeds with multiple stages of refinement, described in Papa, 2016, to confirm or reject the presence of a signal.

### 3.3.5 Frequency Hough

The Frequency Hough method is described in Antonucci et al., 2008; Abbott, 2016a; Isi et al., 2018. The analysis uses time-domain cleaned SFTs with a timespan which depends on the frequency band of the search, and is chosen so that the signal remains within a single Fourier frequency bin. A time-frequency map (peakmap) is constructed from the database by selecting the most significant local maxima on the square root of the equalised power<sup>1</sup>, called peaks, over a threshold of  $\sqrt{2.5} \simeq 1.58$ .

The peakmap is cleaned by removing peaks corresponding to lines at a fixed frequency and to wandering lines. Because of time constraints, this cleaning is not applied in the MDC.

In the Frequency Hough step, the points of the corrected peakmap are mapped onto the signal frequency/spindown plane for every sky position. The parameter space (sky position, frequency, spindown) is suitably discretised. In particular, the frequency resolution is increased by a factor of 10 with respect to the ‘natural’ choice (given by the inverse of the SFT duration). The adaptive procedure on the Hough transform, that would allow to take into account noise non-stationarity, has not been used in this analysis.

A given number of the most significant candidates are selected at each sky position and in each 1-Hz interval. This avoids being blinded by particularly disturbed frequency bands. For each candidate a search, refined in spin-down and sky resolution, is performed around the candidate parameters. The refined candidates are clustered and their coincidences with the candidates of another dataset are computed. The coincident candidates are then ranked by significance and the most significant candidates are subject to a refinement stage.

## 3.4 The mock data challenge

The aim of the MDC is to empirically compare the performance of current all-sky search methods when searching for a standard CW signal from an isolated NS. This is done by simulating the detector response to CW signals in data from the S6 LIGO science run Aasi, 2015b, with software injections at a range of frequencies. Each of the pipelines described in Section 3.3 then performs a search over the data to assess

<sup>1</sup>The equalized power is obtained by dividing the periodogram squared by an auto-regressive estimation of the average power. The result is a quantity that typically has a value close to unity except in correspondence of narrow spectral lines, where it takes values larger than one.

their ability to recover this signal.

### 3.4.1 The data

The MDC search is performed over data from the LIGO S6 science run, in which simulated CW signals are injected. Real LIGO data is used to assess the performance of search methods in the presence of detector artifacts. The software injections are generated with `lalapps_sw_inj_frames` in the LALSuite software package *LIGO Algorithm Library - LALSuite*. There are 3110 injections in total. In general, the SNR of the injections was drawn randomly from a uniform distribution between 0 and 150 for a coherent single detector analysis in S6 H1 data (15 months). 50 of the injections have a coherent SNR between 1000 and 2000.

Between 40–1550 Hz the injections are placed at 0.5 Hz intervals, while 90 further injections between 1550–2000 Hz are placed at 5 Hz intervals. The sky position is isotropically distributed over the sky sphere. The spindown is randomly drawn from a uniform distribution in log space between  $-1 \times 10^{-9}$  and  $-1 \times 10^{-18}$  Hz/s for 95% of injections and between  $1 \times 10^{-18}$  and  $1 \times 10^{-13}$  Hz/s for 5% of injections<sup>2</sup>. A braking index between  $n = 5$  and  $n = 7$  ( $n$  defined implicitly in Equation 3.3) is applied to 25% of the pulsars with spindown. The braking index of  $n = 5$  is for a NS which loses all its rotational energy through emission from a constant mass quadrupole, while  $n = 7$  is for saturated  $r$ -mode emission Wette, 2008; Palomba, 2000; Owen, 2010. From the braking index, and the assigned frequency and frequency derivative, the second and third frequency derivative are assigned via the equation

$$\dot{f} = -Kf^n, \ddot{f} = \frac{n\dot{f}^2}{f}, \ddot{\dot{f}} = \frac{n\dot{f}}{f} \left( 2\ddot{f} - \frac{\dot{f}^2}{f} \right). \quad (3.3)$$

The torque function,  $K$ , is described in Allen and Horvath, 1997. The nuisance parameters of the NS,  $\psi$ ,  $\phi_0$  and  $\cos \iota$ , are randomly drawn from uniform distributions with the ranges  $[-\pi/4, \pi/4]$ ,  $[0, 2\pi]$  and  $[-1, 1]$  respectively.

### 3.4.2 The MDC search

It is not feasible for all pipelines to perform a full all-sky search for the MDC, as limited computational resources must be reserved for searches for real signals. Instead, the search is performed over a reduced volume in parameter space around each injection. This MDC search volume is chosen to be small enough that even the most computationally expensive pipeline can participate in the MDC, and large enough so that the MDC results will accurately represent the result of a full all-sky search.

Each injection is placed roughly at the center of an MDC search volume of 0.1 Hz,  $\max[2 \times 10^{-9} \text{ Hz/s}, \pm 3 \times \text{true spindown/spinup}]$  and a region in sky with a radius of 30 degrees  $\times$   $\min[200 \text{ Hz/injection frequency}, 1]$ . The pipelines are provided with the start point and width of the bands in frequency and frequency derivative, and the center and radius of the sky patch.

The specifics of the MDC search performed by each pipeline are described in Section 3.6. After the analysis, each pipeline provides a list of candidates considered to be detections, with the candidate frequency, spindown, right ascension, declination and reference time.

<sup>2</sup>Some injections have been given spinups as real signals can have observed (rather than necessarily intrinsic) spinups due to, e.g. large proper motions for nearby sources, or accelerations in the centers of globular clusters



The MDC is split into two stages, with each stage covering half of the signals. In the first stage the signal parameters are known. Some search methods use this stage to improve their candidate selection and refinement. In the second stage of the MDC, the signal parameters are unknown, only the boundaries of the search region for each injection are provided. These are referred to as blind injections. This stage is used to verify the results from the search over known injections. Once verified, the results from all injections are combined for the final comparison between pipelines.

### 3.4.3 Defining detections

The search parameters and selection criteria used in all-sky searches depend on the parameter space to be covered. For the MDC, each search is required to use search parameters, significance thresholds and selection criteria that would be used in a search over the complete parameter space in frequency, spindown and sky.

In an all-sky search, all candidates from the initial search would pass through the refinement stages. The number of candidates which can be followed up is limited, and different for each method. The detection threshold applied in the MDC must be shown to result in a manageable number of candidates from noise in a full all-sky search for each pipeline. Therefore, each pipeline must establish the number of false alarms expected in a full all-sky search with the thresholds applied in the MDC.

As mentioned in Section 3.3, the selection criteria applied after the initial search ultimately determine the ability to recover signals, as the refinement stages primarily exclude noise. To avoid excessive computing cost, we determine which candidates would result in a detection without requiring them to pass through all refinement stages. For the Sky Hough and Time domain  $\mathcal{F}$ -statistic searches, no false alarms from random noise outliers are expected among the candidates selected within the MDC search volume. Therefore, all candidates are considered detections. The Powerflux candidates are passed through the first refinement stage, after which no false alarms from random noise outliers are expected in the MDC, so all candidates after the first refinement stage are considered detections.

The Einstein@Home search does expect false alarms from random noise outliers after the initial search in the MDC, as it is set up to refine many more candidates than the other searches. The Frequency Hough search also expects false alarms because it searches the whole parameter space, not just the reduced MDC search volume. In a real search, all of these candidates would be passed through the refinement stages, and candidates from signals would result in detections. In the MDC, we apply a threshold on the distance in parameter space between the signal and the recovered candidates in order to identify the candidates from the initial search which would result in a detection after the refinement stages.

For all pipelines, the refined searches are performed for a few MDC candidates that are close to the selection threshold to demonstrate that signals within this distance threshold are retained after the refinement. We also look at the distance in each dimension of parameter space between the signal and the recovered candidates to check for outliers.

## 3.5 Comparison of methods

### 3.5.1 Detection efficiency

Here we are primarily concerned with the ability of different searches to recover the CW signals. The detection efficiency is the fraction of signals which are considered detected, and it is the benchmark that we will use to compare pipeline performance. The detection efficiency is measured as a function of signal strength,  $h_0$ , expressed by the sensitivity depth  $\sqrt{S_h}/h_0$  ( $1/\sqrt{\text{Hz}}$ ), where  $S_h$  is the harmonic sum over both detectors of the power spectral density of the data, at the frequency of the signal. At fixed detection efficiency, a more sensitive search will detect a weaker signal, i.e. it will have a higher sensitivity depth.

Some injections overlap with known detector artifacts. We examine the detection efficiency separately for these signals to assess the performance of the methods in noisy data. We also separate the detection efficiency by frequency, as S6 data contains fewer instrumental artifacts at frequencies greater than 400 Hz. The detection efficiency is also assessed for signals with positive frequency derivative, and those with non-zero second order spindown.

### 3.5.2 Parameter estimation

In a broad parameter space search, the reduction in parameter uncertainty is achieved through the refinement stages that follow the original search. In the MDC the refinement stages are not systematically carried through, as explained in Section 3.4.3. We examine the parameter uncertainty of detection candidates at the final MDC stage and discuss how each method plans to reduce this uncertainty to the level required for a confident detection. In most cases, this automatically yields good parameters estimation (see e.g. Shaltev et al., 2014).

### 3.5.3 Computational cost

Each of the methods has made different compromises on sensitivity to develop an all-sky search using available computational resources.

The MDC is performed on different CPUs for each method, and some chose to cover a larger parameter space than required. Therefore, an accurate comparison of the computing time of each method based on the MDC results is not possible. Instead, each method provides an estimate of how much computing power is required to perform a realistic all-sky search over the first four months of advanced LIGO data (see Table 3.1). The computing cost for each method is provided in MSU (million standard units), where one SU is one core-hour on a standard core. The standard core used here is an Intel Xeon E5-2670 CPU.

The estimates in Table 3.1 are for the four month observing time of the first advanced LIGO data, which is different to the 9 or 15 month observing times used in the MDC. The estimates are also for searches over different ranges in frequency and spindown for each pipeline. It gives a rough idea of the difference in computing resources actually used by each pipeline. These estimates also do not take into account tuning cost and postprocessing costs. By design Einstein@Home is the most computationally intensive, as it is intended to run on the Einstein@Home grid.

Pipeline	Expected runtime of O1 search
Powerflux	6.8 MSU
Time domain $\mathcal{F}$ -statistic	1.6 MSU
Frequency Hough	0.9 MSU
Sky Hough	0.9 MSU
Einstein@Home	100 - 170 MSU

TABLE 3.1: Expected computational costs of searches using the first four months of advanced LIGO data with each search pipeline. These estimates are for a different data observing time from that of the MDC, and do not cover the same parameter space as each other or the MDC. The Einstein@Home searches use the computing resources of the Einstein@Home project and is designed to run for 6 - 10 months in the Einstein@Home grid.

## 3.6 Implementation

In this section we detail the specific search parameters used by each pipeline for the MDC, and explain why the thresholds chosen here are representative of the values in an all-sky search.

The search grid parameters and thresholds applied here will vary in future searches, depending on the observation length of available data, how well behaved the data is, the parameter spacing being covered by the search, and other factors. Any changes to these parameters will affect the detection efficiency, and the variations will be different for each search method. When presenting the MDC results we consider only statistical uncertainties on the measured efficiency. One should keep in mind that these results are specific to the search implementation presented here.

Instances where the searches were not optimal in the MDC are highlighted. In some cases, predictions for how the sensitivity will change in future searches are included.

### 3.6.1 Powerflux

The Powerflux MDC search uses the same search parameters as the Powerflux all-sky search over S6 data described in Abbott, 2016a, these are summarised in Table 3.2. The S6 search was not tuned for frequencies below 400 Hz, therefore, a loss in performance at low frequencies is expected in the MDC. The tuning for searches in advanced detector data will include the low frequency range, reducing or removing this loss in performance.

The search uses all of the MDC data. The sky grid is isotropic on the celestial sphere, with the angular spacing between grid points given by the formula

$$\frac{4500}{T_{coh} \times (f_0 + f_1) \times 0.5 \times \text{sky refinement}'} \quad (3.4)$$

where  $f_0$  and  $f_1$  are the start and end frequencies of each 0.25 Hz band, and  $T_{coh}$  is the coherent segment length.

Every candidate with an SNR greater than 5 is selected. In order to pass to the first refinement stage, candidates are required to appear in at least six contiguous stretches of data. The number of false alarms in a real search is expected to be dominated by instrumental artifacts, and so is difficult to predict. However, since the

MDC search uses the same parameters as a previous all-sky search over S6 data, we know the number of false alarms is manageable Abbott, 2016a.

Candidates surviving the first refinement stage would normally be passed through further stages, with less than 1% false dismissal in the subsequent stages. For the parameter space covered by the MDC, the false alarm rate after the first refinement stage is expected to be negligible. For the MDC, a signal is considered detected if a candidate survives stage one, as all MDC candidates at this stage are expected to be from signals. This choice is justified by performing all refinement stages for the weakest candidates and demonstrating that they are recovered with high significance close to the signal.

Stage	0	1
$T_{coh}$ (s)	900	900
$\delta f$ (Hz)	$2.78 \times 10^{-4}$	$6.95 \times 10^{-6}$
$\delta \dot{f}$ (Hz/s)	$2 \times 10^{-10}$	$1 \times 10^{-10}$
Sky refinement (rad)	1	0.25
Phase coherence	NA	$\pi/2$

TABLE 3.2: Powerflux MDC search parameters. The sky resolution is given by the sky refinement as shown in Equation 3.4.

### 3.6.2 Sky Hough

The Sky Hough MDC search uses a similar search grid to a previous all-sky search over LIGO data Aasi, 2014a, given in Table 3.3. The search uses all of the MDC data. The equatorial spacing of the sky grid points (in radians) is given by the formula

$$\frac{10^4 \delta f}{f \times \text{Pixel factor}}. \tag{3.5}$$

The post-processing procedure has been updated significantly since the previous search, as described in 2 and briefly in Section 3.3.2. The most significant cluster candidate is required to have  $\text{SNR} \geq 4.5$ , and pass the  $\chi^2$  veto described in Aasi, 2014a. All surviving MDC candidates are considered detections.

By selecting only the most significant cluster per frequency band, there is an upper bound on the number of candidates from the all-sky search to be followed up. Therefore, the number of surviving candidates would not be unreasonable in an all-sky search.

$T_{coh}$ (s)	1800
$\delta f$ (Hz)	$5.55 \times 10^{-4}$
$\delta \dot{f}$ (Hz/s)	$1.37 \times 10^{-11}$
pixel factor	2

TABLE 3.3: Sky Hough MDC search parameters. The sky resolution is determined by the pixel factor as shown in Eq 3.5.

### 3.6.3 Time domain $\mathcal{F}$ -statistic

The Time domain  $\mathcal{F}$ -statistic search divides all of the MDC data into two-day segments, and uses 117 segments for the analysis based on the goodness of data Aasi, 2014b. The construction of the 4-dimensional search grid is described in Astone et al., 2010, to achieve a minimal match of  $\sqrt{3}/2$  using the smallest number of grid points with a frequency spacing of  $5.79 \times 10^{-6}$  Hz.

Candidates with  $\mathcal{F} > 10.5$  (corresponding to an SNR of 4.1) in each segment are selected. The bandwidth of each segment is 0.25 Hz, but only candidates in the 0.1 Hz band defined by the MDC search are selected.

After counting coincidences across two-day segments, the most significant candidate per 0.1 Hz band is considered a detection if it is coincident in at least 60 segments. With a simplified estimation of the false alarm rate, this corresponds with a false alarm probability of less than 0.1% per 1 Hz band.

With only one candidate per 0.25 Hz band and an additional threshold with 0.1% false alarm probability, the number of false alarms will not become unmanageable in an all-sky search, and no false alarms are expected in the reduced parameter space covered by the MDC.

Tcoh (h)	48
$\delta f$ (Hz)	$5.79 \times 10^{-6}$
Minimal Mismatch	$\sqrt{3}/2$

TABLE 3.4: Time domain  $\mathcal{F}$ -statistic search parameters. The minimal mismatch is used to construct the 4-dimensional search grid as described in Astone et al., 2010.

### 3.6.4 Einstein@Home

To cover the available frequency band of 40 to 2000 Hz, the Einstein@Home search uses three separate search configurations for 40 to 500 Hz, 500 to 1000 Hz and 1000 to 2000 Hz. The search configurations are given in Table 3.5.

The searches use nine months of the MDC data. The sky grid is hexagonal and uniform on the ecliptic plane, with the distance between grid points given by

$$\frac{\sqrt{\text{sky factor}}}{\pi \tau_E f}, \quad (3.6)$$

where  $\tau_E$  is the radius of the Earth divided by the speed of light. The sky grid points are then projected to equatorial coordinates for the search.

The  $2\mathcal{F}$  thresholds given in Table 3.5 are chosen to result in 35 million false alarms in Gaussian noise in an all-sky search for each frequency band. The false alarm rate in Gaussian noise is estimated as described in Abbott, 2016c.

In an all-sky search, selected candidates are passed through the refinement stages. In the MDC, the parameter space around the candidates in the first refinement stage is used to determine which candidates from the initial stage would result in a detection, see Section 3.4.3.

For the 40 to 500 Hz search, the first refinement stage searches  $\delta f \pm 1.9 \times 10^{-4}$  Hz,  $\delta \dot{f} \pm 3.46 \times 10^{-11}$  Hz/s and a sky patch with a radius of 1.2 initial-search sky grid bins around the selected candidate. Therefore, candidates within this region of the signal

are considered detections. The 500 to 1000 Hz search uses a larger parameter space for the first refinement stage, candidates within  $\delta f < 6 \times 10^{-4}$  Hz,  $\delta \dot{f} < 1.8 \times 10^{-10}$  Hz/s and 3.2 sky grid bins of the signal are considered detections. The distance threshold is the same for the 1000 to 2000 Hz search, except that the candidate must be within 2.4 sky bins. In each case,  $\sim 90\%$  of signals are expected to have a candidate within this region around the signal parameters.

$f$ band (Hz)	40 to 500	500 to 1000	1000 to 2000
Tcoh (h)	60	60	25
$\delta f$ (Hz)	$3.61 \times 10^{-6}$	$3.95 \times 10^{-6}$	$7.75 \times 10^{-6}$
$\delta \dot{f}$ (Hz/s)	$1.16 \times 10^{-10}$	$1.83 \times 10^{-10}$	$7.46 \times 10^{-10}$
sky factor	0.01	0.04	0.07
$\dot{f}$ refine	230	230	150
min $2\mathcal{F}$	6.17	6.17	5.56

TABLE 3.5: Einstein@Home MDC search parameters. The sky grid resolution is determined by the sky factor as shown in Equation 3.6. The spindown resolution used on the fine grid, for the semi-coherent part of the search, is given by  $\delta \dot{f}$  divided by the  $\dot{f}$ -refine value.

### 3.6.5 Frequency Hough

The Frequency Hough MDC search parameters are given in Table 3.6. The sky grid is constructed in ecliptic coordinates as described in Abbott, 2016a, and is uniform in ecliptic latitude at fixed ecliptic longitude. In a real search the coherent segment length would typically be between 1024 and 8192 s, depending on the frequency band. For the MDC, it is restricted to 1024 s over the whole frequency band of the analysis to reduce the computational cost. This implies a sensitivity loss of up to a factor of  $\sqrt{8}$  with respect to a real search in the lower frequency bands, where the coherent segment length would typically be higher.

The Frequency Hough search is performed using all of the MDC data. For the MDC, the search is performed over the whole parameter space. This is because the analysis procedure depends on ranking the most significant candidates per frequency band, as opposed to applying a threshold, so replicating the detection rate of an all-sky search using a smaller parameter space is not trivial. The results for injections where the signal parameters are known are used to optimise the selection of candidates. The search over injections where the signal parameters are unknown are used to validate these results.

The four most significant candidates per 0.1 Hz frequency band are selected. A signal is considered detected if there is a candidate within a distance of 3, where the distance is defined in Eq. 10 of Isi et al., 2018.

Tcoh (s)	1024
$\delta f$ (Hz)	$9.76 \times 10^{-4}$
$\delta \dot{f}$ (Hz/s)	$2.4 \times 10^{-11}$

TABLE 3.6: Frequency Hough MDC search parameters.

## 3.7 Results

### 3.7.1 Detection efficiency

The detection efficiency, measured on the combined results from the set of known injection and blind injections, is shown in Figure 3.1. (In Appendix 3.A Figure 3.11, we show that the detection efficiency measured using known and blind injections are in agreement.)

The dependence of the detection efficiency on sensitivity depth is obtained with a sigmoidal fit to the MDC results. The uncertainty band around the resulting sigmoid is obtained by fitting sigmoids to the minimum and maximum of the binomial uncertainties (at the  $1\sigma$  level) on the detection efficiency. The uncertainty band represents the statistical uncertainty on the detection efficiency for this particular search implementation over LIGO S6 data. We would expect to see variations in the measured efficiency with changes in the observation time of the data, quieter or noisier data, search improvements and other changes expected in advanced detector data. When considering the results one should also keep in mind that these are for standard CW signals.

The Frequency Hough results are complete up to 1000 Hz, however there are no results above this frequency because of technical difficulties with the computer cluster used to perform the search. Specifically, the duration of searches in some frequency bands exceeded the allowance of the cluster for some CPUs. This occurs more at higher frequencies due to the increase in sky grid templates. This issue is being resolved for the Frequency Hough search, but not within the timescale of this MDC. The Frequency Hough results are scaled so that the detection efficiency is measured for the subset of injections for which the search is complete. The results are displayed with a hatched uncertainty band to highlight the difference with respect to the other searches.

Figure 3.1 shows that the results from the Frequency Hough, Sky Hough and Powerflux searches are comparable. If we compare the sensitivity depth achieved at 60% efficiency we see that Time domain  $\mathcal{F}$ -statistic is less sensitive to these standard CW signals. At the same efficiency, the Einstein@Home search is a factor of two more sensitive than the next most sensitive search. This difference can be attributed to a combination of the significant computing resources of the Einstein@Home project, the longer coherent segment length, recent method improvements, and the intensive refinement procedure which allows for the follow-up of many candidates from the all-sky search.

In Figure 3.1 it is clear that the detection efficiency does not reach 100% for very strong signals. For Einstein@Home, this is due to signals which overlap with known noise lines, as shown in Section 3.7.1.1. For Powerflux, this due to signals below 400 Hz, as shown in 3.7.1.2.

#### 3.7.1.1 Robustness in the presence of detector artifacts

Each method has a different procedure for excluding candidates caused by detector artifacts, also known as noise lines, described in Section 3.3. In Figure 3.2 we separate the detection efficiency measured in quiet data, and the detection efficiency measured for injections whose frequency overlaps with known noise lines.

The top panel of Figure 3.2 shows that the efficiency for the Sky Hough, Time domain  $\mathcal{F}$ -statistic and Frequency Hough searches remains unchanged, within the

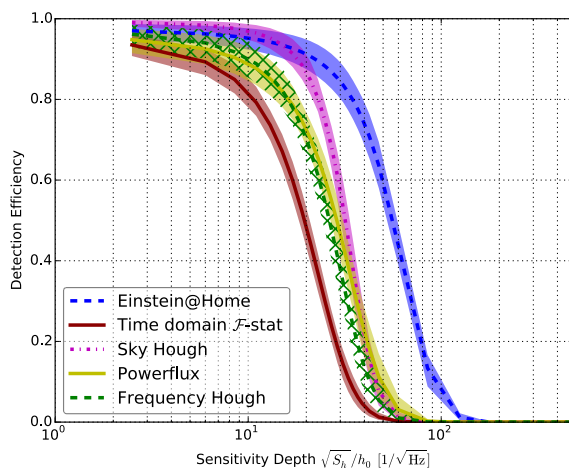


FIGURE 3.1: Detection efficiency measured for all 3110 injections. The Frequency Hough results are shown with a hatched error band because the efficiency is measured for a subset (1920) of the MDC injections. The curves and error bands are obtained by fitting sigmoids to the data, see Section 3.7.1. The error bands represent the statistical uncertainty on the detection efficiency measured for the search implementation and data used in the MDC.

measurement uncertainty, in the presence of noise. The Frequency Hough procedure for handling lines are not included in the MDC, therefore these results are not representative of noise handling in a real search.

As Einstein@Home applies an aggressive cleaning procedure, where known noise lines are replaced by Gaussian noise, any signal which overlaps with a noise line in both detectors is removed. When signal overlaps with a noise line in one detector, the signal is suppressed by the logKeitel:2013wga statistic which downweights signal appearing in one detector. In the case of Powerflux, signals overlapping with noise lines is suppressed by the procedure where SFTs are weighted according to their noise level.

The bottom panel of Figure 3.2 shows that, in the absence of known lines, the efficiency for strong signals has increased for Powerflux and reaches almost 100% for Einstein@Home.

### 3.7.1.2 Dependence on signal frequency or spindown

Here we consider the detection efficiency only for injections that do not overlap with known noise lines. Figure 3.3 shows the detection efficiency separately for injections in the frequency ranges of 40 to 500 Hz, 500 to 1000 Hz and 1000 to 1500 Hz.

The Sky Hough, Time domain  $\mathcal{F}$ -statistic and Frequency Hough results do not depend on frequency. This indicates the Frequency Hough results would not change if injections above 1000 Hz were included. Powerflux measures lower efficiency in the low frequency range. This is expected as the S6 analysis applied in the MDC was only tuned for signals above 400 Hz. In the higher frequency bands, for which the search is designed, the detection efficiency approaches 100% for the strongest signals.

The drop in efficiency for the Einstein@Home search at higher frequencies is expected due to the choice of having equal computing cost assigned to the searches in



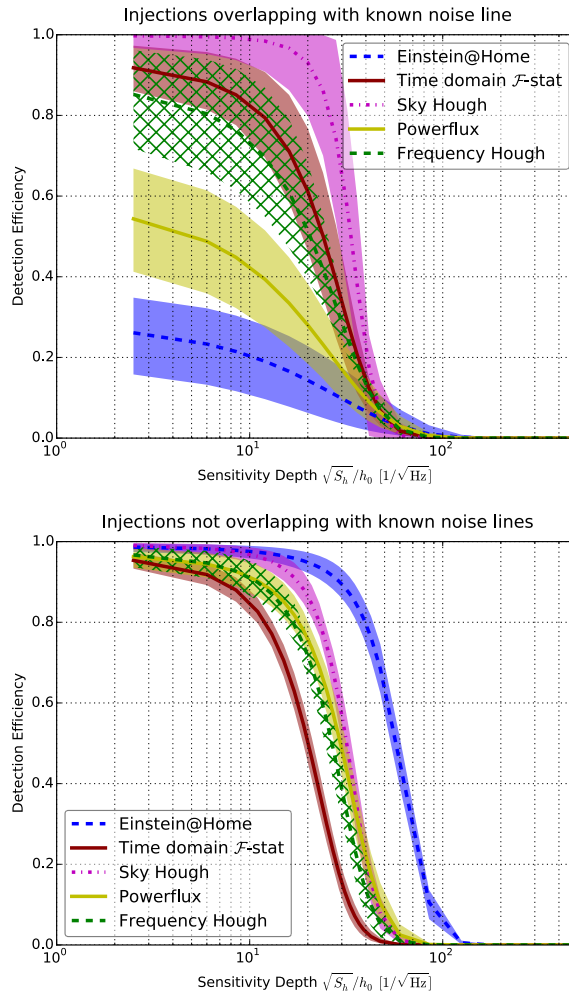


FIGURE 3.2: Detection efficiency measured for injections overlapping with known noise lines (top, 184 injections), and when injections which overlap with known noise lines are excluded (bottom, 2926 injections). The Frequency Hough results are shown with a hatched error band because the efficiency is measured for a subset of the MDC injections (top: 117, bottom: 1803). The curves and error bands are obtained by fitting sigmoids to the data, see Section 3.7.1. The error bands represent the statistical uncertainty on the detection efficiency measured for the search implementation and data used in the MDC.

each of the three frequency bands in Table 3.5. As the frequency increases a higher sky-grid density, and therefore a higher computing cost, is required to achieve the same sensitivity. In order to keep the computing cost fixed, a coarser search grid is used in the higher frequency bands.

Figure 3.4 shows the detection efficiency for injections with large spindown, small spindown and with spinup. There is no dependence on the frequency derivative of the signal for any of the searches.

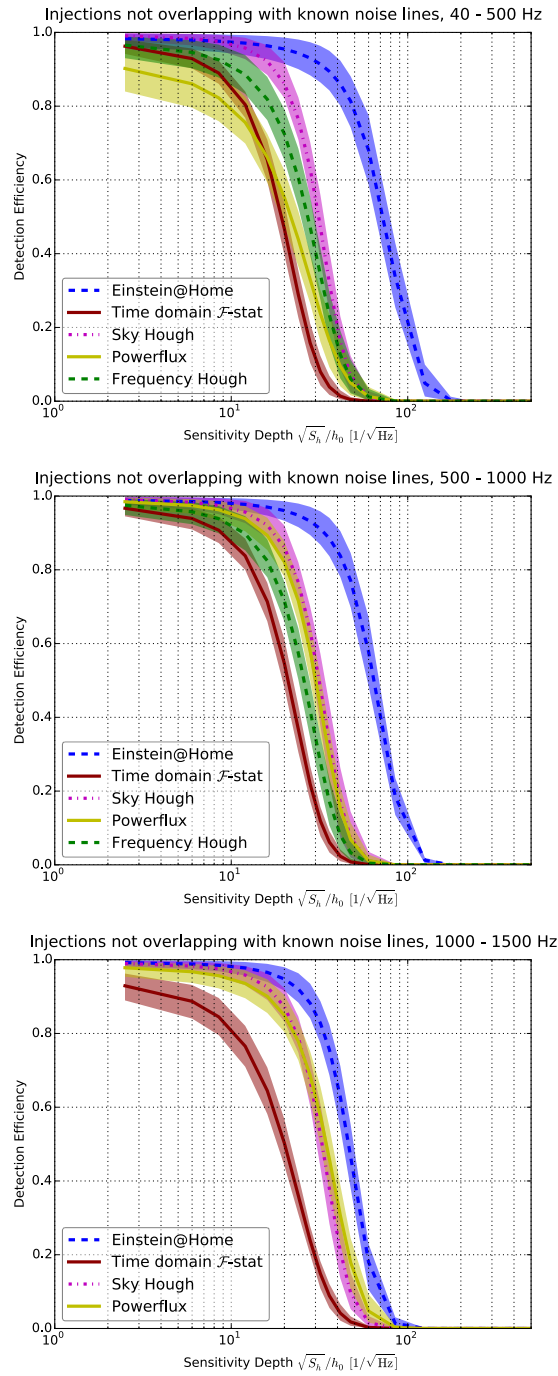


FIGURE 3.3: Detection efficiency measured for injections in the the frequency ranges of 40 to 500 Hz, 500 to 1000 Hz and 1000 to 1500 Hz (859, 944, and 1123 injections respectively). The Frequency Hough results are complete for injections below 1000 Hz. The curves and error bands are obtained by fitting sigmoids to the data, see Section 3.7.1. The error bands represent the statistical uncertainty on the detection efficiency measured for the search implementation and data used in the MDC.

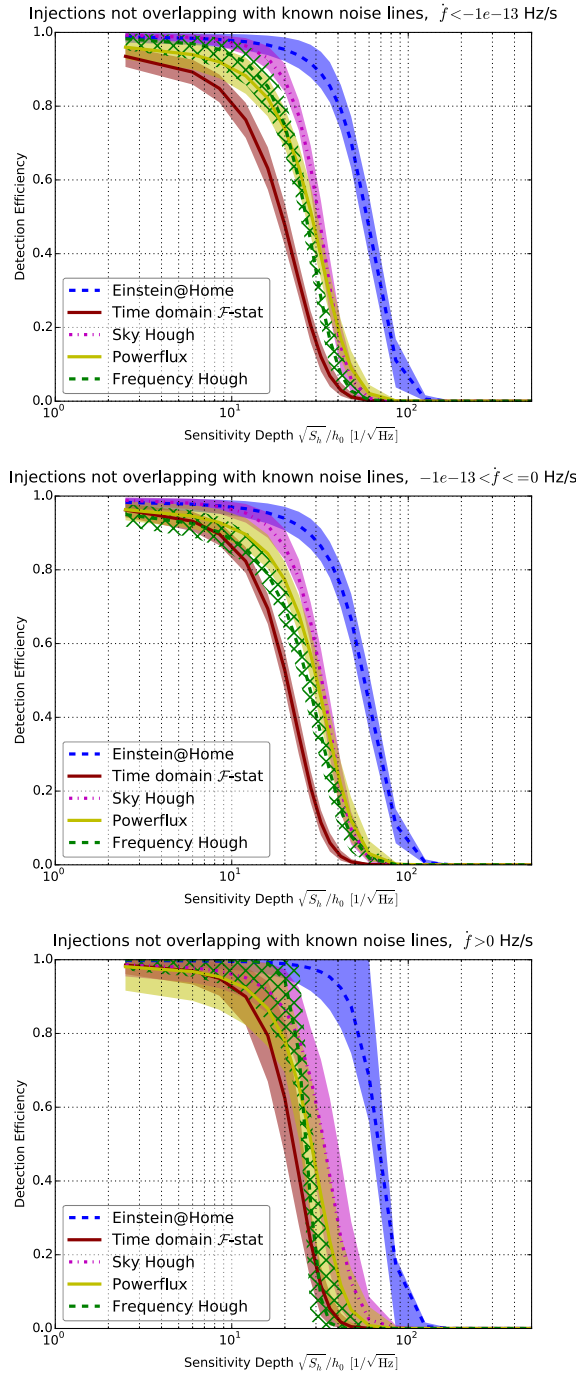


FIGURE 3.4: Detection efficiency measured for injections with small spindown ( $< -1 \times 10^{-13}$  Hz/s, 1260 injections), large spindown ( $-1 \times 10^{-13}$  to 0 Hz/s, 1517 injections) and with spinup ( $> 0$  Hz/s, 149 injections). Frequency Hough results are shown with a hatched error band because the efficiency is measured for a subset of the MDC injections (793, 919, and 457 injections respectively). The curves and error bands are obtained by fitting sigmoids to the data, see Section 3.7.1. The error bands represent the statistical uncertainty on the detection efficiency measured for the search implementation and data used in the MDC.

### 3.7.1.3 Dependence on signal second order spindown

A loss in detection efficiency is expected when the signal  $\ddot{f}$  is greater than the  $\ddot{f}_{\text{critical}}$  for a search, where  $\ddot{f}_{\text{critical}}$  is given by

$$\ddot{f}_{\text{critical}} = \frac{\delta f}{T_{\text{obs}}^2}. \quad (3.7)$$

$\ddot{f}_{\text{critical}}$  is the value of  $\ddot{f}$  at which the signal frequency will vary by more than a frequency bin,  $\delta f$ , over the observation time of the data,  $T_{\text{obs}}$ . In practice, the efficiency loss for  $\ddot{f} \geq \ddot{f}_{\text{critical}}$  is expected to be mitigated to some degree by apparent displacement of the signal parameters in the space of  $(f_0, \dot{f}, \alpha, \delta)$ .

Figure 3.5 shows the non-zero second order spindown values of the MDC signals, for the range specified in Section 3.4.1. The vertical lines show the  $\ddot{f}_{\text{critical}}$  for each of the searches. Some signals have  $\ddot{f} \geq \ddot{f}_{\text{critical}}$  for the Einstein@Home, Time domain  $\mathcal{F}$ -statistic and Powerflux searches. However, in each case, there are too few signals with  $\ddot{f} \geq \ddot{f}_{\text{critical}}$  to determine if they have an appreciable effect on the detection efficiency.

The stability of the detection efficiency for signals with  $\ddot{f} > 0$  is important as none of the pipelines search explicitly over second order spindown, and to do so would add a significant computational burden to the searches. Figure 3.6 shows that the detection efficiency is the same for signals with  $\ddot{f} = 0$  and  $\ddot{f} > 0$ , with at least 99% of injections having  $\ddot{f} < \ddot{f}_{\text{critical}}$ . Due to the lack of injections with  $\ddot{f} \geq \ddot{f}_{\text{critical}}$ , the impact on detection from these injections not examined.

For the Sky Hough and Frequency Hough searches the impact of  $\ddot{f} \geq \ddot{f}_{\text{critical}}$  is less of a concern for future searches, due to the short coherent segment length used by these searches. The  $\ddot{f}_{\text{critical}}$  of the Time domain  $\mathcal{F}$ -statistic search will be larger than the value in the MDC for the first advanced LIGO searches, which will have a lower  $T_{\text{obs}}$  than the 15 months of the MDC data.

The Powerflux  $\ddot{f}_{\text{critical}}$  is calculated for refinement stage 1 in Table 3.2. The  $\delta f$  decreases in the next refinement stages, so  $\ddot{f}_{\text{critical}}$  will decrease. The Einstein@Home search refinement stages also have reduced  $\delta f$  and  $\ddot{f}_{\text{critical}}$ . Therefore, the impact on detection efficiency of  $\ddot{f} \geq \ddot{f}_{\text{critical}}$  may warrant further study for these two searches.

## 3.7.2 Signal parameter recovery

The distance between the signal and recovered candidates is of interest as it determines the region in parameter space around each candidate that must be searched by the next refinement stage. Also, it serves as a useful cross check that candidates being claimed as detections in the MDC are within a reasonable distance of the signal parameters.

Powerflux, Einstein@Home and Frequency Hough can have more than one candidate per injection. For strong signals, there are in fact many detection candidates around the signal's true parameter values. We study the distribution for the distances of candidates from the true signal parameter values for two sets of candidates: the one with the highest SNR and the one that is closest, in frequency, to the signal.

The distance, in frequency, spindown and sky position, is shown for the first set of candidates in Figures 3.7 and 3.8. Here the distance in sky is represented by dR, the angular separation between two sky positions in radians. The dR scales approximately proportional to the frequency of the signal. There are candidates from Powerflux and Time domain  $\mathcal{F}$ -statistic which are not shown because they lie outside the limits of

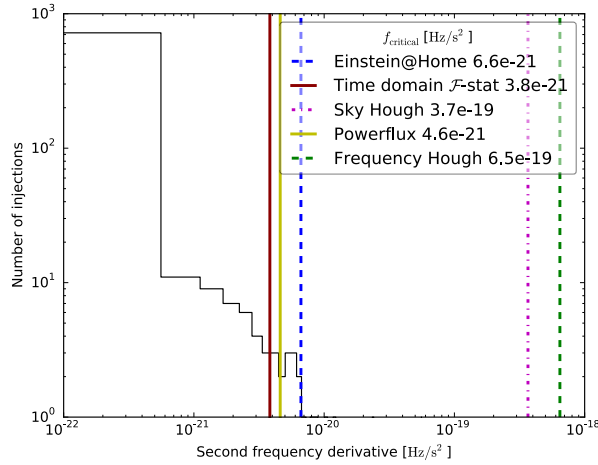


FIGURE 3.5: Distribution of  $\ddot{f}$  values for 781 injections with  $\ddot{f} > 0$ . The vertical lines show  $\ddot{f}_{\text{critical}}$  for each of the pipelines. The  $\ddot{f}_{\text{critical}}$  is calculated after the first refinement stage for Powerflux and for the 40 to 500 Hz search setup for Einstein@Home.

the x-axis. For Powerflux, these amount to 4%, 5% and 0.6% of candidates outside the boundaries in frequency, spindown and dR, with  $< 0.1\%$  of candidates outside all three boundaries. For Time domain  $\mathcal{F}$ -statistic, 27% are  $> 4 \times 10^{-3}$  Hz from the signal while 3% are  $> 4 \times 10^{-10}$  Hz/s, no candidates are outside both boundaries. The Powerflux method recovers candidates up to 0.02 Hz,  $1.5 \times 10^{-9}$  Hz/s or dR = 1.5 from the injected parameters. The Time domain  $\mathcal{F}$ -statistic recovers candidates up to 0.06 Hz,  $1.5 \times 10^{-9}$  Hz/s or dR = 0.4 from the injection. This means the region these searches need to search to recover the signal from these candidates is larger by a factor of  $O(10)$  in each dimension than the other searches. Time domain  $\mathcal{F}$ -statistic can afford to do this because they expect  $\sim 10$  false alarms. Powerflux expects on the order of 10000 false alarms in an all-sky search. While Powerflux may refine more than one candidate from a signal, only one of the candidates needs to pass through the refinement stages in order to recover the signal. Therefore, the minimum search region needed to recover the signal is better represented by examining the closest signal in frequency.

The Einstein@Home and Frequency Hough refinement searches, on candidates from the initial search, cover a predefined region in parameter space around each candidate. In a real search, candidates from a signal within this region will result in a detection after refinement. Therefore, the MDC detection candidates are required to contain the signal within this region (Section 3.6). Figures 3.7 and 3.8 support these choices of refinement parameter space, as the majority of candidates are within a smaller region around the signal and there are few outliers at the bounds of the parameter space.

The Sky Hough search expects  $< 15000$  false alarms in an all-sky search over 1500 Hz, because at most one candidate per 0.1 Hz is selected. The recovered parameters are close to the signal parameters. This allows for quick turnover of results.

Figures 3.9 and 3.10 compare the distance between the signal and recovered candidate, now choosing the nearest candidate in frequency for Powerflux, Frequency Hough and Einstein@Home. The spread of the Powerflux results has decreased significantly, with the furthest outliers at  $7 \times 10^{-3}$  Hz,  $1.5 \times 10^{-9}$  Hz/s or dR 0.5 from

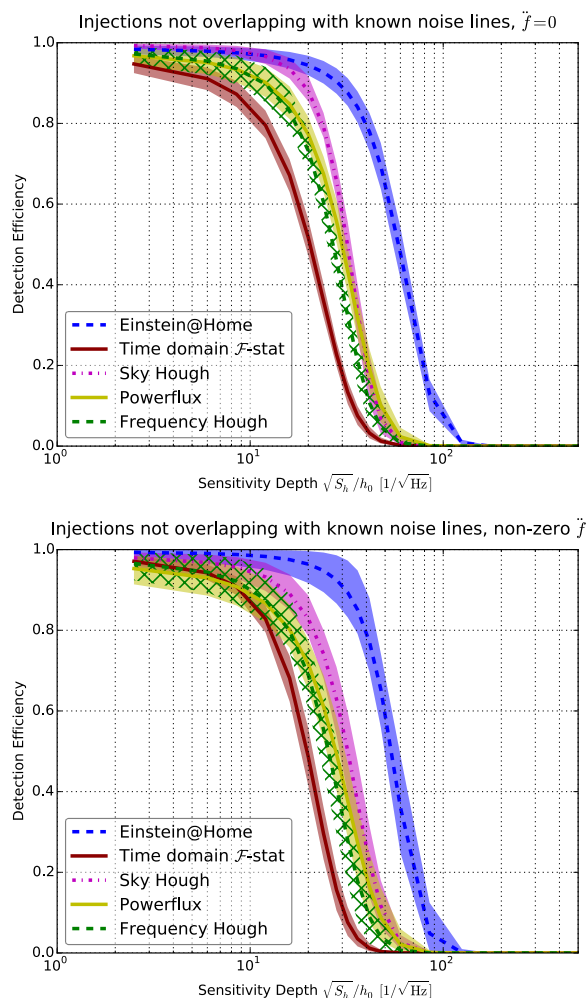


FIGURE 3.6: Detection efficiency measured for injections with zero (2329 injections) and non-zero (781 injections) second order spindown. Frequency Hough results are shown with a hatched error band because the efficiency is measured for a subset of the MDC injections. The curves and error bands are obtained by fitting sigmoids to the data, see Section 3.7.1. The error bands represent the statistical uncertainty on the detection efficiency measured for the search implementation and data used in the MDC.

the signal, and less than 1% of candidates outside the boundaries in any dimension. Powerflux has demonstrated, in the search of S6 data Abbott, 2016a, that they are able to perform refinement searches on all candidates above threshold.

The Frequency Hough results are unchanged, as only a handful of signals result in more than one detection candidate. The inner quartile of the Einstein@Home distribution has changed. However, the presence of candidates at the edge of the refinement region shows that the parameter space can not be reduced without losing detection efficiency.

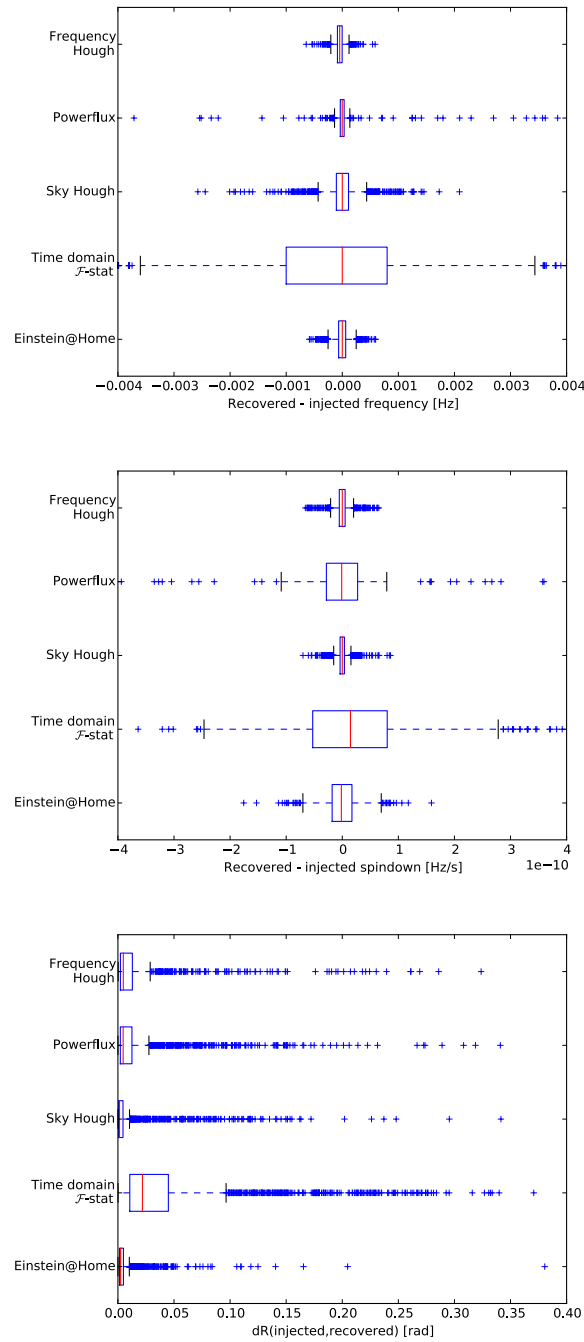


FIGURE 3.7: The distance between the signal and the recovered candidate, in frequency, spindown and sky position, when the candidate with the highest SNR is chosen. The red line is the median. The blue box begins and ends at the first and third quartile respectively. The vertical black bars (whiskers) extend 1.5 times the inner quartile range outside the blue box. The blue crosses are candidates outside this range.

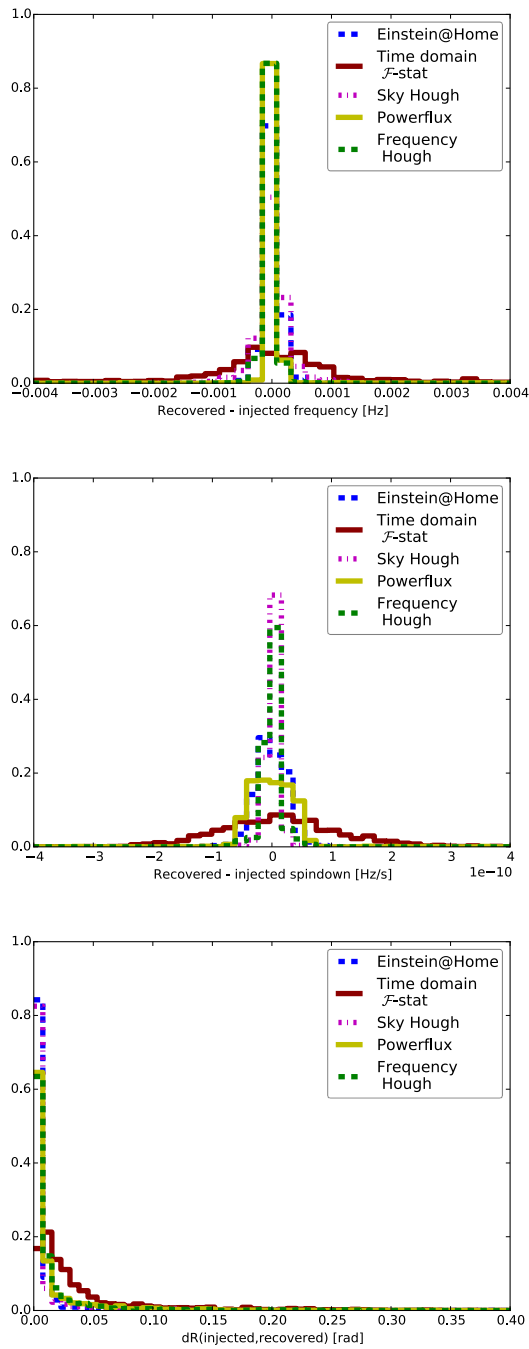


FIGURE 3.8: The distance between the signal and the recovered candidate, in frequency, spindown and sky position, when the candidate with the highest SNR is chosen. This is an alternative representation of the same data as in Figure 3.7.

### 3.8 Conclusion

We have considered five search pipelines currently performing blind all-sky searches for continuous waves from isolated NSs in advanced detector data. An overview of each pipeline has been presented with regards to the semi-coherent method, noise handling, computing cost and the hierarchical refinement procedure.



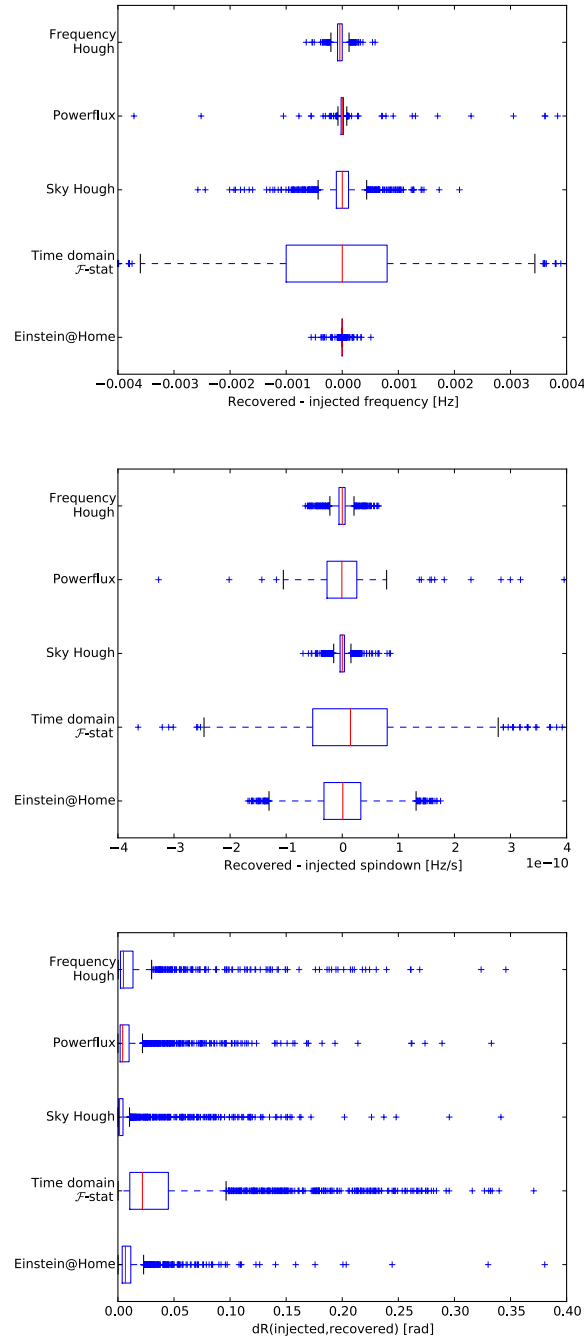


FIGURE 3.9: The distance between the signal and the recovered candidate, in frequency, spindown and sky position, when the candidate with the closest frequency to the signal is chosen. The red line is the median. The blue box begins and ends at the first and third quartile respectively. The vertical black bars (whiskers) extend 1.5 times the inner quartile range outside the blue box. The blue crosses are candidates outside this range.

To compare the methods, an MDC was performed with  $\sim 3000$  simulated signals. Each pipeline has presented the recovered signal candidates, from which the detection efficiency has been calculated. These results were used to compare the pipelines in

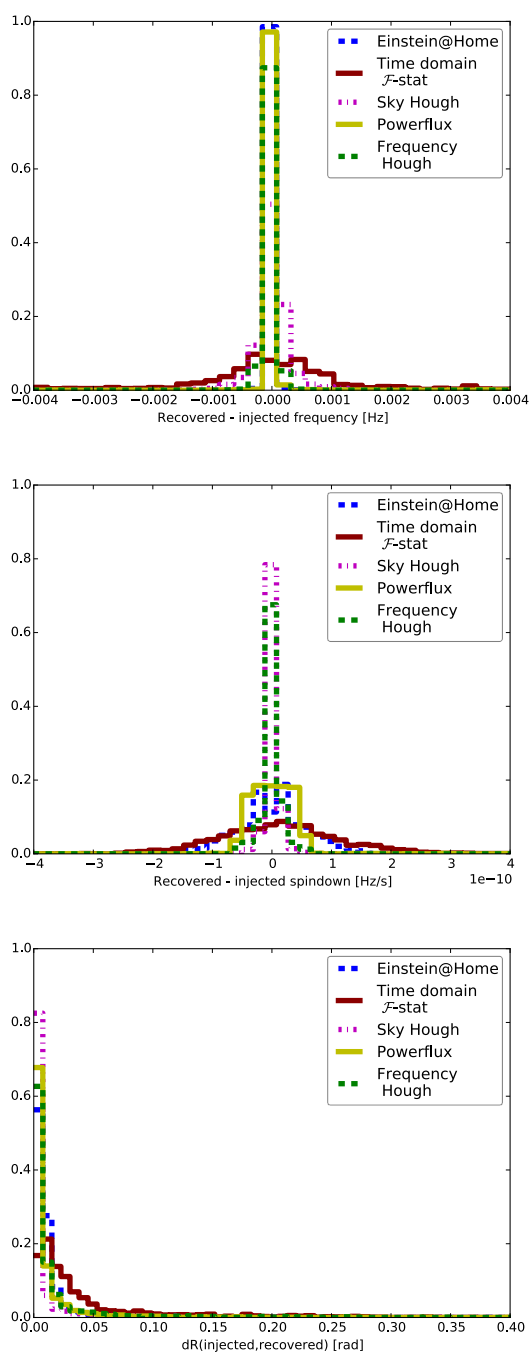


FIGURE 3.10: The distance between the signal and the recovered candidate, in frequency, spindown and sky position, when the candidate with the closest frequency to the signal chosen. This is an alternative representation of the same data as in Figure 3.9.

quiet and noisy data, and to check for dependence on signal frequency and frequency derivatives.

The search methods used by each pipeline make different tradeoffs in sensitivity vs. robustness against deviations from the assumed signal model. In this MDC, the detection efficiency is measured for a strictly continuous and phase coherent wave signal. This serves as a first benchmark in the comparison of these five all-sky pipelines.

For a comprehensive comparison, the MDC must be extended to include signals that deviate from this signal model.

The precision with which the pipelines can be compared is restricted by the dependence of detection efficiency on the observing time of the data and the search configuration, which changes depending on the data available and the parameter space covered. Pipelines are also developing improvements, which will change the detection efficiency of future searches.

With these caveats in mind, we compare the detection efficiency of the pipelines for a standard CW signal. We find similar performance among the Sky Hough, Powerflux and Frequency Hough searches. The detection efficiency for these signals is lower for the Time domain  $\mathcal{F}$ -statistic search. The Einstein@Home search achieved comparable detection efficiency to the other pipelines for signals that are a factor of two weaker, for frequencies below 1000 Hz. The different noise handling approaches left the Sky Hough and Time domain  $\mathcal{F}$ -statistic efficiencies unchanged in the presence of known noise lines, while the Einstein@Home and Powerflux searches lost efficiency. The apparent dependence of detection efficiency on signal frequency for Einstein@Home and Powerflux is understood. There is no measured dependence on spindown for any search method.

Despite not explicitly searching over second order spindown, the detection efficiency is unaffected by signals with non-zero second order spindown. This has been verified for  $\ddot{f} < \ddot{f}_{\text{critical}}$ . Assuming a standard NS model,  $\ddot{f}$  is not expected to exceed  $\ddot{f}_{\text{critical}}$  for the Sky Hough or Frequency Hough searches. The  $\ddot{f}$  may exceed  $\ddot{f}_{\text{critical}}$  for the other searches. The impact of this has not been examined.

This study is a first step towards a quantitative comparison of the different pipelines. Future studies are needed that include signals deviating from the standard CW model to understand and highlight the benefits of each pipeline.

### 3.A Comparing results with known and blind injections

Figure 3.11 shows that each search measures the same detection efficiency with injections where the injection parameters are known, and blind injections where the parameters are unknown. Therefore, we are able to combine the results from both injection sets. This reduces the statistical uncertainty on the measured detection efficiency.

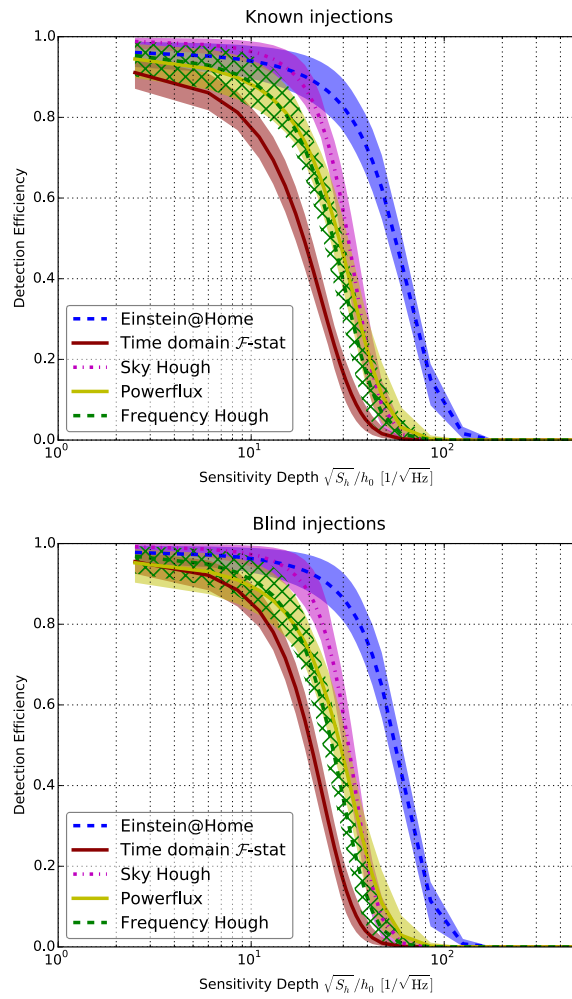


FIGURE 3.11: Detection efficiency measured with known injections (top) and blind injections (bottom).

## Chapter 4

# All-sky Search for periodic gravitational waves in the O1 LIGO data.

### 4.1 Introduction

This chapter summarises the *SkyHough* search for continuous gravitational waves (CW) using the data from the first observing run (O1) of the Advanced Laser Interferometer Gravitational wave Observatory (LIGO) detectors that were lead by us.

Thus far, multiple searches for periodic gravitational waves from neutron stars have been conducted employing the data from previous LIGO and Virgo observing runs (Riles, 2017). These searches included targeted searches to look for continuous gravitational radiation from known radio and X-ray pulsars with known ephemerides like (Abbott, 2017i); directed searches for signals from interesting sky positions like Sco X-1 (Abbott, 2017j) or supernova remnants (Abbott, 2018d), of which no information of the frequency evolution is known, all-sky searches to look for unknown neutron stars in our galaxy (Abbott, 2017g; Abbott, 2017f; Abbott, 2018e), narrow-band search for continuous gravitational waves from known pulsars like (Abbott, 2017h). While none of these searches was sensitive enough to detect any signals, each search pipeline produced separate upper limits, that for the O1 all-sky searches can be found in (Abbott, 2017f; Abbott, 2018e).

The search for unknown isolated neutron stars presented here covered the frequency band between 50 Hz to 2000 Hz and the frequency derivatives range of  $[-1.0, +0.1] \times 10^{-8} \text{ Hz s}^{-1}$ . The all-sky results obtained employing LIGO O1 data were spit in two publications (Abbott, 2017f; Abbott, 2018e), that included the results of other three competing pipelines *PowerFlux*, *Time-Domain  $\mathcal{F}$ -statistic*, and *FrequencyHough*. The later one contributing only to (Abbott, 2017f) that covered the frequency band between 20 Hz to 475 Hz. It is important to notice that no previous search for continuous waves covered the band 1750-2000 Hz.

These different analysis programs employ a variety of algorithmic and parameter choices in order to reduce the possibility of discarding a gravitational wave signal due to suboptimal treatment of detector artifacts or by adhering to an overly restrictive signal model. The treatment of narrow spectral artifacts (“lines”) differs substantially among the different search programs. The latter is an especially important consideration for the O1 data set because lines are, unfortunately, especially prevalent. This chapter will focus just on the results delivered by the *SkyHough* pipeline.

## 4.2 Advanced LIGO interferometers and the O1 observing run

Advanced LIGO consists of two detectors, one in Hanford, Washington, and the other in Livingston, Louisiana, separated by a  $\sim 3000$ -km baseline (Aasi, 2015b). Each site hosts one 4-km-long interferometer inside a vacuum envelope with the primary interferometer optics suspended by a cascaded, quadruple suspension system in order to isolate them from external disturbances. The interferometer mirrors act as test masses, and the passage of a gravitational wave induces a differential-arm length change which is proportional to the gravitational wave strain amplitude. The Advanced LIGO detectors began data collecting in September 2015 after a major upgrade targeting a 10-fold improvement in sensitivity over the initial LIGO detectors. While not yet operating at design sensitivity, both detectors reached an instrument noise 3 to 4 times lower than the previous best with the initial-generation detectors in their most sensitive frequency band between 100 Hz and 300 Hz (Aasi, 2015a; Abbott, 2016b).

Advanced LIGO's first observing run occurred between September 12, 2015 and January 19, 2016, for which approximately 77 days and 66 days of analyzable data was produced by the Hanford (H1) and Livingston (L1) interferometers, respectively. Notable instrumental contaminations affecting the searches described here included spectral combs of narrow lines in both interferometers, many of which were identified after the run ended and mitigated for future running. These artifacts included an 8-Hz comb in H1 with the even harmonics (16-Hz comb) being especially strong, which was later tracked down to digitization roundoff error in a high-frequency excitation applied to servo-control the cavity length of the Output Mode Cleaner (OMC). Similarly, a set of lines found to be linear combinations of 22.7 Hz and 25.6 Hz in the L1 data was tracked down to OMC excitation at a still higher frequency, for which digitization error occurred.

In addition, the low-frequency band of the H1 and L1 data (below  $\sim 140$  Hz) was heavily contaminated by combs with spacings of 1 Hz, near-1 Hz and 0.5 Hz and a variety of nonzero offsets from harmonicity. Many of these lines originated from the observatory timing system, which includes both GPS-locked clocks and free-running local oscillators. The couplings into the interferometer appeared to come primarily through common current draws among power supplies in electronics racks. These couplings were reduced following O1 via isolation of power supplies, and in some cases, reduction of periodic current draws in the timing system itself (blinking LEDs). A subset of these lines with common origins at the two observatories contaminated the O1 search for a stochastic background of gravitational waves, which relies upon cross correlation of H1 and L1 data, requiring excision of affected bands (Abbott, 2017k).

Although most of these strong and narrow lines are stationary in frequency and hence do not exhibit the Doppler modulations due to the Earth's motion expected for a continuous wave signal from most sky locations, the lines pollute the spectrum for such sources. In sky locations near the ecliptic poles, the lines contribute extreme contamination for certain signal frequencies. For a run like O1 that spans only a modest fraction of a full year, there are also other regions of the sky and spin-down parameter space for which the Earth's average acceleration toward the Sun largely cancels a nonzero source frequency derivative, leading to signal templates with substantial contamination from stationary instrumental lines (Abadie, 2012). The search program used here have chosen a variety of methods to cope with this contamination, as described below.

### 4.3 Data selection and preparation

The *SkyHough* search method described in detail in Chapter 2 employs calibrated detector  $h(t)$  data from the O1 run. The calibrated strain data are produced from the differential arm length readout of the Advanced LIGO detectors. The estimate is formed from models of the detectors' actuation and sensing systems and verified with calibrated, frequency-dependent excitations via radiation pressure actuators at reference times. This radiation pressure actuator relies on a NIST-traceable laser power standard and knowledge of the test mass suspension dynamics, which are both known at the 1% level. The reference and subsequent confirmation measurements inform the static, frequency-dependent systematic error and statistical uncertainty in the estimate of  $h(t)$ . Time-dependent correction factors to certain model parameters are monitored with single-frequency excitations during the entire observation period.

The LIGO H1 and L1 data used in this search correspond to the C01 re-calibrated frames at 16 kHz samples per second of 4096s duration each, corresponding to the channels names  $[H1|L1] : DCS - CALIB\_STRAIN\_C01$ , for which starting and end times are listed in Table 4.1. Data quality flags and related detector data information were set up by the LIGO calibration group and the Data and Computing Systems. LIGO data quality categories, or flags, are defined by each analysis group: Compact Binary Coalescence (CBC), Burst, Continuous Waves (CW) and Stochastic. This is because periods of noisy data affect each type of analysis differently.

The reference measurements and time-dependent correction factors were used to estimate the total uncertainty in  $h(t)$ , which is less than 10% in magnitude and  $10^\circ$  in phase from 20 Hz (Abbott, 2017a).

The calibrated frame data was used to create 1800-s Tukey-windowed Short Fourier Transforms (SFTs), covering the 10-2000 Hz range, with the function *lalapps\_MakeSFTs* and the script *MakeSFTDAG* from (*LIGO Algorithm Library - LALSuite*). The script makes a Directed non-cyclic diagram (DAG) file that conveys the generation of the full arrangement of SFTs in various calls to accelerate and resolve conceivable read and write issue in the server. The most relevant parameters for the generation of the SFTs of O1 run are in Table 4.2.

Each SFT was created from a segment of detector data that is at least 1800 s long. From this step, 3684 and 3007 SFTs were created for H1 and L1, respectively. These SFT were replicated via LDR to the different computer clusters of the LSC.

During the O1 run several simulated pulsar signals were injected into the data by applying a small force to the interferometer mirrors with auxiliary lasers or via inductive forces from nearby electrodes (Biwer, 2017). The parameters of the hardware-injected simulated continuous-wave signals during the O1 data run are listed in Table 4.3. Because the interferometer configurations were largely frozen in a preliminary state after the first discovery of gravitational waves from a binary black hole merger, the hardware injections were not applied consistently. There were no injections in the H1 interferometer initially, and the initial injections in the L1 interferometer used an actuation significant inaccuracies at high frequencies. The hardware injection ip3

Detector	Start GPS	End GPS	Start UTC	End UTC
H1	1125969920	1137258496	Sep 11 2015 01:25:03	Jan 19 2016 17:07:59
L1	1126031360	1137258496	Sep 11 2015 18:29:03	Jan 19 2016 17:07:59

TABLE 4.1: The table contains the O1 run starting and end times in UTC and GPS units for LIGO Hanford H1 and Livingston L1.

Parameter	Description	Value
-k	knee frequency for high-pass filter	7 Hz
-F	start-frequency	10 Hz
-B	band width	1990 Hz
-T	coherence length $T_{coh}$	1800s

TABLE 4.2: The most relevant parameters used to generate the SFTs from the O1 run with *lalapps\_MakeSFTs* script.

Label	Frequency Hz	Spindown nHz/s	RA <sub>J2000</sub> degrees	DEC <sub>J2000</sub> degrees
ip0	265.575533	$-4.15 \times 10^{-3}$	71.55193	-56.21749
ip1	848.969641	$-3.00 \times 10^{-1}$	37.39385	-29.45246
ip2	575.163521	$-1.37 \times 10^{-4}$	215.25617	3.44399
ip3	108.857159	$-1.46 \times 10^{-8}$	178.37257	-33.4366
ip4	1393.540559	$-2.54 \times 10^{-1}$	279.98768	-12.4666
ip5	52.808324	$-4.03 \times 10^{-9}$	302.62664	-83.83914
ip6	146.169370	$-6.73 \times 10^0$	358.75095	-65.42262
ip7	1220.555270	$-1.12 \times 10^0$	223.42562	-20.45063
ip8	191.031272	$-8.65 \times 10^0$	351.38958	-33.41852
ip9	763.847316	$-1.45 \times 10^{-8}$	198.88558	75.68959
ip10	26.341917	$-8.50 \times 10^{-2}$	221.55565	42.87730
ip11	31.424758	$-5.07 \times 10^{-4}$	285.09733	-58.27209
ip12	38.477939	$-6.25 \times 10^0$	331.85267	-16.97288
ip13	12.428001	$-1.00 \times 10^{-2}$	14.32394	-14.32394
ip14	1991.092401	$-1.00 \times 10^{-3}$	300.80284	-14.32394

TABLE 4.3: Parameters of the hardware-injected simulated continuous-wave signals during the O1 data run (epoch GPS 1130529362).



was exceptionally strong with a clear signature even in its non-Gaussian band. Note, however that these injections were not enabled for the H1 interferometer in the first part of the O1 run, leading to degraded efficiency for their detections.

The recovery of the hardware injections gave us additional confidence that no potential signals were missed.

## 4.4 The search set-up

The data from the two LIGO interferometers were initially analyzed in separate all-sky searches for continuous gravitational wave signals, and then coincidence requirements on candidates are imposed.

SFT data from a single interferometer were analyzed by creating a peak-gram (a collection of zeros and ones) by setting a threshold of 1.6 on their normalized power, where the averaged spectrum was determined via a running-median estimation (Abbott, 2009a).

An implementation of the weighted Hough transform (Aasi, 2014a; Sintes and Krishnan, 2006) was used to map points from the time-frequency plane of the peak-grams into the space of the source parameters. Similar to the other existing semi-coherent methods, the algorithm searches for signals whose frequency evolution fits the pattern produced by the Doppler shift and spin-down in the time-frequency plane of the data. In this case, the Hough number count is the weighted sum of the ones and zeroes,  $n_k^{(i)}$ , of the different peak-grams along the track corresponding to each point in parameter space. This sum is computed as

$$n = \sum_{i=0}^{N-1} w_k^{(i)} n_k^{(i)}, \quad (4.1)$$

where the choice of weights is given by

$$w_k^{(i)} \propto \frac{1}{S_k^{(i)}} \left\{ \left( F_{+1/2}^{(i)} \right)^2 + \left( F_{\times 1/2}^{(i)} \right)^2 \right\}, \quad (4.2)$$

where  $F_{+1/2}^{(i)}$  and  $F_{\times 1/2}^{(i)}$  are the values of the antenna pattern functions at the mid-point of the  $i^{\text{th}}$  SFT for the sky location of interest and  $S_k^{(i)}$  is the SFT noise level. A particularly useful detection statistic is the *significance* (or critical ratio,  $\Psi$ ), and is given by

$$\Psi = \frac{n - \langle n \rangle}{\sigma}, \quad (4.3)$$

where  $\langle n \rangle$  and  $\sigma$  are the expected mean and standard deviation of the Hough number count for pure noise.

The *SkyHough* search analyses 0.1 Hz bands over the frequency interval 50–2000 Hz, frequency time derivatives in the range  $[-1.0, +0.1] \times 10^{-8} \text{ Hz s}^{-1}$ , and covering the entire sky. A uniform grid spacing, equal to the size of a SFT frequency bin,  $\delta f = 1/T_{\text{SFT}} = 5.556 \times 10^{-4} \text{ Hz}$ , is chosen to cover the frequency range of the search.

The resolution  $\delta \dot{f}$  is given by the smallest value of  $\dot{f}$  for which the intrinsic signal frequency does not drift by more than one frequency bin during the total observation time  $T_{\text{obs}}$ :  $\delta \dot{f} = \delta f / T_{\text{obs}} \sim 4.95 \times 10^{-11} \text{ Hz s}^{-1}$ , as explained in Chapter 2. This yields 224 spin-down values. The sky resolution,  $\delta \theta$  is frequency dependent and two different pixel-factors were selected:  $P_f = 2$  from 50–1200 Hz and  $P_f = 0.5$  from 1200–2000 Hz; thus performing a lower sky grid resolution search at higher frequencies,

decreasing the sensitivity over that range but reducing the computational cost of the search by a factor of 16.

The parameter space was divided into bands of 0.1 Hz and each. For each frequency band, the parameter space is split further into 209 subregions of the sky. For every sky region and frequency band the analysis delivers a toplist with the 300 most significant candidates according to their critical ratio (CR). From those initial 209 toplists per band, a final toplist with the 1000 most significant candidates, again according to the largest CR, is constructed. This procedure reduces the influence of instrumental spectral disturbances that affect specific sky regions.

## 4.5 The post-processing step

The post-processing of the results for each 0.1-Hz band consists of the following steps:

(i) Apply a  $\chi^2$  test, as described and characterised in the next subsection, to eliminate candidates caused by detector artifacts. This veto was applied only to the lowest frequency range.

(ii) Search for coincident candidates among the two data sets, H1 and L1, using a coincidence window of  $d_{\text{SH}} < \sqrt{14}$ . This dimensionless quantity is defined as:

$$d_{\text{SH}} = \sqrt{(\Delta f / \delta f)^2 + (\Delta \dot{f} / \delta \dot{f})^2 + (\Delta \theta / \delta \theta)^2} \quad (4.4)$$

to take into account the distances in frequency, spin-down and sky location with respect to the grid resolution in parameter space. Here,  $\Delta \theta$  is the sky angle separation. Each coincidence pair is then characterized by its harmonic mean significance value and a center in parameter space: the mean weighted value of frequency, spin-down and sky-location obtained by using their corresponding individual significance values. Subsequently, a list containing the 1000 most significant coincident pairs is produced for each 0.1-Hz band.

(iii) The surviving coincidence pairs are clustered, using the same coincidence window of  $d_{\text{SH}} = \sqrt{14}$  applied to the coincidence centers. Each coincident candidate can belong to only a single cluster, and an element belongs to a cluster if there exists at least another element within that distance. Only the highest ranked cluster, if any, will be selected for each 0.1-Hz band. Clusters are ranked based on their mean significance value, but where all clusters overlapping with a known instrumental line are ranked below any cluster with no overlap. A cluster is always selected for each of the 0.1-Hz bands that had coincidence candidates. In most cases the cluster with the largest mean significance value coincides also with the one containing the highest value.

Steps (ii) and (iii) take into account the possibility of coincidences and formation of clusters across boundaries of consecutive 0.1-Hz frequency bands.

The following tests are performed on those candidates remaining:

(iv) Two different population vetos are applied. For the 45–475 Hz frequency range, we require that interesting clusters must have a minimum population of 6 and that coincidence pairs should be generated from at least 2 different candidates per detector. For the higher frequencies, we simply require the clusters to have a minimum population of 2; otherwise, they are discarded. This is similar to the “occupancy veto” described in (Behnke, Papa, and Prix, 2015)

(v) For those candidates remaining, a multi-detector search is performed to verify the consistency of a possible signal. Any candidate that has a combined critical

ratio more than 1.6 below the expected value is discarded. This is the multi-detector consistency veto described in the subsection below.

Outliers that breeze through these tests are manually examined. In particular, outliers are also discarded if the frequency span of the cluster overlaps with contaminated bands (Covas, 2018), or if there are obvious spectral disturbances associated with one of the detectors. Surviving outliers were subjected to the additional systematic follow-up used for Einstein@Home searches (Papa, 2016; Abbott, 2017g), which includes a final stage with full coherence across the entire data run.

#### 4.5.1 The $\chi^2$ veto

The  $\chi^2$  veto was first implemented in the *SkyHough* analysis of initial LIGO era S5 data (Aasi, 2014a), and is used to reduce the number of candidates from single interferometer analysis before the coincidence step. The derivation of this veto is presented in Chapter 2 and a detailed study of the calibration of this  $\chi^2$  test using LIGO O1 data can be found in Covas, 2016. The empirical derivation of the  $\chi^2$  veto threshold involved the addition of a large number of simulated periodic gravitational wave signals into the SFTs, with randomly chosen amplitude, frequency, frequency derivative, sky location, polarization angle, inclination angle, and initial phase.

To determine the  $\chi^2$  veto threshold (characterized by a “veto curve”), 125 0.1-Hz bands were selected for H1 and 107 bands for L1, bands free of known large spectral disturbances. In total 2,340,000. injections were analyzed. The  $\chi^2$  values were defined with respect to a split of the SFT data into  $p = 16$  segments. The results were sorted with respect to the significance and grouped in sets containing 2000 points. For each set the mean value of the significance, the mean of the  $\chi^2$ , and its standard deviation were computed. With this reduced set of points, we fitted two power laws  $p - 1 + A_1\Psi^{A_2}$  and  $\sqrt{2p - 2} + B_1\Psi^{B_2}$  to the mean and standard deviation curve.

This study revealed a frequency-dependent behavior. In particular, the results obtained from injections below 100 Hz differ from those between 100 and 200 Hz, while the characterization of the  $\chi^2$ -significance (or critical ratio,  $\Psi$ ) plane was similar for frequencies higher than 200 Hz. For this reason, three different veto curves were derived for the 50-100 Hz band, 100-200 Hz band, and for frequencies higher than 200 Hz. On the other hand, the characterization was similar for both interferometers. Therefore, common veto curves were derived for H1 and L1 data.

$f$ [Hz]	$A_1$	$A_2$	$B_1$	$B_2$
50-100	0.4902	1.414	0.3581	1.481
100-200	0.2168	1.428	0.1902	1.499
>200	0.1187	1.470	0.0678	1.697

TABLE 4.4: Parameters obtained for the O1  $\chi^2$  veto curve characterization in different frequency bands

The coefficients obtained for the proposed characterization can be found in Table 4.4. Figures 4.1, 4.2, and 4.3 show the fitted curves and resulting veto curves corresponding to the mean  $\chi^2$  plus five times its standard deviation for the H1-L1 combined data. The associated false-dismissal rate for this veto is measured to be 0.12% for the 50-100 Hz band, 0.21% for the 100-200 Hz band, and 0.16% for frequencies higher than 200 Hz. For frequencies higher than 475 Hz this veto was not applied.

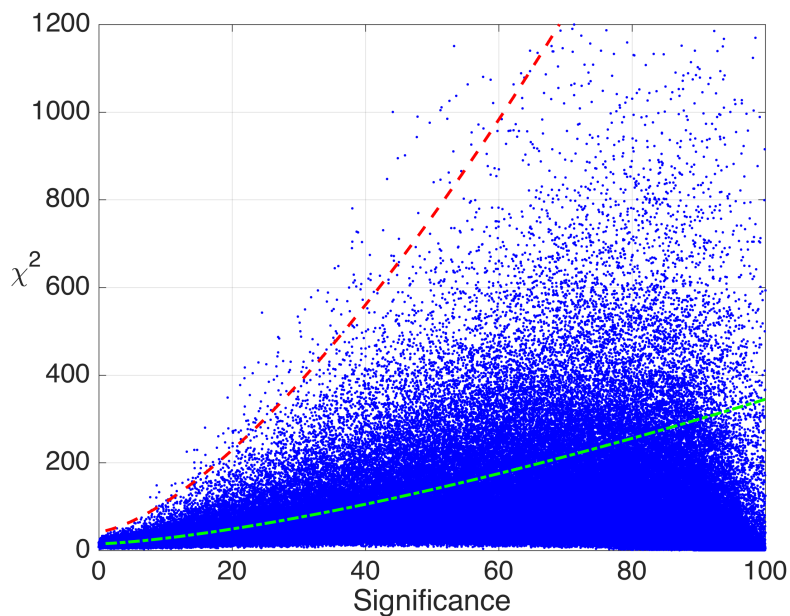


FIGURE 4.1: Significance- $\chi^2$  plane for 180000 simulated injected signals in the 50 to 100 Hz band together with the fitted mean curve (dot-dashed line) and the veto curve (dashed line) corresponding to the mean  $\chi^2$  plus five times its standard deviation for the H1-L1 combined data. The associated false dismissal rate (percentage of injections that are higher than the veto curve) is measured to be 0.12%

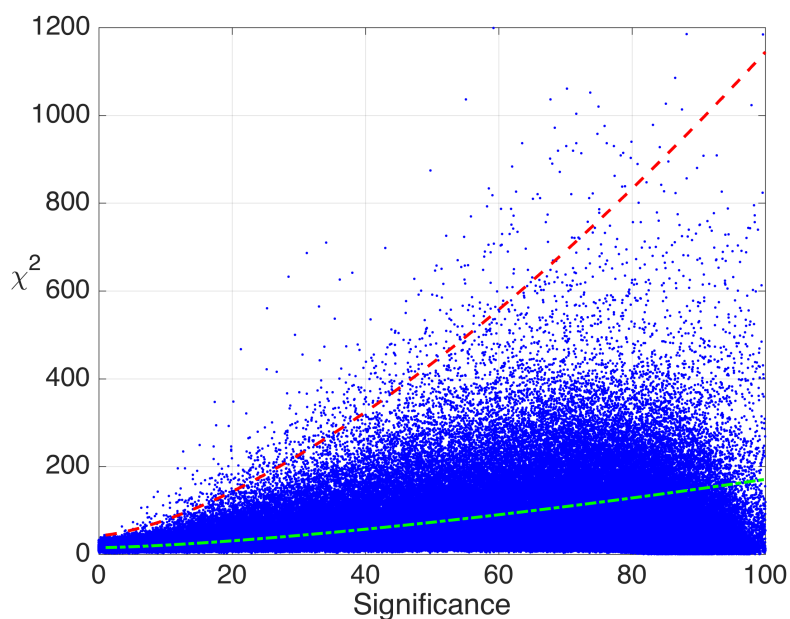


FIGURE 4.2: Same as Fig. 4.1 for 320000 injections in the 100 to 200 Hz band. The false dismissal rate being 0.21%

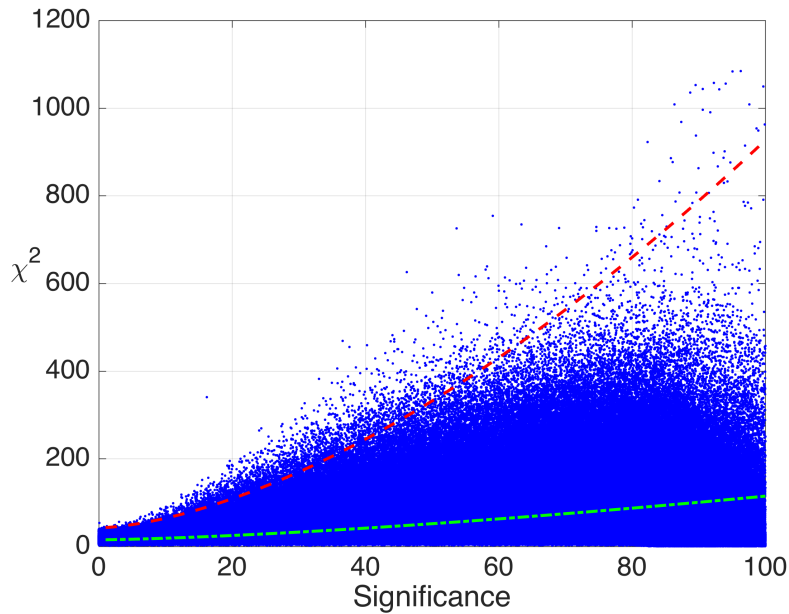


FIGURE 4.3: Same as Fig. 4.1 for 1840000 injections at frequencies higher than 200 Hz for the combined H1-L1 data. The false dismissal rate being 0.16%

#### 4.5.2 The multi-detector consistency veto

Similar to the preceding  $\chi^2$  test, a multi-detector consistency veto can be derived by comparing the critical ratio from a multi-detector search to those obtained by analyzing the data from the H1 and L1 detectors separately.

In particular, for each point in parameter space, we can derive the expected multi-detector critical ratio  $\Psi$  from the significance obtained in the separate analysis of H1 and L1 data by using the weights defined by equation 4.2 and the SFT sets in use. Since in this search the exact value of the weights is not stored, an approximation can be derived by ignoring the effect of the antenna pattern and considering only the influence of the varying noise levels of the different SFTs in a given frequency band.

The following expression can then be derived for the multi-detector search:

$$\Psi_{\text{theo}} = \frac{\Psi_{L1} \sqrt{\sum_{i=0}^{N_{L1}} (S_{L1}^{(i)})^{-2}} + \Psi_{H1} \sqrt{\sum_{i=0}^{N_{H1}} (S_{H1}^{(i)})^{-2}}}{\sqrt{\sum_{i=0}^{N_{L1}} (S_{L1}^{(i)})^{-2} + \sum_{i=0}^{N_{H1}} (S_{H1}^{(i)})^{-2}}} \quad (4.5)$$

where  $N_{H1}$  and  $N_{L1}$  are the number of SFTs of each detector,  $S_{H1}^{(i)}$  and  $S_{L1}^{(i)}$  are the one-sided PSDs of each detector averaged around a small frequency interval, and  $\Psi_{H1}$  and  $\Psi_{L1}$  are the critical ratios of the separate single-detector searches.

Ideally, a coincidence pair from a periodic gravitational wave signal would have  $\Psi_{H1}$ ,  $\Psi_{L1}$ , and  $\Psi_{\text{theo}}$  values consistent with Eq. 4.5 within uncertainties arising from use of nearby—but not identical—templates and from noise fluctuations. Furthermore, we are interested in characterizing its validity when considering the maximum significance values obtained, not just by the same templates, but in a small volume in parameter space.

As explained in detailed in (Abbott, 2017f; Abbott, 2018e), in order to test the validity of the consistency requirement, software injections were performed in the 50-475 Hz, 475-1200 Hz and 1200-2000 Hz bands. These were done separately because of the different cluster population criteria used in the lower and higher frequency band searches and because from 1200 Hz and beyond, the pixelfactor changed from 2 to 0.5. These injections were done randomly covering the same parameters of our search and using  $h_0$  values corresponding to a sensitivity depth between 15 and 30.

For each injection, a full search, but covering only one sky patch, was performed on H1 and L1 data separately, as well as for the combined SFT data for the multi interferometer case, returning a list of the most significant candidates for each of them. Of all the injections performed, we considered only those with amplitudes strong enough that within a frequency and spin-down window of 4 or 8 bins, for the lower and higher frequency band, respectively, around the injected signal parameters, the maximum critical ratio value would be at least 5 for both individual single interferometer searches, and consequently a theoretical combined significance higher than 7.

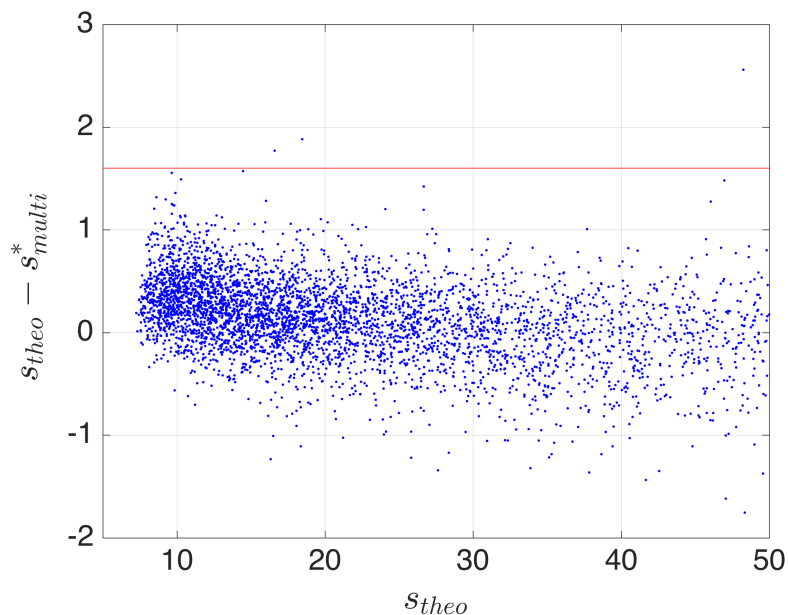


FIGURE 4.4: Characterization of the multi-detector critical ratio consistency veto using 4356 simulated injected signals in the 50-475 Hz range. Each point represents a separate injection. The horizontal axis corresponds to the theoretical expected significance (or critical ratio) value,  $s_{theo}$ , while the vertical axis is the difference between the theoretical and the measured value of significance,  $s_{multi}^*$ . The solid line is placed at a difference in critical ratio of 1.6 that has only been exceeded by 3 injections.

In the lowest frequency range, from 50-4750 Hz, a total of 4356 injections with an expected theoretical combined critical ratio between 7 and 50 were performed. The results are presented in Figure 4.4. This figure shows the characterization of the difference in significance (or critical ratio) obtained in the multi-detector search with respect to the theoretical expected value.

From this plot the multi-detector consistency veto for the O1 data was established: if the maximum multi-detector combined critical ratio had a value more than 1.6 below

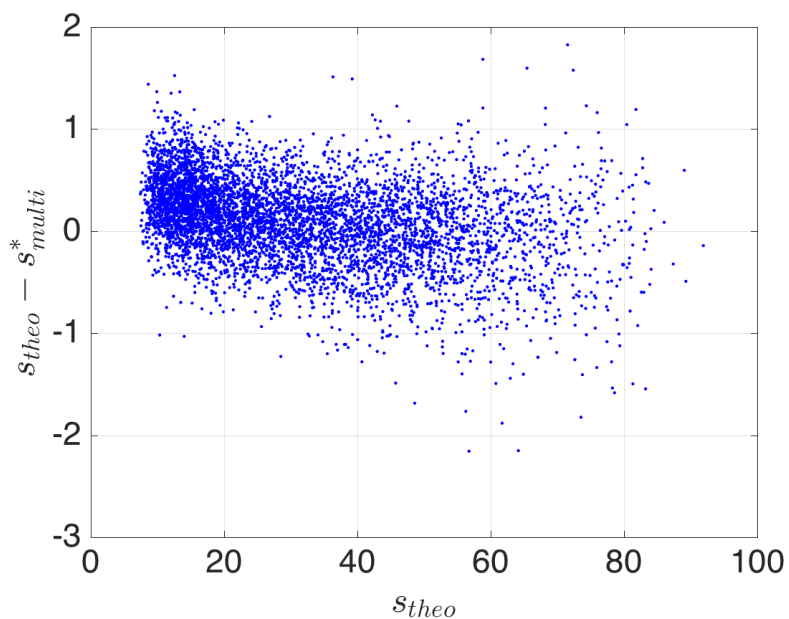


FIGURE 4.5: Characterization of the multi-detector consistency veto in the band 475-1200 Hz. Of a total of 5660 injections, only 2 of them were above the 1.6 threshold, and none of them with a maximum theoretical significance of 50.

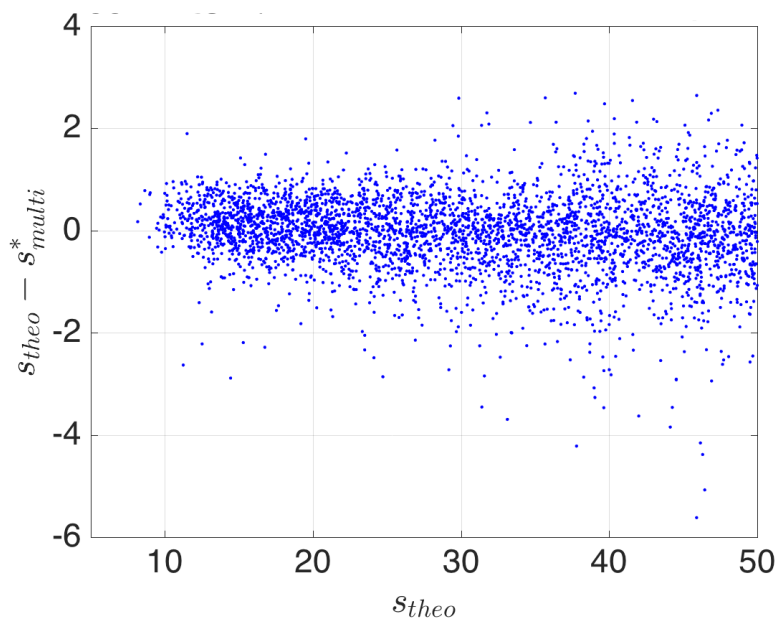


FIGURE 4.6: Characterization of the multi-detector consistency veto in the band 1200-2000 Hz. Considering only those with a maximum theoretical significance of 50, 48 injections were above 1.6 threshold and 3751 were below.

the nominal theoretically expected value, the candidate was vetoed. This value of 1.6 yield a false dismissal rate of 0.07% in this band.

Similar analysis were also performed for the higher frequency search. In the frequency band 475-1200 Hz, of a total of 5660 injections fulfilling our criteria only 2 of them were above the 1.6 threshold, but if we considered only those with a maximum theoretical significance of 50, 4681 in total, none of them was above the threshold. In the highest frequency range, 1200-2000 Hz, where a coarser grid in sky was used, considering only those with a maximum theoretical significance of 50, 48 injections were above 1.6 threshold and 3751 were below. Those results are displayed in Figures 4.5 and 4.6. The corresponding false dismissal rates being of 0.04% and 1.2%, respectively.

## 4.6 Upper limit computation

As in previous searches (Aasi, 2014a; Abbott, 2017f), we set a population-based frequentist upper limit at the 95% confidence level. Upper limits are derived for each 0.1 Hz band from the estimated average sensitivity depth, in a similar way to the procedure used in the Einstein@Home searches (Abbott, 2016c; Abbott, 2017g).

For a given signal strength  $h_0$ , the sensitivity depth is defined as:

$$\mathcal{D} := \frac{\sqrt{S_n}}{h_0} [1/\sqrt{\text{Hz}}]. \quad (4.6)$$

Here,  $S_n$  is the maximum over both detectors of the power spectral density of the data, at the frequency of the signal.  $S_n$  is estimated as the power-2 mean value,  $\left(\sum_{i=1}^N \left(S_k^{(i)}\right)^{-2} / N\right)^{-2}$ , across the different noise levels  $S_k^{(i)}$  of the different  $N$  SFTs.

Three different values of average depth are obtained for the 50–475 Hz, 475–1200 Hz and 1200–2000 Hz frequency bands respectively, consistent with the change in the sky grid resolution during the search and the population veto.

The depth values corresponding to the averaged all-sky 95% confidence detection efficiency are obtained by means of simulated periodic gravitational wave signals added into the SFT data of both detectors H1 and L1 in a limited number of frequency bands. In those bands, the detection efficiency, i.e., the fraction of signals that are considered detected, is computed as a function of signal strength  $h_0$  expressed by the sensitivity depth.

For the 50–475 Hz initial-frequency band 22 different 0.1-Hz bands free of spectral disturbances in both detectors were selected with the following starting frequencies [73.6, 80.8, 98.3, 140.8, 170.2, 177.8, 201.1, 215.1, 240.7, 240.8, 250.7, 305.3, 320.3, 350.6, 381.6, 400.7, 402.1, 406.8, 416.2, 436.9, 446.9, 449.4]. These bands were chosen to be free of known spectral disturbances in both detectors, with no coincidence candidates among the H1 and L1 data sets, and scattered over the whole frequency band.

In all these selected bands, we generated nine sets of 200 signals each, with fixed sensitivity depth in each set and random parameters  $(f, \alpha, \delta, \dot{f}, \varphi_0, \psi, \cos \iota)$ . Each signal was added into the data of both detectors, and an analysis was done using the *SkyHough* search pipeline over a frequency band of 0.1 Hz and the full spin-down range, but covering only one sky-patch. For this sky-patch a list of 300 loudest candidates was produced. Then we imposed a threshold on the critical ratio, based on the minimum value found in the all-sky search in the corresponding 0.1 Hz band before any injections.



The post-processing was then done using the same parameters used in the search, including the population veto. A signal was considered detected if the center of the selected cluster, if any, lay within a distance  $d_{\text{SH}} < 13$  from the real injected value. This window was chosen based on previous studies Walsh, S. and Pitkin, M. and Oliver, M. and D'Antonio, S. and Dergachev, V. and Królak, A. and Astone, P. and Bejger, M. and Di Giovanni, M. and Dorosh, O. and Frasca, S. and Leaci, P. and Mastrogiovanni, S. and Miller, A. and Palomba, C. and Papa, M. A. and Piccinni, O. J. and Riles, K. and Sauter, O. and Sintes, A. M., 2016 and prevented miscounts due to noise fluctuations or artifacts.

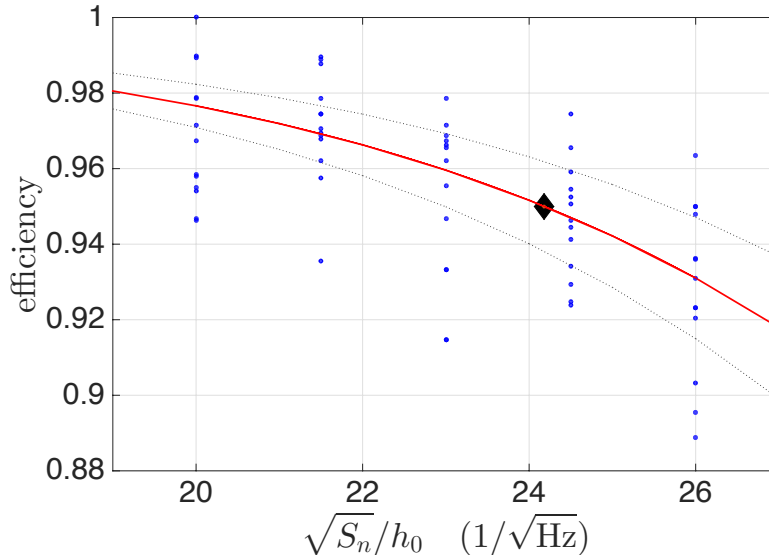


FIGURE 4.7: Detection efficiency as a function of depth obtained for 22 frequency bands in the frequency band 50-475 Hz. Each dot corresponds to a set of 200 signal injections. The solid line (red) correspond to the fitted sigmoid curve. The diamond shows the depth value corresponding to an averaged all-sky 95% detection efficiency,  $\mathcal{D}^{95\%} = 24.2$  ( $1/\sqrt{\text{Hz}}$ ).

For the 22 frequency bands corresponding to the lowest frequency range, a sigmoid curve

$$E(\mathcal{D}) = 1 - \frac{1}{1 + \exp(b(\mathcal{D} - a))}, \quad (4.7)$$

was fitted by means of the least absolute residuals or equivalently a logistic regression. Then the 95% confidence upper limit was deduced from the corresponding value of the depth. With this procedure, the minimum and maximum values of the depth corresponding to the desired upper limit were 21.9 and 26.6 ( $1/\sqrt{\text{Hz}}$ ) respectively.

We also collected the results from all the frequency bands and, as shown in Figure 4.7, performed a sigmoid fitting as before and obtained the following fitted coefficients (with 95% confidence bounds):  $a = 39.83$  (34.93, 44.73) ( $1/\sqrt{\text{Hz}}$ ) and  $b = -0.1882$  (-0.2476, -0.1289) ( $\sqrt{\text{Hz}}$ ), that yields the joint depth for corresponding to the 95% upper limit of  $D^{95\%} = 24.2$  ( $1/\sqrt{\text{Hz}}$ ), its uncertainty being smaller than 7% for undisturbed bands, with the exception of the 98.3 Hz band for which the upper limit using this joint value would be underestimated by 10% and for 406.8 Hz band for which the upper limit is overestimated by 9.5%.

The 95% confidence upper limit on  $h_0$  for undisturbed bands was derived by simply scaling the power spectral density of the data,  $h_0^{95\%} = \sqrt{S_n}/D^{95\%}$ . The computed

upper limits are shown in

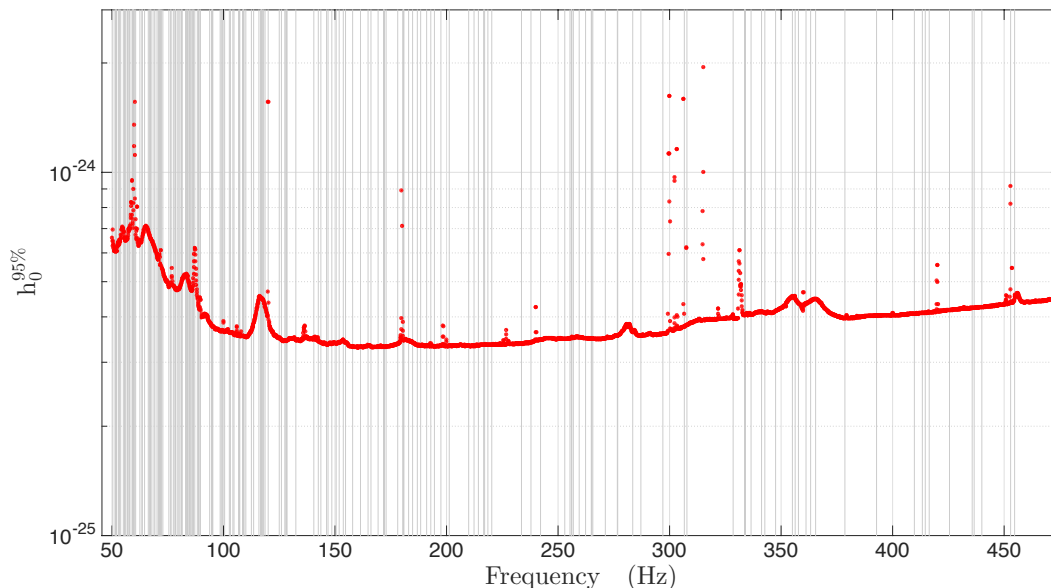


FIGURE 4.8: *SkyHough* O1 upper limits between 50–475 Hz. The dotted (red) curve shows the averaged 95% confidence level upper limits for every analyzed 0.1-Hz band. The vertical (grey) lines indicate 194 0.1-Hz bands in which coincidence candidates were found and consequently no upper limits are set.

The 95% confidence upper limit on  $h_0$  for undisturbed bands can then be derived by simply scaling the power spectral density of the data,  $h_0^{95\%} = \sqrt{S_n/D^{95\%}}$ . The computed upper limits are shown in Figure 4.8. No limits have been placed in 194 0.1-Hz bands in which coincidence candidates were detected, as this scaling procedure can have larger errors in those bands due to the presence of spectral disturbances.

A similar but slightly different procedure was applied to the two higher frequency ranges in order to obtain two different values of average depth for the 475–1200 and 1200–2000 Hz frequency bands, respectively, consistent with the change in the sky grid resolution during the search. For the 475–1200 Hz lower-frequency band, eighteen different 0.1 Hz bands were selected with the following starting frequencies: [532.4, 559.0, 580.2, 646.4, 658.5, 678.0, 740.9, 802.4, 810.2, 865.3, 872.1, 935.7, 972.3, 976.3, 1076.3, 1081.0, 1123.4, 1186.0] Hz. For the 1200–2000 Hz higher-frequency band, the following eighteen different 0.1 Hz bands were selected: [1248.7, 1310.6, 1323.5, 1334.4, 1410.3, 1424.6, 1450.2, 1562.6, 1580.4, 1583.2, 1653.2, 1663.6, 1683.4, 1704.3, 1738.2, 1887.4, 1953.4, 1991.5] Hz. In all these selected bands, the same procedure described above was applied, except that we generated nine sets of 400 signals each, with fixed sensitivity depth in each set and random parameters, instead of just 200.

We collected the results from the two sets of 18 frequency bands and for each frequency the detection efficiency,  $E$ , versus depth,  $\mathcal{D}$ , values were fitted to the sigmoid function, using the nonlinear regression algorithm `nlinfit` provided by `Matlab`. Since the detection rate follows a binomial distribution each data point was weighted by the standard  $\sigma_E$  error given by

$$\sigma_E = \sqrt{\frac{E(1-E)}{N_I}}, \quad (4.8)$$

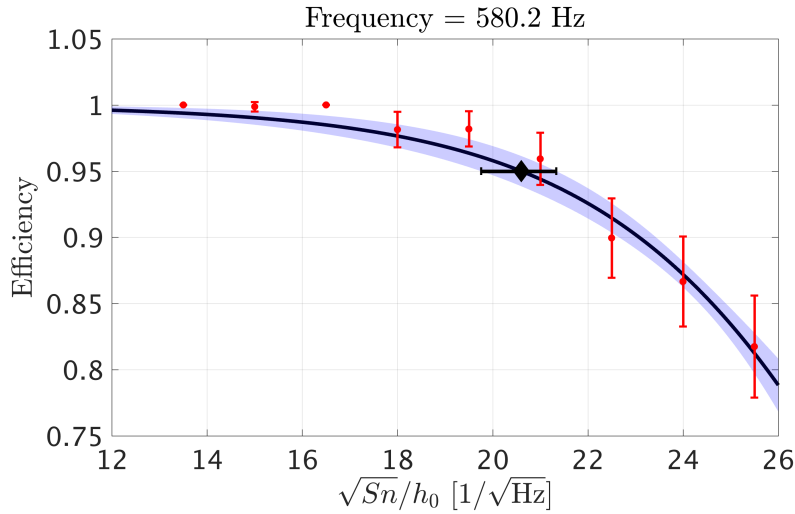


FIGURE 4.9: Detection efficiency as a function of depth obtained for the 0.1 Hz frequency band starting at 580.2 Hz. Each red dot corresponds to a set of 400 signal injections and error bars on the data points represent the  $2\sigma_E$  standard binomial error. The (black) solid line corresponds to the fitted sigmoid curve and the (blue) shaded envelope corresponds to the  $2\sigma_F$  calculated according to Eq. (4.9). The diamond shows the depth value corresponding to the 95% detection efficiency,  $\mathcal{D}^{95\%}$ , along with the  $2\sigma_F$  uncertainty in black markers.

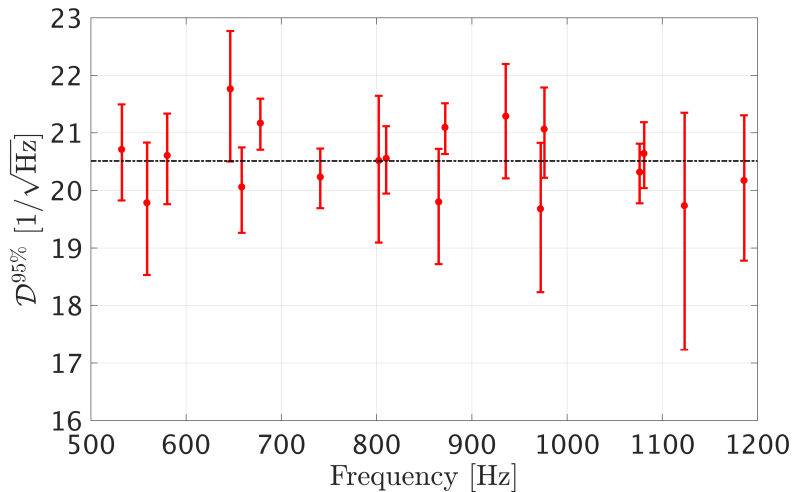


FIGURE 4.10: Depth values corresponding to the 95% detection efficiency,  $\mathcal{D}^{95\%}$ , obtained for 18 0.1 Hz frequency bands between 475 and 1200 Hz, along with their corresponding  $2\sigma_F$  uncertainties from the sigmoid fit in red markers. The average of the measured depths at different frequencies being  $\langle \mathcal{D}^{95\%} \rangle_{\text{Low}} = 20.5 \text{ Hz}^{-1/2}$ .

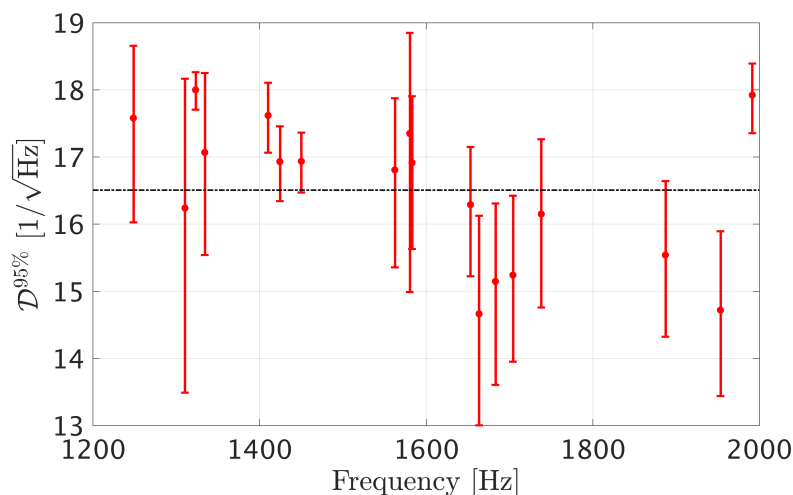


FIGURE 4.11: Depth values corresponding to the 95% detection efficiency,  $\mathcal{D}^{95\%}$ , obtained for 18 0.1 Hz frequency bands between 1200 and 2000 Hz, along with their corresponding  $2\sigma_F$  uncertainties in red markers. The average of the measured depths at different frequencies being  $\langle \mathcal{D}^{95\%} \rangle_{\text{High}} = 16.5 \text{ Hz}^{-1/2}$ .

where  $N_I$  is the number of injections performed. From the estimated coefficients  $a$  and  $b$  along with the covariance matrix  $C$ , we estimated the  $\sigma_F$  envelope on the fit given by

$$\sigma_F = \pm \sqrt{(\partial_a E)^2 C_{aa} + 2(\partial_a E)(\partial_b E)C_{ab} + (\partial_b E)^2 C_{bb}}, \quad (4.9)$$

where  $\partial$  indicates partial derivative, and derived the corresponding depth at the 95% detection efficiency,  $\mathcal{D}^{95\%}$ , as illustrated in Figure 4.9.

Figures 4.10 and 4.11 show the obtained depth values for each frequency corresponding to the 95% efficiency level,  $\mathcal{D}^{95\%}$ , together with their  $2\sigma$  uncertainty  $\delta\mathcal{D}^{95\%} = 2\sigma_F$ .

As representative of the sensitivity depth of the search, we took the average of the measured depths for each of the two sets of 18 different frequencies. This yielded  $\langle \mathcal{D}^{95\%} \rangle_{\text{Low}} = 20.5 \text{ Hz}^{-1/2}$  for the lower 475–1200 Hz band and  $\langle \mathcal{D}^{95\%} \rangle_{\text{High}} = 16.5 \text{ Hz}^{-1/2}$ , for the higher 1200–2000 Hz band, being the range of variation observed on the measured sensitivity depth of individual frequency bands with respect to the averaged values of 7.4% and 15%, respectively.

The 95% confidence upper limit on  $h_0$  for undisturbed bands can then be derived by simply scaling the power spectral density of the data,  $h_0^{95\%} = \sqrt{S_n} / \mathcal{D}^{95\%}$ . The computed upper limits are shown in Figure ???. No limits have been placed in 25 0.1 Hz bands in which coincident candidates were detected, as this scaling procedure can have larger errors in those bands due to the presence of spectral disturbances.

## 4.7 The *SkyHough* search results

In this section we report the main results of the O1 all-sky search, between 50 and 2000 Hz using the *SkyHough* pipeline, as described above. In total of 265 0.1-Hz bands contained coincidence candidates and therefore 265 coincidence clusters were identified and further investigated. The majority of these outliers corresponded to known spectral lines, severe spectral disturbances or hardware injected signals.

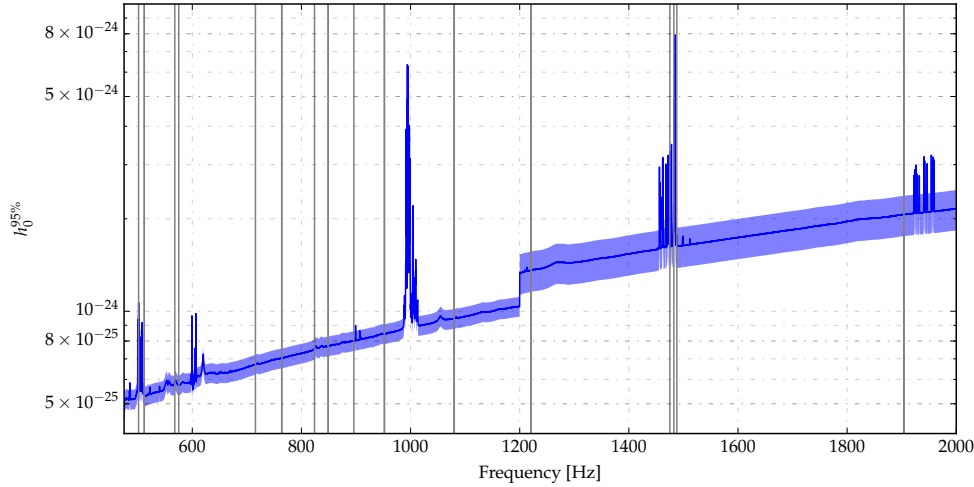


FIGURE 4.12: *SkyHough* O1 upper limits between 475–2000 Hz. The solid (blue) line shows the averaged 95% confidence level upper limits on the gravitational wave amplitude for every analyzed 0.1 Hz band. The vertical (gray) lines indicate 25 0.1 Hz bands in which outliers were found and consequently no upper limits were set. The lighter region around the upper limit represents the 7.4% and 15% uncertainty levels. The jump in sensitivity and uncertainty at 1200 Hz corresponds to the decrease in the sky grid resolution during the search, tuned to reduce the computational load.

A total of 194 coincidence candidates were in the lower frequency range 50–475 Hz. This initial list was reduced to 59 after applying the especial cluster population veto for the lowest frequency range and to 26 after the multi-interferometer consistency veto. A detailed list of these remaining outliers is shown in Table 4.6. Furthermore, the multi-interferometer significance consistency veto alone was able to reduce the initial list of 194 candidates to 33. Of these 26 outliers, 5 corresponded to hardware injected pulsars and 20 to known line artifacts contaminating either H1 or L1 data. The only unexplained outlier around 452.89989 Hz is due to an unknown large spectral disturbance in the H1 detector. Table 4.5 provides details on outliers corresponding to hardware injections.

In the 475–2000 Hz frequency range, a total of 71 0.1 Hz bands contained coincidence candidates: 19 in the 475–1200 Hz band, analyzed with higher sky resolution, and 52 in the 1200–2000 Hz band, analyzed with lower sky resolution. After discarding all the clusters containing only one coincidence pair, this list was reduced to 25 outliers, 17 in the low frequency band and 8 in the high frequency band, which were further inspected. A detailed list of these remaining outliers is shown in Table 4.7, along with comments on their likely origin. None of these outliers show evidence of being a credible gravitational wave signal. Among the 25 outliers, 17 were related to known line artifacts contaminating either H1 or L1 data, and 7 were identified with the hardware-injected pulsars ip1, ip2, ip7, and ip9.

Table 4.5 presents the parameters of the center of the clusters obtained related to these hardware injections. Two hardware injection were not recovered. Ip4 was not found since its spin-down was outside the search range, and ip14 was linearly polarized and had a strain amplitude  $h_0$  below our sensitivity.

The only unexplained outlier around 715.7250 Hz, corresponding to Idx=6 in

Label	$\Psi_{mem}$	Frequency [Hz]	Spin-down [mHz/s]	$\alpha$ [deg]	$\delta$ [deg]
ip0	21.16	265.5736 (0.0020)	0.3441 (0.3482)	68.7247 (2.8272)	-52.1531 (4.0643)
ip1	36.06	848.9657 (0.0053)	0.5497 (0.2497)	37.7549 (0.3611)	-25.2883 (4.1642)
ip2	30.50	575.1635 (0.0001)	0.0170 (0.0171)	215.1005 (0.1557)	3.0138 (0.4302)
ip3	13.61	108.8573 (0.0002)	0.0041 (0.0041)	179.7435 (1.3709)	-32.7633 (0.6733)
ip4	-	-	-	-	-
ip5	24.22	52.8084 (0.0001)	-0.0175 (0.0175)	294.2376 (8.3890)	-83.1460 (0.6932)
ip6	16.08	146.1994 (0.0006)	-6.6167 (0.1133)	362.8627 (1.6137)	-63.7860 (1.6367)
ip7	41.61	1220.5554 (0.0009)	0.5482 (0.5718)	229.2338 (5.8082)	4.1538 (24.6044)
ip8	22.83	191.0716 (0.0009)	-8.7553 (0.1053)	348.0175 (3.3721)	-31.7070 (1.7115)
ip9	35.85	763.8507 (0.0034)	-0.5567 (0.5567)	203.8965 (5.0109)	73.8445 (1.8451)
ip14	-	-	-	-	-

TABLE 4.5: *SkyHough* hardware injection cluster information. The table provides the frequency, spin-down and sky location of the cluster center related to each of the hardware injections found by the *SkyHough* search. In parentheses the distance from the cluster center to the injected values are shown. Frequencies are converted to epoch GPS 1125972653.

Table 4.7, was further investigated. A multidetector Hough search was performed to verify the consistency of a possible signal. In this case the maximum combined critical ratio obtained was 5.98 while we would have expected a minimum value of 8.21 in case of a real signal. This last outlier was also followed up with the Einstein@Home pipeline Papa, 2016 using coherent integration times of 210 and 500 hours. This search covered signal frequencies in the range  $[715.724, 715.726]$  Hz (epoch GPS 1125972653), frequency derivatives over  $[-2.2, -1.9] \times 10^{-9}$  Hz/s, and a sky region  $RA = 1.063 \pm 0.020$  rad,  $DEC = -0.205 \pm 0.020$  rad that included the whole associated cluster. This search showed that this candidate was not interesting and had a very low probability of having astrophysical origin.

Therefore, this *SkyHough* search did not find any evidence of a continuous gravitational wave signal. Upper limits have been computed in each 0.1 Hz band, except for those bands in which outliers were found.

## 4.8 Conclusions

After following up numerous early stage outliers, no evidence was found for continuous gravitational waves in the O1 data over the band and range of frequency derivatives searched. We therefore present bounds on detectable gravitational radiation in the form of 95% confidence level upper limits. Figure 4.13 shows a summary of the strain amplitude upper limits obtained for three competing pipelines using LIGO O1 data. Notice that one pipeline (*PowerFlux*) presents strict all-sky limits for circular-polarization and linear-polarization sources. The other two pipelines (*SkyHough* and *Time-Domain  $\mathcal{F}$ -statistic*) present frequentist population-averaged limits over the full sky and source polarization.

The *SkyHough* pipeline added a viewpoint of robust Hough algorithm. Although the decrease in the sky grid resolution at 1200 Hz, tuned to reduce computational load, produced a jump in sensitivity of about 20%, this method offers an independent check of the other results. Future searches will use longer SFT time duration to allow the attainment of sensitivity close to *PowerFlux* at a reduced computational cost.

These upper limits improve upon those previously obtained from initial LIGO and Virgo data sets. The overall improvements in strain sensitivity come primarily from the improved noise floors of the Advanced LIGO interferometers over previous LIGO and Virgo interferometers, with reductions in upper limits of about a factor of 3 at frequencies above 100 Hz and larger reductions at lower frequencies.

Because these results exclude only maximal deformations in a limited distance range for higher frequencies, they do not permit firm conclusions about the equation of state determining neutron star structure, see (Abbott, 2017f; Abbott, 2018e) for further details. In future data taking, however, as detector sensitivities improve and longer data sets become available, the Galactic volume and bandwidth over which large deformations can be tested will expand to include many star-forming regions not currently accessible.

Idx	Frequency [Hz]	Spin-down [nHz/s]	$\alpha$ [rad]	$\delta$ [rad]	$\Psi_{\text{mean}}$	#cluster	#L1	#H1	$\Psi_{L1}^*$	$\Psi_{H1}^*$	$\Psi_{\text{max}}$	$\Psi_{\text{multi}}^*$	$\Psi_{\text{theo}}$	Description
6	52.8084	-0.0175	-1.1478	-1.4512	24.22	975	554	20	20.36	40.54	27.02	45.61	45.20	1
9	53.8974	0.3693	0.4803	1.5115	6.31	14	6	3	5.66	10.47	6.50	21.20	11.90	2
14	57.0055	-1.0014	-2.2336	-0.1685	9.84	14	7	2	15.84	9.17	11.43	14.28	15.37	3
24	62.4983	0.2480	-1.0927	-1.3699	14.64	1089	45	326	9.13	98.01	16.67	95.25	93.06	3
44	75.5055	-0.9098	-2.5598	-1.1455	10.05	7	2	5	6.44	71.67	11.67	57.12	57.60	3
46	76.4988	0.2207	-1.1572	-1.2721	11.03	1090	34	282	7.59	76.60	11.49	68.14	67.41	3
47	77.4963	0.5741	-0.1180	1.3766	9.54	959	70	121	6.28	76.87	10.61	70.23	66.58	3
49	78.4962	0.5587	-0.2021	1.4096	9.65	308	13	129	6.38	75.89	10.29	69.25	64.34	3
52	79.9990	0.1808	-1.2674	-1.2599	10.05	615	59	175	6.59	107.63	10.90	97.21	91.77	3, 4
53	80.4994	0.0658	-1.5722	1.2107	11.92	1254	97	138	7.41	68.79	13.27	60.94	60.89	3
60	84.4961	0.5454	-0.4443	1.4369	8.95	1002	55	141	5.88	59.19	10.69	56.18	54.21	3
62	85.0013	-0.2165	1.8264	-1.2866	12.08	811	132	83	11.21	15.38	12.96	18.13	18.96	3
63	85.5012	-0.1977	1.7877	-1.2674	33.87	870	198	64	27.44	58.03	36.95	63.92	63.78	3
66	86.4989	0.1618	-1.4494	1.2580	9.08	1357	147	125	6.38	57.24	10.49	54.70	53.67	3
76	98.4983	0.2876	-1.2383	1.2866	10.16	1219	161	158	7.10	28.50	11.30	27.51	26.12	3
79	100.5032	-0.5624	2.5925	-1.3402	8.37	288	39	114	6.02	28	8.85	24.96	24.96	3
88	108.8573	0.0041	-3.1371	-0.5718	13.61	999	296	99	18.79	14.73	15.85	22.93	23.55	1
92	112.5026	-0.4739	-1.8331	0.9775	6.52	68	2	55	5.98	11.70	6.78	11.72	12.84	3
104	127.4964	0.5926	-0.9377	1.3368	6.36	877	204	58	7.04	7.64	6.94	9.08	10.39	3
105	127.9988	0.2101	-1.3924	1.2317	70.70	1165	161	70	61.13	108	78.07	123.85	121.24	3, 4
107	128.4984	0.3602	-1.1366	1.2478	6.94	971	223	82	8.40	7.35	7.60	9.50	11.07	3
112	146.1994	-6.6167	0.0500	-1.1133	16.08	1676	796	22	15.96	22.10	18.11	27.17	26.87	1
136	191.0716	-8.7553	-0.2091	-0.5534	22.83	988	262	107	30.61	22.80	25.66	37.00	37.76	1
153	255.9995	0.0789	-1.5493	1.1792	30.62	1082	203	43	20.10	105.72	33.03	96.46	86.90	3, 4
160	265.5736	0.3441	1.1995	-0.9102	21.16	750	286	18	24.76	25.97	25.19	35.18	35.85	1
193	452.8999	-2.7816	2.5350	-1.3173	10.01	222	4	109	6.68	88.07	10.04	61.91	28.21	5

TABLE 4.6: *SkyHough* outliers after population and multi-interferometer consistency vetoes in the range of frequencies between 50 and 475 Hz. The table provides the frequency, spin-down and sky location of the cluster centers found by the *SkyHough* search.  $\#_{\text{cluster}}$  is the size of the cluster in terms of number of coincident pairs,  $\Psi_{\text{max}}$  and  $\Psi_{\text{mean}}$  are the maximum and mean value of the cluster critical ratio,  $\#_{L1}$  and  $\#_{H1}$  are the number of different candidates producing coincidence pairs from the different data sets,  $\Psi_{L1}^*$  and  $\Psi_{H1}^*$  are the maximum critical ratio values obtained by analysing the data from H1 and L1 separately,  $\Psi_{\text{multi}}^*$  is maximum combined critical ratio when the data from both detectors are analyzed jointly and  $\Psi_{\text{theo}}$  is the expected theoretical combined critical ratio value. Frequencies are converted to epoch GPS 1125972653. The outliers description codes mean the following: 1- hardware injection, 2- associated to unknown comb in H1 starting at 30.9430 Hz with 0.99816 Hz spacing, 3- miscellaneous combs with known or unknown sources at multiples of 0.5 Hz many of them due to blinking LEDs in timing system, 4- associated with the 8 Hz comb in H1 due to the OMC length dither, and 5- spectral disturbance in H1.



Idx	Frequency [Hz]	$\alpha$ [rad]	$\delta$ [rad]	Spin-down [nHz/s]	$\Psi_{mean}$	# <sub>cluster</sub>	# <sub>L1</sub>	# <sub>H1</sub>	$\Psi_{L1}^*$	$\Psi_{H1}^*$	$\Psi_{max}$	Description
1	501.6000	-1.4445	1.2596	0.9374	10.66	5	2	3	11.31	89.18	10.71	Quad violin mode 1st harmonic region (H1 & L1)
2	511.9968	-1.4218	1.2070	0.6773	16.31	4927	298	226	10.47	101.36	18.73	Quad violin mode 1st harmonic region (H1 & L1)
3	512.0027	1.7085	-1.1996	-0.6071	16.33	3007	245	246	11.20	101.55	18.85	Quad violin mode 1st harmonic region (H1 & L1)
4	568.0011	1.5942	-1.1783	-0.1839	7.18	3867	415	125	8.82	9.81	9.05	8 Hz comb (H1 & L1)
5	575.1635	-2.5290	0.0526	0.0170	30.50	1974	275	78	46.66	26.54	33.75	Hardware injection ip2
6	715.7250	1.0629	-0.2049	-2.0400	5.48	5	3	4	6.53	6.50	5.53	Unknown
8	763.8507	-2.7245	1.2888	-0.5567	35.85	6064	297	91	41.29	43.43	42.33	Hardware injection ip9
9	763.9016	-2.1715	0.9109	-7.1318	18.19	611	151	56	17.45	22.99	19.84	Hardware injection child ip9
11	824.0035	1.6679	-1.1996	-0.7762	7.56	1111	81	123	8.09	10.83	8.43	8 Hz comb (H1 & L1)
12	848.9657	0.6589	-0.4414	0.5497	36.06	5329	342	117	48.63	37.64	42.17	Hardware injection ip1
13	849.0020	0.4565	-0.6807	-4.0716	25.19	1983	331	108	31.08	29.57	29.35	Hardware injection child ip1
14	895.9988	-1.5481	1.1744	0.2368	10.33	244	35	79	6.48	69.62	11.45	8 Hz comb (H1 & L1)
15	952.0018	1.5957	-1.1797	-0.3216	18.57	4353	355	189	18.36	27.59	21.86	8 Hz comb (H1 & L1)
16	952.1017	-0.3965	-1.3294	-9.8134	9.08	416	138	62	9.17	15.29	9.98	8 Hz comb (H1 & L1)
17	1079.9981	-1.5517	1.1798	0.3367	22.98	2639	402	129	51.28	17.88	25.90	8 Hz comb (H1 & L1)
18	1080.0022	1.6073	-1.1825	-0.4562	22.95	5276	428	172	52.66	17.84	25.89	8 Hz comb (H1 & L1)
19	1080.1007	-0.2290	-1.3906	-9.9428	10.79	451	117	49	20.45	9.52	12.60	8 Hz comb (H1 & L1)
21	1220.5492	-2.2823	0.0725	0.5482	34.69	291	63	43	66.56	37.98	48.10	Hardware injection ip7
22	1220.7094	-1.6804	-0.5910	-9.6702	6.14	17	12	11	7.37	8.32	6.58	Hardware injection child ip7
44	1475.0997	1.5636	-1.1725	-0.0308	10.87	42	8	19	6.64	77.42	11.72	Quad violin mode 3rd harmonic region (H1 & L1)
45	1482.5000	-2.8976	1.0123	0.7317	9.04	2	1	2	6.58	51.78	9.05	Quad violin mode 3rd harmonic region (H1 & L1)
46	1487.8976	1.8780	1.1717	-1.7738	6.69	2	1	2	6.53	10.19	6.75	Quad violin mode 3rd harmonic region (H1 & L1)
66	1903.9302	-1.8796	1.5402	0.1383	15.51	65	28	12	35.47	39.89	35.48	8 Hz comb (H1 & L1)
67	1904.0020	1.5885	-1.1737	-0.4096	29.00	4779	340	141	34.94	40.65	36.82	8 Hz comb (H1 & L1)
68	1904.1028	0.9560	-1.3834	-10.0406	15.11	925	194	51	16.36	24.82	19.12	8 Hz comb (H1 & L1)

TABLE 4.7: *SkyHough* pipeline outliers in the range of frequencies between 475 and 2000 Hz after the population veto. The table provides the frequency, spin-down and sky location of the cluster centers found by the *SkyHough* search. #<sub>cluster</sub> is the size of the cluster in terms of number of coincident pairs,  $\Psi_{max}$  and  $\Psi_{mean}$  are the maximum and mean value of the cluster critical ratio, #<sub>L1</sub> and #<sub>H1</sub> are the number of different candidates producing coincidence pairs from the different data sets, and  $\Psi_{L1}^*$  and  $\Psi_{H1}^*$  are the maximum critical ratio values obtained by analysing the data from H1 and L1 separately. Frequencies are converted to epoch GPS 1125972653.

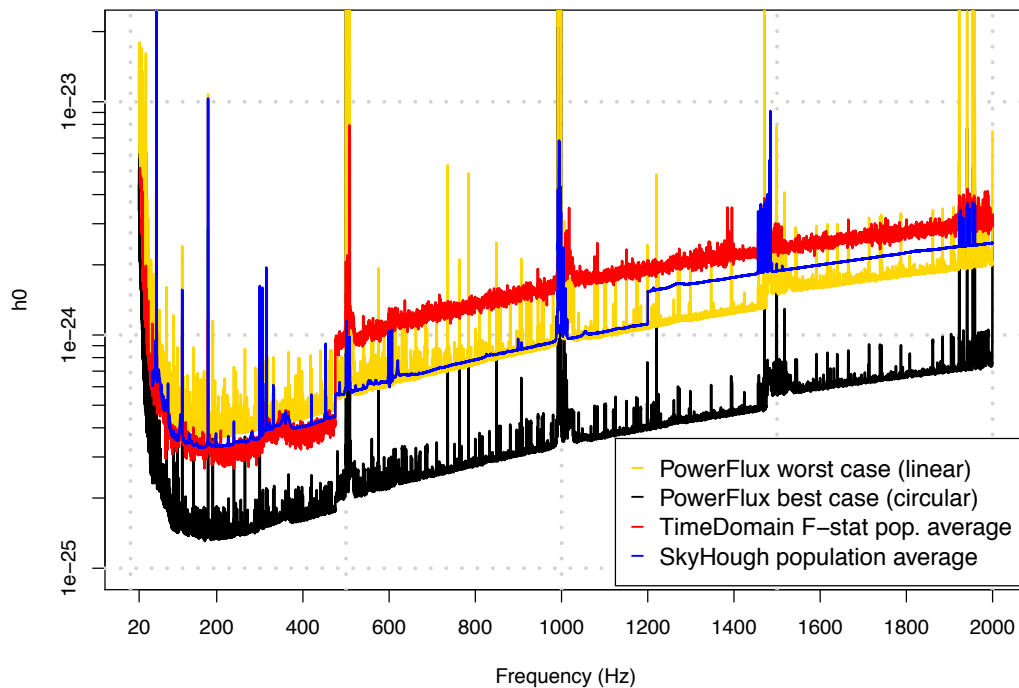


FIGURE 4.13: O1 upper limits. The upper (red) curve shows *Time-Domain  $\mathcal{F}$ -statistic* 95% confidence level population averaged upper limits, the next lower curve (blue) shows maximum population average upper limits from *SkyHough*, followed by yellow curve showing *PowerFlux* worst-case (linearly polarized) 95% confidence level upper limits in analyzed bands. *PowerFlux* upper limits are maximized over sky and all intrinsic signal parameters for each frequency band displayed. The lower (black) curve shows upper limits assuming a circularly polarized source. As the computational demands grow with frequencies each pipeline tuned parameters to reduce computation load. This accounts for jumps in curves at 475, 1200 and 1475 Hz. The *SkyHough* upper limit curve shows maximum of the range of different upper limits shown in Fig. 4.12 with different upper limit values corresponding to different search depths. Because of highly non-Gaussian data the *SkyHough* search depths are not expected to be well-estimated for each individual search band, but are representative of the noise behavior in the entire frequency range.

## Chapter 5

# The Adaptive Transient Hough method for long-duration gravitational wave transients

M. OLIVER, D. KEITEL, A. M. SINTES

Certificate on Appendix B

### 5.1 INTRODUCTION

The advanced `gwdetector` era has provided us with multiple detections from binary compact objects (Abbott, 2018a) including GW170817, the first binary neutron star (BNS) coalescence (Abbott, 2017c). This detection motivated the development of the new search method presented in this work, focusing on the possible birth of a rapidly rotating highly magnetized `NS` spinning down through some combination of GW and electromagnetic emission. For a very massive remnant, the collapse would occur in a short time scale (as explored in Abbott, 2017e; Abbott, 2019a), but for low total mass and some equations of state, the emitted GW signal could have an intermediate duration on the order of hours to days (Baiotti and Rezzolla, 2017; Piro, Giacomazzo, and Perna, 2017).

This regime of GW signal durations has long been mostly unexplored from the data analysis side. The expected rapid frequency and amplitude evolution, in combination with observation times still much longer than e.g. for individual binary coalescences, pose unique challenges on analysis algorithms. Other pre-existing or recently developed methods to search for intermediate-duration signals include the Stochastic Transient Analysis Multi-detector Pipeline (STAMP) (Thrane, 2011), the Hidden Markov model Viterbi algorithm (Sun and Melatos, 2018) and a generalization of the FrequencyHough method (Miller, 2018). The first two are generic unmodeled searches, while the last is a modeled search for power-law spin-downs similar to the one described in this paper. Together with those three pipelines, our new **Adaptive Transient Hough (ATrHough)** method has already contributed to the search for a long-duration transient signal from a putative `NS`remnant of GW170817 described in Abbott, 2018c.

The Adaptive Transient Hough is a semi-coherent analysis adapted from the SkyHough (Sintes and Krishnan, 2007; Sintes and Krishnan, 2006; Krishnan et al., 2004) search for continuous wave (CW) signals. Like most other CW searches (Riles, 2017), the original SkyHough assumes a constant intrinsic amplitude and slowly evolving frequency, and hence cannot be used to search for transient GWs with rapid frequency

and amplitude evolution (see quantitative comparison in Sec. 5.2), for which we have now specifically developed the new method.

The ATrHough method will also have wider applicability beyond the case of BNS remnants, as signals with similar durations and evolutionary behaviour are also possible from young  $\text{ns}[s]$  born through the regular supernova channel (Palomba, 2001; Dall’Osso, Shore, and Stella, 2009; Dall’Osso et al., 2015; Lasky and Glampedakis, 2016; Dall’Osso, Stella, and Palomba, 2018), emitted either by r-mode oscillations (Owen et al., 1998; Andersson and Kokkotas, 2001) or quadrupolar deformations.

The work is organized as follows: section II briefly describes the expected signal from a remnant  $\text{ns}$ . Section III summarizes the general strategy of a hierarchical search and its implementation, section IV studies its statistical properties, and section V introduces the threshold and vetoes required for a robust detection strategy. Finally section VI presents an estimate for the search sensitivity and section VII presents our conclusions.

## 5.2 THE TRANSIENT SIGNAL MODEL

The output of a GW detector can be represented by

$$x(t) = n(t) + h(t), \quad (5.1)$$

where  $n(t)$  is the detector noise at time  $t$ , and  $h(t)$  is the strain induced by a GW signal:

$$h(t) = F_+(\mathbf{n}, \psi, t)h_+(t) + F_\times(\mathbf{n}, \psi, t)h_\times(t), \quad (5.2)$$

where  $F_{+,\times}$  are the detector antenna patterns, which depend on a unit-vector  $\mathbf{n}$  corresponding to the sky location of the source and on the wave polarization angle  $\psi$ , and vary with time due to the movement of the detector frames with the Earth. For ground-based detectors with perpendicular arms, the expressions for  $F_{+,\times}$  are (**grav1**):

$$F_+(\mathbf{n}, \psi, t) = a(t; \mathbf{n}) \cos 2\psi + b(t; \mathbf{n}) \sin 2\psi, \quad (5.3a)$$

$$F_\times(\mathbf{n}, \psi, t) = b(t; \mathbf{n}) \cos 2\psi - a(t; \mathbf{n}) \sin 2\psi, \quad (5.3b)$$

where the functions  $a(t; \mathbf{n})$  and  $b(t; \mathbf{n})$  are independent of  $\psi$ . For convenience, we do not explicitly write out the  $\mathbf{n}$  and  $\psi$  dependence from here on. Now the waveforms for the two polarizations  $h_{+,\times}$  are:

$$h_+(t) = A_+(t) \cos \Phi(t), \quad (5.4a)$$

$$h_\times(t) = A_\times(t) \sin \Phi(t), \quad (5.4b)$$

where  $\Phi(t)$  is the phase evolution of the signal and  $A_{+,\times}(t)$  are the (time-varying) amplitude parameters depending on the orientation  $\cos \iota$  of the source and on the strain amplitude evolution  $h_0(t)$  as follows:

$$A_+(t) = \frac{1}{2}h_0(t) (1 + \cos^2 \iota), \quad (5.5a)$$

$$A_\times(t) = h_0(t) \cos \iota. \quad (5.5b)$$

The time evolution of the dimensionless strain amplitude  $h_0(t)$  depends on the emission mechanism; if for example it is due to a constant non-axisymmetrical deformation

of the source  $_{\text{NS}}$ , but the frequency decays over time, the amplitude evolves as

$$h_0(t) = \frac{4\pi^2 G}{c^4} \frac{I_{zz} \epsilon}{d} f_{\text{gw}}^2(t), \quad (5.6)$$

where  $c$  is the speed of light,  $I_{zz}$  is the z-z component of the star's moment of inertia with the z-axis being its spin axis,  $\epsilon := (I_{xx} - I_{yy})/I_{zz}$  is the equatorial ellipticity of the star, and  $d$  is its distance from Earth. Another mechanism covered by this method is  $_{\text{GW}}$ emission from r-mode oscillations, which are the result of small velocity and density perturbations of the  $_{\text{NS}}$ fluid, causing a time-varying moment of inertia restored through Coriolis force; for these, the amplitude evolution is given by

$$h_0(t) = \sqrt{\frac{3}{80\pi}} \frac{G}{c^5} \frac{1}{d} \alpha M R^3 \tilde{J} f_{\text{r}}^3(t), \quad (5.7)$$

where  $f_{\text{r}}$  is the rotation frequency of the source,  $\tilde{J} = 0.01635$  is a dimensionless constant,  $M$  is the  $_{\text{NS}}$ mass,  $R$  its radius and  $\alpha$  is a dimensionless amplitude described in more detail in Owen et al., 1998.

Independent of the specific emission scenario, the amplitude evolution  $h_0(t)$  can be written in a more general form as:

$$h_0(t) = A_m f_{\text{gw}}^m(t), \quad (5.8)$$

where  $m$  and  $A_m$  are constants defined by the emission mechanism.

To characterize the frequency evolution of a newborn  $_{\text{NS}}$  we apply the waveform model from Lasky et al., 2017; Sarin et al., 2018, originating from the general torque equation

$$\dot{\Omega} = -\kappa \Omega^n, \quad (5.9)$$

where  $\Omega$  and  $\dot{\Omega}$  are the frequency of rotation of the source and its derivative. (When we focus on  $_{\text{GW}}$ emission due to a non-axisymmetrical shape and do not consider the free precession case (Zimmermann and Szedenits, 1979; Jones and Andersson, 2001), the frequency of  $_{\text{GW}}$ emission is  $f_{\text{gw}} = \Omega/\pi$ .) Furthermore,  $n$  is called the star's braking index and  $\kappa$  is associated to the spindown timescale:

$$\tau = -\frac{\Omega_0^{1-n}}{\kappa(1-n)}. \quad (5.10)$$

The solution of Eq. (5.9) for arbitrary braking index  $n$  characterizes the frequency evolution:

$$\hat{f}_{\text{gw}}(t) = \begin{cases} f_{\text{gw},0} \left( \frac{t-T_0}{\tau} + 1 \right)^{\frac{1}{1-n}} & \text{if } t \geq T_0, \\ 0 & \text{if } t < T_0, \end{cases} \quad (5.11)$$

where  $f_{\text{gw},0}$  corresponds to the frequency at the start of the emission ( $t = T_0$ ); for simplicity let us set  $T_0 = 0$  s. A braking index of  $n = 5$  corresponds to pure  $_{\text{GW}}$ emission from a non-axisymmetric rotator. This equation can also be applied to r-modes, for which  $n \lesssim 7$  (Alford and Schwenzer, 2014; Alford and Schwenzer, 2015).

The Eq. (5.11) frequency evolution model and resulting amplitude evolution as per Eq. (5.8) is the key difference between our new search method and the SkyHough search (Krishnan et al., 2004) for CW signals, which instead uses a Taylor expansion for the slowly-evolving frequency of mature  $_{\text{NS}}$ [s] and assumes constant intrinsic amplitude.

To demonstrate explicitly that such an expansion is unsuited to search for signals with rapid spindowns, let us consider that the frequency resolution of a fully-coherent CW-like search over an observation time is  $\delta f_{\text{gw}} = 1/T_{\text{obs}}$ . Hence, for a Taylor expansion model  $\mathcal{T}[f_{\text{gw}}(t), s]$  to order  $s$  in  $f_{\text{gw}}(t)$ , the requirement is  $|f_{\text{gw}}(t) - \mathcal{T}[f_{\text{gw}}(t), s]| < 1/T_{\text{obs}}$ . Now we see that at least a 16th order expansion is required to track sources with astrophysically relevant example parameters (compare Abbott, 2018c)  $f_{\text{gw}}(0) = 1000$  Hz,  $\tau = 10000$  s and  $n = 5$  over  $T_{\text{obs}} = 5000$  s, making this approach computationally prohibitive. On the other hand, the search method introduced in the following uses the exact analytical form with its only three free parameters  $(n, f_{\text{gw},0}, \tau)$  to create a template grid that ensures complete coverage, while keeping the analysis computationally feasible.

As in other semi-coherent searches, this method considers as negligible – and therefore ignores – relativistic corrections, and those due to the time delay between the detector and the solar-system barycenter (SSB). Therefore only the instantaneous signal frequency in the detector frame needs to be calculated:

$$f_{\text{gw}}(t) = \hat{f}_{\text{gw}}(t) \left( 1 + \frac{\mathbf{v}(\mathbf{t}) \cdot \mathbf{n}}{c} \right), \quad (5.12)$$

where  $\mathbf{v}(\mathbf{t})$  is the detector velocity with respect to the SSB frame. Note that now the time coordinate  $t$  corresponds to time at the detector.

### 5.3 The Adaptive Transient Hough Method

This section discusses the implementation of the Adaptive Transient Hough (ATrHough) method, a pipeline based on the semi-coherent SkyHough search for CWs described in Krishnan et al., 2004; Sintes and Krishnan, 2007. The common ground of both searches is the use of a weighted Hough transform on Short-time Fourier Transforms (SFTs) as the input data. The Hough transform is an algorithm widely used in pattern recognition; here the pattern is defined by the frequency evolution of the signal in the detector data. In both CW and transient cases, the weights take into account the amplitude modulation of the signal, caused by the antenna pattern, and the changing noise floor between SFTs. But as a difference to the CW SkyHough search, the new ATrHough method also includes the source amplitude evolution in the weights.

Together with the power-law frequency evolution model from Eq. (5.11), the amplitude weights allow a sensitive search for transient signals from rapidly evolving newborn  $\text{NS}[s]$ . Meanwhile, the main framework and statistical properties are the same as in the SkyHough method. In the following we summarize them in the new context, and add the required transient-specific details.

#### 5.3.1 Length of Short-duration Fourier Transforms

We first obtain a collection of SFTs by dividing the full observation time  $T_{\text{obs}}$  in  $N$  segments of length  $T_{\text{coh}}$ . The maximum length of  $T_{\text{coh}}$  is calculated by imposing the 1/4-cycle criterion introduced in **grav1**: This leads to a requirement  $2|df/dt| \leq T_{\text{coh}}^{-2}$ , ensuring that the maximum modulation corresponds to only half a bin at the search frequency resolution  $\delta f = 1/T_{\text{obs}}$ . From Eq. (5.12) the spin-down modulation is given by two effects, the spin-down of the source and the Doppler modulation resulting from the Earth’s motion. The constraint imposed by the spin-down of the source is:

$$T_{\text{coh}} \leq \frac{\sqrt{(n-1)\tau}}{\sqrt{2f_{\text{gw},0}}}. \quad (5.13)$$

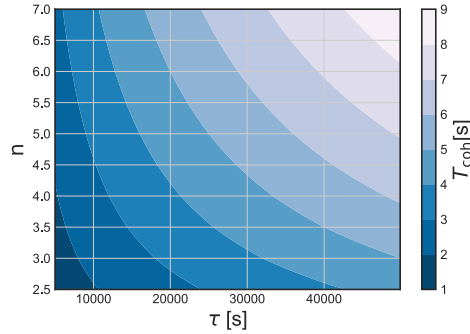


FIGURE 5.1: Search setup: The maximum coherence length  $T_{\text{coh}} = \sqrt{(n-1)\tau} / \sqrt{2f_{\text{gw},0}}$  allowed for signals with fixed  $f_{\text{gw},0} = 2000$  Hz and the other model parameters taking values in the intervals  $\tau \in [1000, 9640]$  s and  $n \in [2.5, 7]$ .

The range of maximum allowed  $T_{\text{coh}}$  for the parameter space covered in Abbott, 2018c is on the order of seconds, as shown in Fig. 5.1. On the other hand, the constraint imposed by Doppler modulation is on the order of hours, as discussed in Krishnan et al., 2004. Therefore we will consider only the spin-down of the source as the dominant threshold for  $T_{\text{coh}}$ .

### 5.3.2 The peak-gram

The Hough transform requires a digitized spectrum as its input, with time-frequency bins categorized in two classes. The ATrHough generates this by setting a threshold  $\rho_{\text{th}}$  on the normalized power spectrum  $\rho_i$  to conduct the bin selection:

$$\rho_{i,k} \approx \frac{2|\tilde{x}_i[f_k]|^2}{T_{\text{SFT}}S_n[f_k]}, \quad (5.14)$$

where  $[\cdot]$  indicates a discrete series and the index  $i$  corresponds to the  $i^{\text{th}}$  time step. That is,  $\tilde{x}_i[f_k]$  is the value obtained from the  $i^{\text{th}}$  SFT on the  $k^{\text{th}}$  frequency bin. Furthermore,  $S_n$  is the single-sided Power Spectral Density (PSD) of the noise in the same bin. In the following, we drop the explicit  $k$  index, as we are only interested in the frequency bins following the signal track. If  $\rho_i \geq \rho_{\text{th}}$ , then a value of 1 is assigned to that bin, and a 0 otherwise. The result of this process is known as the peak-gram.

### 5.3.3 Resolution in $\tau$ and $n$ space

The Hough transform is applied to find the statistical significance of each template in a bank over parameter space. A template is defined by the intrinsic parameters of the signal,  $\vec{\xi} = (f_{\text{gw},0}, n, \tau, T_0)$ . To conduct a wide-parameter space search, we create a grid that ensures contiguous templates to deviate from each other by at most one frequency bin over a duration  $T_{\text{obs}}$ ; this ensures the computation of at least all independent templates (by the 1/4-cycle criterion) between  $t = 0$  s and  $t = T_{\text{obs}}$ . The grid is constructed with the following step sizes:

$$\delta n = \left. \frac{\partial n}{\partial f_{\text{gw}}(t)} \right|_{t=T_{\text{obs}}} \delta f, \quad (5.15a)$$

$$\delta \tau = \left. \frac{\partial \tau}{\partial f_{\text{gw}}(t)} \right|_{t=T_{\text{obs}}} \delta f, \quad (5.15b)$$

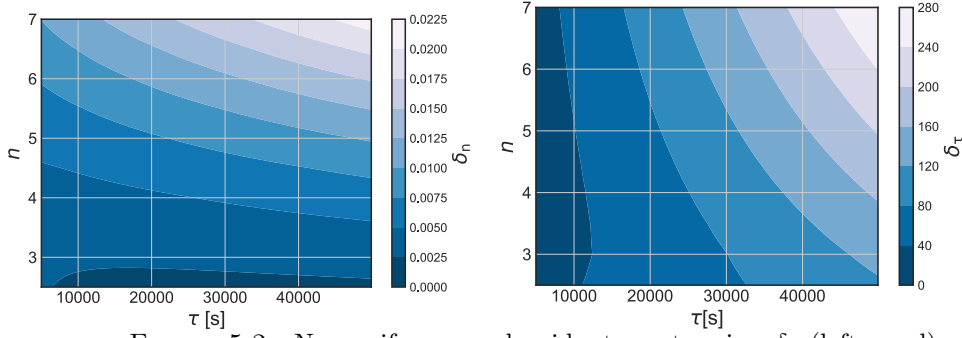


FIGURE 5.2: Non-uniform search grid setup: step sizes  $\delta n$  (left panel) and  $\delta\tau$  (right panel) in the braking index and spin-down timescale obtained by setting  $T_{\text{obs}} = 86400$  s,  $T_{\text{coh}} = 1$  s, fixed  $f_{\text{gw},0} = 2000$  Hz (corresponding to the maximum of the search range), and as a function of  $\tau \in [1000, 9640]$  s and  $n \in [2.5, 7]$ . In practice, while we will follow Eq. (5.16b) to select  $\delta\tau$  at each step (finer grid at smaller  $\tau$ ), we will always select the minimum value of  $\delta n$  (finest grid) in a given parameter range.

where  $\delta f = 1/T_{\text{coh}}$ . Hence,

$$\delta n = \frac{(n-1)^2 \left(\frac{T_{\text{obs}}}{\tau} + 1\right)^{-\frac{1}{1-n}}}{f_{\text{gw},0} T_{\text{coh}} \log\left(\frac{T_{\text{obs}}}{\tau} + 1\right)}, \quad (5.16a)$$

$$\delta\tau = \frac{(n-1)\tau(\tau + T_{\text{obs}}) \left(\frac{T_{\text{obs}}}{\tau} + 1\right)^{-\frac{1}{1-n}}}{f_{\text{gw},0} T_{\text{coh}} T_{\text{obs}}}. \quad (5.16b)$$

The two grid step sizes are inversely proportional to  $f_{\text{gw},0}$ . Fig. 5.2 represents the obtained  $\delta\tau$  and  $\delta n$  for a fixed  $T_{\text{coh}}$ ,  $T_{\text{obs}}$  and  $f_{\text{gw},0}$  inside the  $\tau$ ,  $n$  ranges.

The practical implementation of the grid is defined by a nested loop; a pipeline diagram can be seen in Fig. 5.3. First, we select the minimum value of  $\delta n$  over the  $\tau$  range as shown in Fig. 5.4, given a set of  $(T_{\text{obs}}, T_{\text{coh}}, n)$  and the maximum  $f_{\text{gw},0}$ ; then we calculate  $\delta\tau$  as in Fig. 5.5. We will recalculate  $\delta n$  and  $\delta\tau$  on each iteration of the  $n$  and  $\tau$  loops respectively.

In order to reduce the number of templates or grid points required by the search, we need to split the  $\tau$  and  $f_{\text{gw},0}$  ranges of the whole search space into smaller subdomains. To do so, we will typically create bands for  $\tau$  smaller than 10% of  $T_{\text{obs}}$  and frequency bands between 50 and 100 Hz in width. Each sub-domain will be analyzed independently, making the computational load smaller. It is possible to make the domains larger, but the necessary refinement of the grid in certain areas will make the search less computationally efficient overall.

Fig. 5.6 shows the distribution and number of templates used for different  $T_{\text{obs}}$  given a search that covers an analogous parameter space as Abbott, 2018c. Here templates are calculated with the maximum integer coherence length allowed, and the minimum  $T_{\text{coh}}$  considered for this figure and the search is 1 s.



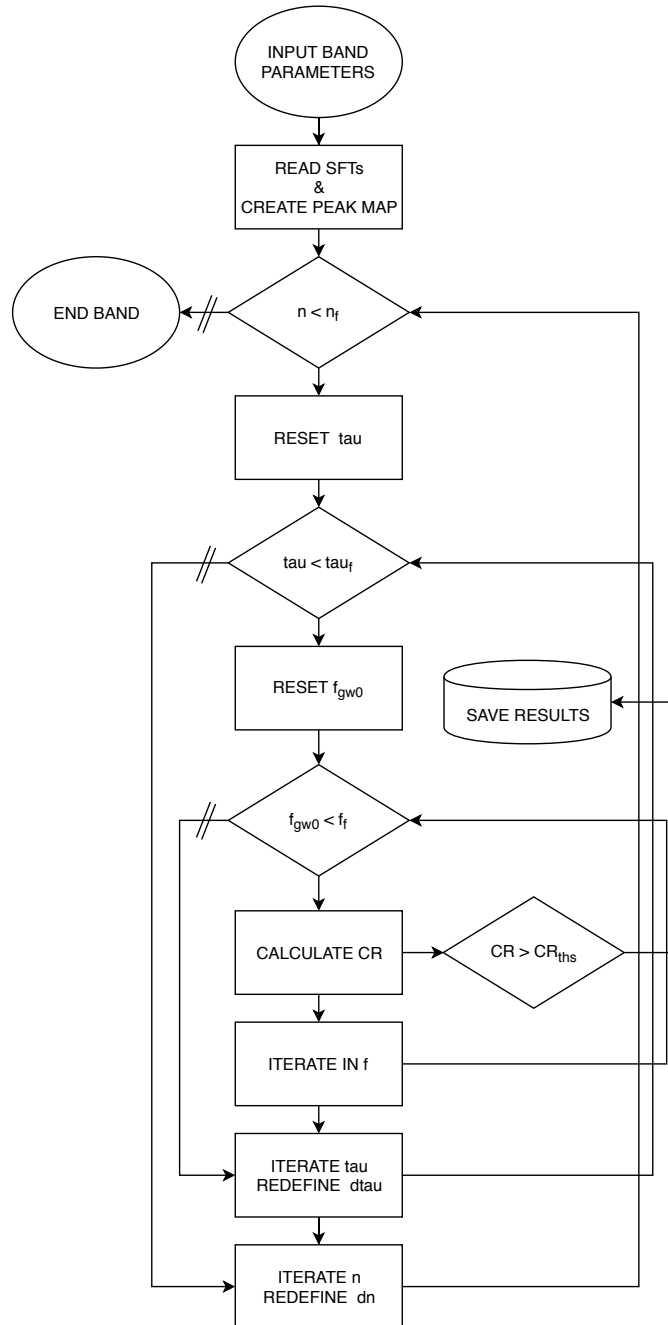


FIGURE 5.3: A diagram of the ATrHough work flow inside a single search band. Arrows indicate the stream direction, squares correspond to input/output calculations and diamonds to if-statements with double lines indicating a 'false' outcome. The entire pipeline includes multiple calls to calculate all bands inside the parameter-space domain.

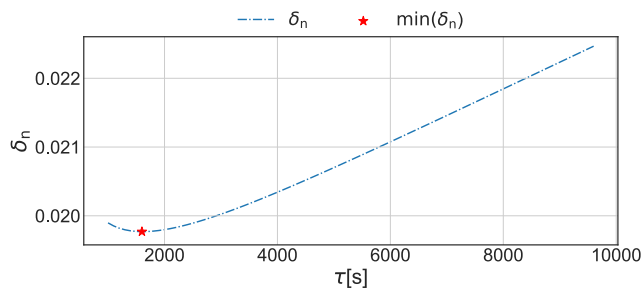


FIGURE 5.4: Example of the grid step size  $\delta n$  as a function of  $\tau \in [1000, 9640]$  s, obtained by setting  $n = 5$ ,  $T_{\text{obs}} = 86400$  s,  $T_{\text{coh}} = 1$  s, and for a frequency range with maximum  $f_{\text{gw},0} = 550$  Hz. The red star corresponds to  $\delta n_{\text{min}}$ , which in the practical search implementation we pick as a fixed value for this parameter range.

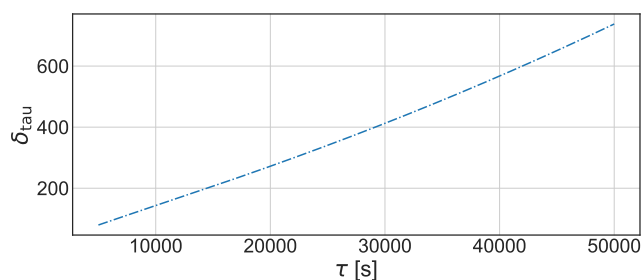


FIGURE 5.5: Example of the grid step size  $\delta n$  as a function of  $\tau \in [1000, 9640]$  s, obtained by setting  $n = 5$ ,  $T_{\text{obs}} = 86400$  s,  $T_{\text{coh}} = 1$  s, and for a frequency range with maximum  $f_{\text{gw},0} = 550$  Hz.

## 5.4 STATISTICAL PROPERTIES

### 5.4.1 The coherent statistic

For the following section we make the assumption of stationary Gaussian noise with zero mean in order to characterize the output of the detectors, for which the normalized power  $2\rho_i$  in the presence of a signal  $h$  follows a non-central  $\chi^2$  distribution with 2 degrees of freedom and a non-centrality parameter

$$\lambda_i = \frac{4|\tilde{h}_i[f_k]|^2}{T_{\text{SFT}}S_n[f_k]}, \quad (5.17)$$

where  $|\tilde{h}_i[f_k]|$  is the Fourier transform of the signal and, as before in Eq. (5.14) for the normalized power  $\rho_i$ , for  $\lambda_i$  we suppress the  $k$  dependence. Then the probability distribution for  $\rho_i$  is:

$$p(\rho_i|\lambda_i) = 2\chi^2(2\rho_i|2, \lambda_i) = \exp(-\rho_i - \frac{\lambda_i}{2})I_0(\sqrt{2\lambda_i\rho_i}), \quad (5.18)$$

where  $I_0$  is the zero-order modified Bessel function of the first kind.

The mean and variance for this distribution are respectively:

$$\mathbf{E}[\rho_i] = 1 + \frac{\lambda_i}{2}, \quad (5.19a)$$

$$\sigma^2[\rho_i] = 1 + \lambda_i. \quad (5.19b)$$

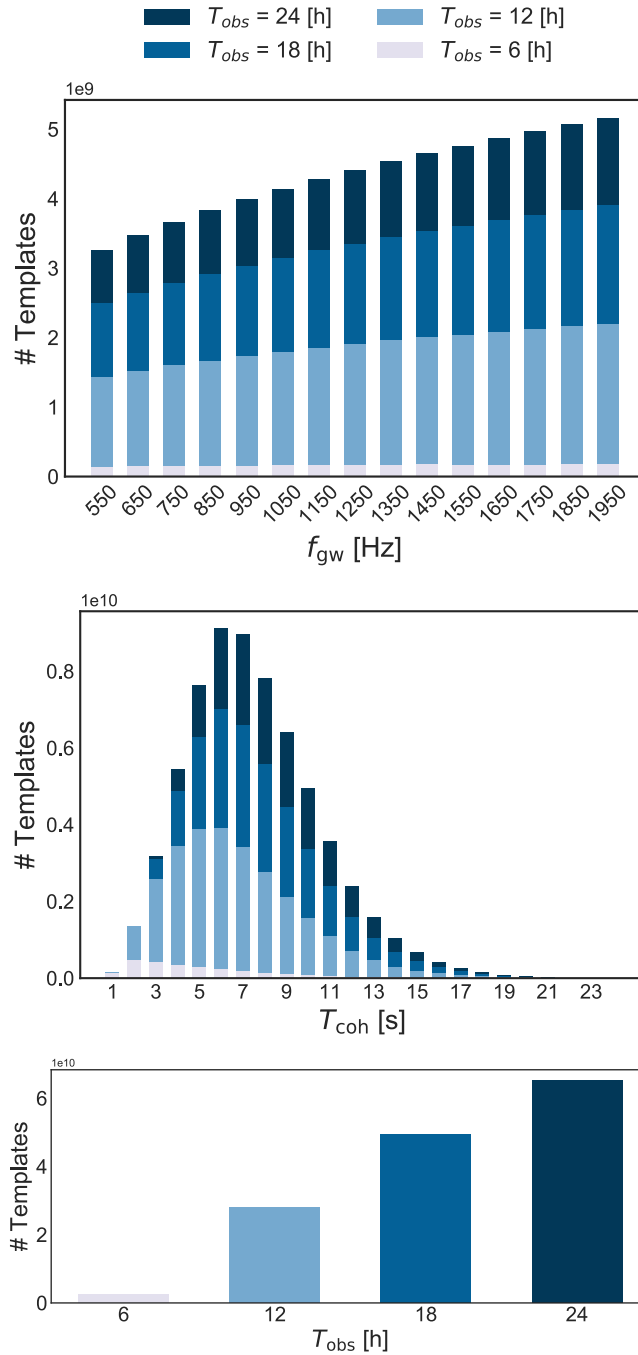


FIGURE 5.6: The number of templates required for searches with four different  $T_{\text{obs}}$ . The total parameter-space covered is  $n \in [2.5, 7]$ ,  $f_{\text{gw},0} \in [500, 2000]$  Hz,  $\tau \in [10^3, 10^5]$  s and is evaluated in independently-processed subdomains, each corresponding to a  $\tau$  band of 100s and a 100 Hz wide frequency band. In this figure, all panels show counts of templates after combining the  $\tau$  bands. The top panel shows the number of templates for each frequency band when using the optimal  $T_{\text{coh}}$  for each  $T_{\text{obs}}$ : it increases with  $f_{\text{gw},0}$  for each  $T_{\text{obs}}$ , and longer  $T_{\text{obs}}$  require more templates at each frequency. The middle panel shows the total number of templates (summed over all frequency bands), for each  $T_{\text{obs}}$ , as a function of  $T_{\text{coh}}$ . The lower panel shows the total number of templates when again using the optimal  $T_{\text{coh}}$  for each  $T_{\text{obs}}$ .

The false alarm and false dismissal probabilities for a frequency bin to be above the power spectrum threshold are:

$$\alpha(\rho_{\text{th}}) = \int_{\rho_{\text{th}}}^{\infty} p(\rho|0)d\rho = \exp(-\rho_{\text{th}}), \quad (5.20a)$$

$$\beta_i(\rho_{\text{th}}) = \int_0^{\rho_{\text{th}}} p(\rho|\lambda_i)d\rho = 1 - \eta_i(\rho_{\text{th}}|\lambda_i). \quad (5.20b)$$

The probability  $\eta_i$  that a given frequency bin is selected is, in the small-signal approximation:

$$\eta_i(\rho_{\text{th}}|\lambda_i) = \int_{\rho_{\text{th}}}^{\infty} p(\rho|\lambda)d\rho = \alpha\left(1 + \frac{\rho_{\text{th}}}{2}\lambda_i + O(\lambda_i^2)\right). \quad (5.21)$$

### 5.4.2 The incoherent number-count statistic

If a signal is present, the non-centrality parameter  $\lambda_i$  will change for different SFTs. As pointed out previously, this can happen both because the noise may not be stationary and because the amplitude modulation of the signal changes over time. In other words, the observed signal power  $|h|^2$  changes due to the non-uniform antenna pattern of the detector and due to the intrinsic spindown. Therefore, the detection probability  $\eta_i$  changes across SFTs. This is taken into account by adapting the non-demodulated weighted Hough approach mentioned before and covered in Sintès and Krishnan, 2007; it is a similar strategy to the one applied in the StackSlide (Krishnan et al., 2004; Brady and Creighton, 2000) and PowerFlux (Dergachev, 2005; Dergachev and Riles, 2005) algorithms. The starting point is to generalize the integer number-count statistic, which we would obtain directly from the peak-map, to a non-integer weighted statistic

$$\nu = \sum_{i=1}^N w_i \nu_i, \quad (5.22)$$

where  $N$  is the number of SFTs,  $\nu_i$  is the value assigned to the bin selected from the peak-gram in the  $i^{\text{th}}$  time step for the current template, and  $w_i$  are a constant set of weights given for each template with  $w_i \propto 1/N$ . It is important to notice that in order to maximize the sensitivity of the search the selection of weights is not arbitrary; we will derive the optimal choice in Sec. 5.4.4. For now, we define the normalization terms

$$A = \sum_{i=1}^N w_i, \quad (5.23a)$$

$$\|w\|^2 = \sum_{i=1}^N w_i^2, \quad (5.23b)$$

This step in the search (computing  $\nu$ ) is known as the incoherent sum; the templates in a search are then ranked based on their number count  $\nu$ . Applying the linearity of the expectation value, the mean and variance for the incoherent step in the absence of a signal are:

$$\langle \nu \rangle = A \alpha, \quad (5.24a)$$

$$\sigma^2 = \langle \nu^2 \rangle - \langle \nu \rangle^2 = \|w\|^2 \alpha (1 - \alpha). \quad (5.24b)$$

As shown in Sintès and Krishnan, 2007 and applied in multiple CW searches like Astone et al., 2014, when optimal weights are chosen we can, for a sufficient number of SFTs, evaluate the significance of an observation by approximating the number count distribution by a Gaussian with the right mean and variance:

$$p(\nu|\rho_{\text{th}}, \lambda) = \frac{1}{\sqrt{2\pi\sigma^2}} e^{-(\nu - A\alpha)^2/2\sigma^2}. \quad (5.25)$$

This becomes a very good approximation for  $N > 1000$ , and e.g. the typical number of SFTs searched in Abbott, 2018c is indeed above that number. We provide some empirical tests of this approximation in appendix 5.A.

Thus one can derive the number count threshold  $\nu_{\text{th}}$  based on the incoherent false-alarm rate as

$$\alpha_{\text{I}} = \int_{\nu_{\text{th}}}^{\infty} p(\nu|\rho_{\text{th}}, 0) d\nu = \frac{1}{2} \operatorname{erfc}\left(\frac{\nu_{\text{th}} - \langle \nu \rangle}{\sqrt{2}\sigma}\right). \quad (5.26)$$

For a given set of weights and peak selection threshold, this equation decides what number count threshold must be used to obtain a desired  $\alpha_{\text{I}}$ . We can solve this as

$$\nu_{\text{th}} = A\alpha + \sqrt{2\|w\|^2\alpha(1-\alpha)} \operatorname{erfc}^{-1}(2\alpha_{\text{I}}). \quad (5.27)$$

The false-dismissal rate requires the computation of the mean and variance, which in the presence of a small signal are:

$$\langle \eta \rangle = \sum_{i=1}^N w_i \eta_i \sim A\alpha + \frac{\alpha\rho_{\text{th}}}{2} \sum_{i=1}^N w_i \lambda_i, \quad (5.28a)$$

$$\sigma_{\text{I}}^2 = \sum_{i=1}^N w_i^2 \eta_i (1 - \eta_i). \quad (5.28b)$$

If the small-signal approximation is applied,  $\sigma_{\text{I}}^2$  can be expanded to first order in  $\lambda_i$ :

$$\sigma_{\text{I}}^2 = \|w\|^2 \alpha (1 - \alpha) \left(1 + \frac{\rho_{\text{th}}}{2\|w\|^2} \frac{1 - 2\alpha}{1 - \alpha} \sum_{i=1}^N w_i^2 \lambda_i\right). \quad (5.29)$$

We again approximate the number count distribution  $p(\eta|h)$  by a Gaussian distribution with the above mean and variance, yielding the false-dismissal rate as follows:

$$\beta_{\text{I}} \approx \int_{-\infty}^{\nu_{\text{th}}} p(\eta|h) d\eta = \frac{1}{2} \operatorname{erfc}\left(\frac{\langle \eta \rangle - \nu_{\text{th}}}{\sqrt{2}\sigma_{\text{I}}}\right). \quad (5.30)$$

### 5.4.3 Setting up the threshold

Considering the statistical significance in a template as  $s := 1 - \alpha_{\text{I}} - \beta_{\text{I}}$  and using the properties of the complementary error function, we can introduce a quantity

$$S = \operatorname{erfc}^{-1}(2\alpha_{\text{I}}) + \operatorname{erfc}^{-1}(2\beta_{\text{I}}). \quad (5.31)$$

This equation can be shown to reduce to  $s$  when  $S = 0$ , and as it grows monotonically we can take it as a measure of the statistical significance of the search. By expanding

to the first order in  $\lambda_i$ , we derive the following expression:

$$S = \sqrt{\frac{\alpha \rho_{\text{th}}^2}{8(1-\alpha)} \frac{\sum_{i=1}^N w_i \lambda_i}{\|w\|}} + \frac{\rho_{\text{th}}}{4} \frac{1-2\alpha}{1-\alpha} \frac{\sum_{i=1}^N w_i \lambda_i}{\|w\|^2} \text{erfc}^{-1}(2\alpha). \quad (5.32)$$

Imposing again optimal weights which are proportional to  $1/N$ , for large values of  $N$  the first term on the right-hand side of this equation is proportional to  $\sqrt{N}$ , while the second term does not grow with  $N$ . Thus the first term dominates, yielding

$$S \sim \sqrt{\frac{\alpha \rho_{\text{th}}^2}{8(1-\alpha)} \frac{\sum_{i=1}^N w_i \lambda_i}{\|w\|}}. \quad (5.33)$$

The peak selection threshold is chosen to minimize  $\beta_{\text{I}}$ , or equivalently maximize  $S$  for fixed  $\alpha_{\text{I}}$ :

$$\frac{d}{d\rho_{\text{th}}} \sqrt{\frac{\alpha \rho_{\text{th}}^2}{8(1-\alpha)}} = 0. \quad (5.34)$$

As derived in Krishnan et al., 2004, this threshold is independent of the choice of weights; and the solution of the previous equation is  $\rho_{\text{th}} = 1.6$  which leads to  $\alpha = e^{-\rho_{\text{th}}} = 0.2$ . Different thresholds can be imposed, yielding different  $\alpha$ , but they would not maximize the statistical significance of the template.

#### 5.4.4 Calibration of the weights

To define an appropriate set of weights, we start by considering the modulus square of the signal's Fourier transform on the  $i^{\text{th}}$  SFT, depending on the antenna patterns  $F_{+, \times}$  from Eq. (5.3) and amplitudes  $A_{+, \times}$  from Eq. (5.5):

$$|\tilde{h}_i[f_k]|^2 = \frac{A_{+,i}^2 F_{+,i}^2 + A_{\times,i}^2 F_{\times,i}^2}{4} \frac{\sin^2[\pi(f_{\text{gw},i} - f_k)T_{\text{coh}}]}{\pi(f_{\text{gw},i} - f_k)}. \quad (5.35)$$

From here on, the subindex  $i$  runs over segments and in the case of a function it imposes a time average of length  $T_{\text{coh}}$ , e.g. for the time-evolving gw frequency from Eq. (5.11):  $f_{\text{gw},i} = \int_{T_i - T_{\text{coh}}/2}^{T_i + T_{\text{coh}}/2} f_{\text{gw}}(t) dt / T_{\text{coh}}$ . The subindex  $k$  corresponds to the  $k^{\text{th}}$  frequency bin, selected so that  $f_{\text{gw},i} \in (f_k - \delta f/2, f_k + \delta f/2)$ . The average over that interval is

$$\int_{-\frac{1}{2}}^{\frac{1}{2}} \frac{\sin^2[\pi x]}{(\pi x)^2} = 0.7737. \quad (5.36)$$

Now we can average over the NS[']s orientation  $\cos \iota$  and the polarization angle  $\psi$  appearing in the antenna patterns and find the following relationships:

$$\langle (F_{+,i})^2 \rangle_{\iota, \Phi} = \langle (F_{\times,i})^2 \rangle_{\iota, \psi} = \frac{a_i^2 + b_i^2}{2}, \quad (5.37a)$$

$$\langle (A_{+,i})^2 + (A_{\times,i})^2 \rangle_{\iota, \psi} \sim \frac{4h_{0,0}^2}{5} \left( \frac{f_{\text{gw},i}}{f_{\text{gw},0}} \right)^{2m}, \quad (5.37b)$$

where  $h_{0,0} = h_0(t = t_0)$  is the initial amplitude at  $t_0$ .

Combining all these results:

$$\langle \lambda_i \rangle_{i,\psi} = 0.7737 \frac{2h_{0,0}^2 T_{\text{coh}} (a_i^2 + b_i^2)}{5S_{n,i}} \left( \frac{f_{\text{gw},i}}{f_{\text{gw},0}} \right)^{2m}, \quad (5.38)$$

and substituting this into Eq. (5.33), the sensitivity is

$$S = \sqrt{\frac{\alpha \rho_{\text{th}}^2}{8(1-\alpha)}} \frac{2h_{0,0}^2 T_{\text{coh}}}{5\|\mathbf{w}\|} \sum_{i=1}^N w_i \frac{(a_i^2 + b_i^2)}{S_{n,i}} \left( \frac{f_{\text{gw},i}}{f_{\text{gw},0}} \right)^{2m}. \quad (5.39)$$

From this, we see that the sensitivity is related to the detector response and the amplitude modulation of the signal, which we can summarize in a quantity

$$X_i := \frac{(a_i^2 + b_i^2)}{S_{n,i}} \left( \frac{f_{\text{gw},i}}{f_{\text{gw},0}} \right)^{2m}. \quad (5.40)$$

Calculating the maximum of the inner product  $\mathbf{w} \cdot \mathbf{X}$  shows that the weights guarantee the best sensitivity for a given template if the two vectors are proportional to each other, i.e.  $w_i \propto X_i$ . At the same time, we see that any overall rescaling of the weights ( $\hat{w}_i = kw_i$ ) has no impact on  $S$ , as for any constant  $k$  the value of the detectable dimensionless strain amplitude  $h_{0,0}$  at  $t = 0$ s remains unchanged.

In summary, as also illustrated for an example simulated signal in Fig. 5.7, the use of appropriate weights ensures our search properly accounts for both the source's amplitude decay and the effects of the detector response changing with time. This gives us the ability to compare templates across the search parameter space, comparing very fast frequency decays with slower ones.

If the value  $\rho_{\text{th}} = 1.6$  is substituted in Eq. (5.39), the minimum theoretical value of  $h_0$  that the search can recover is:

$$h_{0,0} = 3.38 \sqrt{\frac{S^{1/2}}{T_{\text{coh}}}} \left( \frac{\|\mathbf{w}\|}{\mathbf{w} \cdot \mathbf{X}} \right)^{(1/2)}. \quad (5.41)$$

#### 5.4.5 Critical Ratio $\Psi$

The critical ratio  $\Psi$  is a new statistic that quantifies the significance of a given template. Based on the weighted number count and quantities from Eqs. (5.22)–(5.24), we define

$$\begin{aligned} \Psi &= \frac{v - \langle v \rangle}{\sigma_v^2} \\ &= \frac{\sum_{i=1}^N (w_i v_i) - \sum_{i=1}^N (w_i \alpha)}{\sqrt{\sum_{i=1}^N (w_i)^2 \alpha (1 - \alpha)}}. \end{aligned} \quad (5.42)$$

As mentioned before, any normalization of the weights will not change the sensitivity of the search. It will also leave the significance or critical ratio in each template unchanged. Considering the previous equation as the single-detector case, the multi-detector critical ratio is defined as

$$\Psi_M = \frac{\sum_{k=1}^{N_M} (\sum_{i=1}^{N_k} (w_{i;k} v_{i;k}) - \sum_{i=1}^{N_k} (w_{i;k} \alpha))}{\sqrt{\sum_{k=1}^{N_M} \sum_{i=1}^{N_k} (w_{i;k})^2 \alpha (1 - \alpha)}}, \quad (5.43)$$

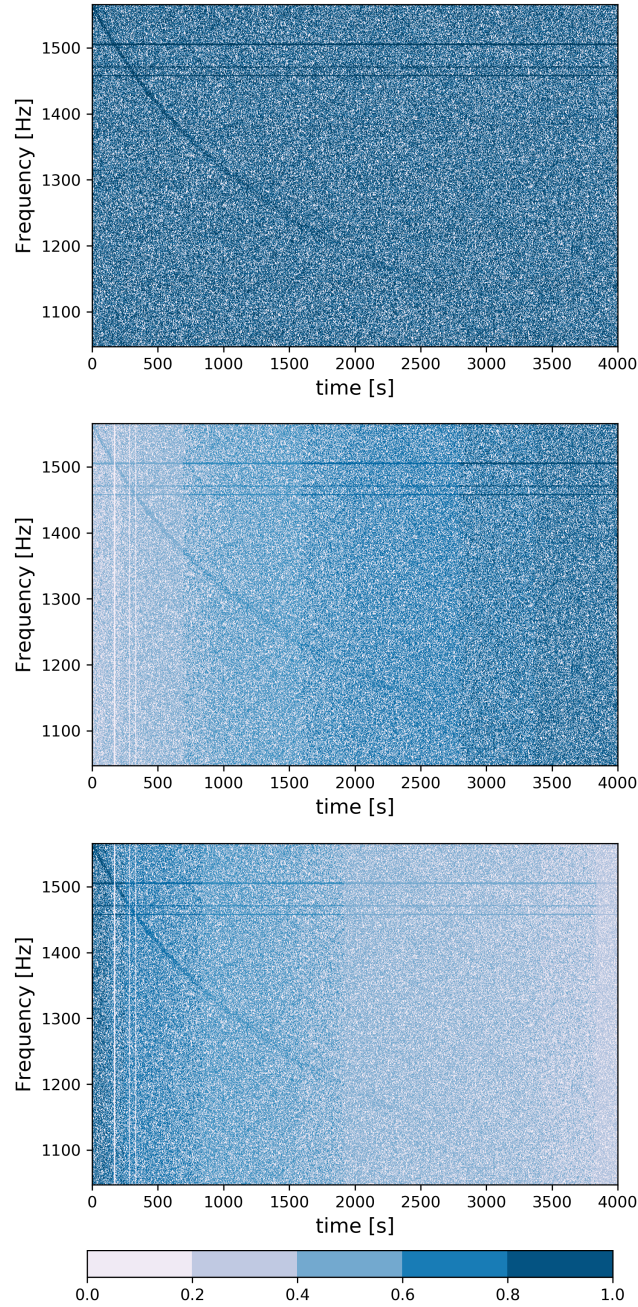


FIGURE 5.7: Peak-maps for an example simulated signal at 0.1 Mpc using  $T_{\text{coh}} = 1$  s in the actual aLIGO data after GW170817 with NS parameters  $f_{gw,i} = 1565.8$  Hz,  $\tau = 1000$  s,  $n = 5$ ,  $I_{zz} = 4.34 \times 10^{38}$  kg m<sup>2</sup> and  $\cos \iota = 1$ . The top panel does not use weights, the middle panel uses weights as in Sintes and Krishnan, 2007 which do not include the source amplitude modulation, and the bottom panel corresponds to the new weights derived in Sec. 5.4.4. The color scale is  $w_i v_i$ , normalized to be comparable between panels. In all cases, the signal disappears below the noise floor at around 2000 s, as expected from the injection parameters and the detector noise curve. In the first two panels we see that noise contributions from the later part of the observing window will decrease significance with time. However in the bottom panel, these are weighted down, increasing the significance of the recovered track.



where  $N_M$  is the number of detectors and  $N_k$  is the number of SFTs in detector  $k$ , while  $w_{i;k}$  and  $v_{i;k}$  are the weights and number count assigned to the  $i^{\text{th}}$  SFT for that detector and a given template. We can also rewrite this as

$$\Psi_M = \frac{\sum_{k=1}^{N_M} \Psi_k \sqrt{\sum_{i=1}^{N_k} (w_{i;k})^2}}{\sqrt{\sum_{k=1}^{N_M} \sum_{i=1}^{N_k} (w_{i;k})^2}}, \quad (5.44)$$

where  $\Psi_k$  is the critical ratio for each single detector  $k$ .

In a multi-detector search, the duty factors (fraction of time a detector is recording usable data) and noise floors may differ between detectors. To quantify the contribution of each detector to the multi-detector critical ratio, the relative contribution ratio is defined as

$$r_j = \sqrt{\frac{\sum_{i=1}^{v_j} (w_{i;j})^2}{\sum_{k=1}^{N_M} \sum_{i=1}^{v_k} (w_{i;j})^2}}. \quad (5.45)$$

Using the previous equations, the critical ratio for a multi-detector search takes a very simple form:

$$\Psi_M = \sum_{k=1}^{N_M} \Psi_k r_k. \quad (5.46)$$

## 5.5 Vetoes on Critical ratio and Time Consistency

Candidates that appear significant by their critical ratio can be due to astrophysical sources, but also due to non-Gaussian noise artifacts in the data. To make the search robust against such artifacts, we introduce vetoes that test for each candidate (i) its consistency between detectors and (ii) the consistency of its transient behavior with the target astrophysical model.

### 5.5.1 The Critical ratio $\Psi$ -veto

The threshold for a search is determined under the assumption of detector noise following a stationary zero-mean Gaussian distribution with a power spectral density  $S_n(f)$ . A template is considered as a candidate when its  $\Psi$  exceeds a pre-specified threshold for which the probability of a false alarm due to noise alone is small. (See Fig. 5.8.) The overall false-alarm probability  $\alpha_S$  of the search can be approximated as the product of the number of trials (i.e number of templates  $N_t$ ) and the previously introduced false-alarm probability  $\alpha_I$ . Now we can rewrite Eq. (5.26) in terms of the critical-ratio threshold  $\Psi_{\text{th}}$ :

$$\Psi_{\text{th}} = \sqrt{2} \operatorname{erfc}^{-1} \left( 2 \frac{\alpha_S}{N_t} \right), \quad (5.47)$$

If the critical ratio in a template exceeds the threshold, as a follow-up veto we can rephrase the question and consider each detector as an independent single trial, obtaining a threshold  $\Psi_{\text{th}}^D$  for each detector. This threshold will correspond to Eq. (5.47) with  $N_t = 1$  and any given template that fails to satisfy it in either detector will be vetoed.

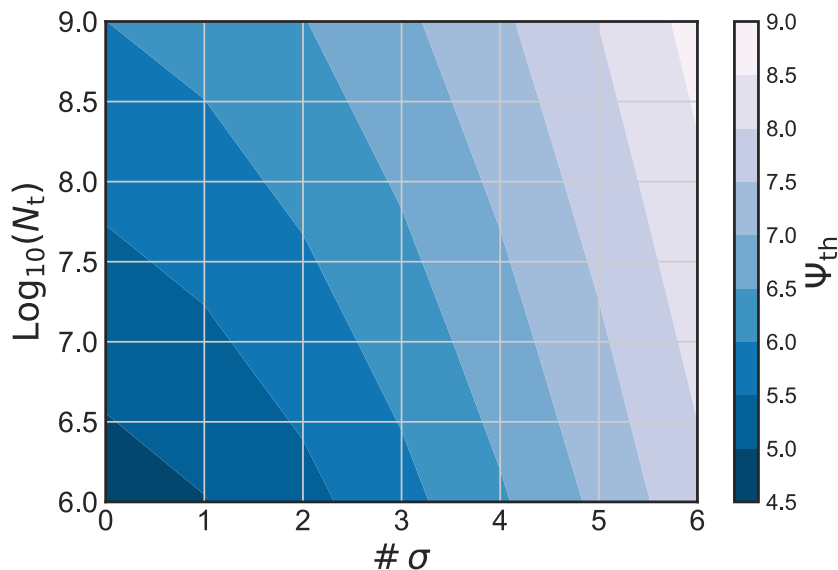


FIGURE 5.8: This contour plot shows how to choose a threshold  $\Psi_{\text{th}}$  for different false-alarm configurations. The vertical axis gives the number of templates used in a search and the horizontal axis shows the desired significance of candidates above threshold in terms of a ‘number of sigmas’ for a Gaussian distribution. The color scale gives the required  $\Psi_{\text{th}}$  for candidates to reach the desired significance when including the trials factor from the large template bank.

### 5.5.2 The time-inconsistency veto

To check that the transient behavior of the signal matches our model, we introduce an additional veto. Let us consider a candidate template  $\vec{\zeta}_C = (f_{\text{gw},0}, n, \tau, T_0 = T_{\text{event}})$  and a time-shifted version  $\vec{\zeta}_F = (f_{\text{gw},0}, n, \tau, T_0 = T_{\text{event}} + T_F)$ . These will be completely independent if  $T_F = -T_{\text{obs}}$ ; see Fig. 5.9 for an example. Other time shifts could be used for a veto as well, as long as the contribution of the candidate signal  $\vec{\zeta}_C$  to  $\Psi_F$  of the shifted template  $\vec{\zeta}_F$  is zero.

The obtained value  $\Psi_F$  will indicate how much of the original candidate’s  $\Psi_C$  seems to come from a stationary contribution instead. Stationary spectral line artifacts are common in the LIGO data (Covas, 2018) and hence this veto is important to remove non-astrophysical false candidates. In other words, we assign a probability to stationary lines to be the cause of the candidate. To estimate this probability we reuse Eq. (5.47) for a single follow-up trial. If the resulting probability corresponds to more than 6 sigmas, we can safely reject the candidate.

## 5.6 Search sensitivity

In Eq. (5.41) we have obtained an estimate for the sensitivity of a search as the smallest amplitude that would cross the number-count threshold for a given false-alarm rate  $\alpha_I$  and false-dismissal rate  $\beta_I$ .

As a specific astrophysical case, let us concentrate on the isolated non-axisymmetric magnetar scenario as considered in the GW170817 long-duration postmerger search

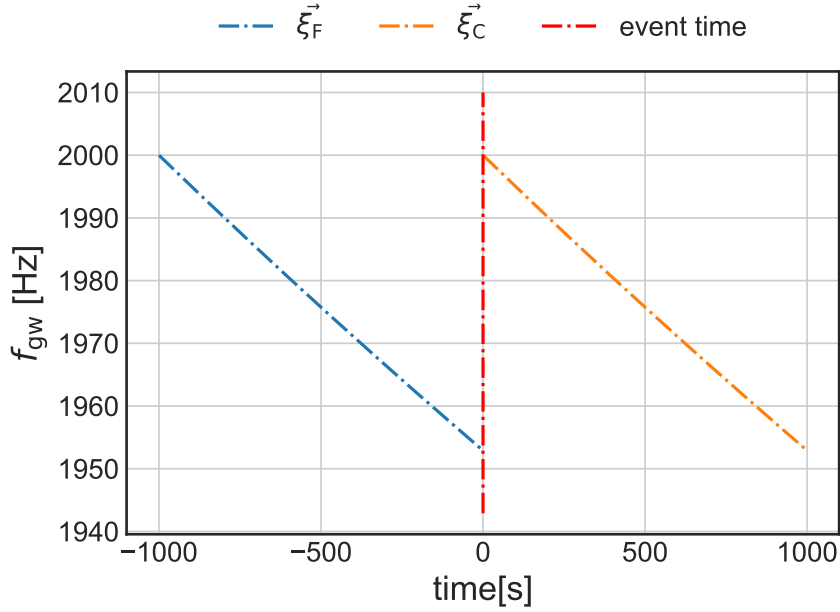


FIGURE 5.9: For the time-inconsistency veto, we consider time-shifted frequency tracks. The plot shows the frequency track in time domain for a candidate template  $\vec{\xi}_C = (f_{\text{gw},0} = 500 \text{ Hz}, n = 5, \tau = 10^4 \text{ s}, T_0 = 0 \text{ s})$  and a shifted template  $\vec{\xi}_F = (f_{\text{gw},0} = 500 \text{ Hz}, n = 5, \tau = 10^4 \text{ s}, T_0 = -T_{\text{obs}})$ , showing that there is no overlap between the two tracks. Hence, the significance  $\Psi_F$  of the shifted track can be used for a veto.

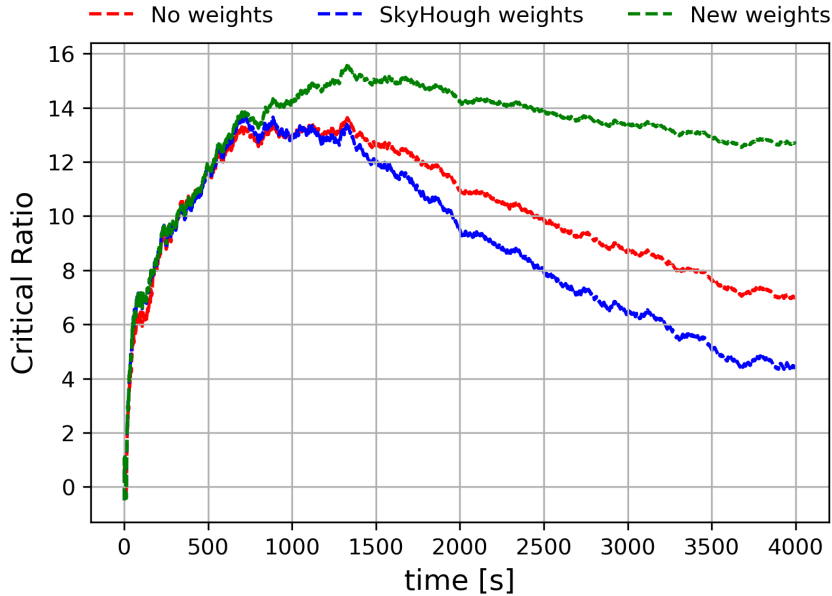


FIGURE 5.10: Critical ratio as a function of time using  $T_{\text{coh}} = 1 \text{ s}$  and different weights, for an injection at 0.1 Mpc in the actual aLIGO data after GW170817 with NS parameters  $f_{\text{gw},i} = 1565.8 \text{ Hz}$ ,  $\tau = 1000 \text{ s}$ ,  $n = 5$ ,  $I_{\text{zz}} = 4.34 \times 10^{38} \text{ kg m}^2$  and  $\cos \iota = 1$  (same as in Fig. 5.7). The ‘SkyHough weights’ correspond to the scheme from (Sintes and Krishnan, 2007), whereas the ‘new weights’ include source amplitude decay.

(Abbott, 2018c). In this model, the amplitude exponent  $m$  in Eq. (5.8) takes a nominal value of 2 and the signal amplitude  $h_0(t)$  is given by Eq. (5.6).<sup>1</sup>

In Fig. 5.10 we show an example signal recovery for the same injection as in Fig. 5.7. As we can see, power-law templates in principle allow to successfully track this type of signal even without weights, but including the source’s amplitude decay in the weights from Sec. 5.4.4 is crucial for robust recovery and to fully profit from long observation times.

Combining the amplitude from Eq. (5.6) with the sensitivity as given by Eq. (5.41), the astrophysical range of the search is

$$d = \frac{4\pi^2 G I_{zz} \epsilon f_{\text{gw},0}^2}{c^4} \frac{\sqrt{T_{\text{coh}}}}{3.38 S^{1/2}} \left( \frac{\mathbf{w} \cdot \mathbf{X}}{\|\mathbf{w}\|} \right)^{(1/2)}. \quad (5.48)$$

We now calculate an astrophysical range estimate for a search setup corresponding to the ATrHough analysis performed as one of four searches in Abbott, 2018c. We use the aLIGO O2 sensitivity  $S_n$  during the GW170817 event to calculate the weights, and for the remnant’s moment of inertia we use the same value as in Abbott, 2018c,  $I_{zz} = 100 M_{\odot}^3 G^2 / c^4 \approx 4.34 \times 10^{38} \text{ kg m}^2$ .

In Fig. 5.11 we compare the analytical estimate with the empirical recovery fraction for a set of injections. Those were originally performed for the sensitivity estimate in the GW170817 post-merger search (Abbott, 2018c). The recovery criterion corresponds to  $\Psi_{\text{th}} = 9$ , or a  $5\sigma$  significance. We have concentrated here on a braking index  $n = 5$  that corresponds to pure  $\text{gw}_{\text{emission}}$ , and covered ranges of  $f_{\text{gw},0}$  and  $\tau$  as shown in Fig. 5.12. The procedure to obtain the experimental results consisted in selecting 10 Hz wide frequency bands, for each band injecting 1000 simulated signals into O2 data with amplitudes around the astrophysical range estimate. The purpose was to find the amplitude corresponding to 90% recovery efficiency. The parameters  $\tau$  and  $f_{\text{gw},0}$  were randomized within 10 bins of their nominal value; i.e. the injection parameters are not perfectly aligned with the search grid, thus allowing for a realistic exploration of search mismatch in the recovery.

We do not expect an exact agreement between analytical prediction and sensitivity measured from injections, as the analytical estimate is based on a Gaussian noise approximation. But the results are sufficiently close to demonstrate that Eq. (5.41) is useful for the purpose of setting up future searches.

## 5.7 CONCLUSIONS

In this work we have described a new semi-coherent search method for quasi-monochromatic gravitational waves, using short incoherent steps of the order of seconds with the intention to track signals of intermediate durations (of the order of hours to days) even if these show rapid frequency evolution. The main innovations compared to previous versions of the Hough transform method (Sintes and Krishnan, 2007; Sintes and Krishnan, 2006; Krishnan et al., 2004) are the new frequency-evolution templates and the additional inclusion of amplitude evolution in the Hough weights.

In introducing this new method and estimating its sensitivity, we have concentrated on the model of power-law spin-down for a newborn  $\text{ns}$ . As applied in the GW170817 post-merger remnant search (Abbott, 2018c), the astrophysical range of this method at 90% detection confidence is at  $\sim 1$  Mpc with LIGO sensitivity at the

<sup>1</sup>In the case of  $\text{gw}[s]$  emitted from r-mode oscillations, we have instead  $n \lesssim 7$ ,  $m = 3$  and  $h_0(t)$  is given by Eq. (5.7). This case is described in more detail e.g. in Owen et al., 1998.

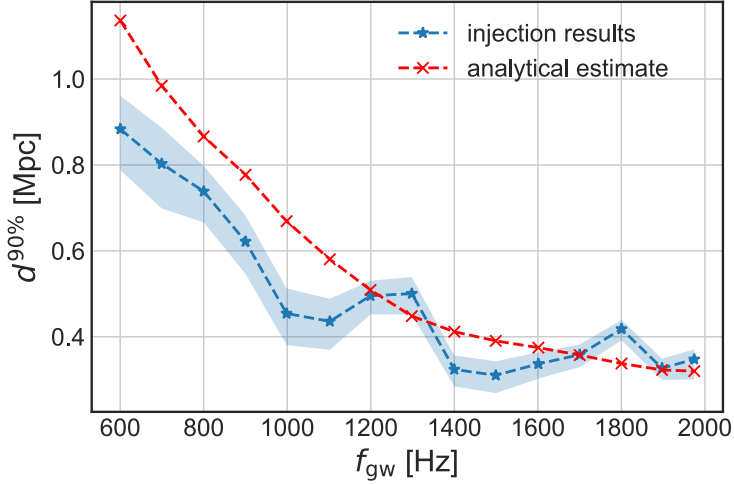


FIGURE 5.11: A comparison of analytically and empirically obtained sensitivity estimates for a GW170817 post-merger analysis with the ATrHough method. The analytic sensitivity estimate was done for aLIGO sensitivity  $S_n$  during the GW170817 event (end of O2) and for  $T_{\text{coh}} = 8$  s. The empirical results correspond to the sensitive distance at 90% detectability,  $d^{90\%}$ , obtained for the  $T_{\text{coh}} = 8$  s injection set in Abbott, 2018c, using actual aLIGO data after GW170817 and NS parameters of  $I_{zz} = 4.34 \times 10^{38}$  kg m<sup>2</sup> and  $\cos \iota = 1$ , as well as  $f_{\text{gw},0}$ ,  $\tau$  and  $\epsilon$  as given in Fig. 5.12. See the appendix B of Abbott, 2018c for additional results at different  $T_{\text{coh}}$ .

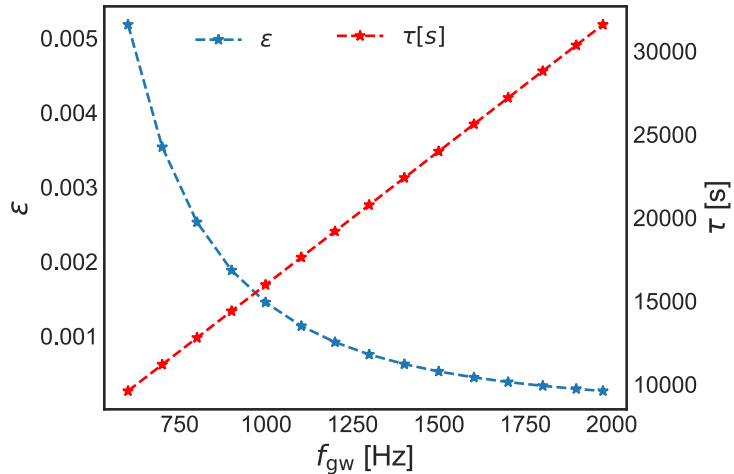


FIGURE 5.12: Parameters for the  $T_{\text{coh}} = 8$  s injection set from Abbott, 2018c, as also used for the comparison with the empirical sensitivity estimate in Fig. 5.11. Each set of values shown corresponds to the central value of an injection subset, with the parameters then further randomized in narrow ranges as described below.

end of the second observing run. With future instruments like the Einstein Telescope (Punturo, 2010; Hild, 2011; Sathyaprakash, 2012), this range could increase by a factor of  $\sim 20$ .

One disadvantage of modeled semi-coherent methods like this one is the need to explicitly set a starting time for the signal model. On the other hand, it is a suitable method to perform fast and economic follow-ups of known merger events or for promising candidates identified by more generic searches, allowing to reliably set up a fixed false-alarm rate of the overall search.

The same strategy can also easily be translated to signals following other spin-down patterns than the power-law model we focused on so far, with the definition of weights and parameter space grids following the same procedure as introduced in this work.

## 5.A Testing the Gaussian approximation for the weighted number count $\nu$

In Eq. (5.25) we have approximated the distribution  $p(\nu|\rho_{\text{th}}, \lambda)$  of the weighted number-count statistic  $\nu$ , when using appropriate weights and for a sufficient number of SFTs, by a Gaussian. Here we present some simple empirical tests of this limiting behaviour in configurations similar to the search implemented in Abbott, 2018c.

Using the same machinery as before, we have analysed 100 simulated data sets, each consisting of 1000 segments of Gaussian noise with no GW injection ( $h_0 = 0$ ). For each, we have computed the number count for 10000 template trials, covering a small fraction of the parameter space around a random point corresponding to the ‘null injection’, and using the weights proportional to  $X_i$  as introduced in Sec. 5.4.4. We have then compared the resulting empirical distribution of  $\nu$  with our Gaussian approximation from Eq. (5.25). An example is shown in Fig. 5.13 to illustrate the agreement between the two distributions.

To further evaluate the (dis-)agreement between two distributions  $P$  and  $Q$ , one can compute the Kullback-Leibler (KL) divergence (Kullback and Leibler, 1951) (in bits):

$$D_{\text{KL}}(P \parallel Q) = \sum_{x \in \mathcal{X}} P(x) \log_2 \left( \frac{P(x)}{Q(x)} \right), \quad (5.49)$$

for a discrete set  $\mathcal{X}$  of measured values. Note the asymmetry in this definition; here we take the Gaussian for  $P$  and the empirical results for  $Q$ . A histogram of KL divergences between the Gaussian from Eq. (5.25) and the empirical distributions from the 1000 simulations is shown in Fig. 5.14. We see that there is far less than 1 bit of information between the two distributions in all draws. Hence, based on the KL divergence we can consider the approximation from Eq. (5.25) as a sufficiently robust basis for estimating significance of our search results.

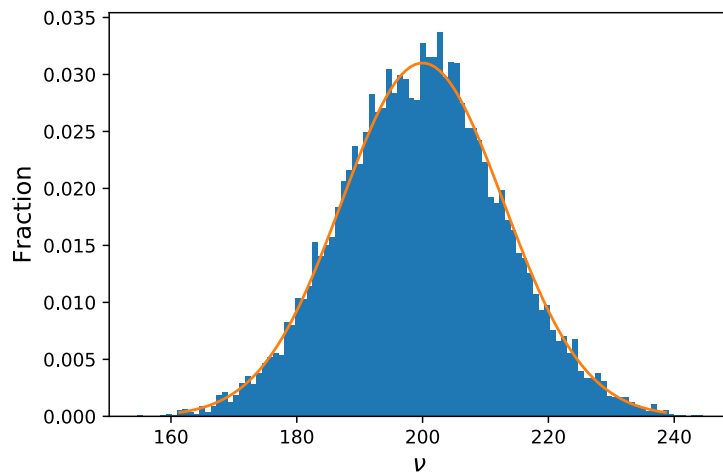


FIGURE 5.13: Example of the close agreement between empirical  $\nu$  results in pure Gaussian noise and the Gaussian approximation from Eq. (5.25). Over 10000 templates, this example yields a KL divergence of  $\approx 3 \times 10^{-5}$ .

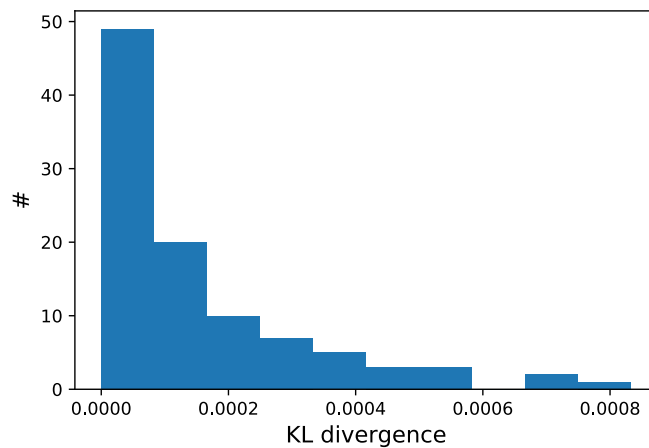


FIGURE 5.14: Histogram of KL divergences for 100 simulations ( $h_0 = 0$ ) on 1000 segments of Gaussian noise each, analysed with 10000 templates.





## Chapter 6

# Matched-filter study and energy budget suggest no detectable gravitational-wave ‘extended emission’ from GW170817

M. OLIVER, D. KEITEL, A. MILLER, H. ESTELLES, A. M. SINTES

Certificate on Appendix C

### 6.1 Introduction

GW170817 (Abbott, 2017c) was the first binary neutron star coalescence observed by the Advanced LIGO (Aasi, 2015a) and Virgo (Acernese, 2015) detectors and the first gravitational-wave (GW) event with multi-messenger counterpart observations (Abbott, 2017d). The merger remnant remained undetermined, and several LIGO-Virgo (LVC) searches (Abbott, 2017e; Abbott, 2018c) have found no evidence of a post-merger signal from the location of GW170817. For various emission mechanisms, it was estimated that a signal would have needed to be unphysically energetic to be detectable with current detector sensitivity and the deployed analysis methods.

Meanwhile, Putten and Della Valle, 2018 (hereafter: vP-DV) have reported a putative detection of GW ‘extended emission’ lasting for several seconds after the merger. No detailed physical model for this emission was provided, but they attribute it to the spin-down of a remnant neutron star (NS) with exponentially decaying rotation frequency. Exploring possible amplitude evolutions, a signal with the reported properties would be very difficult to explain with conventional NS physics. Even under optimistic assumptions and in an ideal single-template matched-filter analysis, much more extreme parameters and an increased energy budget would be required to detect such signals.

In Sec. 6.2 we first summarize the signal candidate reported by vP-DV. While there is no known exact physical model for the vP-DV candidate, we make a first approach in using a conventional NS spindown model to construct a representative GW template waveform, and discuss the corresponding energy budget and physical constraints. We then calculate the optimal signal-to-noise ratio for this template in Sec. 6.3, finding that, even under optimistic assumptions, more energy would be required for detectable signals. To verify these results, in Sec. 6.4 we briefly describe a single-template matched-filter analysis on open LIGO data for a signal with the vP-DV best-fit parameters, and its null result. We repeat this analysis on data with added simulated signals, reproducing the optimal-SNR estimate of required GW energy for

a detectable signal. We conclude in Sec. 6.5. Since our main waveform model was by necessity an ad-hoc choice, the appendices include some checks of alternative waveform models with different amplitude evolution, which are briefly summarized in the appropriate sections of the main paper, generally supporting the results obtained for the reference model.

## 6.2 Signal model and energy budget

vP-DV have performed an analysis of GW data around GW170817 with a pipeline previously described and used in different contexts (Putten, Guidorzi, and Frontera, 2014; Van Putten, 2016). It is a semi-coherent method, similar in that respect e.g. to the LVC methods described in Miller (2018) and Oliver, Keitel, and Sintes (2019). But unlike these, it does not work with specific model-based template waveforms. The single-detector data is first filtered with a bank of generic short time-symmetric templates. Candidates are then identified through edge detection on merged multi-detector outlier spectrograms.

They report a GW signal candidate following a decaying exponential track in the time-frequency plane:

$$f_{\text{gw}}(t) = (f_s - f_0) e^{-(t-t_s)/\tau} + f_0 \quad \text{for } t > t_s, \quad (6.1)$$

where  $f_s$  is the starting frequency of the signal,  $f_0$  is the frequency that the signal asymptotically approaches,  $\tau$  is a decay time scale constant,  $t$  is time, and  $t_s$  is the reference time for  $f_s$ . The best-fit values are given as  $f_s = 650$  Hz,  $f_0 = 98$  Hz,  $t_s = 0.67$  s after the merger (at nominal coalescence time of  $T_c = 1187008882.43$ , Abbott, 2017c), and  $\tau = 3.01 \pm 0.2$  s. The emitted GW energy in this signal is quoted as  $E_{\text{gw}} \simeq 0.002 M_\odot c^2$ , where  $M_\odot$  is a solar mass and  $c$  is the speed of light.

For comparison, Abbott (2017e) performed unmodelled searches for short ( $\lesssim 1$  s) and intermediate-duration ( $\lesssim 500$  s) signals. For simulated waveforms of various types and durations, they were sensitive to energy emission of  $0.6\text{--}19.6 M_\odot c^2$  (see correction in footnote of Abbott, 2018c). No evidence of GW emission was found in either range. The longer-duration search in Abbott (2018c) was not aimed at the  $\lesssim 10$  s relevant for the vP-DV candidate. Hence, the vP-DV claim concerns a much weaker signal than could have been found with those searches.

Turning to a physical understanding of the vP-DV time-frequency track, one would conventionally expect the angular rotation frequency  $\Omega = 2\pi f_{\text{rot}}$  of a NS to follow a solution of the general torque equation,  $\dot{\Omega} = -k\Omega^n$ , where the constant  $k$  and braking index  $n$  depend on the processes of energy loss. For  $n > 1$  the solution is a power law (Shapiro and Teukolsky, 1983; Palomba, 2001; Lasky et al., 2017), yielding the GW waveform model considered for longer-duration postmerger signals in Abbott (2017e) and Abbott (2018c). While the  $n = 1$  limit would give an exponential decay as in Eq. (6.1), the asymptotic  $f_0$  term cannot be interpreted this way. Still, the torque equation might not apply for an extremely young merger remnant, or  $f_{\text{gw}}$  might not be a simple multiple of  $f_{\text{rot}}$ . Hence, we will not attempt here to find any extended physical explanation for Eq. (6.1), but simply consider it as an ad-hoc input and investigate its claimed detectability.

However, to construct a complete waveform model for matched filtering, and to connect with the energy budget, we also need the corresponding GW amplitude. Again, no clearly defined model was suggested by vP-DV, and hence we need to explore some possible assumptions. As long as the signal is quasi-monochromatic following Eq. (6.1), we can describe it with a simple dimensionless timeseries  $h_0(t)$ ,

corresponding to the amplitude envelope of the rapidly oscillating strain  $h(t)$  at a detector induced by an optimally oriented source. The emitted energy up to a time  $T$  is then

$$E_{\text{gw}} = \int_{t=t_s}^T dt \frac{2\pi^2 c^3}{5G} d^2 h_0^2(t) f_{\text{gw}}^2(t), \quad (6.2)$$

at a distance  $d \approx 40$  Mpc from the source, with  $G$  being Newton's gravitational constant. It is difficult to make any unique physically motivated choice for  $h_0(t)$ , as the dynamics of a merger remnant during the first few seconds could deviate from expectations for older objects.

We will first consider the conventional case of GW emission from a fixed quadrupolar deformation, which seems to be the explanation implied by vP-DV. This might not actually be realistic for a very young object, but allows to study the detectability of a signal with the Eq. (6.1) frequency evolution and given energy budget under a specific amplitude model. We later discuss how the results change when relaxing this amplitude assumption. We aim to be as optimistic as possible, assuming a perfectly orthogonal deformation with respect to the rotational axis, which results in a single frequency of GW emission at  $f_{\text{gw}} = 2f_{\text{rot}}$ , and the extreme case of an inclination  $\cos \iota = 1$ , which for a given  $h_0(t)$  yields the strongest strain signal at the detectors.

For a rotating body with fixed quadrupolar deformation, the GW amplitude at a distance  $d$  would be (Zimmermann and Szedenits, 1979; Jaranowski, Krolak, and Schutz, 1998)

$$h_0(t) = \frac{4\pi^2 G \epsilon I}{c^4 d} f_{\text{gw}}(t)^2. \quad (6.3)$$

Here,  $\epsilon = (I_{\text{xx}} - I_{\text{yy}})/I_{\text{zz}}$  is the NS ellipticity and  $I = I_{\text{zz}}$  its principal moment of inertia. This does not require spin-down dominated by GW emission (which instead of the exponential  $f_{\text{gw}}(t)$  would yield a  $n = 5$  power law), but only that the NS has fixed  $\epsilon$  and  $I$  while following the  $f_{\text{gw}}(t)$  spin-down track, including if that track is dominated by other energy loss processes.

Inserting  $h_0(t)$  into  $E_{\text{gw}}$  yields an integral over  $f_{\text{gw}}^6$ , which is explicitly performed in appendix 6.A. <sup>1</sup> Due to the asymptotic  $f_0$  term, this diverges for  $T \rightarrow \infty$ . But vP-DV only claim an observable GW track for 7 s (see A4.2 in their supplement) and, with their best-fit parameters,  $E_{\text{gw}}$  changes only very slowly after 7 s (e.g. by 0.1% up to 20 s); with this in mind we fix  $T = 7$  s.

In both  $h_0$  and  $E_{\text{gw}}$  expressions, only the product  $\epsilon I$  appears, and for fixed  $E_{\text{gw}} = 0.002 M_{\odot} c^2$  we can eliminate it, yielding an expected initial strain amplitude of  $h_0(t = t_s) \approx 2.38 \times 10^{-23}$ . Studying the detectability of such a signal will be the subject of the following sections.

But to get a better intuition about the physical constraints on this (or any similar) emission model for GWs from a young postmerger remnant NS, we can also for a moment consider  $I$  and  $\epsilon$  separately, and compare with the available energy budget. The energy stored in the NS's rotation is  $E_{\text{rot}} = \frac{1}{2} I \Omega^2$ . Additional energy could be extracted e.g. from the magnetic field or fallback accretion, but most of the total energy budget should be lost through non-GW channels. As a starting point,  $E_{\text{rot}}(\Omega = \pi f_s) = E_{\text{gw}}$  would yield  $I \approx 1.7 \times 10^{38} \text{ kg m}^2$ , between the 'canonical'  $1 \times 10^{38} \text{ kg m}^2$  typically assumed for isolated NSs (Riles, 2017) and the  $\approx 4 \times 10^{38} \text{ kg m}^2$  assumed in Abbott, 2018c for a heavy and rapidly rotating merger remnant. Inserting this value into Eq. (6.2) and solving for the ellipticity leads to a huge  $\epsilon \gtrsim 1.2$ . If

<sup>1</sup>A simple python implementation of the waveform model, and also the energy equation, is available at <https://git.ligo.org/david-keitel/vanPuttenWaveform>.

instead  $E_{\text{gw}} < E_{\text{rot}}$ , then  $I$  will be larger and  $\epsilon$  can be smaller, but at most a factor of a few can be gained without making  $I$  unphysical.

To our knowledge there is no solid estimate for  $\epsilon$  in a very young remnant NS. But compared with theoretical and observational constraints of  $\epsilon \ll 1$  for older objects (Cutler, 2002; Johnson-McDaniel and Owen, 2013) and even for quite young magnetars (e.g. Palomba, 2001; Lasky and Glampedakis, 2016; Ho, 2016; Dall'Osso, Stella, and Palomba, 2018), we see that for the model of a NS with constant  $\epsilon I$ , this factor would need to be several orders of magnitude higher than in those regimes to emit  $E_{\text{gw}} \simeq 0.002 M_{\odot} c^2$  along the vP-DV signal track. Extreme ellipticities would also typically require extreme magnetic fields, which then may not even allow for the orthogonal rotator configuration required to generate strong GW emission (Ho, 2016; Dall'Osso, Stella, and Palomba, 2018).

It might be possible to circumvent this argument in models with different  $h_0(t)$ , e.g. through time-varying quadrupole amplitudes or different emission channels. Since the physics of a newborn remnant NS are uncertain, and since vP-DV have heuristically fitted the  $f_{\text{gw}}(t)$  model to the detection candidate's time-frequency-track without specific physical assumptions, this is an attractive option. In the next two sections, we will mainly take the ad-hoc model defined by Eqs. (6.1) and (6.3) at face value, constraining its detectability as a function of  $E_{\text{gw}}$ . However we also consider some representative examples of alternative models in appendix 6.C, also including some that are very optimistic and not physically motivated, finding no qualitative differences in our conclusions.

### 6.3 Optimal matched-filter (non-)detectability

For known waveforms in stationary Gaussian noise, the optimal detection strategy (among linear filters: Wainstein and Zubakov, 1962; Helstrom, 1968) is matched filtering; see e.g. Maggiore (2008) and Jaranowski and Królak (2009) for modern textbook treatments. While LIGO data is not fully Gaussian, in the absence of sporadic short-duration glitches (see e.g. Zevin, 2017; Nuttall, 2018) it can be approximated well as coloured Gaussian noise (with additional narrow spectral line artifacts, Covas, 2018). A strong glitch in the Livingston detector during the inspiral of GW170817 has already been subtracted, as described in Abbott, 2017c, from the released data (GWOSC, 2017).

To our knowledge, no sensitivity curves are available for this specific signal type with the vP-DV cross-correlation pipeline (previously described and used in different contexts: Putten, Guidorzi, and Frontera, 2014; Van Putten, 2016). But for any specific given waveform it cannot be more sensitive than matched filtering. Note that the appeal of semi-coherent methods such as that of vP-DV is that they can retain most of their sensitivity even if an actual signal is not fully phase-coherent. However, here we will study the optimistic case of a signal fully coherently following Eq. (6.1); if such an ideal signal is not detectable by fully-coherent matched filtering, then any practical analysis cannot be more sensitive either for signals with loss of phase coherence.

To quantify detectability, let us first define the product of a template with a data stream which leads to the complex matched-filter output function (following the notation of Allen et al., 2012)

$$z(t_s) = 4 \int_0^{\infty} df \frac{\tilde{h}_{\text{data}}(f) \tilde{h}_{\text{template}}^*(f, t_s = 0, \phi_0 = 0)}{S_n(f)} e^{2\pi i f t_s} \quad (6.4)$$

where  $\tilde{h}(f)$  is the Fourier transform of the  $h(t)$  timeseries and  $S_n(f)$  is the single-sided noise power spectral density (PSD) of a detector. Provided the PSD is reasonably well estimated, this whitening factor will take proper care of any spectral noise artifacts in the data.

Before looking at actual data, let us consider the optimal signal-to-noise ratio (SNR)  $\rho_{\text{opt}}$  for a waveform template  $h(t)$ . In the frequency domain, this is given (Flanagan and Hughes, 1998) by

$$\rho_{\text{opt}}^2 = 4 \int_0^{\infty} df \frac{|\tilde{h}(f)|^2}{S_n(f)}. \quad (6.5)$$

The optimal SNR corresponds to a scalar product of the template with itself and it is a measure for the sensitivity of the detector to such a given template; this quantity is commonly used as a normalization factor when constructing the matched-filter SNR detection statistic

$$\rho(t_s) = \frac{|z(t_s)|}{\rho_{\text{opt}}}. \quad (6.6)$$

Taking the absolute value of the complex  $z(t_s)$  is equivalent to optimizing over an unknown phase offset  $\phi_0$ , so that  $\rho(t_s)$  is a SNR timeseries for sliding the template against the data. In contrast with coalescence searches, we use the signal start time  $t_s$  instead of the end-time as a reference.

We use the `pyCBC` matched-filtering engine (Nitz et al., 2018) that was also used in one of the pipelines detecting GW170817 (Usman, 2016; Abbott, 2017c). The PSD estimate (Cornish and Littenberg, 2015; Littenberg and Cornish, 2015) is taken from Abbott (2019a).<sup>2</sup>

We construct the strain  $h(t)$  at a GW detector from Eqs. (6.1) and (6.3) with the frequency-evolution parameters given by vP-DV, the distance  $d = 40$  Mpc and sky location of GW170817, the best-case  $\cos \iota = 1$ , and a factor  $\epsilon I$  matching the  $E_{\text{gw}} = 0.002 M_{\odot} c^2$  budget, using standard `LALSuite` (*LIGO Algorithm Library - LALSuite*) functions to apply the detector response. (See Jaranowski, Krolak, and Schutz, 1998, for the full equations.)

For both LIGO detectors at Hanford (H1) and Livingston (L1), we obtain  $\rho_{\text{opt}} \approx 1.8$ , which is a rather low value, as we will see in the following. In Gaussian noise, the squared SNR is  $\chi_{\kappa}^2$ -distributed with  $\kappa = 2$  degrees of freedom, with mean of 2 and variance of 4, which in the presence of a signal becomes a non-central  $\chi^2$  with mean  $2 + \rho_{\text{opt}}^2$ . Thus, a vP-DV type signal with the given parameters and the Eq. (6.3) amplitude model should not be confidently detectable with aLIGO at its sensitivity at the time of GW170817, since there is significant overlap between the pure-noise and noise+signal distributions.

For a given threshold  $\rho_{\text{thr}}$ , the false-alarm probability and false-dismissal probability – for a single trial, i.e. a fixed start time and single waveform template – are given by:

$$p_{\text{FA}}(\rho_{\text{thr}}) = \int_{\rho_{\text{thr}}}^{\infty} p(\rho|\text{noise}) d\rho, \quad (6.7)$$

$$p_{\text{FD}}(\rho_{\text{thr}}, \rho_{\text{opt}}) = \int_0^{\rho_{\text{thr}}} p(\rho|\text{noise} + \text{signal}) d\rho, \quad (6.8)$$

<sup>2</sup>A file with these PSDs is available for download at [https://dcc.ligo.org/public/0150/P1800061/010/GW170817\\_PSDs.dat](https://dcc.ligo.org/public/0150/P1800061/010/GW170817_PSDs.dat). We have checked that the SNRs change by no more than 5% when instead using a simpler `pyCBC` Welch's method estimate of the PSD from the GWOSC 2048s data set.

where the 'noise+signal' model is evaluated at fixed  $\rho_{\text{opt}}$ , and the detection probability is  $p_{\text{det}} = 1 - p_{\text{FD}}$ .

Still assuming Gaussian noise, the matched-filter SNR from Eq. (6.6) is a Neyman-Pearson optimal statistic: it maximizes  $p_{\text{det}}$  at fixed  $p_{\text{FA}}$ .  $\rho_{\text{thr}}$  is thus usually chosen at an acceptable  $p_{\text{FA}}$  level after taking into account the trials factor from analysing a certain length of data and multiple templates. To deal with long data stretches and contamination by non-Gaussian noise artifacts,  $\rho_{\text{thr}} = 8$  is often considered (e.g. Abbott, 2018b); however for targeted post-merger searches where only a short interval of time is of interest, thresholds as low as 5 have been suggested (Clark et al., 2014; Clark et al., 2016).

The optimal SNR is proportional to  $1/d$ ,  $\sqrt{E_{\text{gw}}}$  or  $\epsilon I$  respectively. For illustration, Fig. 6.1 shows the scaling with both  $E_{\text{gw}}$  and  $\epsilon I$  assuming the fixed-quadrupole amplitude model from Eq. (6.3), as well as the corresponding  $p_{\text{det}}$  at a nominal threshold of 5. We see that a much higher emitted energy over the proposed exponential track would be needed to make a signal confidently detectable. In addition, Fig. 6.2 illustrates the general relations between  $p_{\text{det}}$ ,  $p_{\text{FA}}$ ,  $\rho_{\text{opt}}$  and  $\rho_{\text{thr}}$  for the  $\chi^2_2$  distribution, which do not depend on the waveform model. Choosing  $\rho_{\text{thr}} = 5$  yields a single-trial  $p_{\text{FA}} \approx 4 \times 10^{-6}$ , which e.g. for data sampled at 4096 Hz corresponds to about one false alarm per minute, or  $\approx 0.025$  expected noise events above threshold for the 1.7 s window between GW170817 and GRB170817A (Abbott, 2017b) suggested as a reference duration by vP-DV.

If we consider this  $p_{\text{FA}}$  level acceptable for that narrow time window of interest,  $\rho_{\text{opt}} \approx 1.8$  for the suggested vP-DV signal parameters and energy yields a negligible  $p_{\text{det}}(\rho_{\text{thr}} = 5) \sim 10^{-3}$ . Single-detector  $p_{\text{det}}$  of 50% and 90% would require 8 and 12 times, respectively, higher energy content of the emitted signal than suggested by vP-DV, with the associated problems of making the supposed NS spindown model work becoming correspondingly more grave. Note again that here we have assumed optimal orientation,  $\cos \iota = 1$ , making these estimates rather conservative.

The combination of both LIGO detectors cannot improve the situation sufficiently either. While e.g. the standard pyCBC search (Dal Canton, 2014; Usman, 2016) uses coincidences of single-detector peaks, in principle the optimal  $p_{\text{det}}$  would be obtained by coherent combination of the detector data (e.g. Bose, Pai, and Dhurandhar, 2000; Cutler and Schutz, 2005; Harry and Fairhurst, 2011). The optimal approach yields an expected sensitivity improvement of  $\sqrt{2}$  in amplitude, which is insufficient to bring the vP-DV signal into a confidently detectable regime. Furthermore, to be robust on real (glitchy) data this approach needs to be augmented by additional coincidence criteria (e.g. Veitch and Vecchio, 2010; Keitel et al., 2014; Isi et al., 2018), so this factor can be considered as an upper limit of achievable improvement. Meanwhile, in an actual search a higher threshold would also be required to account for the additional trials factor from searching many templates with different parameters, further decreasing  $p_{\text{det}}$ .

In summary, even under the most optimistic assumptions we find that the proposed signal, with our reference amplitude model, only produces a low  $\rho_{\text{opt}}$ . Even with lenient thresholds and not accounting for the additional trials factor from multiple search templates, this  $\rho_{\text{opt}}$  results in a negligible detection probability. A confident detection would require a large increase in emitted GW energy.

In appendix 6.C we discuss optimal SNRs for alternative amplitude evolutions. GWs from the r-mode emission channel produce slightly lower SNRs than the mass quadrupole model. Highly optimistic ad-hoc models with  $h_0(t)$  either constant or following the detector PSD, which result in less energy emitted early on when  $f_{\text{gw}}(t)$  corresponds to low detector sensitivity and more emitted in the 'bucket' region of

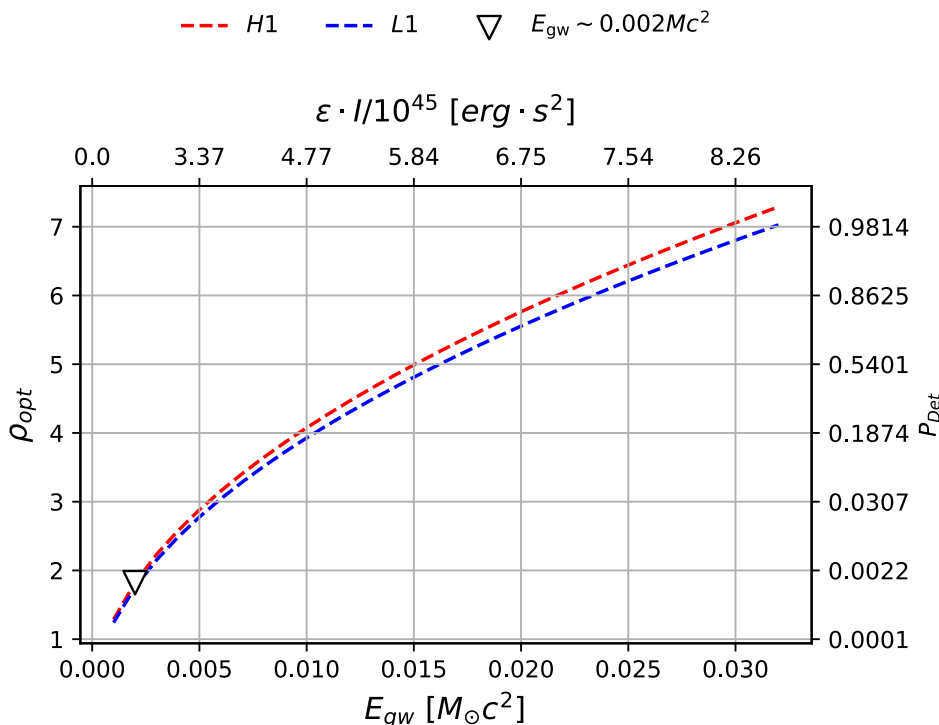


FIGURE 6.1: Detectability of a vP-DV type signal after GW170817, assuming a constant-quadrupole model, according to the optimal SNR  $\rho_{\text{opt}}$  in each LIGO detector (H1 and L1). The factor  $\epsilon I$  is adapted to scale the emitted energy  $E_{\text{gw}}$ , keeping all other waveform parameters fixed. The detection probability  $p_{\text{det}}$  is evaluated at a SNR threshold of 5.

best sensitivity, can still only bring  $\rho_{\text{opt}}$  up to  $\sim 3$ – $3.6$  and thus  $p_{\text{det}}(\rho_{\text{thr}} = 5)$  to 3–10%. There is no physical motivation for those ad-hoc models, and to make up for the decaying frequency, there would need to be a quadrupole growing by 2 orders of magnitude over the signal duration.

## 6.4 Practical checks on real and simulated data

Based on the optimal SNR alone, we have argued that a higher  $E_{\text{gw}}$  would be needed for a detectable signal of the vP-DV type. To verify this, here we will demonstrate that, as expected, a single-template matched filter does not return interesting candidates on the actual post-merger detector data, and neither when a simulated signal of the suggested energy is injected; but we can recover injections when their strength is sufficiently increased, as predicted in the previous section.

We apply a matched-filter analysis to the openly available LIGO data (GWOSC, 2017) around the time of GW170817, but restrict it to the best-fit waveform parameters reported by vP-DV, essentially sliding a template of fixed shape against the data while only varying its start time and phase. A more computationally expensive full search over alternative waveform templates in the same Eq. (6.1) family, i.e. over certain ranges in all parameters, does not seem warranted given the expected non-detectability inferred from energy budget considerations and optimal SNR results.

We perform pyCBC matched filtering over 64 s of data around the merger time of GW170817. The only pre-processing step is a high-pass filter with cutoff at 15 Hz to remove strong low-frequency noise components of the LIGO data, all other features

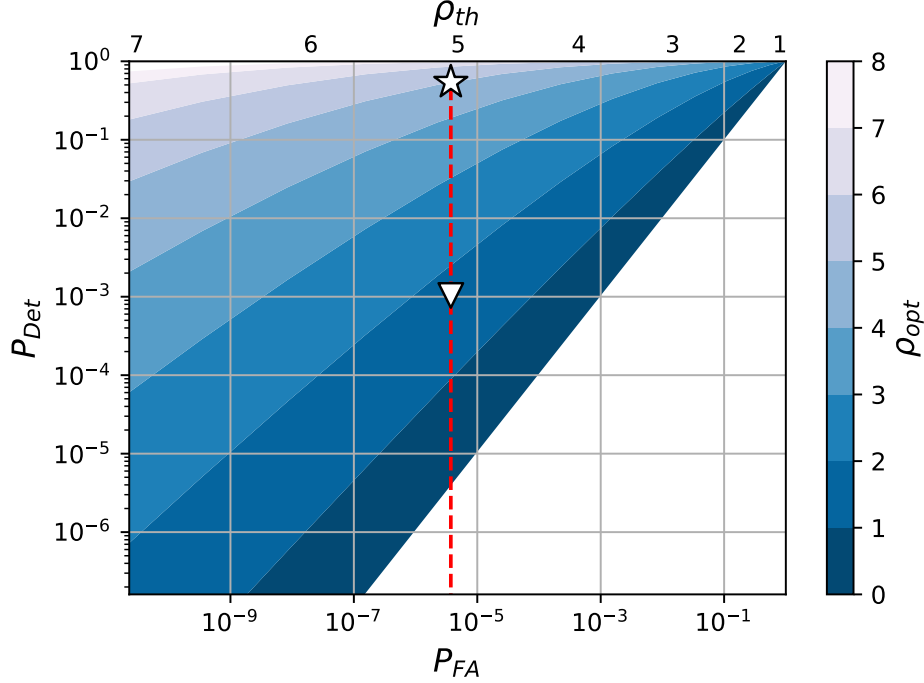


FIGURE 6.2: Single-trial detection and false-alarm probabilities for the single-detector matched-filter SNR. Each  $p_{FA}$  corresponds to a fixed threshold  $\rho_{thr}$  (given by the two horizontal axes) while  $p_{det}$  (vertical axis) also depends on the optimal SNR  $\rho_{opt}$  of the signal population (colour scale). For an example threshold  $\rho_{thr} = 5$ , the star indicates the  $(p_{FA}, p_{det})$  operating point for signals with  $\rho_{opt}$  near threshold, while the triangle corresponds to the  $\rho_{opt} \approx 1.8$  we obtain for the best-fit vP-DV parameters and  $E_{gw} = 0.002 M_{\odot} c^2$ .

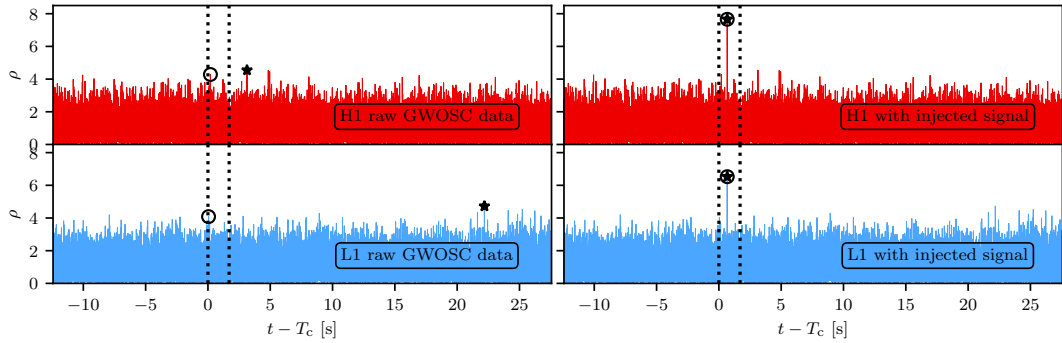


FIGURE 6.3: Frequency-domain matched-filter SNR time series  $\rho(t_s)$  obtained with pyCBC on GWOSC LIGO data around the time of GW170817 for the best-fit waveform parameters reported by vP-DV and a constant-quadrupole model. Stars mark the loudest outlier in a whole analysis window, and open circles mark the loudest candidate in a 1.7s window after merger time ( $T_c = 1187008882.43$  GPS seconds). First column: raw data with no significant coincident peak (loudest peaks of  $\rho_{H1} = 4.28$  and  $\rho_{L1} = 4.08$  separated by 0.15 s). Second column: data with an injected signal matching the vP-DV best-fit parameters but a factor  $\approx 16$  higher emitted energy, with consistent peaks recovered in both detectors at  $T_c + 0.67$  s.



of the noise spectrum being sufficiently addressed by whitening with the noise PSD in the matched-filter scalar product.

The matched-filter SNR does not depend on any overall amplitude normalization constant, but does depend on the shape of  $h_0(t)$ . Fig. 6.3 shows the results for the model from Eq. (6.3) (constant quadrupolar deformation). As seen in the left panels for the raw detector data, there are abundant single-detector outliers of  $\rho \approx 4$ , but no particularly prominent local peaks. In particular, vP-DV have emphasized the importance of their signal candidate falling within the 1.7s window between GW-inferred merger time and the following GRB signal. The loudest matched-filter SNR peaks within this window reach only  $\rho_{\text{H1}} = 4.28$  and  $\rho_{\text{L1}} = 4.08$ . (Corresponding to single-trial  $p_{\text{FA}}$  of  $10^{-4}$  and  $2.4 \times 10^{-4}$  from a  $\chi^2_2$  distribution, i.e. about one expected outlier of this strength or higher from pure Gaussian noise for the  $4096 \times 1.7$  trials within the window.) In each detector there are several louder peaks within tens of seconds around this window, and even those are fully compatible with Gaussian noise expectations, see Fig. 6.4. Furthermore, the loudest single-detector peaks do not line up with each other and there is no coincident peak with both single-detector SNRs above 4.

Injecting simulated signals following the vP-DV waveform model with varying amplitudes and repeating the analysis, we confirm that about an order of magnitude more total emitted GW energy would be required for a confidently detectable signal under this model. See the right column of Fig. 6.3 for an example SNR timeseries with a clearly recoverable injection (of  $\approx 15$  times higher  $E_{\text{gw}}$ ), and Fig. 6.5 for the scaling of both optimal and matched-filter SNR with injected  $E_{\text{gw}}$ . Again we note that this is a single-template analysis for a fully-coherent template perfectly matching a fully-coherent injection, which sets an upper limit on the sensitivity achievable with any realistic (coherent or semi-coherent) search for any (fully or only partially coherent) signals following the same frequency and amplitude evolution.

Furthermore, the obtained SNRs both without and with injections remain consistent when exchanging the real LIGO data for simulated coloured Gaussian noise generated from a smoothed PSD, demonstrating that the real data set is close enough to Gaussian and the Gaussian-noise assumption inherent in the matched-filter calculation did not bias the results. As an additional check, we have compared these results with an independent time-domain matched-filtering implementation in appendix 6.B, again finding consistent results.

## 6.5 Conclusions

We have investigated the detection candidate for GW170817 post-merger gravitational waves reported by Putten and Della Valle (2018). Even in the best case, i.e. an ideal matched-filter analysis for a fully phase-coherent signal following their best-fit time-frequency evolution model, and under additional optimistic assumptions, an increase in energy and extreme parameters would be required for a confident detection under LIGO sensitivity at the time of GW170817. By extension, any wide search like that of vP-DV should not be sensitive to this class of signals at the expected energy budget and at current detector sensitivity. Hence, while a detection of post-merger GWs would have profound consequences, this study suggests that no claim of such a signal from a neutron star remnant can be made at this point.

It could still be possible that vP-DV found a real signature in the detector strain

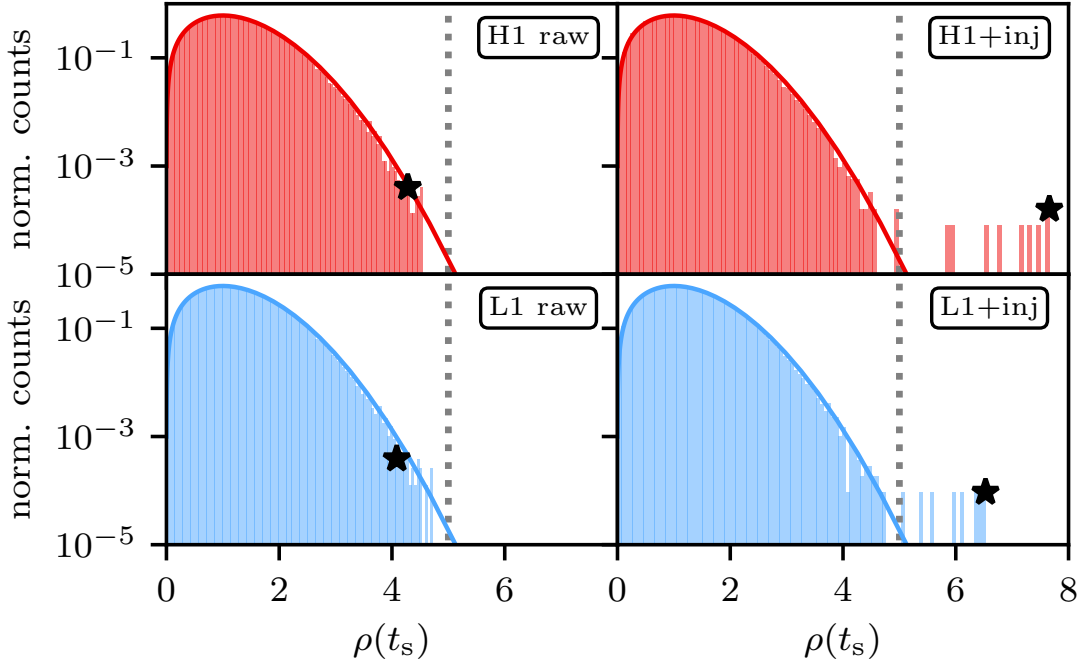


FIGURE 6.4: Histograms of the SNR timeseries from Fig. 6.3 (for the best-fit waveform parameters). The solid line indicates the expected  $\chi^2$  distribution in Gaussian noise, the black stars in each case mark the loudest candidate from a  $[T_c, T_c + 1.7\text{s}]$  window, and the dotted grey line corresponds to a nominal threshold of  $\rho = 5$ .

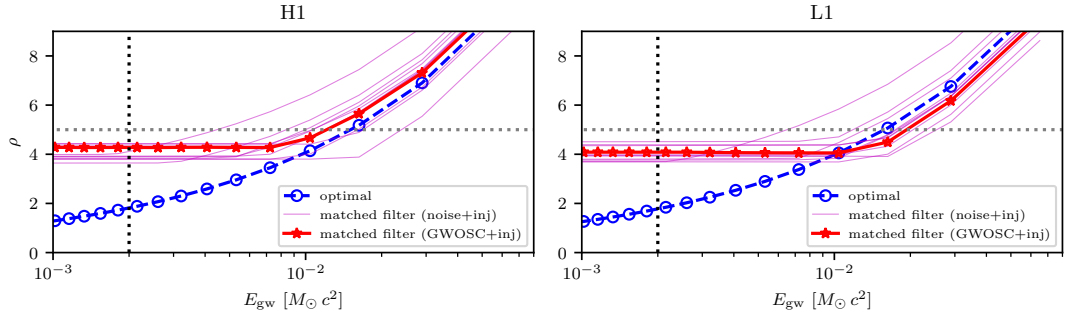


FIGURE 6.5: Comparison of optimal SNRs and single-template matched-filter SNRs obtained on data with injected signals, with both injections and templates using the best-fit vP-DV parameters, as a function of changing the GW energy content  $E_{\text{gw}}$  of the injection. The matched-filter SNRs are maximized over start times  $t_s$  within the nominal 1.7 s window between GW170817 and GRB170817A. The solid red line is for injections into real LIGO data around GW170817, and the weaker magenta lines are for the same simulated signals added to several realizations of coloured Gaussian noise following a smoothed PSD. We see that the matched-filter SNR follows the optimal SNR (dashed blue line) for strong injections, but already far above the energy reported by vP-DV (dotted vertical line) it flattens out to an injection-strength-independent level, which in both detectors is consistent with the spread in Gaussian noise realizations. A nominal  $\rho = 5$  threshold is also indicated (dotted horizontal line).

data, but that it might be an artifact of terrestrial origin. While neither our (single-template) matched-filter analysis following the time-frequency evolution of the vP-DV candidate, nor the previous generic post-merger searches (Abbott, 2017e; Abbott, 2018c), have found any suspicious outliers, the specific filtering implementation of the vP-DV pipeline could react differently to artifacts. More detailed characterization of their pipeline on simulated or off-source data would be necessary to understand the candidate's provenance. But even with optimistic model and parameter choices, there seems to be no realistic possibility of an astrophysical origin.

## Acknowledgements

We thank LIGO and Virgo collaboration members including G. Ashton, S. Banagiri, M.A. Bizouard, J. Clark, M. Coughlin, R. Frey, I. Harry, I.S. Heng, J. Kanner, A. Królak, P. Lasky, A. Lundgren, M. Millhouse, C. Palomba, P. Schale, L. Sun, and G. Vedovato for many fruitful discussions. M.O., H.E. and A.M.S. acknowledge the support of the Spanish Agencia Estatal de Investigación and Ministerio de Ciencia, Innovación y Universidades grants FPA2016-76821-P, FPA2017-90687-REDC, FPA2017-90566-REDC, and FPA2015-68783-REDC, the Vicepresidencia i Conselleria d'Innovació, Recerca i Turisme del Govern de les Illes Balears, the European Union FEDER funds, and the EU COST actions CA16104, CA16214 and CA17137. During part of this work D.K. was funded through EU Horizon2020 MSCA grant 704094. Some calculations were performed on the LIGO Caltech cluster.

## 6.A GW energy integral

Inserting the amplitude model from Eq. (6.3) into Eq. (6.2), the emitted GW energy along a vP-DV type signal track from start time  $t_s$  up to an end time  $T$  is obtained from the sixth-order integral of the frequency evolution from Eq. (6.1):

$$E_{\text{gw}} = \int_{t=t_s}^T dt \frac{32G}{5c^5} I^2 \epsilon^2 \pi^6 f_{\text{gw}}^6(t) = \frac{32\pi^6 G}{5c^5} I^2 \epsilon^2 F(T) \quad (6.9)$$

with

$$\begin{aligned} F(T) &= \int_{t=t_s}^T dt f_{\text{gw}}^6(t) \\ &= f_0^6 (T - t_s) + \tau \left( \begin{array}{ll} 6 & (e^{-(t-t_s)/\tau} - 1) f_0^5 (f_0 - f_s) \\ -\frac{15}{2} & (e^{-2(t-t_s)/\tau} - 1) f_0^4 (f_0 - f_s)^2 \\ +\frac{20}{3} & (e^{-3(t-t_s)/\tau} - 1) f_0^3 (f_0 - f_s)^3 \\ -\frac{15}{4} & (e^{-4(t-t_s)/\tau} - 1) f_0^2 (f_0 - f_s)^4 \\ +\frac{6}{5} & (e^{-5(t-t_s)/\tau} - 1) f_0 (f_0 - f_s)^5 \\ -\frac{1}{6} & (e^{-6(t-t_s)/\tau} - 1) (f_0 - f_s)^6 \\ ) & \end{array} \right) \end{aligned} \quad (6.10)$$

for  $T > t_s$ .

## 6.B Time-Domain Matched Filtering

Since the waveform model of Eq. (6.1) is quasi-monochromatic (dominated by a single frequency at each time step, and varying over slower timescales than the inverse of the GW frequency) we can equivalently compute SNRs with a simple time-domain approach. A time-domain scalar product between two time-series is given by

$$\langle h_1(t) | h_2(t) \rangle = 2 \sum_{k=1}^{T_{\text{obs}}/dt} dt \frac{h_1(t_k) h_2(t_k)}{S_n(f(t_k))} \quad (6.11)$$

In analogy with the frequency-domain case, the SNR (for a fixed template reference time) is then

$$\rho = \frac{|z|}{\sigma} = \frac{|\langle h_{\text{data}}(t) | h_{\text{template}}(t) \rangle|}{\sqrt{\langle h_{\text{template}}(t) | h_{\text{template}}(t) \rangle}}. \quad (6.12)$$

To deal with narrow spectral artifacts (lines, see Covas, 2018) in the LIGO data, we could go to the frequency domain, whiten, and transform back to the time domain. As a more independent cross-check of the FD calculation in the previous section, we instead choose the simpler (though potentially not optimal) method of notching out pre-selected frequency bands around strong lines identified from the PSD. Many different implementations of such notch filters are possible; here we use finite-impulse-response filters from the `scipy.signal` package (Virtanen et al., 2018). A bandpass filter in [30,750] Hz is also applied using the same functions. We note that it is easily possible to erroneously obtain significantly higher SNRs from the GWOSC data if the notches are not strict enough, as the exponential  $f_{\text{gw}}(t)$  track then accumulates contributions from several strong lines in the frequency regions it traverses.

We obtain consistent results both for the optimal SNR and for the matched-filter SNR on real or simulated data with injections following the vP-DV model: optimal SNRs agree within 1% with pyCBC results and on real data with injections the notches cost about 5% of SNR.

## 6.C Modified signal models

In the main part of this chapter, we have assumed the  $f_{\text{gw}}(t)$  model (Eq. 6.1) provided by vP-DV and have made the additional assumption of a constant amplitude of the quadrupole moment (constant  $\epsilon I$ ) during the NS spindown, to get the amplitude and energy estimates needed for matched-filtering (Eqs. 6.3 and 6.10). These are not unique choices, and especially given the apparent difficulties pointed out in Sec. 6.2 to make this model physically consistent, it seems prudent to check if our conclusion of non-detectability still holds for reasonable modifications to the waveform model. Let us briefly consider the following alternatives, as also summarized in Fig. 6.6:

1. Removing the asymptotic  $f_0$  term.
2. Considering the r-mode emission channel instead of GWs from a stationary deformation.
3. An ad-hoc model with constant signal amplitude (not physically motivated).
4. An ad-hoc model (again not physically motivated) where the signal amplitude tracks the detector noise PSD as the signal frequency decays, thus producing roughly constant SNR contributions throughout the vP-DV candidate's time-frequency track.

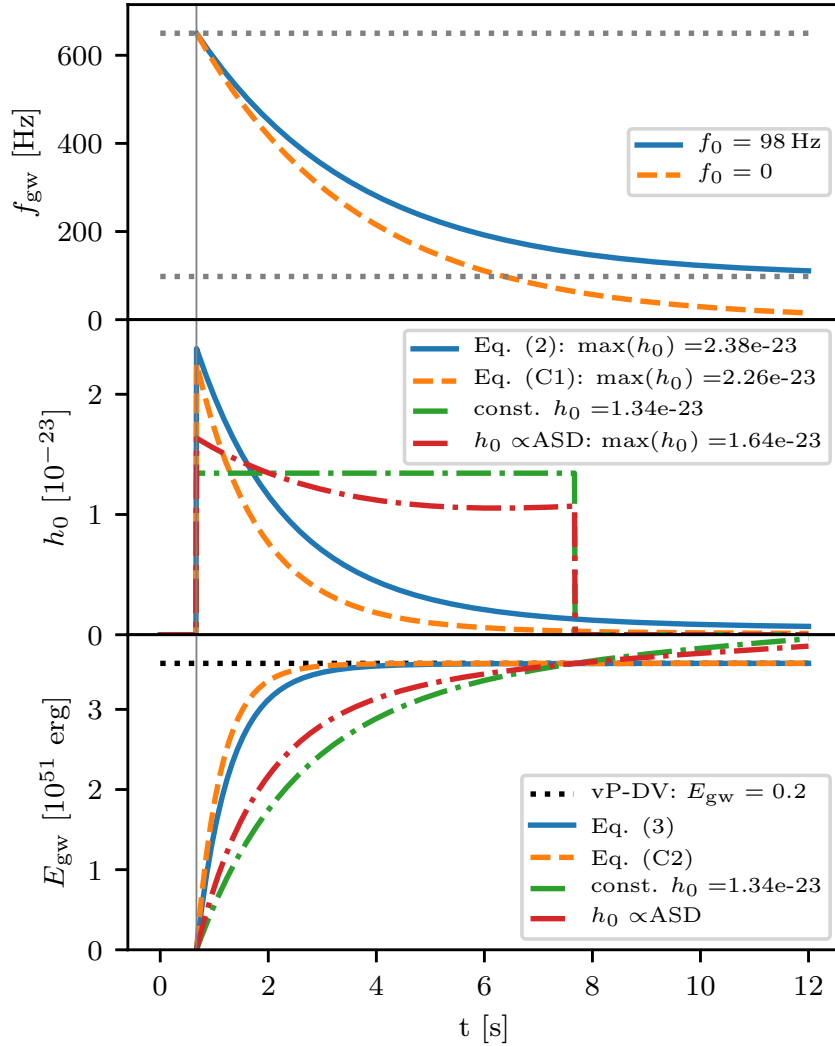


FIGURE 6.6:  $f_{\text{gw}}$ ,  $h_0$  and  $E_{\text{gw}}$  for the alternative models considered. In the top panel,  $f_{\text{gw}}$  from Eq. (6.1) is considered with and without the  $f_0$  term. In the  $h_0$  and  $E_{\text{gw}}$  panels,  $f_0 = 98$  Hz is always assumed, and we show both the constant-quadrupole and r-mode models, as well as the alternative ad-hoc models of constant  $h_0$  or of  $h_0(t)$  following a smoothed ASD at  $f_{\text{gw}}(t)$ .

### 6.C.1 Setting $f_0 = 0$

This makes  $f_{\text{gw}}(t)$  decay faster, reaching 30 Hz less than 10 s after starting at 650 Hz. To achieve the same emitted energy, a slightly higher  $\epsilon I$  factor is required, leading to higher initial  $h_0(t)$ . However, since the signal leaves the 'bucket' region of best detector sensitivity faster, the optimal SNRs at  $E_{\text{gw}} \simeq 0.002 M_{\odot} c^2$  come out about 4% lower than for the fiducial model.

### 6.C.2 r-mode GW emission

A class of inertial neutron star oscillations, r-modes can enter an unstable growing regime and become efficient GW emitters (Andersson and Kokkotas, 2001). They could be an important contribution in newborn magnetars (Ho, 2016). For this example, we make the usual simplified assumption of  $f_{\text{gw}} \approx \frac{4}{3} f_{\text{rot}} = \frac{2}{3\pi} \Omega$  (for a more accurate treatment, see Idrisy, Owen, and Jones, 2015). From Eq. (23) in Owen, 2010,

$$h_0 = \sqrt{\frac{8\pi}{5}} \frac{G}{c^5} \frac{MR^3 \tilde{f}}{d} \alpha (2\pi f_{\text{gw}})^3, \quad (6.13)$$

where the NS mass  $M$  and radius  $R$  and the density parameter  $\tilde{f}$  depend on the equation of state. From Eq. (6) of Ho (2016), the corresponding emitted GW energy is

$$\begin{aligned} E_{\text{gw}} &= \int_{t=t_s}^T dt \frac{96\pi}{15^2} \left(\frac{4}{3}\right)^6 \frac{GMR^4 \tilde{f}^2 I}{c^7 \tilde{I}} \alpha^2 \Omega^8(t) \\ &= \frac{3}{25} (2\pi)^9 \frac{GM^2 R^6 \tilde{f}^2}{c^7} \alpha^2 F_r(T) \end{aligned} \quad (6.14)$$

and inserting  $f_{\text{gw}}(t)$  from Eq. (6.1), the integral  $F_r(T) = \int_{t=t_s}^T dt f_{\text{gw}}^8(t)$  can be evaluated in analogy with Eq. (6.10).

We only aim for an order-of-magnitude estimate in this section, conservatively allowing  $M \in [2.4, 3.0] M_{\odot}$  and  $R \in [10, 15]$  km, but simply assuming the usual  $\tilde{f} = 0.01635$ .<sup>3</sup> This yields  $E_{\text{gw}} \approx \alpha^2 (0.5-9) \times 10^{48}$  erg  $\approx \alpha^2 (0.2-5) \times 10^{-6} M_{\odot} c^2$ . Hence an r-mode amplitude  $\alpha \in [20, 100]$  would be required to match the vP-DV energy estimate.

Assuming equal energy, the GW strain amplitude starts out slightly lower and decays more quickly; hence, the optimal SNRs are even lower than discussed in the main part of the chapter, even if, against conventional wisdom (Arras et al., 2003; Bondarescu, Teukolsky, and Wasserman, 2009),  $\alpha \gg 1$  would be possible.

### 6.C.3 Constant $h_0$

As an extreme case, let us also make an ad-hoc model with constant  $h_0$  for times  $t_s < t < T$ , without claiming a physical justification for it. In this model, most of the SNR would be accumulated not at the start, but towards the end of the signal. If the GW frequency still follows Eq. (6.1) without an explicit cutoff  $T$ , and the emitted energy follows Eq. (6.2), it would quickly diverge. For a cutoff  $T = t_s + 7$  s (matching the track length reported in appendix A4.2 of vP-DV), the nominal  $E_{\text{gw}} \simeq 0.002 M_{\odot} c^2$  corresponds to  $h_0 \approx 1.34 \times 10^{-23}$  and an optimal SNR  $\rho_{\text{opt}} = 3.58$  (in H1) that yields

<sup>3</sup>Though the heavy remnant of GW170817 will presumably have a quite different density structure than the  $M \approx 1.4$  regime usually considered in most of the literature, the ranges in  $M$  and  $R$  should be large enough to make  $\tilde{f}$  not a decisive parameter.

a  $p_{\text{det}} \approx 10\%$  at a threshold of 5. This is not completely negligible like the  $p_{\text{det}} \sim 10^{-3}$  obtained in Sec. 6.3, but still far from enabling confident detection. Also note that this still corresponds to the optimal case of  $\cos \iota = 1$ .

In addition, producing a constant  $h_0$  at rapidly decreasing  $f_{\text{gw}}(t)$  requires a rapidly increasing quadrupole moment, at the end of the track achieving a value 20 times larger than the one found in Sec. 6.2.

#### 6.C.4 Ad-hoc $h(t)$ model for constant SNR contribution over time

While the amplitude evolutions from Eqs. (6.1) and (6.13) would lead to most SNR accumulated at the start of the signal, another possibility to reproduce more closely the 7 s long signal track claimed by vP-DV is another ad-hoc model where we make  $h(t)$  follow the detector noise spectral density as the signal sweeps through the band with decaying  $f_{\text{gw}}(t)$ , i.e. we use an approximate fit

$$h_0(t) \propto \sqrt{S_n(f_{\text{gw}}(t))} \quad (6.15)$$

$$\approx A f_{\text{gw}}(t)^2 \left( \frac{1}{f_{\text{gw}}(t)^4} + \frac{0.00013125}{f_{\text{gw}}(t)^2} + \frac{3.1875 \cdot 10^{-7}}{f_{\text{gw}}(t)} \right)$$

As shown in Fig. 6.6, this gives a bit more early and less late emission than  $h_0 = \text{const.}$ , but is indeed qualitatively similar. In H1 we obtain  $\rho_{\text{opt}} = 3.06$ , corresponding to  $p_{\text{det}} \approx 3\%$  at a threshold of 5, higher than our reference  $h_0(t)$  model but lower than for  $h_0 = \text{const.}$  Again this would require a rapidly increasing quadrupole moment over time.





## Chapter 7

# Conclusions

This thesis devoted its work to the search of gravitational wave emissions from isolated compact objects e.g neutron stars. The gravitational-wave strain amplitudes we have targeted is of magnitude weaker than those seen from compact binary mergers, i.e.,  $O(10^{-25})$  compared to  $O(10^{-21})$ .

This thesis has described two search methods one for continuous waves and the other for long transients both targeting isolated compact objects. On chapter 2 I describe a semi-coherent method to search for continuous gravitational waves based on the Hough transform. A fair comparison between CW searches in chapter 3. Chapter 4 introduces the results from two all-sky searches for periodic gravitational waves during the Advanced LIGO's first observational run. Chapter 5 describes a new semi-coherent method to search for transient gravitational waves of intermediate duration (hours to days). Chapter 6 responds to the van Putten & Della Valle (2018) possible detection of gravitational-wave 'extended emission' from a neutron star remnant of GW170817 report.

Continued work on all the above concepts will bring us closer to one day observing gravitational radiation from isolated compact objects. This thesis deals with the analysis of advanced LIGO design data, in future runs we expect to threshold the spindown limit of more known pulsars and improve them by a factor 100 for Crab and Vela. We are at the same time working on a deep neural network to substitute the post-processing presented in chapter 2 and we are developing a new drivehoughmulti code that is more robust in a non Gaussian background. The resulting discoveries from the observation of GWs from isolated compact objects will undoubtedly be a new view of some of the most complex states in which we can observe matter, as well as open a new window to study space time.



# Bibliography

- Aasi, J. et al. (2014a). “Application of a Hough search for continuous gravitational waves on data from the fifth LIGO science run”. In: *Class. Quant. Grav.* 31, p. 085014. DOI: [10.1088/0264-9381/31/8/085014](https://doi.org/10.1088/0264-9381/31/8/085014). arXiv: [1311.2409 \[gr-qc\]](https://arxiv.org/abs/1311.2409).
- (2014b). “Implementation of an  $\mathcal{F}$ -statistic all-sky search for continuous gravitational waves in Virgo VSR1 data”. In: *Class. Quant. Grav.* 31, p. 165014. DOI: [10.1088/0264-9381/31/16/165014](https://doi.org/10.1088/0264-9381/31/16/165014). arXiv: [1402.4974 \[gr-qc\]](https://arxiv.org/abs/1402.4974).
- (2015a). “Advanced LIGO”. In: *Class. Quant. Grav.* 32, p. 074001. DOI: [10.1088/0264-9381/32/7/074001](https://doi.org/10.1088/0264-9381/32/7/074001). arXiv: [1411.4547 \[gr-qc\]](https://arxiv.org/abs/1411.4547).
- (2015b). “Characterization of the LIGO detectors during their sixth science run”. In: *Class. Quant. Grav.* 32.11, p. 115012. DOI: [10.1088/0264-9381/32/11/115012](https://doi.org/10.1088/0264-9381/32/11/115012). arXiv: [1410.7764 \[gr-qc\]](https://arxiv.org/abs/1410.7764).
- Abadie, J. et al. (2012). “All-sky Search for Periodic Gravitational Waves in the Full S5 LIGO Data”. In: *Phys. Rev. D* 85, p. 022001. DOI: [10.1103/PhysRevD.85.022001](https://doi.org/10.1103/PhysRevD.85.022001). arXiv: [1110.0208 \[gr-qc\]](https://arxiv.org/abs/1110.0208).
- Abbott, B. et al. (2008). “All-sky search for periodic gravitational waves in LIGO S4 data”. In: *Phys. Rev. D* 77. [Erratum: *Phys. Rev. D* 80, 129904(2009)], p. 022001. DOI: [10.1103/PhysRevD.77.022001](https://doi.org/10.1103/PhysRevD.77.022001), [10.1103/PhysRevD.80.129904](https://doi.org/10.1103/PhysRevD.80.129904). arXiv: [0708.3818 \[gr-qc\]](https://arxiv.org/abs/0708.3818).
- (2009a). “The Einstein@Home search for periodic gravitational waves in LIGO S4 data”. In: *Phys. Rev. D* 79, p. 022001. DOI: [10.1103/PhysRevD.79.022001](https://doi.org/10.1103/PhysRevD.79.022001). arXiv: [0804.1747 \[gr-qc\]](https://arxiv.org/abs/0804.1747).
- Abbott, B. P. et al. (2009b). “LIGO: The Laser interferometer gravitational-wave observatory”. In: *Rept. Prog. Phys.* 72, p. 076901. DOI: [10.1088/0034-4885/72/7/076901](https://doi.org/10.1088/0034-4885/72/7/076901). arXiv: [0711.3041 \[gr-qc\]](https://arxiv.org/abs/0711.3041).
- (2016a). “Comprehensive all-sky search for periodic gravitational waves in the sixth science run LIGO data”. In: *Phys. Rev. D* 94.4, p. 042002. DOI: [10.1103/PhysRevD.94.042002](https://doi.org/10.1103/PhysRevD.94.042002). arXiv: [1605.03233 \[gr-qc\]](https://arxiv.org/abs/1605.03233).
- (2016b). “GW150914: The Advanced LIGO Detectors in the Era of First Discoveries”. In: *Phys. Rev. Lett.* 116.13, p. 131103. DOI: [10.1103/PhysRevLett.116.131103](https://doi.org/10.1103/PhysRevLett.116.131103). arXiv: [1602.03838 \[gr-qc\]](https://arxiv.org/abs/1602.03838).
- (2017a). “Calibration of the Advanced LIGO detectors for the discovery of the binary black-hole merger GW150914”. In: *Phys. Rev. D* 95.6, p. 062003. DOI: [10.1103/PhysRevD.95.062003](https://doi.org/10.1103/PhysRevD.95.062003). arXiv: [1602.03845 \[gr-qc\]](https://arxiv.org/abs/1602.03845).
- (2017b). “Gravitational Waves and Gamma-rays from a Binary Neutron Star Merger: GW170817 and GRB 170817A”. In: *Astrophys. J.* 848.2, p. L13. DOI: [10.3847/2041-8213/aa920c](https://doi.org/10.3847/2041-8213/aa920c). arXiv: [1710.05834 \[astro-ph.HE\]](https://arxiv.org/abs/1710.05834).
- (2017c). “GW170817: Observation of Gravitational Waves from Binary Neutron Star Inspiral”. In: *Phys. Rev. Lett.* 119.16, p. 161101. DOI: [10.1103/PhysRevLett.119.161101](https://doi.org/10.1103/PhysRevLett.119.161101). arXiv: [1710.05832 \[gr-qc\]](https://arxiv.org/abs/1710.05832).
- (2017d). “Multi-messenger Observations of a Binary Neutron Star Merger”. In: *Astrophys. J.* 848.2, p. L12. DOI: [10.3847/2041-8213/aa91c9](https://doi.org/10.3847/2041-8213/aa91c9). arXiv: [1710.05833 \[astro-ph.HE\]](https://arxiv.org/abs/1710.05833).

- 
- Abbott, B. P. et al. (2017e). “Search for Post-merger Gravitational Waves from the Remnant of the Binary Neutron Star Merger GW170817”. In: *The Astrophysical Journal* 851.1, p. L16. DOI: [10.3847/2041-8213/aa9a35](https://doi.org/10.3847/2041-8213/aa9a35). URL: <https://doi.org/10.3847/2F2041-8213%2Faa9a35>.
- (2018a). “GWTC-1: A Gravitational-Wave Transient Catalog of Compact Binary Mergers Observed by LIGO and Virgo during the First and Second Observing Runs”. In: arXiv: [1811.12907](https://arxiv.org/abs/1811.12907) [[astro-ph.HE](#)].
- (2018b). “Prospects for Observing and Localizing Gravitational-Wave Transients with Advanced LIGO, Advanced Virgo and KAGRA”. In: *Living Rev. Rel.* 21.1, p. 3. DOI: [10.1007/s41114-018-0012-9](https://doi.org/10.1007/s41114-018-0012-9), [10.1007/lrr-2016-1](https://doi.org/10.1007/lrr-2016-1). arXiv: [1304.0670](https://arxiv.org/abs/1304.0670) [[gr-qc](#)].
- (2018c). “Search for gravitational waves from a long-lived remnant of the binary neutron star merger GW170817”. In: DOI: [10.3847/1538-4357/ab0f3d](https://doi.org/10.3847/1538-4357/ab0f3d). arXiv: [1810.02581](https://arxiv.org/abs/1810.02581) [[gr-qc](#)].
- (2018d). “Searches for Continuous Gravitational Waves from Fifteen Supernova Remnants and Fomalhaut b with Advanced LIGO”. In: arXiv: [1812.11656](https://arxiv.org/abs/1812.11656) [[astro-ph.HE](#)].
- (2019a). “Properties of the binary neutron star merger GW170817”. In: *Phys. Rev. X* 9.1, p. 011001. DOI: [10.1103/PhysRevX.9.011001](https://doi.org/10.1103/PhysRevX.9.011001). arXiv: [1805.11579](https://arxiv.org/abs/1805.11579) [[gr-qc](#)].
- (2019b). “Searches for Gravitational Waves from Known Pulsars at Two Harmonics in 2015-2017 LIGO Data”. In: arXiv: [1902.08507](https://arxiv.org/abs/1902.08507) [[astro-ph.HE](#)].
- Abbott, Benjamin P. et al. (2016c). “Results of the deepest all-sky survey for continuous gravitational waves on LIGO S6 data running on the Einstein@Home volunteer distributed computing project”. In: *Phys. Rev. D* 94.10, p. 102002. DOI: [10.1103/PhysRevD.94.102002](https://doi.org/10.1103/PhysRevD.94.102002). arXiv: [1606.09619](https://arxiv.org/abs/1606.09619) [[gr-qc](#)].
- (2017f). “All-sky Search for Periodic Gravitational Waves in the O1 LIGO Data”. In: *Phys. Rev. D* 96.6, p. 062002. DOI: [10.1103/PhysRevD.96.062002](https://doi.org/10.1103/PhysRevD.96.062002). arXiv: [1707.02667](https://arxiv.org/abs/1707.02667) [[gr-qc](#)].
- (2017g). “First low-frequency Einstein@Home all-sky search for continuous gravitational waves in Advanced LIGO data”. In: *Phys. Rev. D* 96.12, p. 122004. DOI: [10.1103/PhysRevD.96.122004](https://doi.org/10.1103/PhysRevD.96.122004). arXiv: [1707.02669](https://arxiv.org/abs/1707.02669) [[gr-qc](#)].
- (2017h). “First narrow-band search for continuous gravitational waves from known pulsars in advanced detector data”. In: *Phys. Rev. D* 96.12. [Erratum: *Phys. Rev. D* 97, no.12, 129903(2017), p. 122006. DOI: [10.1103/PhysRevD.96.122006](https://doi.org/10.1103/PhysRevD.96.122006), [10.1103/PhysRevD.97.129903](https://doi.org/10.1103/PhysRevD.97.129903). arXiv: [1710.02327](https://arxiv.org/abs/1710.02327) [[gr-qc](#)].
- (2017i). “First search for gravitational waves from known pulsars with Advanced LIGO”. In: *Astrophys. J.* 839.1. [Erratum: *Astrophys. J.* 851, no.1, 71(2017)], p. 12. DOI: [10.3847/1538-4357/aa9aee](https://doi.org/10.3847/1538-4357/aa9aee), [10.3847/1538-4357/aa677f](https://doi.org/10.3847/1538-4357/aa677f). arXiv: [1701.07709](https://arxiv.org/abs/1701.07709) [[astro-ph.HE](#)].
- (2017j). “Search for gravitational waves from Scorpius X-1 in the first Advanced LIGO observing run with a hidden Markov model”. In: *Phys. Rev. D* 95.12, p. 122003. DOI: [10.1103/PhysRevD.95.122003](https://doi.org/10.1103/PhysRevD.95.122003). arXiv: [1704.03719](https://arxiv.org/abs/1704.03719) [[gr-qc](#)].
- (2017k). “Upper Limits on the Stochastic Gravitational-Wave Background from Advanced LIGO’s First Observing Run”. In: *Phys. Rev. Lett.* 118.12. [Erratum: *Phys. Rev. Lett.* 119, no.2, 029901(2017)], p. 121101. DOI: [10.1103/PhysRevLett.118.121101](https://doi.org/10.1103/PhysRevLett.118.121101), [10.1103/PhysRevLett.119.029901](https://doi.org/10.1103/PhysRevLett.119.029901). arXiv: [1612.02029](https://arxiv.org/abs/1612.02029) [[gr-qc](#)].
- (2018e). “Full Band All-sky Search for Periodic Gravitational Waves in the O1 LIGO Data”. In: *Phys. Rev. D* 97.10, p. 102003. DOI: [10.1103/PhysRevD.97.102003](https://doi.org/10.1103/PhysRevD.97.102003). arXiv: [1802.05241](https://arxiv.org/abs/1802.05241) [[gr-qc](#)].
- Acernese, F. et al. (2008). “Status of Virgo”. In: *Class. Quant. Grav.* 25, p. 114045. DOI: [10.1088/0264-9381/25/11/114045](https://doi.org/10.1088/0264-9381/25/11/114045).

- 
- (2015). “Advanced Virgo: a second-generation interferometric gravitational wave detector”. In: *Class. Quant. Grav.* 32.2, p. 024001. DOI: [10.1088/0264-9381/32/2/024001](https://doi.org/10.1088/0264-9381/32/2/024001). arXiv: [1408.3978 \[gr-qc\]](https://arxiv.org/abs/1408.3978).
- Alford, Mark G. and Kai Schwenzer (2014). “Gravitational wave emission and spin-down of young pulsars”. In: *Astrophys. J.* 781, p. 26. DOI: [10.1088/0004-637X/781/1/26](https://doi.org/10.1088/0004-637X/781/1/26). arXiv: [1210.6091 \[gr-qc\]](https://arxiv.org/abs/1210.6091).
- (2015). “Gravitational wave emission from oscillating millisecond pulsars”. In: *Mon. Not. Roy. Astron. Soc.* 446.4, pp. 3631–3641. DOI: [10.1093/mnras/stu2361](https://doi.org/10.1093/mnras/stu2361). arXiv: [1403.7500 \[gr-qc\]](https://arxiv.org/abs/1403.7500).
- Allen, Bruce et al. (2012). “FINDCHIRP: An Algorithm for detection of gravitational waves from inspiraling compact binaries”. In: *Phys. Rev. D* 85, p. 122006. DOI: [10.1103/PhysRevD.85.122006](https://doi.org/10.1103/PhysRevD.85.122006). arXiv: [gr-qc/0509116 \[gr-qc\]](https://arxiv.org/abs/gr-qc/0509116).
- Allen, M. P. and J. E. Horvath (1997). “Glitches, torque evolution and the dynamics of young pulsars”. In: *Mon. Not. Roy. Astron. Soc.* 287, p. 615. DOI: [10.1093/mnras/287.3.615](https://doi.org/10.1093/mnras/287.3.615). arXiv: [astro-ph/9701108 \[astro-ph\]](https://arxiv.org/abs/astro-ph/9701108).
- Andersson, Nils and Kostas D. Kokkotas (2001). “The R mode instability in rotating neutron stars”. In: *Int. J. Mod. Phys. D* 10, pp. 381–442. DOI: [10.1142/S0218271801001062](https://doi.org/10.1142/S0218271801001062). arXiv: [gr-qc/0010102 \[gr-qc\]](https://arxiv.org/abs/gr-qc/0010102).
- Antonucci, F. et al. (2008). “Detection of periodic gravitational wave sources by Hough transform in the  $f$  versus  $f(\cdot)$  plane”. In: *Class. Quant. Grav.* 25, p. 184015. DOI: [10.1088/0264-9381/25/18/184015](https://doi.org/10.1088/0264-9381/25/18/184015). arXiv: [0807.5065 \[gr-qc\]](https://arxiv.org/abs/0807.5065).
- Arras, Phil et al. (2003). “Saturation of the R mode instability”. In: *Astrophys. J.* 591, pp. 1129–1151. DOI: [10.1086/374657](https://doi.org/10.1086/374657). arXiv: [astro-ph/0202345 \[astro-ph\]](https://arxiv.org/abs/astro-ph/0202345).
- Astone, Pia et al. (2010). “Data analysis of gravitational-wave signals from spinning neutron stars. V. A narrow-band all-sky search”. In: *Phys. Rev. D* 82, p. 022005. DOI: [10.1103/PhysRevD.82.022005](https://doi.org/10.1103/PhysRevD.82.022005). arXiv: [1003.0844 \[gr-qc\]](https://arxiv.org/abs/1003.0844).
- Astone, Pia et al. (2014). “Method for all-sky searches of continuous gravitational wave signals using the frequency-Hough transform”. In: *Phys. Rev. D* 90.4, p. 042002. DOI: [10.1103/PhysRevD.90.042002](https://doi.org/10.1103/PhysRevD.90.042002). arXiv: [1407.8333 \[astro-ph.IM\]](https://arxiv.org/abs/1407.8333).
- Baiotti, Luca and Luciano Rezzolla (2017). “Binary neutron star mergers: a review of Einstein’s richest laboratory”. In: *Rept. Prog. Phys.* 80.9, p. 096901. DOI: [10.1088/1361-6633/aa67bb](https://doi.org/10.1088/1361-6633/aa67bb). arXiv: [1607.03540 \[gr-qc\]](https://arxiv.org/abs/1607.03540).
- Behnke, Berit, Maria Alessandra Papa, and Reinhard Prix (2015). “Postprocessing methods used in the search for continuous gravitational-wave signals from the Galactic Center”. In: *Phys. Rev. D* 91.6, p. 064007. DOI: [10.1103/PhysRevD.91.064007](https://doi.org/10.1103/PhysRevD.91.064007). arXiv: [1410.5997 \[gr-qc\]](https://arxiv.org/abs/1410.5997).
- Biver, C. et al. (2017). “Validating gravitational-wave detections: The Advanced LIGO hardware injection system”. In: *Phys. Rev. D* 95.6, p. 062002. DOI: [10.1103/PhysRevD.95.062002](https://doi.org/10.1103/PhysRevD.95.062002). arXiv: [1612.07864 \[astro-ph.IM\]](https://arxiv.org/abs/1612.07864).
- Bondarescu, Ruxandra, Saul A. Teukolsky, and Ira Wasserman (2009). “Spinning down newborn neutron stars: nonlinear development of the r-mode instability”. In: *Physical Review D* 79, p. 104003. DOI: [10.1103/PhysRevD.79.104003](https://doi.org/10.1103/PhysRevD.79.104003). arXiv: [0809.3448 \[astro-ph\]](https://arxiv.org/abs/0809.3448).
- Bose, Sukanta, Archana Pai, and Sanjeev V. Dhurandhar (2000). “Detection of gravitational waves from inspiraling compact binaries using a network of interferometric detectors”. In: *Int. J. Mod. Phys. D* 9, pp. 325–329. DOI: [10.1142/S0218271800000360](https://doi.org/10.1142/S0218271800000360). arXiv: [gr-qc/0002010 \[gr-qc\]](https://arxiv.org/abs/gr-qc/0002010).
- Brady, Patrick R. and Teviet Creighton (2000). “Searching for periodic sources with LIGO. 2. Hierarchical searches”. In: *Phys. Rev. D* 61, p. 082001. DOI: [10.1103/PhysRevD.61.082001](https://doi.org/10.1103/PhysRevD.61.082001). arXiv: [gr-qc/9812014 \[gr-qc\]](https://arxiv.org/abs/gr-qc/9812014).

- Clark, J. et al. (2014). “Prospects For High Frequency Burst Searches Following Binary Neutron Star Coalescence With Advanced Gravitational Wave Detectors”. In: *Phys. Rev. D* 90.6, p. 062004. DOI: [10.1103/PhysRevD.90.062004](https://doi.org/10.1103/PhysRevD.90.062004). arXiv: [1406.5444](https://arxiv.org/abs/1406.5444) [[astro-ph.HE](#)].
- Clark, James Alexander et al. (2016). “Observing Gravitational Waves From The Post-Merger Phase Of Binary Neutron Star Coalescence”. In: *Class. Quant. Grav.* 33.8, p. 085003. DOI: [10.1088/0264-9381/33/8/085003](https://doi.org/10.1088/0264-9381/33/8/085003). arXiv: [1509.08522](https://arxiv.org/abs/1509.08522) [[astro-ph.HE](#)].
- Cornish, Neil J. and Tyson B. Littenberg (2015). “BayesWave: Bayesian Inference for Gravitational Wave Bursts and Instrument Glitches”. In: *Class. Quant. Grav.* 32.13, p. 135012. DOI: [10.1088/0264-9381/32/13/135012](https://doi.org/10.1088/0264-9381/32/13/135012). arXiv: [1410.3835](https://arxiv.org/abs/1410.3835) [[gr-qc](#)].
- Covas, P. B. (2016). *Characterization of the Hough all-sky search for continuous gravitational wave signals using LIGO data*. Tech. rep. LIGO-P1600302. URL: <https://dcc.ligo.org/LIGO-P1600302/public>.
- Covas, P. B. et al. (2018). “Identification and mitigation of narrow spectral artifacts that degrade searches for persistent gravitational waves in the first two observing runs of Advanced LIGO”. In: *Phys. Rev.* 97.8, p. 082002. DOI: [10.1103/PhysRevD.97.082002](https://doi.org/10.1103/PhysRevD.97.082002). arXiv: [1801.07204](https://arxiv.org/abs/1801.07204) [[astro-ph.IM](#)].
- Cutler, C. (Oct. 2002). “Gravitational waves from neutron stars with large toroidal B fields”. In: *Physical Review D*. 66.8, 084025, p. 084025. DOI: [10.1103/PhysRevD.66.084025](https://doi.org/10.1103/PhysRevD.66.084025). eprint: [gr-qc/0206051](https://arxiv.org/abs/gr-qc/0206051).
- Cutler, Curt and Bernard F. Schutz (2005). “The Generalized F-statistic: Multiple detectors and multiple GW pulsars”. In: *Phys. Rev. D* 72, p. 063006. DOI: [10.1103/PhysRevD.72.063006](https://doi.org/10.1103/PhysRevD.72.063006). arXiv: [gr-qc/0504011](https://arxiv.org/abs/gr-qc/0504011) [[gr-qc](#)].
- Dal Canton, Tito et al. (2014). “Implementing a search for aligned-spin neutron star-black hole systems with advanced ground based gravitational wave detectors”. In: *Phys. Rev. D* 90.8, p. 082004. DOI: [10.1103/PhysRevD.90.082004](https://doi.org/10.1103/PhysRevD.90.082004). arXiv: [1405.6731](https://arxiv.org/abs/1405.6731) [[gr-qc](#)].
- Dall’Osso, S., S. N. Shore, and L. Stella (2009). “Early evolution of newly born magnetars with a strong toroidal field”. In: *Mon. Not. Roy. Astron. Soc.* 398, p. 1869. DOI: [10.1111/j.1365-2966.2008.14054.x](https://doi.org/10.1111/j.1365-2966.2008.14054.x). arXiv: [0811.4311](https://arxiv.org/abs/0811.4311) [[astro-ph](#)].
- Dall’Osso, Simone, Luigi Stella, and Cristiano Palomba (2018). “Neutron star bulk viscosity, ‘spin-flip’ and GW emission of newly born magnetars”. In: *Mon. Not. Roy. Astron. Soc.* 480.1, pp. 1353–1362. DOI: [10.1093/mnras/sty1706](https://doi.org/10.1093/mnras/sty1706). arXiv: [1806.11164](https://arxiv.org/abs/1806.11164) [[astro-ph.HE](#)].
- Dall’Osso, Simone et al. (2015). “Gravitational waves from massive magnetars formed in binary neutron star mergers”. In: *Astrophysical Journal* 798.1, p. 25. DOI: [10.1088/0004-637X/798/1/25](https://doi.org/10.1088/0004-637X/798/1/25). arXiv: [1408.0013](https://arxiv.org/abs/1408.0013) [[astro-ph.HE](#)].
- Dergachev, V. (2005). *Description of PowerFlux Algorithms and Implementation LIGO Technical Document*. Tech. rep. LIGO-T050186. URL: <https://dcc.ligo.org/LIGO-T050186/public>.
- (2010). “On blind searches for noise dominated signals: a loosely coherent approach”. In: *Class. Quant. Grav.* 27, p. 205017. DOI: [10.1088/0264-9381/27/20/205017](https://doi.org/10.1088/0264-9381/27/20/205017). arXiv: [1003.2178](https://arxiv.org/abs/1003.2178) [[gr-qc](#)].
- Dergachev, V. and K. Riles (2005). *Description of PowerFlux Algorithms and Implementation LIGO Technical Document*. Tech. rep. LIGO-T050187. URL: <https://dcc.ligo.org/LIGO-T050187/public>.
- Dreissigacker, Christoph, Reinhard Prix, and Karl Wette (2018). “Fast and Accurate Sensitivity Estimation for Continuous-Gravitational-Wave Searches”. In: *Phys.*

- Rev.* D98.8, p. 084058. DOI: [10.1103/PhysRevD.98.084058](https://doi.org/10.1103/PhysRevD.98.084058). arXiv: [1808.02459](https://arxiv.org/abs/1808.02459) [[gr-qc](#)].
- Einstein@Home*. URL: [einsteinathome.org](http://einsteinathome.org).
- Flanagan, Eanna E. and Scott A. Hughes (1998). “Measuring gravitational waves from binary black hole coalescences: 1. Signal-to-noise for inspiral, merger, and ringdown”. In: *Phys. Rev.* D57, pp. 4535–4565. DOI: [10.1103/PhysRevD.57.4535](https://doi.org/10.1103/PhysRevD.57.4535). arXiv: [gr-qc/9701039](https://arxiv.org/abs/gr-qc/9701039) [[gr-qc](#)].
- Frasca, S., P. Astone, and C. Palomba (2005). “Evaluation of sensitivity and computing power for the Virgo hierarchical search for periodic sources”. In: *Class. Quant. Grav.* 22, S1013–S1019. DOI: [10.1088/0264-9381/22/18/S15](https://doi.org/10.1088/0264-9381/22/18/S15).
- Glendenning, N. K. (1997). *Compact stars: Nuclear physics, particle physics, and general relativity*.
- GWOSC (2017). *Data release for event GW170817*. DOI: [10.7935/K5B8566F](https://doi.org/10.7935/K5B8566F).
- Harry, Ian W. and Stephen Fairhurst (2011). “A targeted coherent search for gravitational waves from compact binary coalescences”. In: *Phys. Rev.* D83, p. 084002. DOI: [10.1103/PhysRevD.83.084002](https://doi.org/10.1103/PhysRevD.83.084002). arXiv: [1012.4939](https://arxiv.org/abs/1012.4939) [[gr-qc](#)].
- Helstrom, Carl W (1968). *Statistical Theory of Signal Detection*. Vol. 9. International Series of Monographs in Electronics and Instrumentation. Pergamon, London.
- Hild, S. et al. (2011). “Sensitivity Studies for Third-Generation Gravitational Wave Observatories”. In: *Class. Quant. Grav.* 28, p. 094013. DOI: [10.1088/0264-9381/28/9/094013](https://doi.org/10.1088/0264-9381/28/9/094013). arXiv: [1012.0908](https://arxiv.org/abs/1012.0908) [[gr-qc](#)].
- Ho, Wynn C. G. (2016). “Gravitational waves within the magnetar model of superluminous supernovae and gamma-ray bursts”. In: *Mon. Not. Roy. Astron. Soc.* 463.1, pp. 489–494. DOI: [10.1093/mnras/stw2016](https://doi.org/10.1093/mnras/stw2016). arXiv: [1606.00454](https://arxiv.org/abs/1606.00454) [[astro-ph.HE](#)].
- Hobbs, G. et al. (2004). “The atnf pulsar catalogue”. In: *IAU Symp.* 218, p. 139. arXiv: [astro-ph/0309219](https://arxiv.org/abs/astro-ph/0309219) [[astro-ph](#)].
- Idrisy, Ashikuzzaman, Benjamin J. Owen, and David I. Jones (2015). “R-mode frequencies of slowly rotating relativistic neutron stars with realistic equations of state”. In: *Phys. Rev.* D91.2, p. 024001. DOI: [10.1103/PhysRevD.91.024001](https://doi.org/10.1103/PhysRevD.91.024001). arXiv: [1410.7360](https://arxiv.org/abs/1410.7360) [[gr-qc](#)].
- Isi, Maximiliano et al. (2018). “Enhancing confidence in the detection of gravitational waves from compact binaries using signal coherence”. In: *Phys. Rev.* D98.4, p. 042007. DOI: [10.1103/PhysRevD.98.042007](https://doi.org/10.1103/PhysRevD.98.042007). arXiv: [1803.09783](https://arxiv.org/abs/1803.09783) [[gr-qc](#)].
- Jaranowski, Piotr and Andrzej Krolak (1999). “Data analysis of gravitational wave signals from spinning neutron stars. 2. Accuracy of estimation of parameters”. In: *Phys. Rev.* D59, p. 063003. DOI: [10.1103/PhysRevD.59.063003](https://doi.org/10.1103/PhysRevD.59.063003). arXiv: [gr-qc/9809046](https://arxiv.org/abs/gr-qc/9809046) [[gr-qc](#)].
- Jaranowski, Piotr and Andrzej Królak (2009). *Analysis of Gravitational-Wave Data*. Cambridge Monographs on Particle Physics, Nuclear Physics and Cosmology 29. Cambridge University Press.
- Jaranowski, Piotr, Andrzej Krolak, and Bernard F. Schutz (1998). “Data analysis of gravitational - wave signals from spinning neutron stars. 1. The Signal and its detection”. In: *Phys. Rev.* D58, p. 063001. DOI: [10.1103/PhysRevD.58.063001](https://doi.org/10.1103/PhysRevD.58.063001). arXiv: [gr-qc/9804014](https://arxiv.org/abs/gr-qc/9804014) [[gr-qc](#)].
- Johnson-McDaniel, Nathan K. and Benjamin J. Owen (2013). “Maximum elastic deformations of relativistic stars”. In: *Phys. Rev.* D88, p. 044004. DOI: [10.1103/PhysRevD.88.044004](https://doi.org/10.1103/PhysRevD.88.044004). arXiv: [1208.5227](https://arxiv.org/abs/1208.5227) [[astro-ph.SR](#)].
- Jones, D. I. and N. Andersson (2001). “Freely precessing neutron stars: model and observations”. In: *Mon. Not. Roy. Astron. Soc.* 324, p. 811. DOI: [10.1046/j.1365-8711.2001.04251.x](https://doi.org/10.1046/j.1365-8711.2001.04251.x). arXiv: [astro-ph/0011063](https://arxiv.org/abs/astro-ph/0011063) [[astro-ph](#)].

- Jordana, Lucia Sancho de la and Alicia M. Sintes (2008). “A  $\chi^2$  veto for continuous wave searches”. In: *Class. Quant. Grav.* 25, p. 184014. DOI: [10.1088/0264-9381/25/18/184014](https://doi.org/10.1088/0264-9381/25/18/184014). arXiv: [0804.1007](https://arxiv.org/abs/0804.1007) [gr-qc].
- Keitel, David et al. (2014). “Search for continuous gravitational waves: Improving robustness versus instrumental artifacts”. In: *Phys. Rev.* D89.6, p. 064023. DOI: [10.1103/PhysRevD.89.064023](https://doi.org/10.1103/PhysRevD.89.064023). arXiv: [1311.5738](https://arxiv.org/abs/1311.5738) [gr-qc].
- Krishnan, Badri et al. (2004). “The Hough transform search for continuous gravitational waves”. In: *Phys. Rev.* D70, p. 082001. DOI: [10.1103/PhysRevD.70.082001](https://doi.org/10.1103/PhysRevD.70.082001). arXiv: [gr-qc/0407001](https://arxiv.org/abs/gr-qc/0407001) [gr-qc].
- Kullback, S. and R. A. Leibler (Mar. 1951). “On Information and Sufficiency”. In: *Ann. Math. Statist.* 22.1, pp. 79–86. DOI: [10.1214/aoms/1177729694](https://doi.org/10.1214/aoms/1177729694). URL: <https://doi.org/10.1214/aoms/1177729694>.
- Landau, L. D. and E. M. Lifschits (1975). *The Classical Theory of Fields*. Vol. Volume 2. Course of Theoretical Physics. Oxford: Pergamon Press. ISBN: 9780080181769.
- Landau, L.D. and E.M. Lifshitz (1976). “Chapter VI - Motion of a rigid body”. In: *Mechanics (Third Edition)*. Ed. by L.D. Landau and E.M. Lifshitz. Third Edition. Oxford: Butterworth-Heinemann, pp. 96–130. ISBN: 978-0-7506-2896-9. DOI: <https://doi.org/10.1016/B978-0-08-050347-9.50011-3>. URL: <http://www.sciencedirect.com/science/article/pii/B9780080503479500113>.
- Lasky, Paul D and Kostas Glampedakis (2016). “Observationally constraining gravitational wave emission from short gamma-ray burst remnants”. In: *Mon. Not. Roy. Astron. Soc.* 458.2, pp. 1660–1670. DOI: [10.1093/mnras/stw435](https://doi.org/10.1093/mnras/stw435). arXiv: [1512.05368](https://arxiv.org/abs/1512.05368) [astro-ph.HE].
- Lasky, Paul D. et al. (2017). “The braking index of millisecond magnetars”. In: *Astrophys. J.* 843.1, p. L1. DOI: [10.3847/2041-8213/aa79a7](https://doi.org/10.3847/2041-8213/aa79a7). arXiv: [1705.10005](https://arxiv.org/abs/1705.10005) [astro-ph.HE].
- LIGO Algorithm Library - LALSuite*. free software (GPL). DOI: [10.7935/GT1W-FZ16](https://doi.org/10.7935/GT1W-FZ16).
- Littenberg, Tyson B. and Neil J. Cornish (2015). “Bayesian inference for spectral estimation of gravitational wave detector noise”. In: *Phys. Rev.* D91.8, p. 084034. DOI: [10.1103/PhysRevD.91.084034](https://doi.org/10.1103/PhysRevD.91.084034). arXiv: [1410.3852](https://arxiv.org/abs/1410.3852) [gr-qc].
- Maggiore, Michele (2008). *Gravitational Waves*. Oxford University Press.
- Miller, Andrew et al. (2018). “Method to search for long duration gravitational wave transients from isolated neutron stars using the generalized frequency-Hough transform”. In: *Phys. Rev.* D98.10, p. 102004. DOI: [10.1103/PhysRevD.98.102004](https://doi.org/10.1103/PhysRevD.98.102004). arXiv: [1810.09784](https://arxiv.org/abs/1810.09784) [astro-ph.IM].
- Ming, Jing et al. (2016). “Optimal directed searches for continuous gravitational waves”. In: *Phys. Rev.* D93.6, p. 064011. DOI: [10.1103/PhysRevD.93.064011](https://doi.org/10.1103/PhysRevD.93.064011). arXiv: [1510.03417](https://arxiv.org/abs/1510.03417) [gr-qc].
- Nitz, Alex et al. (Nov. 2018). *PyCBC v1.13.0 Release*. DOI: [10.5281/zenodo.1479480](https://doi.org/10.5281/zenodo.1479480).
- Nuttall, L. K. (2018). “Characterizing transient noise in the LIGO detectors”. In: *Phil. Trans. Roy. Soc. Lond.* A376.2120, p. 20170286. DOI: [10.1098/rsta.2017.0286](https://doi.org/10.1098/rsta.2017.0286). arXiv: [1804.07592](https://arxiv.org/abs/1804.07592) [astro-ph.IM].
- Oliver, Miquel, David Keitel, and Alicia M. Sintes (2019). “The Adaptive Transient Hough method for long-duration gravitational wave transients”. In: *preprint arXiv:1901.01820*. arXiv: [1901.01820](https://arxiv.org/abs/1901.01820) [gr-qc].
- Oliver, Miquel et al. (2018). “Matched-filter study and energy budget suggest no detectable gravitational-wave ‘extended emission’ from GW170817”. In: DOI: [10.1093/mnras/stz439](https://doi.org/10.1093/mnras/stz439). arXiv: [1812.06724](https://arxiv.org/abs/1812.06724) [astro-ph.HE].
- Owen, Benjamin J. (2010). “How to adapt broad-band gravitational-wave searches for r-modes”. In: *Phys. Rev.* D82, p. 104002. DOI: [10.1103/PhysRevD.82.104002](https://doi.org/10.1103/PhysRevD.82.104002). arXiv: [1006.1994](https://arxiv.org/abs/1006.1994) [gr-qc].



- Owen, Benjamin J. et al. (1998). “Gravitational waves from hot young rapidly rotating neutron stars”. In: *Phys. Rev. D* 58, p. 084020. DOI: [10.1103/PhysRevD.58.084020](https://doi.org/10.1103/PhysRevD.58.084020). arXiv: [gr-qc/9804044](https://arxiv.org/abs/gr-qc/9804044) [gr-qc].
- Palomba, C. (Feb. 2001). “Gravitational radiation from young magnetars: Preliminary results”. In: *Astronomy & Astrophysics* 367, pp. 525–531. DOI: [10.1051/0004-6361:20000452](https://doi.org/10.1051/0004-6361:20000452).
- Palomba, Cristiano (2000). “Pulsars ellipticity revised”. In: *Astron. Astrophys.* 354, p. 163. arXiv: [astro-ph/9912356](https://arxiv.org/abs/astro-ph/9912356) [astro-ph].
- Papa, Maria Alessandra et al. (2016). “Hierarchical follow-up of subthreshold candidates of an all-sky Einstein@Home search for continuous gravitational waves on LIGO sixth science run data”. In: *Phys. Rev. D* 94.12, p. 122006. DOI: [10.1103/PhysRevD.94.122006](https://doi.org/10.1103/PhysRevD.94.122006). arXiv: [1608.08928](https://arxiv.org/abs/1608.08928) [astro-ph.IM].
- Piro, Anthony L., Bruno Giacomazzo, and Rosalba Perna (2017). “The Fate of Neutron Star Binary Mergers”. In: *Astrophys. J.* 844.2, p. L19. DOI: [10.3847/2041-8213/aa7f2f](https://doi.org/10.3847/2041-8213/aa7f2f). arXiv: [1704.08697](https://arxiv.org/abs/1704.08697) [astro-ph.HE].
- Pletsch, Holger J. and Bruce Allen (2009). “Exploiting global correlations to detect continuous gravitational waves”. In: *Phys. Rev. Lett.* 103, p. 181102. DOI: [10.1103/PhysRevLett.103.181102](https://doi.org/10.1103/PhysRevLett.103.181102). arXiv: [0906.0023](https://arxiv.org/abs/0906.0023) [gr-qc].
- Popov, S. B. et al. (2000). “Population synthesis of old neutron stars in the Galaxy”. In: *Astron. Astrophys. Trans.* 19, p. 471. DOI: [10.1080/10556790008238592](https://doi.org/10.1080/10556790008238592). arXiv: [astro-ph/9910320](https://arxiv.org/abs/astro-ph/9910320) [astro-ph].
- Prix, Reinhard (2007). “Search for continuous gravitational waves: Metric of the multi-detector F-statistic”. In: *Phys. Rev. D* 75. [Erratum: *Phys. Rev. D* 75,069901(2007)], p. 023004. DOI: [10.1103/PhysRevD.75.023004](https://doi.org/10.1103/PhysRevD.75.023004), [10.1103/PhysRevD.75.069901](https://doi.org/10.1103/PhysRevD.75.069901). arXiv: [gr-qc/0606088](https://arxiv.org/abs/gr-qc/0606088) [gr-qc].
- Punturo, M. et al. (2010). “The third generation of gravitational wave observatories and their science reach”. In: *Class. Quant. Grav.* 27, p. 084007. DOI: [10.1088/0264-9381/27/8/084007](https://doi.org/10.1088/0264-9381/27/8/084007).
- Putten, Maurice H. P. M. van and Massimo Della Valle (2018). “Observational evidence for Extended Emission to GW170817”. In: *Monthly Notices of the Royal Astronomical Society* 482.1, pp. L46–L49. DOI: [10.1093/mnrasl/sly166](https://doi.org/10.1093/mnrasl/sly166). arXiv: [1806.02165](https://arxiv.org/abs/1806.02165) [astro-ph.HE].
- Putten, Maurice H. P. M. van, Cristiano Guidorzi, and Filippo Frontera (2014). “Broad band turbulent spectra in gamma-ray burst light curves”. In: *The Astrophysical Journal* 786, p. 146. DOI: [10.1088/0004-637X/786/2/146](https://doi.org/10.1088/0004-637X/786/2/146). arXiv: [1411.6940](https://arxiv.org/abs/1411.6940) [astro-ph.HE].
- Rezzolla, Luciano, Elias R. Most, and Lukas R. Weih (2018). “Using gravitational-wave observations and quasi-universal relations to constrain the maximum mass of neutron stars”. In: *Astrophys. J.* 852.2. [*Astrophys. J. Lett.* 852,L25(2018)], p. L25. DOI: [10.3847/2041-8213/aaa401](https://doi.org/10.3847/2041-8213/aaa401). arXiv: [1711.00314](https://arxiv.org/abs/1711.00314) [astro-ph.HE].
- Riles, Keith (2017). “Recent searches for continuous gravitational waves”. In: *Mod. Phys. Lett. A* 32.39, p. 1730035. DOI: [10.1142/S021773231730035X](https://doi.org/10.1142/S021773231730035X). arXiv: [1712.05897](https://arxiv.org/abs/1712.05897) [gr-qc].
- Sarin, Nikhil et al. (2018). “X-ray guided gravitational-wave search for binary neutron star merger remnants”. In: *Phys. Rev. D* 98.4, p. 043011. DOI: [10.1103/PhysRevD.98.043011](https://doi.org/10.1103/PhysRevD.98.043011). arXiv: [1805.01481](https://arxiv.org/abs/1805.01481) [astro-ph.HE].
- Sathyaprakash, B. et al. (2012). “Scientific Objectives of Einstein Telescope”. In: *Class. Quant. Grav.* 29. [Erratum: *Class. Quant. Grav.* 30,079501(2013)], p. 124013. DOI: [10.1088/0264-9381/29/12/124013](https://doi.org/10.1088/0264-9381/29/12/124013), [10.1088/0264-9381/30/7/079501](https://doi.org/10.1088/0264-9381/30/7/079501). arXiv: [1206.0331](https://arxiv.org/abs/1206.0331) [gr-qc].

- Schmidt, J. G., M. M. Hohle, and R. Neuhauser (2014). “Determination of a temporally and spatially resolved supernova rate from OB stars within 5 kpc”. In: *Astron. Nachr.* 335, pp. 935–948. DOI: [10.1002/asna.201312070](https://doi.org/10.1002/asna.201312070). arXiv: [1409.3357](https://arxiv.org/abs/1409.3357) [[astro-ph.SR](#)].
- Schutz, Bernard F. and Massimo Tinto (Jan. 1987). “Antenna patterns of interferometric detectors of gravitational waves – I. Linearly polarized waves”. In: *Monthly Notices of the Royal Astronomical Society* 224.1, pp. 131–154. ISSN: 0035-8711. DOI: [10.1093/mnras/224.1.131](https://doi.org/10.1093/mnras/224.1.131). eprint: <http://oup.prod.sis.lan/mnras/article-pdf/224/1/131/4099535/mnras224-0131.pdf>. URL: <https://dx.doi.org/10.1093/mnras/224.1.131>.
- SFT Data Format Version 2 Specification*. URL: [dcc.LIGO-T070124-00-Z](https://dcc.ligo.org/LIGO-T070124-00-Z).
- Shaltev, M. et al. (2014). “Fully coherent follow-up of continuous gravitational-wave candidates: an application to Einstein@Home results”. In: *Phys. Rev.* D89.12, p. 124030. DOI: [10.1103/PhysRevD.89.124030](https://doi.org/10.1103/PhysRevD.89.124030). arXiv: [1405.1922](https://arxiv.org/abs/1405.1922) [[gr-qc](#)].
- Shapiro, S. L. and S. A. Teukolsky (1983). *Black holes, white dwarfs, and neutron stars: The physics of compact objects*. Wiley, New York.
- Sintes, Alicia M. and Badri Krishnan (2006). “Improved hough search for gravitational wave pulsars”. In: *J. Phys. Conf. Ser.* 32, pp. 206–211. DOI: [10.1088/1742-6596/32/1/031](https://doi.org/10.1088/1742-6596/32/1/031). arXiv: [gr-qc/0601081](https://arxiv.org/abs/gr-qc/0601081) [[gr-qc](#)].
- (2007). *Hough search with improved sensitivity*. Tech. rep. LIGO-T070124. URL: <https://dcc.ligo.org/LIGO-T070124/public>.
- Sun, Ling and Andrew Melatos (2018). “Application of hidden Markov model tracking to the search for long-duration transient gravitational waves from the remnant of the binary neutron star merger GW170817”. In: arXiv: [1810.03577](https://arxiv.org/abs/1810.03577) [[astro-ph.IM](#)].
- Thorne, K. S. (1980). “Multipole Expansions of Gravitational Radiation”. In: *Rev. Mod. Phys.* 52, pp. 299–339. DOI: [10.1103/RevModPhys.52.299](https://doi.org/10.1103/RevModPhys.52.299).
- Thrane, Eric et al. (2011). “Long gravitational-wave transients and associated detection strategies for a network of terrestrial interferometers”. In: *Phys. Rev.* D83, p. 083004. DOI: [10.1103/PhysRevD.83.083004](https://doi.org/10.1103/PhysRevD.83.083004). arXiv: [1012.2150](https://arxiv.org/abs/1012.2150) [[astro-ph.IM](#)].
- Usman, Samantha A. et al. (2016). “The PyCBC search for gravitational waves from compact binary coalescence”. In: *Class. Quant. Grav.* 33.21, p. 215004. DOI: [10.1088/0264-9381/33/21/215004](https://doi.org/10.1088/0264-9381/33/21/215004). arXiv: [1508.02357](https://arxiv.org/abs/1508.02357) [[gr-qc](#)].
- Van Putten, Maurice H. P. M. (2016). “Directed searches for broadband extended gravitational-wave emission in nearby energetic core-collapse supernovae”. In: *Astrophys. J.* 819, p. 169. DOI: [10.3847/0004-637X/819/2/169](https://doi.org/10.3847/0004-637X/819/2/169). arXiv: [1602.03634](https://arxiv.org/abs/1602.03634) [[astro-ph.HE](#)].
- Veitch, J. and A. Vecchio (2010). “Bayesian coherent analysis of in-spiral gravitational wave signals with a detector network”. In: *Phys. Rev.* D81, p. 062003. DOI: [10.1103/PhysRevD.81.062003](https://doi.org/10.1103/PhysRevD.81.062003). arXiv: [0911.3820](https://arxiv.org/abs/0911.3820) [[astro-ph.CO](#)].
- Virtanen, Pauli et al. (Apr. 2018). *Scipy 1.1.0rc1*. DOI: [10.5281/zenodo.1218715](https://doi.org/10.5281/zenodo.1218715).
- Wainstein, L.A. and V.D. Zubakov (1962). *Extraction of Signals from Noise*. Prentice-Hall, Englewood Cliffs.
- Walsh, S. and Pitkin, M. and Oliver, M. and D’Antonio, S. and Dergachev, V. and Królak, A. and Astone, P. and Bejger, M. and Di Giovanni, M. and Dorosh, O. and Frasca, S. and Leaci, P. and Mastrogiovanni, S. and Miller, A. and Palomba, C. and Papa, M. A. and Piccinni, O. J. and Riles, K. and Sauter, O. and Sintes, A. M. (2016). “Comparison of methods for the detection of gravitational waves from unknown neutron stars”. In: *Phys. Rev.* D94.12, p. 124010. DOI: [10.1103/PhysRevD.94.124010](https://doi.org/10.1103/PhysRevD.94.124010). arXiv: [1606.00660](https://arxiv.org/abs/1606.00660) [[gr-qc](#)].

- 
- Wette, K. et al. (2008). “Searching for gravitational waves from Cassiopeia A with LIGO”. In: *Class. Quant. Grav.* 25, p. 235011. DOI: [10.1088/0264-9381/25/23/235011](https://doi.org/10.1088/0264-9381/25/23/235011). arXiv: [0802.3332](https://arxiv.org/abs/0802.3332) [gr-qc].
- Wette, Karl (2012). “Estimating the sensitivity of wide-parameter-space searches for gravitational-wave pulsars”. In: *Phys. Rev. D* 85 (4), p. 042003. DOI: [10.1103/PhysRevD.85.042003](https://doi.org/10.1103/PhysRevD.85.042003). URL: <https://link.aps.org/doi/10.1103/PhysRevD.85.042003>.
- Zevin, Michael et al. (2017). “Gravity Spy: Integrating Advanced LIGO Detector Characterization, Machine Learning, and Citizen Science”. In: *Class. Quant. Grav.* 34.6, p. 064003. DOI: [10.1088/1361-6382/aa5cea](https://doi.org/10.1088/1361-6382/aa5cea). arXiv: [1611.04596](https://arxiv.org/abs/1611.04596) [gr-qc].
- Zimmermann, M. and E. Szedenits (1979). “Gravitational Waves from rotating and precessing rigid bodies: simple models and applications to pulsars”. In: *Phys. Rev. D* 20, pp. 351–355. DOI: [10.1103/PhysRevD.20.351](https://doi.org/10.1103/PhysRevD.20.351).





## Appendix A

# Permissions for Chapter 3

Dr. **Orest Dorosh**, as co-author of the following article:

Comparison of methods for the detection of gravitational waves from unknown neutron stars

S. Walsh, M. Pitkin, M. Oliver, S. D'Antonio, V. Dergachev, A. Królak, P. Astone, M. Bejger, M. Di Giovanni, O. Dorosh, S. Frasca, P. Leaci, S. Mastrogiovanni, A. Miller, C. Palomba, M. A. Papa, O. J. Piccinni, K. Riles, O. Sauter, and A. M. Sintes  
Phys. Rev. D 94 124010

I DECLARE:

That I accept that Mr. Miquel Oliver Almiñana presents the cited article as one of the principal authors leading the Sky-Hough pipeline results as part of his doctoral thesis. Therefore, this article can not be part of any other doctoral thesis.

And for all intents and purposes, hereby signs this document.

Signature *Dorosh*

Warsaw, 21st December 2018

Prof. **Andrzej Królak**, as co-author of the following article:

Comparison of methods for the detection of gravitational waves from unknown neutron stars

S. Walsh, M. Pitkin, M. Oliver, S. D'Antonio, V. Dergachev, A. Królak, P. Astone, M. Bejger, M. Di Giovanni, O. Dorosh, S. Frasca, P. Leaci, S. Mastrogiovanni, A. Miller, C. Palomba, M. A. Papa, O. J. Piccinni, K. Riles, O. Sauter, and A. M. Sintes  
Phys. Rev. D 94 124010

I DECLARE:

That I accept that Mr. Miquel Oliver Almiñana presents the cited article as one of the principal authors leading the Sky-Hough pipeline results as part of his doctoral thesis. Therefore, this article can not be part of any other doctoral thesis.

And for all intents and purposes, hereby signs this document.

Signature



Warsaw, 21st December 2018

MAX-PLANCK-INSTITUT FÜR GRAVITATIONSPHYSIK  
ALBERT-EINSTEIN-INSTITUT  
Teilinstitut Hannover

MPI für Gravitationsphysik Callinstraße 38, 30167 Hannover



TO WHOM IT MAY CONCERN

cc/  
- Miquel Oliver Almiñana <miquel\_oli@me.com>  
- Alicia Sintes <alicia.sintes@uib.es>

**Dr. Maria Alessandra Papa**  
Searches for Continuous  
Gravitational Waves  
Tel.: +49 511 762 17160  
Fax: +49 511 762 17182  
Email: Maria.Alessandra.Papa@aei.mpg.de

Hannover, 13 February 2019

As co-author of the following article:

**Comparison of methods for the detection of gravitational waves from unknown neutron stars**

S. Walsh, M. Pitkin, M. Oliver, S. D'Antonio, V. Dergachev, A. Królak, P. Astone, M. Bejger, M. Di Giovanni, O. Dorosh, S. Frasca, P. Leaci, S. Mastrogiovanni, A. Miller, C. Palomba, M. A. Papa, O. J. Piccinni, K. Riles, O. Sauter, and A. M. Sintes  
*Phys. Rev. D* 94 124010

I DECLARE:

That I accept that Mr. Miquel Oliver Almiñana presents the cited article as one of the principal authors leading the Sky-Hough pipeline results as part of his doctoral thesis. Therefore, the sky-Hough results of this article cannot be part of any other doctoral thesis.

And for all intents and purposes, I hereby sign this document.

Hannover, 13 February 2019

Dr. Maria Alessandra Papa  
Leader of the Independent Research Group  
"Searches for Continuous Gravitational Waves"



Paris, 13 February 2019

To whom it may concern:

I, dr Michał Bejger, as co-author of the following article:

*Comparison of methods for the detection of gravitational waves from unknown neutron stars*,  
S. Walsh, M. Pitkin, M. Oliver, S. D'Antonio, V. Dergachev, A. Królak, P. Astone, M. Bejger,  
M. Di Giovanni, O. Dorosh, S. Frasca, P. Leaci, S. Mastrogiovanni, A. Miller, C. Palomba, M. A. Papa,  
O. J. Piccinni, K. Riles, O. Sauter, and A. M. Sintes, *Phys. Rev. D* 94 124010

DECLARE,

that I accept that Mr. Miquel Oliver Almiñana presents the cited article as one of the principal authors leading the Sky-Hough pipeline results as part of his doctoral thesis. Therefore, the Sky-Hough results of this article can not be part of any other doctoral thesis.

And for all intents and purposes, hereby sign this document.

Sincerely,

Michał Bejger

A handwritten signature in blue ink, appearing to read 'M Bejger', is written over the printed name 'Michał Bejger'.

Dr. Orion Sauter, as co-author of the following article:

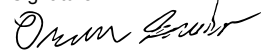
Comparison of methods for the detection of gravitational waves from unknown neutron stars  
S. Walsh, M. Pitkin, M. Oliver, S. D'Antonio, V. Dergachev, A. Królak, P. Astone, M. Bejger, M.  
Di Giovanni, O. Dorosh, S. Frasca, P. Leaci, S. Mastrogiovanni, A. Miller, C. Palomba, M. A.  
Papa, O. J. Piccinni, K. Riles, O. Sauter, and A. M. Sintes  
Phys. Rev. D 94 124010

I DECLARE:

That I accept that Mr. Miquel Oliver Almiñana presents the cited article as one of the principal authors leading the Sky-Hough pipeline results as part of his doctoral thesis. Therefore, this article can not be part of any other doctoral thesis.

And for all intents and purposes, hereby signs this document.

Signature



Annecy, France 19 Dec 2018

Dr. Ornella Juliana Piccinni, as co-author of the following article:

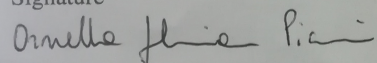
Comparison of methods for the detection of gravitational waves from unknown neutron stars  
S. Walsh, M. Pitkin, M. Oliver, S. D'Antonio, V. Dergachev, A. Królak, P. Astone, M. Bejger, M. Di  
Giovanni, O. Dorosh, S. Frasca, P. Leaci, S. Mastrogiovanni, A. Miller, C. Palomba, M. A. Papa, O. J.  
Piccinni, K. Riles, O. Sauter, and A. M. Sintes  
Phys. Rev. D 94 124010

I DECLARE:

That I accept that Mr. Miquel Oliver Almiñana presents the cited article as one of the principal authors leading the Sky-Hough pipeline results as part of his doctoral thesis. Therefore, this article can not be part of any other doctoral thesis.

And for all intents and purposes, hereby signs this document.

Signature



ROME, 19-12-2018

Prof. Paola Leaci, as co-author of the following article:

*Comparison of methods for the detection of gravitational waves from unknown neutron stars*

S. Walsh, M. Pitkin, M. Oliver, S. D'Antonio, V. Dergachev, A. Królak, P. Astone, M. Bejger, M. Di Giovanni, O. Dorosh, S. Frasca, P. Leaci, S. Mastrogiovanni, A. Miller, C. Palomba, M. A. Papa, O. J. Piccinni, K. Riles, O. Sauter, and A. M. Sintes  
Phys. Rev. D 94 124010

I DECLARE:

That I accept that Mr. Miquel Oliver Almiñana presents the cited article as one of the principal authors leading the Sky-Hough pipeline results as part of his doctoral thesis. Therefore, the sky-Hough results of this article can not be part of any other doctoral thesis.

And for all intents and purposes, hereby signs this document.

Signature



Rome, February 13 (2019)



School of Physics & Astronomy  
University of Glasgow  
Glasgow,  
G12 8QQ, UK

19/12/2018

Dr. Matthew Pitkin, as co-author of the following article:

Comparison of methods for the detection of gravitational waves from unknown neutron stars, S. Walsh, M. Pitkin, M. Oliver, S. D'Antonio, V. Dergachev, A. Królak, P. Astone, M. Bejger, M. Di Giovanni, O. Dorosh, S. Frasca, P. Leaci, S. Mastrogiovanni, A. Miller, C. Palomba, M. A. Papa, O. J. Piccinni, K. Riles, O. Sauter, and A. M. Sintes  
Phys. Rev. D 94 124010

I DECLARE:

That I accept that Mr. Miquel Oliver Almiñana presents the cited article as one of the principal authors leading the Sky-Hough pipeline results as part of his doctoral thesis. Therefore, this article can not be part of any other doctoral thesis.

And for all intents and purposes, hereby signs this document.

A handwritten signature in purple ink, appearing to be "M. Pitkin", written over a light grey rectangular background.

**Dr Matthew Pitkin**

**Dr Matthew Pitkin**  
Post-doctoral Research Fellow  
School of Physics & Astronomy

Kelvin Building, University of Glasgow, University Avenue,  
Glasgow, G12 8QQ. Direct Line +44 (0)141 330 7168  
Email: matthew.pitkin@glasgow.ac.uk  
The University of Glasgow, charity number SC004401

Dr. Simone Mastrogiovanni, as co-author of the following article:

*Comparison of methods for the detection of gravitational waves from unknown neutron stars*

S. Walsh, M. Pitkin, M. Oliver, S. D'Antonio, V. Dergachev, A. Królak, P. Astone, M. Bejger, M. Di Giovanni, O. Dorosh, S. Frasca, P. Leaci, S. Mastrogiovanni, A. Miller, C. Palomba, M. A. Papa, O.J. Piccinni, K. Riles, O. Sauter, and A. M. Sintes  
Phys. Rev. D 94 124010

I DECLARE:

That I accept that Mr. Miquel Oliver Almiñana presents the cited article as one of the principal authors leading the Sky-Hough pipeline results as part of his doctoral thesis. Therefore, the sky-Hough results of this article can not be part of any other doctoral thesis.

And for all intents and purposes, hereby signs this document.

Signature



where, date

Amsterdam, 13th Feb 2019

Dr. Sinéad Walsh, as co-author of the following article:

Comparison of methods for the detection of gravitational waves from unknown neutron stars  
S. Walsh, M. Pitkin, M. Oliver, S. D'Antonio, V. Dergachev, A. Królak, P. Astone, M. Bejger, M.  
Di Giovanni, O. Dorosh, S. Frasca, P. Leaci, S. Mastrogiovanni, A. Miller, C. Palomba, M. A.  
Papa, O. J. Piccinni, K. Riles, O. Sauter, and A. M. Sintes  
Phys. Rev. D 94 124010

I DECLARE:

That I accept that Mr. Miquel Oliver Almiñana presents the cited article as one of the principal authors leading the Sky-Hough pipeline results as part of his doctoral thesis. Therefore, this article can not be part of any other doctoral thesis.

And for all intents and purposes, hereby signs this document.

Signature



where, date

Milwaukee, 7/1/19

Dr. Vladimir Dergachev, as co-author of the following article:

Comparison of methods for the detection of gravitational waves from unknown neutron stars  
S. Walsh, M. Pitkin, M. Oliver, S. D'Antonio, V. Dergachev, A. Królak, P. Astone, M. Bejger, M. Di  
Giovanni, O. Dorosh, S. Frasca, P. Leaci, S. Mastrogiovanni, A. Miller, C. Palomba, M. A. Papa,  
O. J. Piccinni, K. Riles, O. Sauter, and A. M. Sintes  
Phys. Rev. D 94 124010

I DECLARE:

That I accept that Mr. Miquel Oliver Almiñana presents the cited article as one of the principal authors leading the Sky-Hough pipeline results as part of his doctoral thesis. Therefore, this article can not be part of any other doctoral thesis.

And for all intents and purposes, hereby signs this document.



Herndon, Virginia, 2018-Dec-26



---

**DIPARTIMENTO DI FISICA - UNIVERSITA' DEGLI STUDI DI TRENTO**

**MATTEO DI GIOVANNI** 26 febbraio 2019  
[matteo.digiovanni@unitn.it](mailto:matteo.digiovanni@unitn.it)

Dipartimento di Fisica  
Università degli Studi di  
Trento  
Via Sommarive 14  
38123  
Povo (TN)

Alicia Sintès  
UIB  
Fac. de Ciències. U. de Balears  
Carretera de Valldemossa Km 7.5  
Palma de Mallorca  
Balearic Islands  
07122 Spain

Mr Matteo Di Giovanni, as co-author of the following article:

*Comparison of methods for the detection of gravitational waves from unknown neutron stars*

S. Walsh, M. Pitkin, M. Oliver, S. D'Antonio, V. Dergachev, A. Królak, P. Astone, M. Bejger, M. Di Giovanni, O. Dorosh, S. Frasca, P. Leaci, S. Mastrogiovanni, A. Miller, C. Palomba, M. A. Papa, O. J. Piccinni, K. Riles, O. Sauter, and A. M. Sintès

**Phys. Rev. D 94 124010**

I DECLARE:

That I accept that Mr. Miquel Oliver Almiñana presents the cited article as one of the principal authors leading the Sky-Hough pipeline results as part of his doctoral thesis. Therefore, the sky-Hough results of this article can not be part of any other doctoral thesis. And for all intents and purposes, hereby signs this document.

Trento, 26/02/2019



Professor Sergio Frasca as co-author of the following article:

Comparison of methods for the detection of gravitational waves from unknown neutron stars  
S. Walsh, M. Pitkin, M. Oliver, S. D'Antonio, V. Dergachev, A. Królak, P. Astone, M. Bejger, M. Di  
Giovanni, O. Dorosh, S. Frasca, P. Leaci, S. Mastrogiovanni, A. Miller, C. Palomba, M. A. Papa, O.  
J. Piccinni, K. Riles, O. Sauter, and A. M. Sintes  
Phys. Rev. D 94 124010

I DECLARE:

That I accept that Mr. Miquel Oliver Almiñana presents the cited article as one of the principal  
authors leading the Sky-Hough pipeline results as part of his doctoral thesis. Therefore, this  
article cannot be part, as a whole, of any other doctoral thesis.  
And for all intents and purposes, hereby signs this document.

Sergio Frasca



2019, February, 19

Dr. Pia Astone as co-author of the following article:

Comparison of methods for the detection of gravitational waves from unknown neutron stars  
S. Walsh, M. Pitkin, M. Oliver, S. D'Antonio, V. Dergachev, A. Królak, P. Astone, M. Bejger, M. Di  
Giovanni, O. Dorosh, S. Frasca, P. Leaci, S. Mastrogiovanni, A. Miller, C. Palomba, M. A. Papa, O. J.  
Piccinni, K. Riles, O. Sauter, and A. M. Sintes  
Phys. Rev. D 94 124010

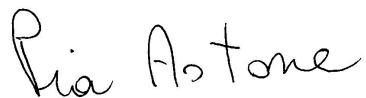
I DECLARE:

That I accept that Mr. Miquel Oliver Almiñana presents the cited article as one of the principal authors leading the Sky-Hough pipeline results as part of his doctoral thesis. Therefore, this article cannot be part, as a whole, of any other doctoral thesis.

And for all intents and purposes, hereby signs this document.

2019, February, 19

Signature

A handwritten signature in black ink that reads "Pia Astone". The signature is written in a cursive, flowing style.

Paris, 13 February 2019

To whom it may concern:

I, dr Michał Bejger, as co-author of the following article:

*Comparison of methods for the detection of gravitational waves from unknown neutron stars*,  
S. Walsh, M. Pitkin, M. Oliver, S. D'Antonio, V. Dergachev, A. Królak, P. Astone, M. Bejger,  
M. Di Giovanni, O. Dorosh, S. Frasca, P. Leaci, S. Mastrogiovanni, A. Miller, C. Palomba, M. A. Papa,  
O. J. Piccinni, K. Riles, O. Sauter, and A. M. Sintes, *Phys. Rev. D* 94 124010

DECLARE,

that I accept that Mr. Miquel Oliver Almiñana presents the cited article as one of the principal authors leading the Sky-Hough pipeline results as part of his doctoral thesis. Therefore, the Sky-Hough results of this article can not be part of any other doctoral thesis.

And for all intents and purposes, hereby sign this document.

Sincerely,

Michał Bejger





**Universitat**  
de les Illes Balears

Dr. Alicia M Sintes Olives  
Departament de Física & IAC3  
Universitat de les Illes Balears &  
Institut d'Estudis Espacials de Catalunya  
Cra. Valldemossa km 7.5  
E-07122 Palma de Mallorca, Spain  
Tel.: +34 971 25 98 34  
Fax: +34 971 17 34 26

To whomsoever it may concern

Dr. Alicia Sintes Olives, as co-author of the following article:

"Comparison of methods for the detection of gravitational waves from unknown neutron stars" by S. Walsh, M. Pitkin, M. Oliver, S. D'Antonio, V. Dergachev, A. Królak, P. Astone, M. Bejger, M. Di Giovanni, O. Dorosh, S. Frasca, P. Leaci, S. Mastrogiovanni, A. Miller, C. Palomba, M. A. Papa, O. J. Piccinni, K. Riles, O. Sauter, and A. M. Sintes, published in Phys. Rev. D 94 124010

I DECLARE:

That I accept that Mr. Miquel Oliver Almiñana presents the cited article as one of the principal authors leading the Sky-Hough pipeline results as part of his doctoral thesis. Therefore, this article cannot be part, as a whole, of any other doctoral thesis.

And for all intents and purposes, hereby signs this document.

Signature

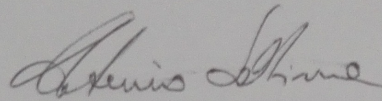
Palma, February 19th 2019

I DECLARE:

That I accept that Mr. Miquel Oliver Almiñana presents the cited article as one of the principal authors leading the Sky-Hough pipeline results as part of his doctoral thesis. Therefore, the sky-Hough results of this article can not be part of any other doctoral thesis.

And for all intents and purposes, hereby signs this document.

Signature



Rome Italy 13/02/2019

---

Mr Andrew Miller, as co-author of the following article

Comparison of methods for the detection of gravitational waves from unknown neutron stars

S. Walsh, M. Pitkin, M. Oliver, S. D'Antonio, V. Dergachev, A. Królak, P. Astone, M. Bejger, M. Di Giovanni, O. Dorosh, S. Frasca, P. Leaci, S. Mastrogiovanni, A. Miller, C. Palomba, M. A. Papa, O. J. Piccinni, K. Riles, O. Sauter, and A. M. Sintes  
Phys. Rev. D 94 124010

I DECLARE:

Accepts that Mr Miquel Oliver Almiñana presents the cited article in his doctoral thesis as one of the principal authors being the leather of Skyhough's pipeline results and that said article cannot, therefore, form part of any doctoral thesis.

And for all intents and purposes, hereby signs this document.

Signature

A handwritten signature in black ink that reads "Andrew Miller". The signature is written in a cursive style with a light blue horizontal line underneath the text.



SEZIONE DI ROMA  
c/o Dip. Di Fisica  
Universita' di Roma "Sapienza"  
Piazzale Aldo Moro, 2  
00185 Roma - Italy

Dr. Cristiano Palomba, as co-author of the following article:

Comparison of methods for the detection of gravitational waves from unknown neutron stars

S. Walsh, M. Pitkin, M. Oliver, S. D'Antonio, V. Dergachev, A. Królak, P. Astone, M. Bejger, M. Di Giovanni, O. Dorosh, S. Frasca, P. Leaci, S. Mastrogiovanni, A. Miller, C. Palomba, M. A. Papa, O. J. Piccinni, K. Riles, O. Sauter, and A. M. Sintes  
Phys. Rev. D [94 124010](#)

I DECLARE:

That I accept that Mr. Miquel Oliver Almiñana presents the cited article as one of the principal authors leading the Sky-Hough pipeline results as part of his doctoral thesis. Therefore, this article cannot be part of any other doctoral thesis.

And for all intents and purposes, hereby signs this document.

Sincerely,  
Cristiano Palomba

Rome, December 20th, 2018







## Appendix B

# Permissions for Chapter 5

Dr. ~~Mr~~ David Keitel as co-author of the following article:

The Adaptive Transient Hough method for long-duration gravitational  
wave transients  
Miquel Oliver, David Keitel, Alicia M. Sintes  
arxiv:1901.01820

I DECLARE:

That I accept that Mr. Miquel Oliver Almiñana presents the cited  
article as the principal author in his doctoral thesis. Therefore,  
this article can not be part of any other doctoral thesis.

And for all intents and purposes, hereby signs this document.

Signature

David Keitel 2019109/22



**Universitat**  
de les Illes Balears

Dr. Alicia M Sintes Olives  
Departament de Física & IAC3  
Universitat de les Illes Balears &  
Institut d'Estudis Espacials de Catalunya  
Cra. Valldemossa km 7.5  
E-07122 Palma de Mallorca, Spain  
Tel.: +34 971 25 98 34  
Fax: +34 971 17 34 26

To whomsoever it may concern

Dr. Alicia Sintes Olives, as co-author of the following article:

"The Adaptive Transient Hough method for long-duration gravitational wave transients" by [Miquel Oliver](#), [David Keitel](#), [Alicia M. Sintes](#)  
[arXiv:1901.01820](#)

*Submitted to Physical Review D*

I DECLARE:

That I accept that Mr. Miquel Oliver Almiñana presents the cited article as the principal author in his doctoral thesis. Therefore, this article cannot be part of any other doctoral thesis.

And for all intents and purposes, hereby signs this document.

Signature

A handwritten signature in black ink, appearing to read 'Alicia M. Sintes', written over a horizontal line.

Palma, February 19th 2019





## Appendix C

# Permissions for Chapter 6



**Universitat**  
de les Illes Balears

Dr. Alicia M Sintes Olives  
Departament de Física & IAC3  
Universitat de les Illes Balears &  
Institut d'Estudis Espacials de Catalunya  
Cra. Valldemossa km 7.5  
E-07122 Palma de Mallorca, Spain  
Tel.: +34 971 25 98 34  
Fax: +34 971 17 34 26

To whomsoever it may concern

Dr. Alicia Sintes Olives, as co-author of the following article:

"Matched-filter study and energy budget suggest no detectable gravitational-wave 'extended emission' from GW170817" by Miquel Oliver, David Keitel, Andrew L. Miller, Hector Estelles, and Alicia M. Sintes arXiv:1812.06724 published in

*Monthly Notices of the Royal Astronomical Society*, stz439,  
<https://doi.org/10.1093/mnras/stz439>  
Published:15 February 2019

I DECLARE:

That I accept that Mr. Miquel Oliver Almiñana presents the cited article as the principal author in his doctoral thesis. Therefore, this article cannot be part of any other doctoral thesis.

And for all intents and purposes, hereby signs this document.

Signature

A handwritten signature in black ink, appearing to read 'Alicia M. Sintes Olives', written over a horizontal line.

Palma, February 19th 2019

Dr. ~~Mr~~ David Keitel as co-author of the following article:

Matched-filter study and energy budget suggest no detectable  
gravitational-wave 'extended emission' from GW170817  
Miquel Oliver, David Keitel, Andrew L. Miller, Hector Estelles,  
Alicia M. Sintes  
arXiv:1812.06724

I DECLARE:

That I accept that Mr. Miquel Oliver Almiñana presents the cited  
article as the principal author in his doctoral thesis. Therefore,  
this article can not be part of any other doctoral thesis.

And for all intents and purposes, hereby signs this document.

Signature

David Keitel 2019/01/22

Dr./Mr Hector Estellés Estrella as co-author of the following article:

Matched-filter study and energy budget suggest no detectable gravitational-wave 'extended emission' from GW170817  
Miquel Oliver, David Keitel, Andrew L. Miller, Hector Estelles, Alicia M. Sintes  
arXiv:1812.06724

I DECLARE:

That I accept that Mr. Miquel Oliver Almiñana presents the cited article as the principal author in his doctoral thesis. Therefore, this article can not be part of any other doctoral thesis.

And for all intents and purposes, hereby signs this document.

Signature

\_\_\_\_\_





---

Dr./Mr Andrew L. Miller as co-author of the following article:

Matched-filter study and energy budget suggest no detectable gravitational-wave 'extended emission' from GW170817

Miquel Oliver, David Keitel, Andrew L. Miller, Hector Estelles, Alicia M. Sintes  
arXiv:1812.06724

I DECLARE:

That I accept that Mr. Miquel Oliver Almiñana presents the cited article as the principal author in his doctoral thesis. Therefore, this article can not be part of any other doctoral thesis.

And for all intents and purposes, hereby signs this document.

Signature

A handwritten signature in black ink that reads "Andrew Miller". The signature is written in a cursive style with a light blue horizontal line underneath it.